

Theory of Light – Atomic Ensemble Interactions: Entanglement, Storage, and Retrieval

A Thesis
Presented to
The Academic Faculty

by

Stewart D. Jenkins

In Partial Fulfillment
of the Requirements for the Degree
Doctor of Philosophy

School of Physics
Georgia Institute of Technology
December 2006

Copyright © 2006 by Stewart D. Jenkins

Theory of Light – Atomic Ensemble Interactions: Entanglement, Storage, and Retrieval

Approved by:

Prof. T. A. Brian Kennedy, Advisor
School of Physics
Georgia Institute of Technology

Prof. Chandra Raman
School of Physics
Georgia Institute of Technology

Prof. Alex Kuzmich
School of Physics
Georgia Institute of Technology

Prof. Thomas D. Morley
School of Mathematics
Georgia Institute of Technology

Prof. Michael S. Chapman
School of Physics
Georgia Institute of Technology

Date Approved: September 21, 2006

ACKNOWLEDGEMENTS

I would first like to express my gratitude to my thesis advisor, Brian Kennedy, for his continuous guidance and support. His physical understanding and attention to detail have greatly benefited me throughout the performance of my research. I would also like to thank Prof. Alex Kuzmich, whose experimental collaboration was an integral part of the work presented here. I further thank the members of my thesis committee, Prof. Michael Chapman, Prof. Chandra Raman, for beneficial discussions and collaborations, and Prof. Tom Morley.

I also acknowledge the contributions to this work of my collaborators and friends Dr. D. N. Matsukevich, Dr. T. Chanelière, and S.-Y. Lan, without whose collaboration, this work would not have been possible. Furthermore, I would like to thank O. A. Collins, H.-H. Jen, Dr. D. S. Naik, K. Fortier, Dr. M. S. Chang, C. Campbell, and R. Zhao for useful discussions. I also thank my cat, Guinness, who serves a metaphor for my friends and family who have provided me with continuous love and support.

TABLE OF CONTENTS

ACKNOWLEDGEMENTS	iii
LIST OF TABLES	vii
LIST OF FIGURES	viii
SUMMARY	xv
1 INTRODUCTION	1
1.1 Quantum Communication	3
1.2 Quantum Networks and Atomic Ensembles	4
1.2.1 Atomic ensembles as quantum memories	7
1.3 Outline	9
2 REVIEW OF THE QUANTUM THEORY OF LIGHT-ATOM INTERACTIONS	12
2.1 Electric Dipole Hamiltonian	12
2.1.1 The atomic Hamiltonian $\hat{H}_0^{(\mu)}$	16
2.1.2 The atomic dipole operator $\hat{\mathbf{d}}$	22
2.1.3 The Interaction Picture	24
2.1.4 Decomposition of the electromagnetic field	25
2.2 Ensemble Interactions with Narrow Bandwidth Fields	31
3 ENTANGLING A PHOTON WITH A COLLECTIVE ATOMIC EXCITATION	34
3.1 Introduction	34
3.2 Theory	38
3.2.1 The Write Process: Raman Scattering from a Collection of Atoms	40
3.2.2 The Read Process: Transferring the Spin Wave to the Idler Field	55
3.3 Experiment	62

4	QUANTUM TELECOMMUNICATION BASED ON ATOMIC CASCADE TRANSITIONS	66
4.1	Introduction	66
4.2	Proposal	67
4.3	Theory	70
4.4	Experiment	77
5	DETERMINISTIC SINGLE PHOTONS VIA CONDITIONAL QUANTUM EVOLUTION	85
5.1	Introduction	85
5.2	Heralded Single Photon Source	88
5.3	Protocol for Generation of Deterministic Single Photons	93
6	STORAGE AND RETRIEVAL OF SINGLE PHOTONS TRANSMITTED BETWEEN REMOTE QUANTUM MEMORIES . . .	100
6.1	Introduction	100
6.2	Experiment	102
6.3	Measurement Procedure	110
6.4	Photoelectric counting statistics	111
6.5	Conclusion	114
7	DARK-STATE POLARITON COLLAPSES AND REVIVALS .	115
7.1	Introduction	116
7.2	Theory	117
7.3	Experimental Observation	127
7.4	Conclusion	135
8	ENTANGLEMENT OF REMOTE ATOMIC QUBITS	136
8.1	Introduction	136
8.2	Theory and Experiment	138
8.3	Measurement of Bell's Inequality Violation	145
8.3.1	Fidelity of entanglement between remote Sites A and B . . .	146
8.4	Conclusion	147

9	CONCLUSION	149
APPENDIX A	— POLARIZATION CONVENTIONS	151
APPENDIX B	— DERIVATION OF THE EFFECTIVE HAMIL- TONIAN FOR SCATTERING FROM ATOMIC ENSEMBLES	153
APPENDIX C	— DYNAMICS OF LIGHT PROPAGATION IN A GAS OF THREE-LEVEL ATOMS	161
APPENDIX D	— PHOTON COUNTING STATISTICS FOR A PAIR OF CORRELATED SINGLE MODE FIELDS	187
REFERENCES	198

LIST OF TABLES

2.1	The magnetic dipole constants A_{hfs} and electric quadrapole constants B_{hfs} for the hyperfine interaction within ^{85}Rb atoms. These quantities are given as a function of fine structure level j for the ground state and first two excited state fine structure levels. The numerical values have been obtained from Ref. [82]. The values of B_{hfs} are not given for the $5^2S_{1/2}$ and $5^2P_{1/2}$ manifolds since the electric quadrapole interaction (the second term in Eq. (2.23)) is identically zero for these levels [81].	20
3.1	Measured correlation function $E(\theta_s, \theta_i)$ and S for $\Delta t = 200$ ns delay between <i>write</i> and <i>read</i> pulses; all the errors are based on the statistics of the photon counting events.	63
4.1	Measured correlation function $E(\theta_s, \theta_i)$ and S for $\lambda_s = 776$ nm and $\lambda_s = 1.53\mu\text{m}$	81
8.1	Measured values of the correlation function $E(\theta_A, \theta_B)$ at particular polarization settings and the Bell parameter S	146
8.2	Inferred density matrix elements ρ_{ij} . Error bars represent \pm one standard deviation and are based on the statistics of the photoelectric counting events.	147

LIST OF FIGURES

2.1	A diagram illustrates a sample of fine structure levels for ^{85}Rb . The fine structure levels are organized according to their orbital angular momentum and total electronic angular momentum, as indicated by the labels across the top of the diagram. The levels are arranged vertically according to their energies. A sample of allowed transitions between the levels is illustrated by color lines connecting the various levels, where the resonance frequency of the transition is given by the color coded text. The energy differences between two adjacent levels is given by $2\pi\hbar$ times the indicated frequency.	19
2.2	Shows a diagram of the energy levels of ^{85}Rb that form the ground state $5^2S_{1/2}$, and excited state $5^2P_{1/2}$ and $5^2P_{3/2}$ fine structure levels. These levels are involved in the $D1$ ($5^2S_{1/2} \leftrightarrow 5^2P_{1/2}$) and $D2$ ($5^2S_{1/2} \leftrightarrow 5^2P_{3/2}$) line transitions. The energies difference between two adjacent hyperfine levels is by $2\pi\hbar$ times the indicated frequency.	21
3.1	(a) Schematic of experimental setup. P_1 and P_2 , polarizers; D1 and D2, detectors; $\lambda/4$, quarter-waveplate. (b) The structure of atomic transitions leading to generation of atom-photon entanglement and of the subsequent read-out of atomic qubit.	36
3.2	Measured coincidence fringe for $\theta_i = 67.5^\circ$. The curve is a fit based on Eq.(3.5), augmented by a background contribution, with $\eta = 0.81 \times \pi/4$, with visibility and amplitude being adjustable parameters. The visibility of the fit is 90%. Uncertainties are based on the statistics of the photon counting events.	63
3.3	Normalized signal-idler intensity correlation function g_{si} as a function of storage time. Uncertainties are based on the statistics of the photon counting events. The full curve is the best exponential fit with time constant $\tau = 3.7\mu\text{s}$	64

4.1	(a) The atomic structure for the proposed cascade emission scheme involving excitation by pumps I and II. Pump II and the signal photons lie in the telecommunication wavelength range when a suitable level of orbital angular momentum $L = 0$ or $L = 2$ is used as level $ d\rangle$. For atomic rubidium, the signal wavelength is $1.32\mu\text{m}$ ($6S_{1/2} \rightarrow 5P_{1/2}$ transition), $1.37\mu\text{m}$ ($6S_{1/2} \rightarrow 5P_{3/2}$ transition), $1.48\mu\text{m}$ ($4D_{3/2(5/2)} \rightarrow 5P_{1/2}$ transition), $1.53\mu\text{m}$ ($4D_{3/2(5/2)} \rightarrow 5P_{3/2}$ transition). For atomic cesium, the signal wavelength is $1.36\mu\text{m}$ ($7S_{1/2} \rightarrow 6P_{1/2}$ transition), $1.47\mu\text{m}$ ($7S_{1/2} \rightarrow 6P_{3/2}$ transition). For Na and K the corresponding wavelengths are in the $1.1\text{-}1.4\mu\text{m}$ range. (b) Schematic of experimental setup based on ultra-cold ^{85}Rb atomic gas. For $\lambda_s = 776\text{ nm}$, phase matching results in the angles $\varepsilon' \approx \varepsilon \approx 1^\circ$, while for $\lambda_s = 1.53\mu\text{m}$, $\varepsilon' \approx 2\varepsilon \approx 2^\circ$. P_1 and P_2 are polarizers; D1 and D2 are detectors.	69
4.2	(a) Count rate proportional to the signal-idler intensity correlation function G_{si} as a function of signal-idler delay τ , $ d\rangle = 5d_{5/2}, F = 4\rangle$. The quantum beats are associated with 120 MHz hyperfine splitting, $F = 3$ and 4, of the $5p_{3/2}$ level [97]. The solid curve is a fit of the form $\beta + A \exp(-t/\alpha) \sin^2(\pi\Omega t)$, where $\beta = 63$, $A = 2972$, $\alpha = 11\text{ ns}$ and $\Omega = 117\text{ MHz}$ are adjustable parameters. (b) Same as (a), but for $ d\rangle = 5d_{5/2}, F = 5\rangle$. Since this state can only decay through the $F = 4$ component of the $5p_{3/2}$ level, there are no quantum beats. The solid curve is an exponential fit with decay time of 3.2 ns. (c) The measured decay time vs the inverse measured optical thickness. (d) Measured coincidence fringes for $\theta_s = 45^\circ$ (red diamonds) and $\theta_s = 135^\circ$ (blue circles). The solid curves are fits based on Eqs. (4.1)(4.2), with $\cos \chi = 1/\sqrt{5}$	79
4.3	(a) Same as Figure 4.2(a,b), but for $ d\rangle = 4d_{5/2}, F = 5\rangle$. The solid curve is an exponential fit with decay time of 6.7 ns. (b) Measured coincidence fringes for $\theta_i = 45^\circ$ (red diamonds) and $\theta_i = 135^\circ$ (blue circles). The solid curves are fits based on Eqs. (4.1)(4.2), with $\cos \chi = 1/\sqrt{5}$	80
4.4	Efficiency of storage and subsequent retrieval of a coherent idler field with decay time of 6 ns in an auxiliary atomic ensemble, obtained by numerical integration of the Maxwell-Bloch equations [18, 19] as discussed in the text. The atomic coherence time is assumed to be much longer than the storage time.	81
5.1	Schematic of experimental setup, with the inset showing the atomic level scheme (see text).	86

5.2	Correlation functions g_{si} (panel (a)) and $\bar{\alpha}$ (panel (b)) as a function of p_1 , taken at $\tau = 80$ ns. The solid lines are based on Eq. (5.5,5.6), with addition of a nearly-negligible background contribution, as in Ref. [18]. The inset shows normalized signal-idler intensity correlation function g_{si} as a function of the storage time τ . The full curve is a fit of the form $1 + B \exp(-\tau^2/\tau_c^2)$ with $B = 16$ and the collapse time $\tau_c = 31.5 \mu s$ as adjustable parameters.	92
5.3	Predicted efficiency to generate and detect a single photon η_D as a function of N and p_1 . These predictions are based on Eq. (5.8) with the values of efficiencies and coherence times given in the text. . . .	94
5.4	Predicted values of η_D as a function of N and p_1 . These predictions are based on Eq. (5.8) with the values of efficiencies and coherence times given in the text.	95
5.5	$g_D^{(2)}(0)$ as a function of maximum number of trials N (panel (a)) and p_1 (panel (c)); measured efficiency to generate and detect a single photon η_D as a function of N (panel (b)) and p_1 (panel (d)). For panels (a) and (b) $p_1 = 0.003$ (about 6×10^5 photons per <i>write</i> pulse were used), whereas for panels (c) and (d) $N = 150$. The full curves are based on Eq. (5.8) with the values of efficiencies and coherence times given in the text, with however η_D multiplied by an empirical factor of $2/3$. We believe this reduced efficiency is due to imperfect switching of the <i>read</i> light in the feedback-based protocol (we note that there are no other adjustable parameters in the simple theory presented). Evident deviations from the theory in panels (c) and (d), beyond the statistical uncertainties associated with photoelectric counting events, could be explained either by inadequacies of the theory, or slow systematic drifts in the residual magnetic field and the <i>read</i> light leakage. . . .	96
5.6	$g_D^{(2)}$ as a function of N and p_1 in the limit of infinite atomic memory. The values for the efficiencies η_s and η_i are given in the text.	98
5.7	η_D as a function of N and p_1 in the limit of infinite atomic memory. The values for the efficiencies η_s and η_i are given in the text.	99

6.1	A schematic diagram of our experimental setup demonstrating generation, transmission, storage and retrieval of single photon excitations of the electromagnetic field. Two atomic ensembles at Sites <i>A</i> and <i>B</i> are connected by a single-mode fiber. The insets show the structure and the initial populations of atomic levels for the two ensembles. All the light fields responsible for trapping and cooling, as well as the quadrupole magnetic fields in both MOTs, are shut off during the period of the protocol. The ambient magnetic field at each Site is compensated by three pairs of Helmholtz coils (not shown). Correlated signal and idler fields are generated at Site <i>A</i> . The signal field is transmitted via optical fiber from Site <i>A</i> to Site <i>B</i> , where it is converted to atomic excitation, stored for a duration T_s , and subsequently retrieved. A Hanbury Brown-Twiss setup consisting of a beamsplitter BS and two detectors D2 and D3, together with detector D1 for the idler field, are used to verify the single photon character of the retrieved field.	103
6.2	Measured transmission spectra of a coherent probe field as the function of probe detuning in the presence of, and absence of, EIT. Data are taken using 700 ns long coherent laser pulses. T is the intensity transmittance, Δ is the probe detuning and Γ is the decay rate of level $ c\rangle$. In the absence of <i>control</i> field (circles) the probe is strongly absorbed near resonance, whereas with the <i>control</i> field on (diamonds) the medium becomes transparent. Each probe pulse contains on average 0.3 photons. Each data point is an average of 2×10^5 experimental trials. The optical thickness $d = 8$ and the <i>control</i> field Rabi frequency $\Omega = 3\Gamma$ are used to obtain the solid curves, based on the theoretical model discussed in Appendix C.	104
6.3	Experimental and theoretical pulse shapes as a function of time, showing EIT, storage and retrieval. The color code is: <i>control</i> field - black, pulse in vacuum - blue, delayed, stored and retrieved field - red. Panel (a) with a cw <i>control</i> field shows EIT pulse delay. In panel (b) the <i>control</i> field is switched off and then on again after 500 ns, shows light storage and retrieval. Panel (c) is similar to (b) but with a 15 μ s storage. Panels (d), (e), and (f) are corresponding theoretical plots. .	106
6.4	Measured intensity cross-correlation function g_{si} and anticorrelation function $\bar{\alpha}$ as a function of the idler photoelectric detection probability \mathbf{p}_1 . Panels (a) and (b) are for the source (propagation in vacuum). Panels (c) and (d) are for stopped, stored for 500 ns, and retrieved signal field. The solid lines are based on a theoretical model that includes losses and background. Error bars represent \pm one standard deviation and are based on the statistics of the photoelectric counting events.	108

6.5	Normalized signal-idler intensity correlation function g_{si} as a function of the storage time T_s at Site B . Data (diamonds) are taken for $p_1 = 0.0047$, but with a smaller background contribution than that of Figure 6.4, c and d. The full curve is a fit of the form $1+B \exp(-t^2/\tau^2)$ with $B = 7$ and the collapse time $\tau = 11 \mu s$ as adjustable parameters. Error bars represent \pm one standard deviation and are based on the statistics of the photoelectric counting events.	109
6.6	Normalized intensity autocorrelation functions g_{ii} (triangles) and g_{ss} (circles for the source, squares for the stored and retrieved field). Uncertainties are based on the statistics of the photon counting events.	113
7.1	On the left, a diagram shows an atomic ensemble interacting with copropagating signal and control fields. The signal (helicity α), resonant on the $ b\rangle \leftrightarrow c\rangle$ transition, is stored and subsequently retrieved by variation of a control field (helicity β), which resonantly couples levels $ a\rangle$ and $ c\rangle$. A constant magnetic field \vec{B} , oriented at an angle θ from the propagation axis, rotates the atomic coherences during the storage. For each state $ b, m\rangle$ in level $ b\rangle$, there is either an associated Λ configuration, as shown on the right, or an unconnected one, as discussed in the text. The signal connects the states $ b, m\rangle$ and $ c, m + \alpha\rangle$, while the control field drives transitions between $ c, m + \alpha\rangle$ and $ a, m + \alpha - \beta\rangle$	118
7.2	Numerical results illustrate the storage and retrieval of a signal pulse from an atomic ensemble as described in the text. We show results for two values of the magnetic field oriented along the z axis. Panels (A) and (B) correspond to a magnetic field $B = 0.267$ G, so that the signal is stored for $T_L/4$, where $T_L = 8 \mu s$ is the Larmor period. Panels (C) and (D) show results for $B = 0.535$ G, corresponding to a signal storage time of $T_L/2$, where $T_L = 4 \mu s$. The signal field intensity transmittance $I(t)/I_0$ (Solid line) and control field Rabi frequency (dot-dashed line), displayed in arbitrary units, are shown in panels (B) and (D). Panels (A) and (C) display scaled dark state p_D (solid line) and bright state p_B (dashed line) polariton components, as explained in the text. In panel (B) the ratio of retrieved to input signal pulse energy is 4.38% while in (D) the ratio is 25.09%.	125
7.3	The DSP population fraction $f_\alpha(t_s)$ calculated for orientations of the magnetic field $0 \leq \theta \leq \pi/2$ over one Larmor period. These results illustrate collapses and revivals whose features are dependent on θ . The atomic configuration and field polarizations α and β are described in the text.	126

7.4	A schematic diagram illustrates our experimental setup. A signal field from either a laser, or a DLCZ source of conditional single photons at Site A is carried by a single-mode fiber to an atomic ensemble at Site B , where it is resonant on the $ b\rangle \leftrightarrow c\rangle$ transition. The signal field is stored, for a duration T_s , and subsequently retrieved by time-dependent variation of a control field resonant between levels $ a\rangle$ and $ c\rangle$. All the light fields responsible for trapping and cooling, as well as the quadrupole magnetic field in the MOT, are shut off during the period of the storage and retrieval process. An externally applied magnetic field created by three pairs of Helmholtz coils (not shown) makes an angle θ with the signal field wavevector. The inset shows the structure and the initial populations of atomic levels involved. The signal field is measured by detectors D2 and D3, while detector D1 is used in the conditional preparation of single photon states of the signal field at Site A	128
7.5	Panels (a)-(e) show the ratio of the number of photoelectric detection events for the retrieved and incident signal fields for various orientations, $\theta = 0, \pi/8, \pi/4, 3\pi/8, \pi/2$, of the applied magnetic field, and as a function of storage time. The incident signal field is a weak coherent laser pulse. In all cases the control pulse is switched off at $T_s = 0$. We observe a series of collapses and revivals at multiples of the half Larmor period of $2.3 \mu\text{s}$. The observed damping over several Larmor periods is likely caused by residual magnetic field gradients. The inset in Panel (e) demonstrates the observed substructure within the first Larmor period. Panels (f) through (j) are corresponding theoretical plots of the dark-state polariton number calculated using Eq. (7.17).	132
7.6	Diamonds show the measured collapse time T_C of the first revival at half the Larmor period as a function of the measured revival time T_R , for magnetic field values of 0.8, 0.6, 0.4, and 0.2 G, respectively, and for fixed orientation $\theta = \pi/2$. The line shows the corresponding theoretical prediction $T_C \approx 0.082T_R$ from Eq. (7.17).	133
7.7	Squares show the measured rate of coincidence detections between D1 and D2,3, $N_{si} = N_{12} + N_{13}$ as a function of the storage time. Diamonds show the measured level of random coincidences N_R . The ratio of squares to diamonds gives g_{si} . Uncertainties are based on the statistics of the photoelectric counting events.	134

8.1	A schematic diagram of our experimental setup. Two cold atomic ensembles of ^{85}Rb , an unpolarized sample at Site A , and a spin-polarized sample at Site B , separated by 5.5 m, are connected by a single-mode fiber. The insets show the structure and the initial populations of the atomic levels for the two ensembles. An entangled state of a collective atomic qubit and a signal field is generated at Site A by Raman scattering of the write laser field. The orthogonal helicity states of the generated signal field are transmitted via optical fiber from Site A to Site B , where they are converted to orthogonal collective atomic excitations, stored for a duration T_s , and subsequently converted into an idler field by adiabatic variation of the control field amplitude. The atomic qubit at Site A is similarly converted into an idler field by a read laser pulse, counterpropagating with respect to the write pulse. For polarization analysis, each idler field propagates through a quarter-wave plate (not shown), a half-wave plate ($\lambda/2$) and a polarizing beamsplitter (PBS). Polarization correlations of the idler fields are recorded by photoelectric detection using the single photon detectors D1-D4.	140
8.2	Measured coincidence fringes $C_{n3}(\theta_A, \theta_B)$ as a function of θ_A , for $\theta_B = 135^\circ$, $n = 1$, diamonds, $n = 2$, squares. The curves are sinusoidal fits to the data. Each point is acquired for 15 minutes. The effective repetition rate is 108 kHz, each trial takes $1.1 \mu\text{s}$	144
8.3	Measured correlation function $E(\theta_A, \theta_B)$ as a function of θ_A . (a), $\theta_B = 0^\circ$, squares, and 90° , diamonds. (b), $\theta_B = 45^\circ$, squares, and 135° , diamonds. The curves are sinusoidal fits to the data.	145

SUMMARY

In this thesis, we explore the quantum dynamics of light interactions with optically thick collections of atoms. We provide a theoretical description of several recent experiments in which some key operations necessary for the implementation of quantum communication networks are demonstrated. Collective Raman scattering from an atomic ensemble is shown to produce probabilistic entanglement between the polarization of a scattered photon and an associated collective atomic excitation. The predicted correlations agree with experimental observations. We also propose a method to use cascade transitions to produce entanglement between a photon with a frequency in the telecom range (ideal for transmission over optical fibers) and a near infrared photon (ideal for storage in an atomic ensemble), and a description of the experimental demonstration is provided. We also propose and describe the implementation of a deterministic source of single photons.

In addition, we generalize the theory of dark-state polaritons in ensembles of three level Λ atoms to account for the nuclear spin degeneracy of alkali atoms. This generalized theory provides a description of the first demonstration of single photon storage and retrieval from atomic ensembles. Additionally, in the presence of a uniform magnetic field, we predict the occurrence of collapses and revivals of the photon retrieval efficiency as a function of storage time within the ensemble. These predictions are in very good agreement with subsequent experimental observations. We also exploit the ability of photon storage to entangle remote atomic qubits.

CHAPTER 1

INTRODUCTION

The dynamical law of quantum mechanics has inspired a number of potentially revolutionary ideas in recent decades. Quantum computing (see Ref. [1], and references therein), for example, holds the promise of solving several problems much faster than can be achieved classically. The prime factorization of large numbers could be performed exponentially faster [2]. The task of searching a large unsorted list scales with the square root of the list's size, where classically the task scales linearly [3]. Quantum cryptographic key distribution (QCKD) could ensure completely secure communication between two remote parties [4, 5]. Where private cryptographic keys distributed classically may be intercepted, without the knowledge of the sender or receiver, by a malicious (or simply overly curious) party, the security risk can be nullified when the ideas of QCKD are implemented. In addition to quantum computation and communication, non classical correlations between many particles can also help to improve high precision measurements [6, 7, 8, 9, 10, 11, 12, 13, 14, 15].

The essential feature of quantum mechanics that enables these possibilities is the notion of entanglement. An entangled state of two systems is one which cannot be characterized by identifying the state of either system individually, i.e. it cannot be expressed as a product state. One of the most elementary examples of an entangled state is a Bell state consisting of two qubits (two level quantum systems), labeled A and B , and is given by the state vector $(|0\rangle_A |1\rangle_B - |1\rangle_A |0\rangle_B)/\sqrt{2}$. In this two qubit entangled state, a measurement of one particle, gives automatic knowledge of the state of the other. The nonclassical nature of the correlations of the Bell state can be quantified by the violation of Bell's inequality (see Chapter 14 of Ref.[16] and

references therein). In this system of 2 qubits, the Hilbert space of state vectors has four dimensions. More generally, for a system composed of N two-level subsystems, the state space has dimension 2^N . The vastness of this state space, along with the potential for complex interparticle correlations which are not possible classically, is what permits the possibility of the technologies mentioned above.

In practice, however, creating, manipulating, and distributing, an entangled pair of qubits, let alone the numbers of these required for a useful quantum computer, presents enormous technical hurdles. The reason for this is that, in addition to the interactions between qubits that we can conceivably control, the system also interacts with the surrounding environment. Spins may interact with ambient magnetic fields; qubits encoded in atomic or ionic states also interact with the electromagnetic vacuum field. These uncontrolled interactions lead to dissipation in the system, and ultimately, a decay of useful interparticle correlations; the system would behave classically.

In this thesis, we provide a theoretical description of several recent experiments in which key building blocks of quantum networks for use in quantum communication are implemented [17, 18, 19, 20, 21, 22, 23]. In these experiments, interactions between the light field and a cold atomic gas, or atomic ensemble, are used to generate, store and retrieve quantum information stored in nonclassical states of the light field. These atomic ensembles serve as “quantum memories,” which could be used to implement quantum repeaters. Realization of the latter would make it possible to distribute entangled particles over great distances (example: intercontinental).

The remainder of this Chapter is organized as follows. In Section 1.1, we provide an overview of quantum communication and some of the difficulties that arise in implementing it over long distances. Section 1.2 introduces the concepts of quantum networks and quantum repeaters. Finally, in Section 1.3, we provide an outline for the remainder of this thesis, in which we describe recent experiments that lay the

foundation for the implementation of the ideas discussed here.

1.1 *Quantum Communication*

Producing and maintaining entanglement between two remote qubits, or two-level quantum systems is an essential ingredient in quantum communication schemes. We first consider the example of quantum teleportation[24]. Suppose a party, Alice, has produced a qubit in an arbitrary state $|\phi\rangle$, and wishes to send it to her colleague, Bob. This is accomplished producing a pair of qubits – one located with Alice at Site A and the other with Bob at site B – in a Bell state, a maximally entangled state

$$|\Psi_{\text{Bell}}\rangle_{A,B} = \frac{1}{\sqrt{2}} (|0\rangle_A |1\rangle_B - |1\rangle_A |0\rangle_B). \quad (1.1)$$

Alice then performs a joint measurement on her original qubit and particle A , and sends the results of her measurement over a classical channel to Bob. It is shown in Ref. [24] that Bob can use these results to reconstruct the original qubit $|\phi\rangle$ on his particle at B . We emphasize that this reconstruction does not involve any knowledge of the original particle, but rather, only depends on the classical information sent to Bob. In order to transmit arbitrary qubits between remote locations, one therefore only needs to reliably generate Bell states in entangled pairs of qubits. Quantum teleportation has been implemented experimentally using entangled photons produced by parametric down conversion [25, 26, 27], where photons serve as the information carriers.

In quantum cryptography, entangled particles are used to securely transmit the cryptographic key [4, 5]. The BB84 protocol involves either remote state preparation or teleportation of a qubit [24, 25, 26, 28]. The Ekert protocol, on the other hand, directly uses the measurement on an pair of entangled qubits to generate the cryptographic key [5].

A requirement of these quantum communication protocols is the distribution of entangled qubits. While parametric down conversion provides a robust mechanism

to produce entangled photons for use in quantum communication [24, 25, 26, 28, 27], distributing entangled photons over great distances is problematic. Due to absorption in optical fiber and the probabilistic nature of photon pair generation, the communication rate decreases exponentially with the distance.

This limitation can be overcome through the use of a quantum repeater architecture [29, 30], in which a quantum memory element (capable of storing a qubit) is inserted into the quantum communication channel every attenuation length or so. Long distance entanglement distribution is achieved by first generating entanglement between two neighboring quantum memory qubits. This can be done efficiently since light will not be appreciably absorbed within a short segment length. After entanglement between each pair of memory qubits has been established, a joint measurement on each neighboring pair of qubits is performed. The quantum state of the intermediate qubits is destroyed by the measurement, thus achieving entanglement swapping such that two memory qubits at the ends are entangled. After the entanglement swapping, the number of entangled memory qubit pairs is reduced by a half, while the distance over which the entanglement is distributed doubles. One subsequently performs entanglement purification and additional entanglement swapping until the quantum states of all of the intermediate qubits are destroyed, leaving the memory elements at the two ends of the channel entangled. With the use of a quantum repeater architecture, the communication rate only scales polynomially with distance [29, 30].

1.2 Quantum Networks and Atomic Ensembles

The quantum repeater architecture discussed above is an example of the more general concept of a quantum network. A quantum network consists of quantum memory nodes at which quantum information is generated, stored, and manipulated, and quantum channels over which qubits are transmitted. Photons are ideal information

carriers over the quantum channels since they can propagate quickly over relatively long distances (shorter than an attenuation length) without suffering from losses, or appreciably interacting with the environment. Atoms, on the other hand, make favorable building blocks for quantum memory elements since they can be well isolated from the environment, and their states may be manipulated by laser fields or applied dc electric and magnetic fields. Here, we discuss some important primitives of a quantum network: the ability to entangle a node and a photon, the generation of deterministic single photons, the ability to map the quantum state of a photon onto a quantum memory element, and vice versa.

Proposed quantum network architectures implement quantum memory nodes in a number of different ways. In the microwave domain, single Rydberg atoms and single photons have been entangled [31]. An entangled state between a photon and a single ion has also been recently produced [32, 33]. A proposal for a quantum network architecture for distributed quantum computing using trapped ions has recently been made [34]. Another scheme involves the use of single atoms/ions within a high finesse optical cavity [35]. Indeed, cavity QED shows promise for generating entanglement between neutral atoms and photons, with deterministic single photon generation being an important step in that direction [36, 37]. Entanglement between a photon and a single trapped neutral atom has also been achieved [38]. A proposal also exists for solid state based photon emitters [39].

Collective enhancement of atom-photon interactions in optically thick ensembles of atoms provides a somewhat simpler route toward the construction of quantum networks [40, 41, 42, 43, 44, 45, 46]. The atom photon entanglement, however, is often probabilistic in nature. Duan, Lukin, Cirac, and Zoller (DLCZ) [47] have developed a scheme for long distance quantum networking based on atomic ensembles and linear optics. The dynamics of this paradigm turn out to be remarkably similar to parametric down conversion with the additional capability of quantum memory.

In parametric down conversion, nonlinear interactions in an optical medium produce entangled pairs of photons. The DLCZ protocol, on the other hand, uses collective Raman scattering from an atomic ensemble to create nonclassical correlations between a scattered photons and collective atomic excitations. The equivalence of this DLCZ write process and parametric down conversion is discussed in more detail in Chapter 3. Heterogeneous quantum network schemes employing both single-atom and collective atomic qubits are also being actively pursued [48, 49, 50].

Non-classical radiation has been produced from the first generation of atomic ensemble experiments [51, 52, 53, 54, 55, 56]. The ability to prepare a quantum memory qubit based on two atomic ensembles and subsequently transfer the information onto a photonic qubit was then later demonstrated [57]. These experiments [51, 52, 53, 54, 55, 56, 57] employed copropagating *write* and *read* laser fields and on-axis Raman-scattered light was collected. In contrast to these works, Braje and coworkers pioneered off-axis four-wave mixing [58] and efficient photon-pair production [59] in a cold atomic ensemble, using counter-propagating *write* and *read* fields deep in the regime of electromagnetically-induced transparency. We exploited this geometry in Chapter 3, in which we report probabilistic entanglement between a photonic and collective atomic qubit [17].

The capability to generate nonclassical correlations between a scattered photon and a collective atomic excitation combined with relatively long atomic memory coherence times allows one to produce another primitive operation of a quantum network, the production of deterministic single photons. In Chapter 5, we propose and implement a source of deterministic single photons utilizing the conditional, or heralded, single photon sources involved in a DLCZ paradigm for an ensemble of atomic emitters with a measurement based feedback protocol. In the past, deterministic single photon sources have been produced using single emitters, such as quantum dots [60, 61, 62], color centers [63, 64], neutral atoms [36, 37, 65], ions [66], and molecules

[67]. The measured efficiency to detect a single photon per trial with these single emitter sources is typically less than 1%, with the highest reported measured value of about 2.4% [36, 37], to the best of our knowledge. We report the implementation of our scheme for an ensemble of atomic emitters using a cold rubidium vapor, with a measured efficiency of 1 - 2% (see Chapter 5[23]). In common with the cavity QED systems, our source is suitable for reversible quantum state transfer between atoms and light. Unlike cavity QED implementations [36, 37], however, our source is unaffected by intrinsically probabilistic single atom loading. Therefore it is stationary and produces a photoelectric detection record with truly sub-Poissonian statistics.

1.2.1 Atomic ensembles as quantum memories

Above, we discussed the use of atomic ensembles to generate entanglement between quantum memory and photonic qubits. One infers this entanglement by mapping the atomic qubit onto a photonic qubit, and performing appropriate measurements on the correlated two-photon system [17]. Another elementary quantum network operation involves storing a qubit state in an atomic quantum memory node, and then retrieving and transporting the information through a single photon excitation to a remote quantum memory node for further storage or analysis. To accomplish this, it is necessary to map the quantum state of the light field onto the remote quantum memory node. The potential of atomic ensembles to serve as quantum memories has recently attracted considerable attention [68, 41, 69, 47, 13, 70].

Electromagnetically Induced Transparency (EIT) [71, 72] provides a route toward the implementation of quantum memories within optically thick atomic ensembles. In a collection of three level Λ atoms, the application of a classical control field resonant on one transition renders the medium transparent to a signal, or probe, field resonant on the other. Whereas in the absence of the control field, the atoms would absorb the signal, and the atomic medium would be opaque. The detailed

theory of electromagnetically induced transparency in a degenerate three level atomic medium, such as rubidium or other alkali atoms, is presented in Appendix C. The transparency induced by the control field is accompanied by a reduced group velocity. This phenomenon was observed first in the seminal “slow light” experiments [73], and coherent light pulses were later “stopped” and subsequently retrieved [44, 45, 74].

The mechanism for “storing” light pulses can be understood through a collective excitation known as a dark-state polariton first introduced by Fleischhauer and Lukin [69, 75]. A dark-state polariton (DSP) excitation consists of a photonic component, and a hyperfine spin wave (a collective matter excitation) component. As a light pulse enters an atomic medium, it transforms into a DSP excitation with a reduced group velocity. By adiabatically extinguishing the control field, the signal can be stopped, converting the DSP entirely into a hyperfine spin wave. The quantum state of the light field has thus been mapped onto the quantum memory. The signal can then later be retrieved through reactivation of the control field, allowing the DSP to propagate out of the sample. Additionally, when EIT is operative, retrieval of atomic qubits created in a DLCZ style write process can be understood through the DSP paradigm (see Chapter 3). In this way, optically thick atomic ensembles are excellent candidates for implementation of quantum memories when EIT is operative.

In this thesis, we generalize the treatment of Fleischhauer and Lukin [69, 75] to treat atoms with nuclear spin degeneracy as used in the experiments we report. It was found that the DSP’s in degenerate atomic ensembles consist of an electric field excitation with a particular linear combination of hyperfine spin wave excitations (see Chapters 6 and 7 and Appendix C). Orthogonal spin wave components couple to optical coherences and result in spontaneous emission. In the presence of a uniform magnetic field, we predict and subsequently measure the occurrence of collapses and revivals in the quantum memory retrieval efficiency as a function of storage time. In a separate work, it is shown that additional magnetic field gradients are responsible

for the current upper bound on the quantum memory lifetime [76].

When the atomic sample is spin polarized, the DSP mechanism allows the storage of a qubit encoded in the polarization of a photon. We exploited this in Chapter 8 to produce entanglement between two remote atomic qubits [21].

1.3 Outline

In this thesis, we provide theoretical descriptions of recent experiments that implement several primitive operations necessary for the construction of quantum networks using atomic ensembles. These descriptions were born from a close collaboration with the individuals who performed the experiments, in which theoretical and experimental developments occurred in parallel. At several instances in the performance of this work, theoretical predictions were made within days of the corresponding experimental observations (see, for example, Chapter 7 and Refs. [19, 20]). Much of this work was published in joint theoretical and experimental articles. Experimental details are, therefore, provided in this thesis to put the theoretical developments into context. Note, however, that when the pronoun “we” is used in the presentations of the experimental details, it is used to refer to the individuals who performed the experiments, and not the author of this thesis.

The remainder of this thesis is organized as follows. In Chapter 2, we review the theory of atomic ensemble interactions with the quantized electromagnetic field beginning with the standard Hamiltonian for quantum electrodynamics in the Coulomb gauge. The formalism developed in that Chapter is used throughout the remainder of the thesis.

In Chapters 3 and 4, we describe experiments in which interaction of atomic ensembles with classical laser fields probabilistically produce entangled pairs of qubits. Chapter 3 describes the experiment of Ref.[17], in which collective Raman scattering from a classical *write* laser field results in the emission of photons, imprinting

entangled collective excitations onto the atomic medium. We show that the Raman scattering dynamics reduces to that of a nondegenerate parametric amplifier [16] involving a single mode of the collected signal field and the corresponding idler atomic excitation. When the *write* pulse is sufficiently weak, these dynamics result in the probabilistic entanglement of a photonic, and a collective atomic qubit. Entanglement was verified experimentally through measurement of the violation of Bell's inequality. In Chapter 4 [22], we propose and implement a key feature of a quantum repeater using atomic cascade transitions. Whereas the photons produced from ensembles of alkali atoms by collective Raman scattering have frequencies in the near infrared region, the proposal involving cascade emission provides the freedom to choose particular atomic transitions such that one of the entangled photons lies in the telecom range of frequencies. Photons with telecom frequencies propagate through much greater distances in optical fibers without attenuation than their near infrared counterparts. The correlated idler photon, on the other hand, is of a frequency ideal for storage in atomic ensembles.

The collective Raman scattering paradigm in Chapter 3 is exploited in Chapter 5 to produce a source of deterministic single photons [23]. The experimental advances leading to increased quantum memory lifetimes allow us to implement a measurement-based quantum feedback protocol to arm an atomic ensemble with a single atomic excitation with high probability. This excitation can then be mapped to the state of the electromagnetic field at a predetermined time, yielding a deterministic photon source. Relevant aspects of the theory of photoelectric detection are presented in Appendix D.

In Chapters 6 through 8, we turn our attention to the task of storing the quantum state of an electromagnetic field mode and subsequently retrieving it. In Chapter 6, we report the first experimental demonstration of storage and retrieval of a single photon state from an atomic ensemble [18]. EIT for single photons was concurrently

reported by Eisaman *et al* [77].

In Ref. [18] (see Chapter 6) we hypothesized that the observed limitation of the quantum memory lifetime was due to a Larmor collapse of the dark-state polariton in our degenerate atomic gas. That is, the magnetic field rotates the stored atomic excitation away from the dark-state polariton mode. We provide support this idea in Chapter 7, in which we present the theory of EIT and dark-state polariton storage for an unpolarized degenerate atomic medium. We predicted the occurrence of collapses and revivals or the retrieval efficiency as a function of storage time in the presence of a uniform magnetic field. In this chapter, we also present an experimental verification of this prediction.

In Chapter 8, we report the synthesis of the ideas of Chapters 3 and 6 to produce probabilistic entanglement between two remote quantum memories. Entanglement between the polarization of a photon and a collective atomic qubit is generated at Site *A*. The photon is then transmitted to a polarized atomic ensemble at Site *B* where the photon's polarizations are mapped to orthogonal collective spin wave excitations. We follow with some concluding remarks in Chapter 9.

In the Appendices, we provide additional information on the theory of quantum optics with atomic ensembles. The polarization conventions used throughout the thesis are discussed in Appendix A. In Appendix B, we derive the effective Hamiltonian describing scattering of an off-resonant laser field from an ensemble of degenerate three-level atoms. We provide the detailed theory of signal propagation through an ensemble of degenerate three-level atoms in Appendix C. In this treatment, we account for the presence of the control field and dc magnetic fields. The conditions under which our model is valid are also discussed. Finally, some relevant aspects of the theory of photoelectric detection and photon counting statistics are presented in Appendix D.

CHAPTER 2

REVIEW OF THE QUANTUM THEORY OF LIGHT-ATOM INTERACTIONS

In this Chapter, we explore the basic physical mechanisms that facilitate the manipulation of quantum information and quantum states of light within atomic ensembles. The material presented here, lays the foundation for the presentations we will give in later chapters regarding photon storage and retrieval , electromagnetically induced transparency in a degenerate atomic ensemble, dark state polariton collapses and revivals, and effective qubit entanglement generated by Raman scattering from an atomic ensemble. We begin in Section 2.1 by considering the Hamiltonian which describes the interaction of distinct atoms with the the quantized electromagnetic field. In Section 2.1.1, we describe the level structure of alkali atoms, using ^{85}Rb as an example. Section 2.1.2 establishes the formalism and notation for the electric dipole operator in a general multi-level atom. We describe the electromagnetic field and its decomposition into “system” fields and the reservoir field in Section 2.1.4. Finally, in Section 2.2, we briefly discuss the dynamics that arises from the atom-field interactions.

2.1 Electric Dipole Hamiltonian

In Chapters 3 through 8 we consider a system of N atoms coupled to the quantized electromagnetic field. We assume that the atoms are at a sufficiently high temperature that we may consider the position of the μ^{th} atom \vec{r}_μ ($\mu = 1 \dots N$) as a classical variable. We assume, however, that the atomic velocities are sufficiently low so that we may neglect atomic motion over the time scales of the experiments we will describe

[17, 22, 23, 18, 20, 21]. In these experiments, ensembles of ^{85}Rb atoms are cooled in a magneto-optical trap. The temperature of the ensemble is roughly $\sim 100\ \mu\text{K}$, which corresponds to a thermal velocity of $\sim 10\ \text{cm/s}$. Typical experimental trials, which include storage time of a collective excitation are on the order of $10\ \mu\text{s}$. In these time scales, an atom would move about $1\ \mu\text{m}$, much less than the wavelengths of the stored spin waves (see Chapters 3, 5, 6, 7, and 8.). The stationary atom approximation is, therefore, sufficient for our theoretical models.

We will describe the electromagnetic field in terms of creation and annihilation operators for plane waves with wavevector \vec{k} and linear polarization $\vec{\varepsilon}_\lambda(\hat{k})$ ($\lambda = H, V$), $\hat{a}_\lambda^\dagger(\vec{k})$ and $\hat{a}_\lambda(\vec{k})$ respectively. The possible linear polarization vectors $\{\vec{\varepsilon}_\lambda(\hat{k})\}$ for a given propagation direction $\hat{k} \equiv \vec{k}/k$, are orthogonal to each other and the direction of propagation \hat{k} . The linear polarizations are labeled by the index $\lambda \in \{H, V\}$ and are defined such that $\{\vec{\varepsilon}_H, \vec{\varepsilon}_V, \hat{k}\}$ form a right handed coordinate system. In this thesis, whenever it is convenient to choose a specific set of polarization vectors, we adopt the convention presented in Appendix A. The operators $\hat{a}_\lambda(\vec{k})$ and $\hat{a}_\lambda^\dagger(\vec{k})$ obey the Bosonic commutation relations

$$\left[\hat{a}_\lambda(\vec{k}), \hat{a}_{\lambda'}(\vec{k}') \right] = \left[\hat{a}_\lambda^\dagger(\vec{k}), \hat{a}_{\lambda'}^\dagger(\vec{k}') \right] = 0 \quad (2.1a)$$

$$\left[\hat{a}_\lambda(\vec{k}), \hat{a}_{\lambda'}^\dagger(\vec{k}') \right] = \delta_{\lambda\lambda'} \delta(\vec{k} - \vec{k}') \quad (2.1b)$$

In the Coulomb gauge, the magnetic vector potential is expressed in terms of these plane wave mode operators as

$$\hat{\mathbf{A}}(\vec{r}) = \int d^3k \sum_{\lambda \in \{H, V\}} \vec{\varepsilon}_\lambda(\hat{k}) \frac{\mathcal{E}(ck)}{ck} \left(e^{i\vec{k} \cdot \vec{r}} \hat{a}_\lambda(\vec{k}) + e^{-i\vec{k} \cdot \vec{r}} \hat{a}_\lambda^\dagger(\vec{k}) \right), \quad (2.2)$$

where $\mathcal{E}(\omega) \equiv (\hbar\omega / (2\epsilon_0(2\pi)^3))^{1/2}$. The Coulomb gauge scalar potential $U(\vec{r})$ is a function only of the positions of the electrons and atomic nuclei composing the atoms.

This potential can be expressed as

$$U(\vec{r}) = \frac{1}{4\pi\epsilon_0} \sum_{\mu=1}^N \sum_v \frac{q_{\mu,v}}{|\vec{r} - \hat{\mathbf{r}}_{\mu,v}|}, \quad (2.3)$$

where the particles that compose atom μ are labeled by the index v , $q_{\mu,v}$ is the charge of the v^{th} particle of atom μ , and $\hat{\mathbf{r}}_{\mu,v}$ is the position of this particle. The Hamiltonian for the atom-field system is given by

$$\begin{aligned} \hat{H} = & \sum_{\mu,v} \frac{\left[\hat{\mathbf{p}}_{\mu,v} - q_{\mu,v} \hat{\mathbf{A}}(\hat{\mathbf{r}}_{\mu,v}) \right]^2}{2m_{\mu,v}} + \int d^3k \sum_{\lambda} \hat{a}_{\lambda}^{\dagger}(\vec{k}) \hat{a}_{\lambda}(\vec{k}) \\ & + g_{\mu,v} \mu_B \hat{\mathbf{s}}_{\mu,v} \cdot \hat{\mathbf{B}}(\hat{\mathbf{r}}_{\mu,v}) + \hat{V}_{Coul} \end{aligned} \quad (2.4)$$

where $m_{\mu,v}$ is the mass of particle μ, v , $g_{\mu,v}$ is the Landé g factor of particle μ, v , $\hat{\mathbf{s}}_{\mu,v}$ is the spin of this particle, μ_B is the Bohr magneton, $\hat{\mathbf{p}}_{\mu,v}$ is the conjugate momentum of the position $\hat{\mathbf{r}}_{\mu,v}$, and

$$\hat{V}_{Coul} = \frac{1}{16\pi\epsilon_0} \sum_{\mu=1}^N \sum_{\mu'=1}^N \sum_{\{v,v': v \neq v'\}} \frac{q_{\mu,v} q_{\mu',v'}}{|\hat{\mathbf{r}}_{\mu,v} - \hat{\mathbf{r}}_{\mu',v'}|} \quad (2.5)$$

is the Coulomb interaction between particles.

When the atoms are well localized in comparison to the wavelengths of light we consider, (e.g. classical laser fields, signal and idler quantum fields, etc.) it is convenient to make the Power-Zienau-Woolley transformation [78] by applying the unitary operator

$$\hat{T} \equiv \exp \left(\frac{1}{i\hbar} \int d^3r \hat{\mathbf{P}}(\vec{r}) \cdot \hat{\mathbf{A}}(\vec{r}) \right), \quad (2.6)$$

where

$$\hat{\mathbf{P}}(\vec{r}) = \sum_{\mu} \hat{\mathbf{P}}_{\mu}(\vec{r}) \quad (2.7)$$

is the polarization density within the atomic sample, and

$$\hat{\mathbf{P}}_{\mu}(\vec{r}) = \sum_v \int_0^1 du \, q_{\mu,v} (\hat{\mathbf{r}}_{\mu,v} - \vec{r}_{\mu}) \delta(\vec{r} - \vec{r}_{\mu} - u(\hat{\mathbf{r}}_{\mu,v} - \vec{r}_{\mu})) \quad (2.8)$$

is the polarization density associated with atom μ , where \vec{r}_{μ} is the center of mass position of atom μ . Recall that we are considering the atom's center of mass position to be a classical variable. In the long-wavelength approximation, we perform a multipole expansion of $\hat{\mathbf{P}}_{\mu}(\vec{r})$, keeping only the lowest order contribution. When this is

done, the polarization density of atom μ may be approximated as

$$\hat{\mathbf{P}}_\mu(\vec{r}) \approx \hat{\mathbf{d}}_\mu \delta(\vec{r} - \vec{r}_\mu) \quad (2.9)$$

where

$$\hat{\mathbf{d}}_\mu \equiv \sum_v q_{\mu,v} (\hat{\mathbf{r}}_{\mu,v} - \vec{r}_\mu) \quad (2.10)$$

is the electric dipole operator for atom μ . An operator \hat{A} in the Power-Zienau-Woolley (PZW) picture is related to the corresponding Coulomb gauge operator by

$$\hat{A}^{(PZW)} = \hat{T} \hat{A}^{(Coul)} \hat{T}^\dagger. \quad (2.11)$$

A detailed description of how various physical operators transform is given in Refs. [78, 79]

The displacement field is defined $\hat{\mathbf{D}}(\vec{r}) = \epsilon_0 \hat{\mathbf{E}}(\vec{r}) + \hat{\mathbf{P}}(\vec{r})$, where $\hat{\mathbf{E}}(\vec{r})$ is the electric field at position \vec{r} . In Ref. [78], it is shown that because we are dealing exclusively with neutral atoms, the displacement field is transverse, i.e. $\nabla \cdot \hat{\mathbf{D}}(\vec{r}) = 0$. Therefore, the electric displacement operator is given in the Schrödinger picture after the PZW transformation by

$$\hat{\mathbf{D}}(\vec{r}) = \epsilon_0 \left(\hat{\mathbf{E}}^{(+)}(\vec{r}) + \hat{\mathbf{E}}^{(-)}(\vec{r}) \right) \quad (2.12)$$

where

$$\hat{\mathbf{E}}^{(+)}(\vec{r}) = i \sum_\lambda \int d^3k \mathcal{E}(ck) \vec{\varepsilon}_\lambda(\vec{k}) \hat{a}_\lambda(\vec{k}) \exp \left(i \left(\vec{k} \cdot \vec{r} \right) \right), \quad (2.13)$$

is the positive frequency component of the transverse electric field at position \vec{r} in the Coulomb representation, and $\hat{\mathbf{E}}^{(-)}(\vec{r}) = \hat{\mathbf{E}}^{(+)\dagger}(\vec{r})$ is the corresponding negative frequency component. Similarly, the magnetic field is described by the Schrödinger picture operator

$$\hat{\mathbf{B}}(\vec{r}) = \hat{\mathbf{B}}^{(+)}(\vec{r}) + \hat{\mathbf{B}}^{(-)}(\vec{r}) \quad (2.14)$$

where

$$\hat{\mathbf{B}}^{(+)}(\vec{r}) = i \sum_\lambda \int d^3k \frac{\mathcal{E}(ck)}{c} (\hat{k} \times \vec{\varepsilon}_\lambda(\hat{k})) \hat{a}_\lambda(\vec{k}) \exp \left(i \left(\vec{k} \cdot \vec{r} \right) \right), \quad (2.15)$$

and $\hat{\mathbf{B}}^{(-)}(\vec{r}) = \hat{\mathbf{B}}^{(+)\dagger}(\vec{r})$.

Having applied the Power-Zienau-Wolley transformation the dynamics of the electromagnetic field - atomic ensemble system by the electric dipole Hamiltonian [78, 79]

$$\hat{H} = \hat{H}_{Rad} + \sum_{\mu=1}^N \left(\hat{H}_0^{(\mu)} - \frac{1}{\epsilon_0} \hat{\mathbf{d}}^{(\mu)} \cdot \hat{\mathbf{D}}(\vec{r}_\mu) \right) \quad (2.16)$$

where

$$\hat{H}_{Rad} = \sum_{\lambda} \int d^3k \, \hbar c k \hat{a}_{\lambda}^{\dagger}(\vec{k}) \hat{a}_{\lambda}(\vec{k}) \quad (2.17)$$

is the energy of the free electromagnetic field, and $\hat{H}_0^{(\mu)}$ represents the atomic Hamiltonian for atom μ . The interaction of the μ^{th} atom with the electric field is accounted for by the interaction of the displacement field with the dipole, $-\hat{\mathbf{d}} \cdot \hat{\mathbf{D}}(\vec{r}_\mu)/\epsilon_0$.

In the following subsections, we will discuss the elements of the electric dipole Hamiltonian in greater detail. Section 2.1.1 provides an overview of the structure of alkali atoms. We discuss the electric dipole operator in Section 2.1.2. In Section 2.1.3, we establish some notation within the interaction picture. Finally, in Section 2.1.4, we decompose the electric field into the system fields, which include classical laser fields and detected modes of the quantized field, and the reservoir, which consists of the plethora of undetected field modes.

2.1.1 The atomic Hamiltonian $\hat{H}_0^{(\mu)}$

In this section, we discuss the Hamiltonian for a single atom $\hat{H}_0^{(\mu)}$. The atom is composed of a nucleus of charge Z , surrounded by a cloud of Z electrons. The electrons interact with the nucleus, and with one and other via the coulomb interaction. The atomic Hamiltonian can be expressed as

$$\hat{H}_0^{(\mu)} = \sum_v \frac{\hat{\mathbf{p}}_{\mu,v}^2}{2m_{\mu,v}} + \hat{V}_{Coul}^{\mu} + \hat{H}_{Lamb} + \hat{H}_{fs} + \hat{H}_{hfs}, \quad (2.18)$$

where, again $\hat{\mathbf{p}}_{\mu,v}$ is the momentum of particle v (electron or nucleus) within atom μ ,

$$\hat{V}_{Coul}^{\mu} = \frac{1}{8\pi\epsilon_0} \sum_{\{v,v': v \neq v'\}} \frac{q_{\mu,v} q_{\mu',v'}}{|\hat{\mathbf{r}}_{\mu,v} - \hat{\mathbf{r}}_{\mu',v'}|} \quad (2.19)$$

is the Coulomb interaction between the particles. \hat{H}_{Lamb} accounts for the shift in energy levels resulting from the interaction of the atom with the electromagnetic vacuum. The fine structure interaction, which accounts for relativistic corrections to the classical Hamiltonian, is contained in \hat{H}_{fs}^μ , and the hyperfine interaction, which results from a coupling of nuclear and electronic angular momenta is described by \hat{H}_{hfs}^μ .

We label the atomic energy levels $|f\rangle$, where f denotes the set of quantum numbers that characterize the energy level. In a hydrogen atom, when one neglects fine structure, radiation shifts of the energy levels, and hyperfine structure, the energy of level $|f\rangle$ is determined entirely by the principal quantum number n . In general, multi-electron atoms are much more complicated, and the eigenstates depend on the configuration of all of the electrons in the atom. The alkali atoms that constitute our ensemble consist of a closed shell with one valence electron. We can make the simplifying assumption that only the valence electron, the electron occupying the outermost energy level, will undergo transitions, and the configuration of the inner electrons will remain unchanged. Because of the spherical symmetry of the atomic Hamiltonian, the total electronic orbital angular momentum $\hat{\mathbf{L}}^2$, spin angular momentum $\hat{\mathbf{S}}^2$ are conserved quantities. The level $|f\rangle$ will therefore depend on the orbital angular momentum L_f and spin angular momentum S_f quantum numbers respectively, so that for a state $|f, m\rangle$ in level $|f\rangle$

$$\hat{\mathbf{L}}^2 |f, m\rangle = L_f(L_f + 1) |f, m\rangle \quad (2.20)$$

$$\hat{\mathbf{S}}^2 |f, m\rangle = S_f(S_f + 1) |f, m\rangle. \quad (2.21)$$

We note that the $Z - 1$ electrons that compose the inner shell have a combined orbital angular momentum and spin angular momentum of zero. The total orbital angular momentum L_f and total spin S_f of level $|f\rangle$ in an alkali atom are, therefore, identical to those of the valence electron.

The fine structure splitting \hat{H}_{fs}^μ arises from relativistic corrections to the total Hamiltonian. This correction results in a coupling between the orbital and spin angular momenta of the outer electron, $\hat{H}_{fs}^\mu \sim \hat{\mathbf{L}} \cdot \hat{\mathbf{S}}$. This coupling lifts the degeneracy of states with equal orbital angular momentum but with different total electronic angular momenta $\hat{\mathbf{J}} = \hat{\mathbf{L}} + \hat{\mathbf{S}}$. The square of the total electronic angular momentum $\hat{\mathbf{J}}^2$ remains a conserved quantity, however, since $\hat{\mathbf{L}} \cdot \hat{\mathbf{S}} = (1/2)(\hat{\mathbf{J}}^2 - \hat{\mathbf{L}}^2 - \hat{\mathbf{S}}^2)$. For the degenerate energy level $|f\rangle$, we introduce the quantum number J_f such that for a state $|f, m\rangle$ in level $|f\rangle$, $\hat{\mathbf{J}}^2 |f, m\rangle = J_f(J_f + 1) |f, m\rangle$, and $|L_f - S_f| \leq J_f \leq L_f + S_f$. Atomic states which share common principal a quantum number n , orbital angular momentum L_f , spin angular momentum S_f , and total electronic angular momentum J_f are said to form a fine structure level. In this thesis, we label fine structure levels using the Russel-Sanders notation, $n^{2S+1}L_J$, where n is the principal quantum number of the valence electron, L is a letter representing the total electronic orbital angular momentum of the atoms ($S \Leftrightarrow L = 0$, $P \Leftrightarrow L = 1$, $D \Leftrightarrow L = 2$ etc.), and J is the total electronic angular momentum. A diagram of selected fine structure levels is shown in Figure 2.1

The smallest correction to the energy, and the last mechanism to remove degeneracy in the absence of external fields is the hyperfine interaction, an effective interaction between the $\hat{\mathbf{J}}$ and the nuclear spin $\hat{\mathbf{I}}$. In the presence of this interaction states within energy level $|f\rangle$ are eigenstates of the total atomic angular momentum operator $\hat{\mathbf{F}}^2$ with eigenvalue $F_f(F_f + 1)$, where $\hat{\mathbf{F}} = \hat{\mathbf{J}} + \hat{\mathbf{I}}$ is the total atomic angular momentum. In the absence of external fields, Level $|f\rangle$ possesses $2F_f + 1$ degenerate Zeeman states. We label the eigenstates of the z -component of the angular momentum \hat{F}_z within level $|f\rangle$ as $|f, m\rangle$ where $m \in \{m_f \in \mathbb{Z} : |m_f| \leq F_f\}$. The hyperfine interaction Hamiltonian may be written as [80][81]

$$\hat{H}_{hfs} = \sum_f E_{hfs}^{(f)} \hat{P}_f, \quad (2.22)$$

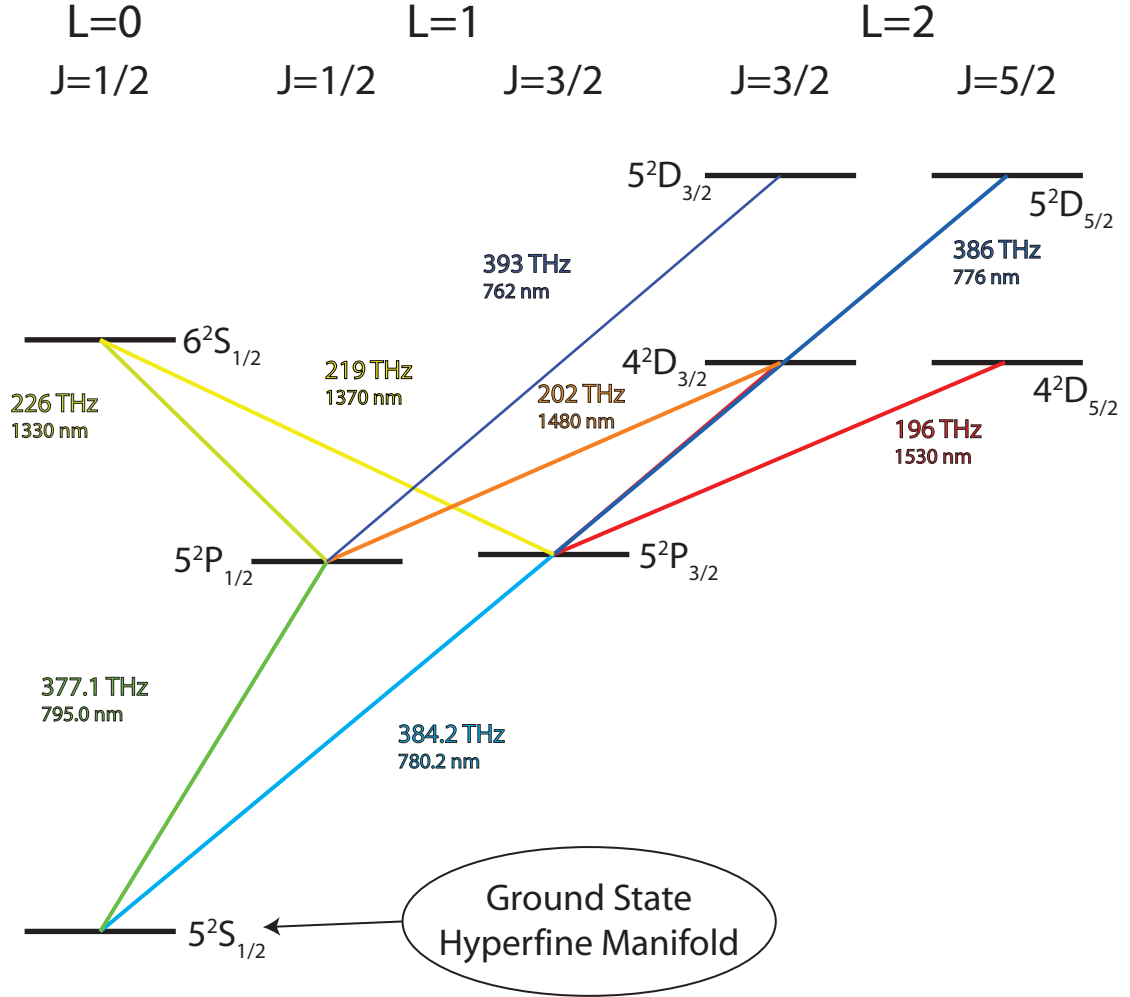


Figure 2.1: A diagram illustrates a sample of fine structure levels for ^{85}Rb . The fine structure levels are organized according to their orbital angular momentum and total electronic angular momentum, as indicated by the labels across the top of the diagram. The levels are arranged vertically according to their energies. A sample of allowed transitions between the levels is illustrated by color lines connecting the various levels, where the resonance frequency of the transition is given by the color coded text. The energy differences between two adjacent levels is given by $2\pi\hbar$ times the indicated frequency.

Table 2.1: The magnetic dipole constants A_{hfs} and electric quadrapole constants B_{hfs} for the hyperfine interaction within ^{85}Rb atoms. These quantities are given as a function of fine structure level j for the ground state and first two excited state fine structure levels. The numerical values have been obtained from Ref. [82]. The values of B_{hfs} are not given for the $5^2S_{1/2}$ and $5^2P_{1/2}$ manifolds since the electric quadrapole interaction (the second term in Eq. (2.23)) is identically zero for these levels [81].

Fine Structure Level j	$A_{hfs}(j)$	$B_{hfs}(j)$
$5^2S_{1/2}$	1.011910 GHz	
$5^2P_{1/2}$	120.72 MHz	
$5^2P_{3/2}$	25.009 MHz	25.88 MHz

where $\hat{P}_f \equiv \sum_{m=-F_f}^{F_f} |f, m\rangle \langle f, m|$ is the projection operator onto level $|f\rangle$ and the hyperfine energy shift is given by [81]

$$E_{hfs}^{(f)} = \pi \hbar A_{hfs}(j\{f\}) K_f + 2\pi \hbar B_{hfs}(j\{f\}) \frac{\frac{3}{2} K_f (K_f + 1) - 2I(I+1) J_f(J_f+1)}{2I(2I-1) 2J_f(2J_f-1)}, \quad (2.23)$$

where $A_{hfs}(j\{f\})$ is the magnetic dipole constant and $B_{hfs}(j\{f\})$ is the electric quadrapole constant for hyperfine manifold $j\{f\}$, $j\{f\} = \{|f'\rangle : n_{f'} = n_f, L_{f'} = L_f, S_{f'} = S_f, J_{f'} = J_f\}$ is the fine structure level to which $|f\rangle$ belongs, I is the nuclear angular momentum quantum number, and $K_f \equiv F_f(F_f+1) - I(I+1) - J_f(J_f+1)$. Numerical values for these constants have been determined experimentally for a number of atoms and hyperfine manifolds [82]. Table 2.1 shows values of A_{hfs} and B_{hfs} for the ground state and first two excited state manifolds of ^{85}Rb . The hyperfine splittings for ^{85}Rb , as calculated from Eq. (2.23), are displayed in Figure 2.2.

To summarize, the atomic Hamiltonian of atom μ , \hat{H}_0^μ , and the angular momentum operators $\hat{\mathbf{L}}^{\mu^2}$, $\hat{\mathbf{S}}^{\mu^2}$, $\hat{\mathbf{I}}^{\mu^2}$, $\hat{\mathbf{J}}^{\mu^2}$, $\hat{\mathbf{F}}^{\mu^2}$ and \hat{F}_z^μ are simultaneously diagonalizable, and the

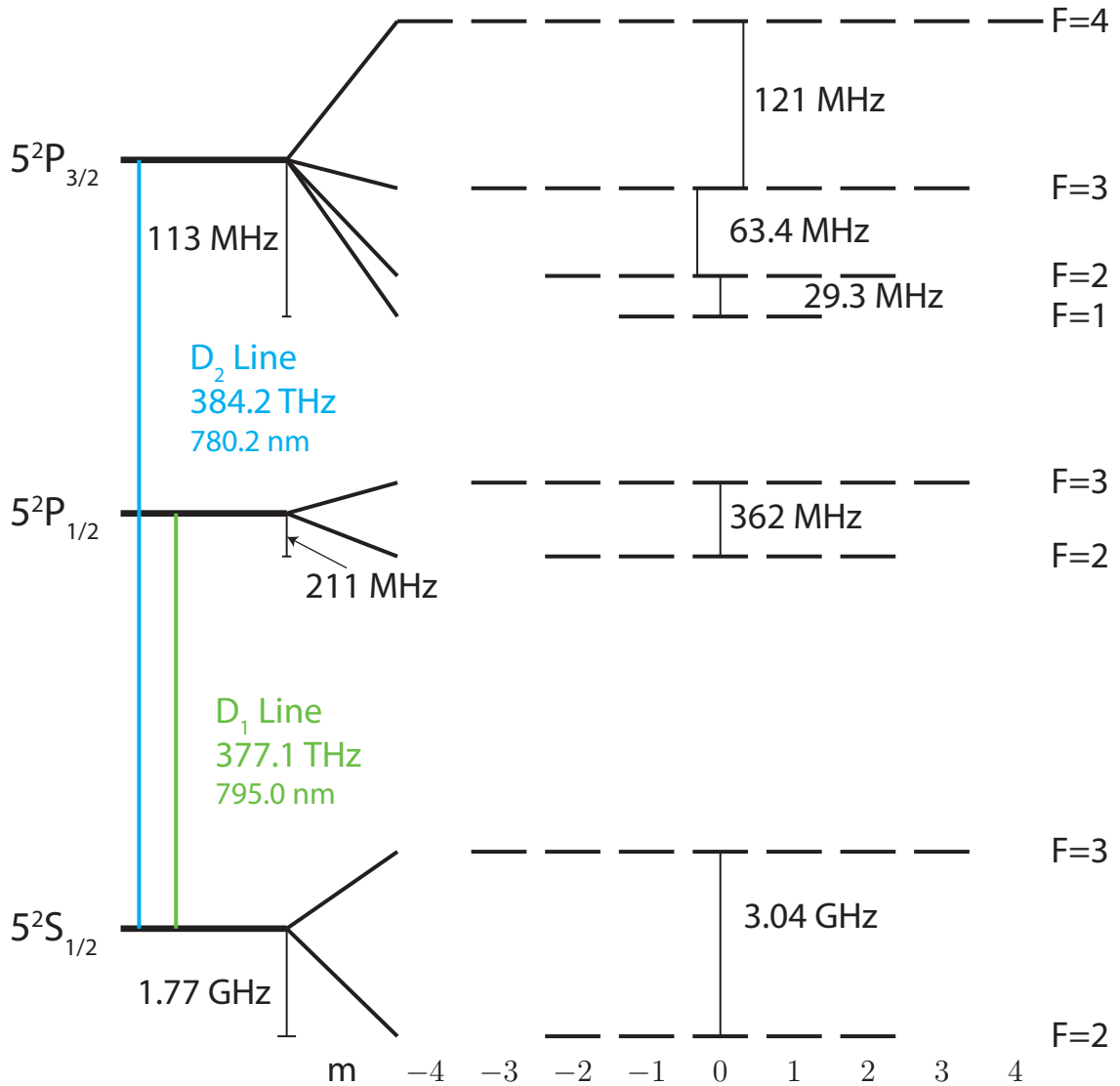


Figure 2.2: Shows a diagram of the energy levels of ^{85}Rb that form the ground state $5^2S_{1/2}$, and excited state $5^2P_{1/2}$ and $5^2P_{3/2}$ fine structure levels. These levels are involved in the $D1$ ($5^2S_{1/2} \leftrightarrow 5^2P_{1/2}$) and $D2$ ($5^2S_{1/2} \leftrightarrow 5^2P_{3/2}$) line transitions. The energies difference between two adjacent hyperfine levels is by $2\pi\hbar$ times the indicated frequency.

state $|f, m\rangle$ in level $|f\rangle$ has the following eigenvalues:

$$\hat{H}_0 |f, m\rangle = \hbar\omega_f |f, m\rangle \quad (2.24a)$$

$$\hat{\mathbf{L}}^2 |f, m\rangle = L_f(L_f + 1) |f, m\rangle \quad (2.24b)$$

$$\hat{\mathbf{S}}^2 |f, m\rangle = S_f(S_f + 1) |f, m\rangle \quad (2.24c)$$

$$\hat{\mathbf{J}}^2 |f, m\rangle = J_f(J_f + 1) |f, m\rangle \quad (2.24d)$$

$$\hat{\mathbf{I}}^2 |f, m\rangle = I_f(I_f + 1) |f, m\rangle \quad (2.24e)$$

$$\hat{\mathbf{F}}^2 |f, m\rangle = F_f(F_f + 1) |f, m\rangle \quad (2.24f)$$

$$\hat{F}_z |f, m\rangle = m |f, m\rangle, \quad (2.24g)$$

where $\hbar\omega_f$ is the energy of level $|f\rangle$ and the angular momentum quantum numbers obey the following restrictions

$$|L_f - S_f| \leq J_f \leq L_f + S_f \quad (2.25a)$$

$$|J_f - I_f| \leq F_f \leq J_f + I_f \quad (2.25b)$$

$$-F_f \leq m \leq F_f. \quad (2.25c)$$

The energies of selected levels are indicated in Figs. 2.1 and 2.2. We may write the Hamiltonian for atom μ resting in the absence of applied fields in terms of its energy Eigenstates as

$$\hat{H}_0^\mu = \sum_f \hbar\omega_f \sum_{m=-F_f}^{F_f} \hat{\sigma}_{f,m;f,m}^\mu. \quad (2.26)$$

where $\hat{\sigma}_{f,m;f',m'}^\mu \equiv |f, m\rangle_\mu \langle f', m'|$ is the Schrödinger picture coherence operator between states $|f, m\rangle_\mu$ and $|f', m'\rangle_\mu$ for atom μ .

2.1.2 The atomic dipole operator $\hat{\mathbf{d}}$

In this section, we examine the atomic dipole operator $\hat{\mathbf{d}}^\mu$ in more detail, and establish a notation which we will use for the remainder of the thesis. It is convenient to separate the dipole operator into positive and negative frequency components. The

dipole operator for atom μ is given by

$$\hat{\mathbf{d}}^\mu = \hat{\mathbf{d}}^{(+)\mu} + \hat{\mathbf{d}}^{(-)\mu} \quad (2.27)$$

where the positive/negative frequency component is given by

$$\hat{\mathbf{d}}^{(\pm)\mu} = \sum_{f,f'} \hat{\mathbf{d}}_{(f,f')}^{(\pm)\mu}, \quad (2.28)$$

and $\hat{\mathbf{d}}_{(f,f')}^{(\pm)\mu}$, the operator that couples levels $|f\rangle$ and $|f'\rangle$, is expressed in terms of the atomic state coherences as

$$\hat{\mathbf{d}}_{(f,f')}^{(-)\mu} = \begin{cases} \sum_{m=-F_f}^{F_f} \sum_{m'=-F_{f'}}^{F_{f'}} \hat{\sigma}_{f',m';f,m}^\mu \langle f', m' | \hat{\mathbf{d}} | f, m \rangle & : \quad \omega_{f'} > \omega_f \\ 0 & : \quad \omega_{f'} \leq \omega_f \end{cases}, \quad (2.29)$$

and $\hat{\mathbf{d}}_{(f,f')}^{(+)\mu} = \hat{\mathbf{d}}_{(f,f')}^{(-)\mu\dagger}$.

We simplify Eq. (2.29) by decomposing the vector operator $\hat{\mathbf{d}}_{(f,f')}^{(-)\mu}$ into its rank-1 spherical tensor components [83]

$$\hat{\mathbf{d}}_{(f,f')}^{(-)\mu} = \sum_{\alpha=-1}^1 \vec{\xi}_\alpha^* \hat{d}_{(f,f')\alpha}^{(-)\mu} \quad (2.30)$$

where

$$\vec{\xi}_{\pm 1} = \frac{1}{2} (\hat{x} \pm i\hat{y}), \quad (2.31a)$$

$$\vec{\xi}_0 = \hat{z}, \quad (2.31b)$$

and

$$\hat{d}_{(f,f')\alpha}^{(-)\mu} \equiv \vec{\xi}_\alpha \cdot \hat{\mathbf{d}}_{(f,f')}^{(-)\mu}. \quad (2.32)$$

We may similarly decompose the positive frequency component of the dipole operator;

$$\hat{\mathbf{d}}_{(f,f')}^{(+)\mu} = \sum_{\alpha=-1}^1 \vec{\xi}_\alpha \hat{d}_{(f,f')\alpha}^{(+)\mu}, \quad (2.33)$$

where $\hat{d}_{(f,f')\alpha}^{(+)\mu} = \hat{d}_{(f,f')\alpha}^{(-)\mu\dagger}$. Using the Wigner-Eckert theorem, we evaluate the dipole matrix elements and arrive at the expression for dipole operator

$$\hat{d}_{(f,f')\alpha}^{(-)\mu} = \begin{cases} \sum_{m=-F_f}^{F_f} \left(f' \parallel \hat{\mathbf{d}} \parallel f \right) C_{m\alpha}^{F_f-1 F_{f'}} \hat{\sigma}_{f',m+\alpha;f,m}^\mu & : \quad \omega_{f'} > \omega_f \\ 0 & : \quad \omega_{f'} \leq \omega_f \end{cases}, \quad (2.34)$$

where $\left(f' \left\| \hat{\mathbf{d}} \right\| f\right)$ is the reduced matrix element of $\hat{\mathbf{d}}$ between the levels $|f\rangle$ and $|f'\rangle$ ¹, and $C_{m\alpha m+\alpha}^{F_f\ 1\ F_{f'}}$ are the Clebsch-Gordan coefficients.

Since the dipole operator only depends on the positions of the atomic constituents (Eq. (2.10)), only the spatial electronic wavefunctions, rather than the particle spins, play a role in electric dipole transitions. To a good approximation, the spatial electronic/nuclear wavefunctions are unaffected by hyperfine interactions between the nuclear spin and the electronic angular momentum [82]. It follows that the reduced matrix element between hyperfine levels $|f\rangle$ and $|f'\rangle$ may be expressed in terms of a reduced matrix element between the fine structure levels, $j\{f\}$ and $j\{f'\}$, in which levels $|f\rangle$ and $|f'\rangle$ reside. One finds that the reduced matrix elements $\left(f' \left\| \hat{\mathbf{d}} \right\| f\right)$ are related to the matrix elements between fine structure levels by [84]

$$\begin{aligned} \left(f' \left\| \hat{\mathbf{d}} \right\| f\right) &= \delta_{I_f, I_{f'}} (-1)^{I+1-J_f-F_f} [(2J_{f'}+1)(2F_f+1)]^{\frac{1}{2}} \\ &\times W(J_f\ F_f\ J_{f'}\ F_{f'}; I_f\ 1) \left(j\{f'\} \left\| \hat{\mathbf{d}} \right\| j\{f\}\right) \end{aligned} \quad (2.35)$$

where $W(J_1\ J_2\ J\ J_3; J'\ J'')$ are the Racah coefficients[84].

2.1.3 The Interaction Picture

In the work we present in this thesis, it is convenient to work in the interaction picture. The interaction picture wavefunction $|\Psi(t)\rangle_I$ is related to the Schrödinger picture wavefunction $|\Psi(t)\rangle_S$ by the relation

$$|\Psi(t)\rangle_S = \hat{U}(t) |\Psi(t)\rangle_I, \quad (2.36)$$

where $\hat{U}(t) = \exp((\hat{H}_{Rad} + \sum_{\mu=1}^N \hat{H}_0^\mu)t/i\hbar)$ is a unitary evolution operator. Similarly, an interaction picture operator $\hat{A}_I(t)$ is related to the Schrödinger picture operator \hat{A} by

$$A_I(t) = \hat{U}^\dagger(t) \hat{A}_S \hat{U}(t). \quad (2.37)$$

¹For reduced matrix elements, we use the conventions of Rose [83].

In the remainder of this document, operators lacking an explicit time argument correspond to Schrödinger picture operators.

The interaction picture Hamiltonian now contains only the electric dipole interaction.

$$\hat{V}(t) = -\frac{1}{\epsilon_0} \sum_{\mu=1}^N \hat{\mathbf{d}}^\mu(t) \cdot \hat{\mathbf{D}}(\vec{r}_\mu, t), \quad (2.38)$$

where

$$\hat{\mathbf{d}}^\mu(t) = \sum_{f,f'} \sum_{\alpha=-1}^1 e^{-i(\omega_{f'} - \omega_f)t} \tilde{d}_{(f,f'),\alpha}^{(+)\mu} \vec{\xi}_\alpha + h.c. \quad , \quad (2.39)$$

and

$$\tilde{d}_{(f,f'),\alpha}^{(+)\mu} = \begin{cases} \sum_{m=-F_f}^{F_f} \left(f' \parallel \hat{\mathbf{d}} \parallel f \right)^* C_{m\alpha}^{F_f-1 F_{f'}} \tilde{\sigma}_{f,m;f',m+\alpha}^\mu & : \quad \omega_{f'} > \omega_f \\ 0 & : \quad \omega_{f'} \leq \omega_f \end{cases} \quad , \quad (2.40)$$

where $\tilde{\sigma}_{f,m;f',m'}^\mu \equiv \exp(i(\omega_{f'} - \omega_f)t) \hat{\sigma}_{f,m;f',m'}^\mu(t)$ is the slowly varying atomic coherence operator. Note that in the interaction picture, the slowly varying atomic operators are time independent, i.e. $\tilde{\sigma}_{f',m+\alpha;f,m}^\mu = \hat{\sigma}_{f',m+\alpha;f,m}^\mu$.

The time dependent displacement field is given in the interaction picture by

$$\hat{\mathbf{D}}(\vec{r}, t) = \epsilon_0 \left(\hat{\mathbf{E}}^{(+)}(\vec{r}, t) + \hat{\mathbf{E}}^{(-)}(\vec{r}, t) \right), \quad (2.41)$$

where

$$\hat{\mathbf{E}}^{(+)}(\vec{r}, t) = i \sum_{\lambda} \int d^3k \mathcal{E}(ck) \vec{\epsilon}_\lambda(\vec{k}) \hat{a}_\lambda(\vec{k}) e^{-ick(t - \hat{k} \cdot \vec{r}/c)} \quad (2.42)$$

and $\hat{\mathbf{E}}^{(-)}(\vec{r}, t) = \hat{\mathbf{E}}^{(+)\dagger}(\vec{r}, t)$. In the next section, we will discuss the decomposition of the electromagnetic field into system fields, which consist of classical laser fields and modes detected by photon counters in the experiments, and the reservoir, which contains the plethora of undetected modes.

2.1.4 Decomposition of the electromagnetic field

When dealing with light interactions with atomic ensembles for the purposes of storing and generating quantum information, one often considers the interaction of the

atoms with several narrow band-width fields. We identify these fields as *system* fields. The system fields may consist of the *write*, *read*, signal and idler fields that we discuss in the context of entanglement and single photon generation in Chapters 3, 4, 5, and 8. They may also include the classical *control* and quantum signal fields that participate in electromagnetically induced transparency and photon storage, as discussed in Chapters 6 through 8.

We decompose the displacement field $\hat{\mathbf{D}}(\vec{r}, t)$ into the system fields plus a contribution from the reservoir.

$$\hat{\mathbf{D}}(\vec{r}, t) = \hat{\mathbf{D}}_R(\vec{r}, t) + \sum_{\iota} \hat{\mathbf{D}}_{\iota}(\vec{r}, t) \quad (2.43)$$

where ι is the index indicating the system field, and $\hat{\mathbf{D}}_R(\vec{r}, t) \equiv \hat{\mathbf{D}}(\vec{r}, t) - \sum_{\iota} \hat{\mathbf{D}}_{\iota}(\vec{r}, t)$ is the contribution to the field of the reservoir modes. The system field ι is described by a set of plane wave modes centered on the wavevector \vec{k}_{ι} . Specifically, field ι is described by the set of annihilation and creation operators $\{\hat{a}_{\lambda}(\vec{k}), \hat{a}_{\lambda}^{\dagger}(\vec{k}) : \lambda \in \{H, V\}, \text{ and } \vec{k} \in D_{\iota}\}$, where $D_{\iota} = \{\vec{k} : |k_{\parallel}^{(\iota)} - k_{\iota}| \leq \Delta k/2, \text{ and } |k_{\perp \lambda}^{(\iota)}| \leq k_{\iota} \vartheta/2 \forall \lambda \in \{H, V\}\}$ is the set of wavevectors for the modes belonging to field ι , $\Delta k \ll k_{\iota}$ is the range of wave numbers in D_{ι} , $k_{\perp \lambda}^{(\iota)} \equiv \vec{\varepsilon}_{\lambda}(\hat{k}_{\iota}) \cdot \vec{k}$ is the component of the wavevector \vec{k} along the linear polarization vector $\vec{\varepsilon}_{\lambda}(\hat{k}_{\iota})$ for the plane wave propagating in the direction $\hat{k}_{\iota} = \vec{k}_{\iota}/k_{\iota}$, and $\vartheta \ll 1$ is the maximum variation of the solid angle for system field ι . For an arbitrary vector \vec{v} , we label the component parallel to \hat{k}_{ι} as $v_{\parallel}^{(\iota)} \equiv \vec{v} \cdot \hat{k}_{\iota}$ and the transverse portion as $\vec{v}_{\perp}^{(\iota)} \equiv \vec{v} - v_{\parallel}^{(\iota)} \hat{k}_{\iota}$.

Like the total displacement field, we decompose the narrow band field into positive and negative frequency components.

$$\hat{\mathbf{D}}_{\iota}(\vec{r}, t) = \epsilon_0 \left(\hat{\mathbf{E}}_{\iota}^{(+)}(\hat{\mathbf{r}}, t) + h.c. \right), \quad (2.44)$$

where

$$\hat{\mathbf{E}}_{\iota}^{(+)}(\vec{r}, t) = i \sum_{\lambda} \int_{D_{\iota}} d^3k \vec{\varepsilon}_{\lambda}(\hat{k}) \mathcal{E}(ck) e^{-ick(t - \hat{k} \cdot \vec{r}/c)} \hat{a}_{\lambda}(\vec{k}). \quad (2.45)$$

We decompose the Reservoir operator in a similar fashion:

$$\hat{\mathbf{D}}_R(\vec{r}, t) = \epsilon_0 \left(\hat{\mathbf{E}}_R^{(+)}(\hat{\mathbf{r}}, t) + h.c. \right), \quad (2.46)$$

where

$$\hat{\mathbf{E}}_R^{(+)}(\vec{r}, t) = \hat{\mathbf{E}}^{(+)}(\vec{r}, t) - \sum_{\iota} \hat{\mathbf{E}}_{\iota}^{(+)}(\vec{r}, t). \quad (2.47)$$

Because the variation of wavenumbers $\Delta k \ll k_{\iota}$ is small, we may make the narrow-bandwidth approximation, replacing $\mathcal{E}(ck)$ with $\mathcal{E}(ck_{\iota})$ for all $\vec{k} \in D_{\iota}$. This approximation allows us to reexpress the system field $\hat{\mathbf{E}}_{\iota}^{(+)}$ in the simplified form

$$\hat{\mathbf{E}}_{\iota}^{(+)} \approx \sqrt{\frac{\hbar k_{\iota}}{2\epsilon_0}} e^{-ick_{\iota}(t-r_{\parallel}^{(\iota)}/c)} \hat{\Phi}^{(\iota)}(\vec{r}, t) \quad (2.48)$$

where we have defined the slowly varying photon flux density operator

$$\hat{\Phi}^{(\iota)}(\vec{r}, t) \equiv i \sqrt{\frac{c}{(2\pi)^3}} \sum_{\lambda} \int_{D_{\iota}} d^3k \vec{\epsilon}_{\lambda}(\hat{k}) e^{i((\vec{k}-\vec{k}_{\iota}) \cdot \vec{r} - c(k-k_{\iota})t)} \hat{a}_{\lambda}(\vec{k}) \quad (2.49)$$

$$\begin{aligned} &= i \sqrt{\frac{c}{(2\pi)^3}} \sum_{\lambda} \int_{D_{\iota}} d^3k \vec{\epsilon}_{\lambda}(\hat{k}) \\ &\quad \times e^{i\vec{k}_{\perp}^{(\iota)} \cdot \vec{r}} e^{-ic(k_{\parallel}^{(\iota)} - k_{\iota})(t-r_{\parallel}^{(\iota)}/c)} e^{-ic(k-k_{\parallel}^{(\iota)})t} \hat{a}_{\lambda}(\vec{k}). \end{aligned} \quad (2.50)$$

As we shall see from the following argument, the last exponential appearing in Eq. (2.50) accounts for diffraction. We may approximate the difference appearing in the last exponential of Eq. (2.50) as $k - k_{\parallel}^{(\iota)} = \sqrt{(k_{\parallel}^{(\iota)})^2 + |\vec{k}_{\perp}^{(\iota)}|^2} - k_{\parallel}^{(\iota)} \approx |\vec{k}_{\perp}^{(\iota)}|^2 / (2k_{\iota})$, so that the slowly varying field becomes

$$\begin{aligned} \hat{\Phi}^{(\iota)}(\vec{r}, t) &= i \sqrt{\frac{c}{(2\pi)^3}} \sum_{\lambda} \int_{D_{\iota}} d^3k \vec{\epsilon}_{\lambda}(\hat{k}) \\ &\quad \times e^{i\vec{k}_{\perp}^{(\iota)} \cdot \vec{r}} e^{-ic(k_{\parallel}^{(\iota)} - k_{\iota})(t-r_{\parallel}^{(\iota)}/c)} e^{-ic|\vec{k}_{\perp}^{(\iota)}|^2 t / (2k_{\iota})} \hat{a}_{\lambda}(\vec{k}) \end{aligned} \quad (2.51)$$

By differentiating Eq. (2.51), we may find the following equation of motion for the slowly varying envelope operator in the interaction picture,

$$\left(\frac{\partial}{\partial t} + c\hat{k}_{\iota} \cdot \vec{\nabla} \right) \hat{\Phi}^{(\iota)} = ic \frac{\nabla_{\perp}^{(\iota)2}}{2k_{\iota}} \hat{\Phi}^{(\iota)}. \quad (2.52)$$

It is convenient to further decompose the slowly varying envelope into its helicity components; $\hat{\Phi}(\vec{r}, t) = \sum_{\alpha=-1}^1 \vec{e}_{\alpha}(\hat{k}_l) \hat{\Phi}_{\alpha}^{(\iota)}(\vec{r}, t)$, where $\vec{e}_{\pm}(\hat{k}_l) \equiv \mp(1/\sqrt{2})(\vec{\varepsilon}_H(\hat{k}_l) \pm i\vec{\varepsilon}_V(\hat{k}_l))$ and $\vec{e}_0(\hat{k}_l) \equiv \hat{k}_l$ are the helicity vectors for a field propagating in the \hat{k}_l direction as described in Appendix A, and $\hat{\Phi}_{\alpha}^{(\iota)}(\vec{r}, t) = \vec{e}_{\alpha}^*(\hat{k}_l) \cdot \hat{\Phi}^{(\iota)}(\vec{r}, t)$ is the component of the slowly varying photon flux density operator with helicity α . In the problems we consider, the distribution of propagation directions \hat{k} within a particular system field is assumed sufficiently narrow so that we may make the paraxial approximation. That is, we may approximate the slowly varying field $\hat{\Phi}^{(\iota)}(\vec{r}, t)$ by replacing the polarization vector $\vec{\varepsilon}_{\lambda}(\hat{k})$ appearing in Eqs. (2.49), (2.50), and (2.51) with the linear polarizations associated with the carrier wave vector $\vec{\varepsilon}_{\lambda}(\hat{k}_l)$. With this approximation, the component of the slowly varying field along \hat{k}_l is negligible, and therefore $\hat{\Phi}_0^{(\iota)} \approx 0$. It can be shown, that in the paraxial approximation, the field operators for system fields ι and ι' obey the commutation relations,

$$\left[\hat{\Phi}_{\alpha}^{(\iota)}(\vec{r}, t), \hat{\Phi}_{\beta}^{(\iota')}(\vec{r}', t') \right] = \left[\hat{\Phi}_{\alpha}^{(\iota)\dagger}(\vec{r}, t), \hat{\Phi}_{\beta}^{(\iota')\dagger}(\vec{r}', t') \right] = 0 \quad (2.53a)$$

$$\begin{aligned} \left[\hat{\Phi}_{\alpha}^{(\iota)}(\vec{r}, t), \hat{\Phi}_{\beta}^{(\iota')\dagger}(\vec{r}', t') \right] &= \delta_{\iota, \iota'} \delta_{\alpha, \beta} \frac{c}{(2\pi)^3} \int_{-\frac{\Delta k}{2}}^{\frac{\Delta k}{2}} dq e^{-icq((t-t')-(r_{\parallel}^{(\iota)}-r_{\parallel}^{(\iota')})/c)} \\ &\times \int_{D_{\iota}} d^2 k_{\perp}^{(\iota)} e^{-ic \frac{k_{\perp}^{(\iota)2}}{2k_{\iota}} t + \vec{k}_{\perp}^{(\iota)} \cdot \vec{r}} \end{aligned} \quad (2.53b)$$

$$\begin{aligned} &= \delta_{\iota, \iota'} \delta_{\alpha, \beta} \frac{c \Delta k}{2\pi} \text{sinc} \left[\frac{c \Delta k}{2} \left((t-t') - (r_{\parallel}^{(\iota)} - r_{\parallel}^{(\iota')}) / c \right) \right] \\ &\times \frac{1}{(2\pi)^2} \int_{D_{\iota}} d^2 k_{\perp}^{(\iota)} e^{-ic \frac{k_{\perp}^{(\iota)2}}{2k_{\iota}} (t-t') + \vec{k}_{\perp}^{(\iota)} \cdot \vec{r}} \end{aligned} \quad (2.53c)$$

These commutation relations are simplified somewhat when they are taken at equal times, $t = t'$,

$$\begin{aligned} \left[\hat{\Phi}_{\alpha}^{(\iota)}(\vec{r}, t), \hat{\Phi}_{\beta}^{(\iota')\dagger}(\vec{r}', t) \right] &= \delta_{\iota, \iota'} \delta_{\alpha, \beta} \frac{c \Delta k}{2\pi} \text{sinc} \left[\frac{c \Delta k}{2} \left((r_{\parallel}^{(\iota)} - r_{\parallel}^{(\iota')}) / c \right) \right] \\ &\times \left(\frac{k_{\iota} \vartheta}{2\pi} \right)^2 \prod_{\lambda \in \{H, V\}} \text{sinc} \left[\frac{k_{\iota} \vartheta}{2} \left(r_{\perp \lambda}^{(\iota)} - r_{\perp \lambda}^{(\iota')} \right) \right] \end{aligned} \quad (2.54)$$

$$\approx c \delta_{\iota, \iota'} \delta_{\alpha, \beta} \delta(\vec{r} - \vec{r}'), \quad (2.55)$$

where we have used the approximation, $(k/\pi) \text{sinc}(k(x-x')) \approx \delta(x-x')$ when we are

concerned only with variations of x much larger than $1/k$. Interestingly, one also finds the slowly varying fields are delta correlated in time for equal propagation distances $r_{\parallel}^{(\iota)} = r_{\parallel}^{(\iota)'}.$

$$\begin{aligned} \left[\hat{\Phi}_{\alpha}^{(\iota)}(\vec{r}_{\perp}^{(\iota)}, r_{\parallel}^{(\iota)}, t), \hat{\Phi}_{\beta}^{(\iota')\dagger}(\vec{r}_{\perp}^{(\iota')'}, r_{\parallel}^{(\iota')'}, t') \right] &= \delta_{\iota, \iota'} \delta_{\alpha, \beta} \frac{c\Delta k}{2\pi} \text{sinc} \left[\frac{c\Delta k}{2} (t - t') \right] \left(\frac{k_{\iota} \vartheta}{2\pi} \right)^2 \\ &\times \prod_{\lambda \in \{H, V\}} \text{sinc} \left[\frac{k_{\iota} \vartheta}{2} \left(r_{\perp \lambda}^{(\iota)} - r_{\perp \lambda}^{(\iota)'} \right) \right] \quad (2.56) \end{aligned}$$

$$\approx \delta_{\iota, \iota'} \delta_{\alpha, \beta} \delta(t - t') \delta(\vec{r}_{\perp}^{(\iota)} - \vec{r}_{\perp}^{(\iota)'}). \quad (2.57)$$

These equal space commutation relations will be helpful in the description of photo detection, where the detector is fixed in space, and we are interested in how a state is conditioned on the photon arrival times, as discussed in Appendix D.

The system fields as we have defined them allow us account for the longitudinal and transverse character of the evolution of the quantum field. Such a general treatment is useful when one studies the propagation and stability properties of quantum electromagnetic fields in a nonlinear medium [85]. In the problems we treat here, however, the dynamics in the transverse dimension of the system fields are unimportant. When quantum fields are detected by photon counters in our experiments, only a single transverse spatial mode – a Gaussian mode, more specifically – is collected by an optical fiber. Further, the classical laser fields in the experimental setups have a controlled transverse spatial structure. For this reason, we will now define effective one dimensional system fields, where the transverse spatial dynamics are frozen out.

To formally accomplish this task, we identify a complete set of mode functions $\{f_i : D_{\iota}^{\perp} \rightarrow \mathbb{C}\}$, where

$$D_{\iota}^{\perp} \equiv \left\{ \vec{k}_{\perp} \in \mathbb{R}^2 : k_{\perp \lambda}^{(\iota)} < k_{\iota} \vartheta, \lambda \in \{H, V\}, i = 0 \dots \infty \right\}. \quad (2.58)$$

These functions are orthonormal on the set D_{ι}^{\perp} , and therefore satisfy the normalization condition,

$$\int_{D_{\iota}^{\perp}} d^2 k_{\perp} f_i^*(\vec{k}_{\perp}^{(\iota)}) f_j(\vec{k}_{\perp}^{(\iota)}) = \delta_{i,j}. \quad (2.59)$$

Having identified this set of functions, we define the transverse mode annihilation operators

$$\hat{a}_{\lambda,i}^{(\iota)}(k_{\parallel}^{(\iota)}, t) \equiv \int d^2 k_{\perp} e^{-ic \frac{|\vec{k}_{\perp}^{(\iota)}|^2}{2k_{\iota}} t} f_i^*(\vec{k}_{\perp}) \hat{a}_{\lambda}(\vec{k}) \quad (2.60)$$

where $k_{\parallel}^{(\iota)}$ is the component of \vec{k} parallel to \hat{k}_{ι} , and t functions as a parameter with units of time. The relationship in Eq. (2.60) can be inverted by

$$\hat{a}_{\lambda}(\vec{k}) = \sum_i f_i(\vec{k}_{\perp}^{(\iota)}) e^{ic \frac{|\vec{k}_{\perp}^{(\iota)}|^2}{2k_{\iota}} t} \hat{a}_{\lambda,i}^{(\iota)}(k_{\parallel}^{(\iota)}, t) \quad (2.61)$$

By inserting the modal expansion of $\hat{a}_{\lambda}(\vec{k})$ of Eq. (2.61) into Eq. (2.51), and again making the paraxial approximation, we find

$$\hat{\Phi}(\vec{r}, t) = \sum_{\lambda} \vec{\varepsilon}_{\lambda}(\hat{k}_{\iota}) \hat{\varphi}_{\lambda,i}^{(\iota)}(r_{\parallel}^{(\iota)}, t) \phi_i^{(\iota)}(\vec{r}), \quad (2.62)$$

where

$$\hat{\varphi}_{\lambda,i}^{(\iota)}(r_{\parallel}^{(\iota)}, t) \equiv \frac{1}{\sqrt{2\pi}} \int dk_{\parallel}^{(\iota)} e^{i(k_{\parallel}^{(\iota)} - k_{\iota})(r_{\parallel}^{(\iota)} - ct)} \hat{a}_{\lambda,i}^{(\iota)}(k_{\parallel}^{(\iota)}, t - r_{\parallel}^{(\iota)}/c) \quad (2.63a)$$

$$= \frac{1}{\sqrt{(2\pi)^3}} \int d^3 k e^{i(k_{\parallel}^{(\iota)} - k_{\iota})(r_{\parallel}^{(\iota)} - ct)} \times e^{i \frac{|\vec{k}_{\perp}^{(\iota)}|^2}{2k_{\iota}} (r_{\parallel}^{(\iota)} - ct)} f_i^*(\vec{k}_{\perp}) \hat{a}_{\lambda}(\mathbf{k}) \quad (2.63b)$$

is the one dimensional photon flux operator, and

$$\phi_i^{(\iota)}(\vec{r}) = \frac{i}{2\pi} \int d^2 k_{\perp} e^{i\vec{k}_{\perp} \cdot \vec{r}} e^{-i \frac{|\vec{k}_{\perp}^{(\iota)}|^2}{2k_{\iota}} r_{\parallel}^{(\iota)}} f_i(\vec{k}_{\perp}^{(\iota)}) \quad (2.64)$$

is the transverse spatial profile associated with $f_i(\vec{k}_{\perp}^{(\iota)})$. One can show that for equal longitudinal positions $r_{\parallel}^{(\iota)}$, the spatial mode functions satisfy the normalization condition

$$\int d^2 r_{\perp} \phi_i^{(\iota)*}(\vec{r}_{\perp}, r_{\parallel}^{(\iota)}) \phi_j^{(\iota)}(\vec{r}_{\perp}, r_{\parallel}^{(\iota)}) = \delta_{i,j}. \quad (2.65)$$

The operators $\hat{\varphi}_{\lambda,i}^{(\iota)}(r_{\parallel}^{(\iota)}, t)$ and $\hat{\varphi}_{\lambda,i}^{(\iota)\dagger}(r_{\parallel}^{(\iota)}, t)$ obey the equal time commutation relations

$$[\hat{\varphi}_i^{(\iota)}(r_{1\parallel}^{(\iota)}, t), \hat{\varphi}_j^{(\iota)}(r_{2\parallel}^{(\iota)}, t)] = 0 \quad (2.66a)$$

$$[\hat{\varphi}_i^{(\iota)}(r_{1\parallel}^{(\iota)}, t), \hat{\varphi}_j^{(\iota)\dagger}(r_{2\parallel}^{(\iota)}, t)] = \delta_{i,j} \delta(r_{1\parallel}^{(\iota)} - r_{2\parallel}^{(\iota)}). \quad (2.66b)$$

Furthermore, in the interaction picture the operator $\hat{\varphi}_{\lambda,i}^{(\iota)}(r_{\parallel}^{(\iota)}, t)$ satisfies the equation of motion

$$\left(\frac{\partial}{\partial t} + c\hat{k}_{\iota} \cdot \nabla \right) \hat{\varphi}_i^{(\iota)} = 0. \quad (2.67)$$

The transverse spatial profiles, on the other hand, are time independent, and solve the differential equation

$$\left(\hat{k}_{\iota} \cdot \nabla \right) \phi_i^{(\iota)}(\vec{r}) = i \frac{\nabla_{\perp}^{(\iota)2}}{2k_{\iota}} \phi_i^{(\iota)}(\vec{r}) \quad (2.68)$$

Having expressed the system field in terms of an expansion of transverse spatial modes, we may easily make the simplification that only one of these transverse modes is populated and/or detected for a given system field. When we keep only the populated/detected transverse mode, the positive frequency component of the electric field for system field ι becomes

$$\hat{\mathbf{E}}_{\iota}^{(+)}(\vec{r}, t) = (2\pi)^{3/2} \mathcal{E}(ck_{\iota}) e^{-ick_{\iota}(t-r_{\parallel}^{(\iota)}/c)} \phi^{(\iota)}(\vec{r}) \sum_{\alpha=\pm 1} \vec{e}_{\alpha}(\hat{k}_{\iota}) \hat{\varphi}_{\alpha}^{(\iota)}(r_{\parallel}^{(\iota)}, t), \quad (2.69)$$

where $\hat{\varphi}_{\alpha}^{(\iota)}(r_{\parallel}^{(\iota)}, t)$ is the photon flux annihilation operator for the field of helicity α , and is given by

$$\hat{\varphi}_{\alpha}^{(\iota)}(r_{\parallel}^{(\iota)}, t) = \sum_{\lambda \in \{H, V\}} \vec{e}_{\alpha}^{*}(\hat{k}_{\iota}) \cdot \vec{\varepsilon}_{\lambda}(\hat{k}_{\iota}) \hat{\varphi}_{\lambda}^{(\iota)}(r_{\parallel}^{(\iota)}, t). \quad (2.70)$$

In the remainder of this thesis, we will assume our system fields are well described by Eq. (2.69).

2.2 *Ensemble Interactions with Narrow Bandwidth Fields*

In this section, we consider the general case in which an atomic ensemble interacts with one or more narrow band-width fields. To explore the interaction of the atomic ensemble with the system fields, we begin with the electric dipole Hamiltonian for the interaction of the ensemble with the full quantized electromagnetic field in the

interaction picture (Eq. (2.38)). We take advantage of the notation developed in the last section.

We will first examine the dynamics of a system field labeled by the index ι which propagates in the direction \hat{k}_ι and has a carrier frequency ck_ι . The contribution to the electric field from system field ι is given by Eq. (2.69). To gain insight into the generalized field propagation dynamics, we write the Heisenberg equation of motion for the slowly varying photon flux operator $\hat{\varphi}_\alpha^{(\iota)}(r_\parallel^{(\iota)}, t)$ for photons of helicity $\alpha = \pm 1$. This equation of motion is given by

$$\left(\frac{\partial}{\partial t} + c\hat{k}_\iota \cdot \nabla \right) \hat{\varphi}_\alpha^{(\iota)}(r_\parallel^{(\iota)}, t) = \frac{i}{\hbar\epsilon_0} \sum_\mu \left[\hat{\varphi}_\alpha^{(\iota)}(r_\parallel^{(\iota)}, t), \hat{\mathbf{D}}(\vec{r}_\mu, t) \right] \cdot \hat{\mathbf{d}}^\mu(t) \quad (2.71)$$

The commutation relation appearing in the Heisenberg equation of motion (Eq. (2.71)) is evaluated by using the decomposition of the displacement field of Eq. (2.43) and applying the commutation relations of Eq. (2.66). We then find that,

$$\begin{aligned} & \left[\hat{\varphi}_\alpha^{(\iota)}(r_\parallel^{(\iota)}, t), \hat{\mathbf{D}}(\vec{r}_\mu, t) \right] \\ &= \sqrt{\frac{\hbar ck_\iota \epsilon_0}{2}} e^{ick_\iota(t-r_\parallel^{(\iota)}/c)} \phi^{(\iota)*}(\vec{r}_\mu) \delta(\hat{k}_\iota \cdot (\vec{r} - \vec{r}_\mu)) \vec{e}_\alpha^*(\hat{k}_\iota) \end{aligned} \quad (2.72)$$

We then have the propagation equation for the Heisenberg field operators

$$\left(\frac{\partial}{\partial t} + c\hat{k}_\iota \cdot \nabla \right) \hat{\varphi}_\alpha^{(\iota)}(r_\parallel^{(\iota)}, t) = i\sqrt{\frac{ck_\iota}{2\hbar\epsilon_0}} e^{ick_\iota(t-r_\parallel^{(\iota)}/c)} \vec{e}_\alpha^*(\hat{k}_\iota) \cdot \hat{\mathcal{P}}(r_\parallel^{(i)}, t) \quad (2.73)$$

where

$$\hat{\mathcal{P}}(r_\parallel^{(i)}, t) \equiv \sum_\mu \hat{\mathbf{d}}^\mu(t) \phi^{(\iota)*}(\mathbf{r}_\mu) \delta(\hat{k}_\iota \cdot (\vec{r} - \vec{r}_\mu)), \quad (2.74)$$

and $\hat{\mathbf{d}}^\mu(t)$ is the Heisenberg picture dipole operator for atom μ , and is given by

$$\hat{\mathbf{d}}^\mu(t) = \sum_{f,f'} e^{-i(\omega_{f'} - \omega_f)t} \tilde{\mathbf{d}}_{(f,f')}^{(+)\mu}(t) + h.c. \quad , \quad (2.75)$$

$\tilde{\mathbf{d}}_{(f,f')}^{(+)\mu}(t) = \sum_{\alpha=-1}^1 \vec{\xi}_\alpha \tilde{d}_{(f,f')\alpha}^{(+)\mu}$ is the positive frequency component of the dipole operator coupling levels $|f\rangle$ and $|f'\rangle$, $\vec{\xi}_\alpha$ are the spherical basis vectors with respect to the

\hat{z} axis as defined in Eq. (2.31), and the spherical component of the dipole operator $\tilde{d}_{(f,f')\alpha}^{(+)\mu}$ is given in the Heisenberg picture by

$$\tilde{d}_{(f,f')\alpha}^{(+)\mu} = \begin{cases} \sum_{m=-F_f}^{F_f} \left(f' \parallel \hat{\mathbf{d}} \parallel f \right)^* C_{m\alpha}^{F_f \ 1 \ F_{f'}} \tilde{\sigma}_{f,m;f',m+\alpha}^{\mu}(t) & : \ \omega_{f'} > \omega_f \\ 0 & : \ \omega_{f'} \leq \omega_f \end{cases}, \quad (2.76)$$

where $\tilde{\sigma}_{f,m;f',m'}^{\mu}(t) \equiv \exp(i(\omega'_{f'} - \omega_f)t) \hat{\sigma}_{f,m;f',m'}^{\mu}(t)$ is the slowly varying coherence operator for atom μ .

Let us now briefly examine the atomic dynamics. The behavior of the atoms within the ensemble can be completely characterized by the slowly varying coherences $\tilde{\sigma}_{f,m;f',m'}^{\mu}(t)$ between atomic states $|f, m\rangle_{\mu}$ and $|f, m'\rangle_{\mu}$. These coherence satisfy the Heisenberg equation of motion

$$\begin{aligned} & \frac{d\tilde{\sigma}_{f,m;f',m'}^{\mu}}{dt} \\ &= \frac{1}{i\hbar} \left[\tilde{\sigma}_{f,m;f',m'}^{\mu}(t), \hat{V}(t) \right] \\ &= \frac{i}{\hbar} \left[\tilde{\sigma}_{f,m;f',m'}^{\mu}(t), \hat{\mathbf{d}}(t) \right] \cdot \left(\hat{\mathbf{E}}_R^{(+)}(\vec{r}_{\mu}, t) + \sum_{\iota} \hat{\mathbf{E}}_{\iota}^{(+)}(\vec{r}_{\mu}, t) + h.c. \right) \end{aligned} \quad (2.77)$$

The equations of motion we have derived in this Section describe the interaction of the electromagnetic fields with an ensemble atoms in an arbitrary configuration. We have now laid the base from which we can explore the dynamics involved in generating entanglement, and storing and retrieving quantum information within atomic ensembles.

CHAPTER 3

ENTANGLING A PHOTON WITH A COLLECTIVE ATOMIC EXCITATION

In this Chapter, we describe a new experimental approach to probabilistic atom-photon (signal) entanglement. Two qubit states are encoded as orthogonal collective spin excitations of an unpolarized atomic ensemble. After a programmable delay, the atomic excitation is converted into a photon (idler). Polarization states of both the signal and the idler are recorded and are found to be in violation of the Bell inequality. Atomic coherence times exceeding several microseconds are achieved by switching off all the trapping fields - including the quadrupole magnetic field of the magneto-optical trap - and zeroing out the residual ambient magnetic field.¹

We will also provide a detailed theoretical model for spontaneous Raman scattering from an atomic ensemble. It is shown how one arrives at an effective two-mode description for the collective scattering dynamics when undetected modes of the electromagnetic field are traced over. This, in turn, serves as the mechanism that generates the observed probabilistic atom-photon entanglement. The dynamics of the conversion of the atomic excitation to a photon are also discussed.

3.1 Introduction

Long-distance quantum cryptographic key distribution (QCKD) is an important goal of quantum information science. Extending the reach of quantum cryptography ideally involves the ability to entangle two distant qubits (two level quantum systems)

¹This chapter contains excerpts from Ref. [17].

[1, 29], using the Bell inequality violation to verify the security of the quantum communication channel. Parametric down conversion is an established technology producing entangled photon pairs. Unfortunately, it is not directly applicable to long-distance QCKD, as the rate scales exponentially with the distance due to probabilistic nature of entangled photon pairs generation. It is necessary to provide a controllable delay between the two photons, that is, to have a means of photon storage.

The latter requirement is problematic as photons are difficult to store for an appreciable period of time. By contrast atomic qubits are long lived and easily manipulated by laser fields; they are well suited for long term quantum information storage. Photonic qubits, however, can propagate for relatively long distances in fibers without absorption, making them excellent carriers of quantum information. Entangled systems of a single photon and a long-lived atomic qubit therefore offer an excellent building block for a quantum network.

A quantum repeater architecture can overcome the limitations of photons by inserting a quantum memory qubit into the quantum channel every attenuation length or so [29]. The idea is to generate entanglement between two neighboring atomic qubits, which can be done efficiently since light will not be appreciably absorbed within the segment length. After entanglement between each pair of atomic qubits has been established, a joint measurement on each neighboring pair of qubits is performed. The quantum states of all the intermediate qubits are destroyed by the measurement, achieving entanglement swapping such that only the two atomic qubits at the two ends are entangled. These two qubits can be used for QCKD, either with the Ekert protocol, that directly uses the entangled pair of qubits, or the BB84 protocol that performs either remote state preparation or teleportation of a qubit [5, 4, 24, 25, 26, 28]. The rate of QCKD using a quantum repeater protocol can scale polynomially with distance [29].

In the microwave domain, single Rydberg atoms and single photons have been

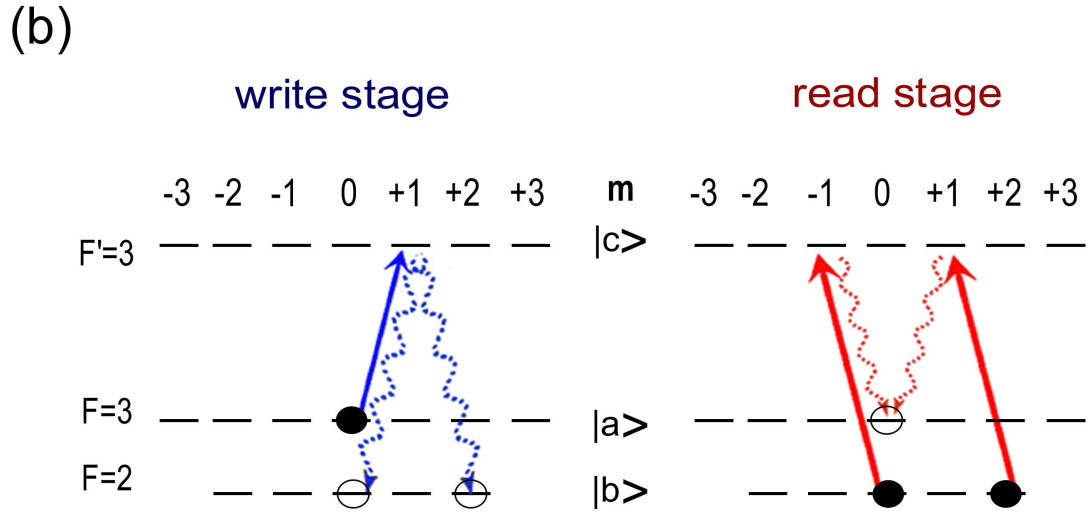
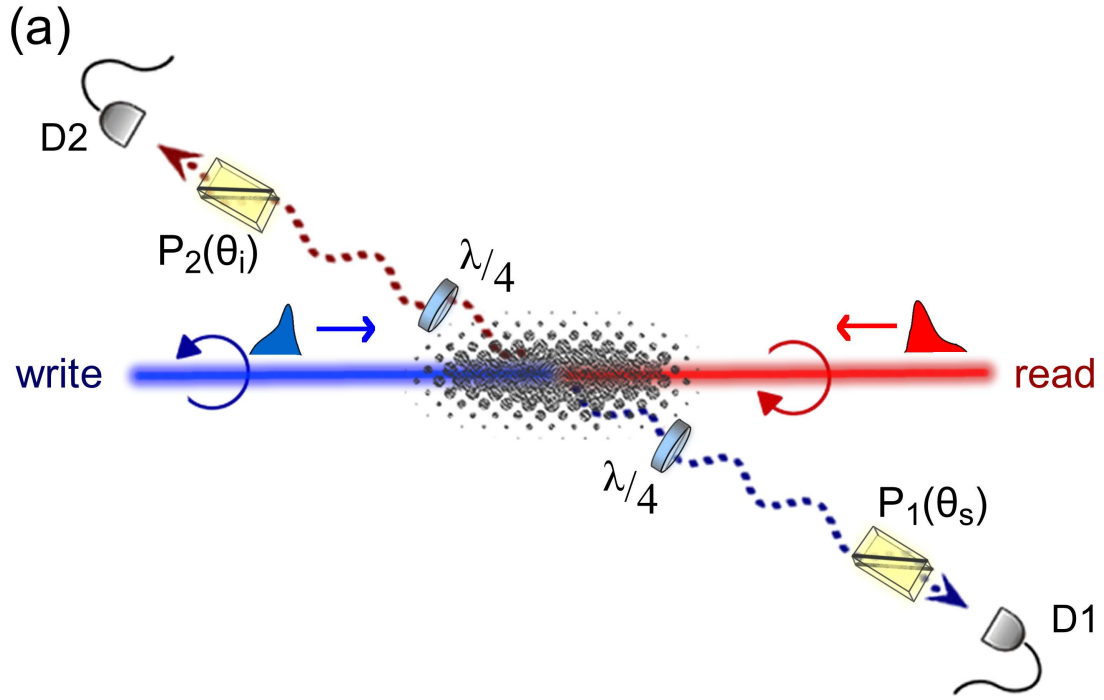


Figure 3.1: (a) Schematic of experimental setup. P_1 and P_2 , polarizers; D1 and D2, detectors; $\lambda/4$, quarter-waveplate. (b) The structure of atomic transitions leading to generation of atom-photon entanglement and of the subsequent read-out of atomic qubit.

entangled [86]. An entangled state of an ion and a photon has also been recently reported [32, 33]. Cavity QED holds promise for generation of deterministic neutral atom-photon entanglement, with single photon generation being an important step in that direction [36, 37]. Collective enhancement of atom-photon interactions in optically thick atomic ensembles offers a somewhat simpler route towards this goal [40, 41, 42, 43, 44, 45, 46]. However, the atom-photon entanglement is often of a probabilistic character.

Duan, Lukin, Cirac, and Zoller (DLCZ) have developed a program of long-distance quantum networking based on atomic ensembles [47]. This paradigm turns out to be remarkably similar to parametric down conversion, with the additional capability of atomic quantum memory. Non-classical radiation has been produced from an atomic ensemble [51, 52, 53, 54, 55, 56], as well as the preparation of a quantum memory qubit based on two atomic ensembles with subsequent quantum state transfer onto a photonic qubit [57]. These experiments [51, 52, 53, 54, 55, 56, 57] employed copropagating *write* and *read* laser fields and on-axis Raman-scattered light was collected. In contrast to these works, Braje and coworkers pioneered off-axis four-wave mixing [58] and efficient photon-pair production [87] in a cold atomic ensemble, using counter-propagating *write* and *read* fields deep in the regime of electromagnetically-induced transparency.

In this Chapter we report probabilistic entanglement of a collective atomic excitation and a photon (signal), achieved using the off-axis, counter-propagating geometry of Braje *et al.*[58, 87]. We propose and experimentally implement here an atomic qubit consisting of two distinct mixed states of collective ground-state hyperfine coherence which contain one spin excitation. The entanglement of the signal photon and the collective spin excitation is inferred by performing quantum state transfer of the atomic qubit onto a photonic qubit (idler) [57], with one of the atomic states being converted into a right-hand polarized photon and the other into a left-hand

polarized one. Polarization correlations of the signal and the idler photons are subsequently recorded and found to be in violation of the Bell inequality. The atom-photon entanglement is probabilistic, with the fundamental quantum state consisting mostly of vacuum. The entangled component of the state is post-selected by coincidence counting. This type of entanglement is similar to two-photon entanglement in spontaneous parametric down-conversion (see [88, 89, 90] and references therein), and to the ion-photon entanglement of Blinov *et al.* [32, 33].

3.2 Theory

As illustrated in Figure 3.1(a), the right circularly polarized *write* pulse generates Raman scattering. We collect a Gaussian mode centered around the momentum \vec{k}_s that forms a 2° angle with the *write* beam. Figure 3.1(b) indicates schematically the structure of the three atomic levels involved, $|a\rangle$, $|b\rangle$ and $|c\rangle$. The experimental sequence starts with all of the atoms prepared in the unpolarized level $|a\rangle$. The initial density operator of atom μ is given by $\hat{\rho}_0^\mu = \sum_{m=-F_a}^{F_a} p_m |a, m\rangle_\mu \langle a, m|$, where $p_m = 1/(2F_a + 1)$ is the probability of an atom is prepared in the state $|a, m\rangle$. A *write* pulse tuned to the $|a\rangle \rightarrow |c\rangle$ transition is directed into a sample of cold ^{85}Rb atoms. The classical *write* pulse is so weak that less than one photon is scattered in this manner on the $|c\rangle \rightarrow |b\rangle$ transition into the collected mode for each pulse.

Using perturbation theory, we show in Section 3.2.1 that the ensemble-photon density operator may be written as

$$\hat{\rho} = \left(1 + \chi \hat{\Psi}^\dagger(\eta)\right) \hat{\rho}_0 \left(1 + \chi \hat{\Psi}(\eta)\right) \quad (3.1)$$

where

$$\hat{\rho}_0 = \left(\bigotimes_{\mu=1}^N \hat{\rho}_0^\mu\right) \otimes |vac\rangle \langle vac| \quad (3.2)$$

is the initial density matrix of the ensemble-signal system, $|vac\rangle$ is the signal photon

vacuum state, $\chi \ll 1$ is an interaction parameter given by Eq. (3.53), and

$$\hat{\Psi}(\eta) = \cos \eta \hat{S}_{+1}^{(i)} \hat{a}_{+1}^{(s)} + \sin \eta \hat{S}_{-1}^{(i)} \hat{a}_{-1}^{(s)}, \quad (3.3)$$

where

$$\cos^2 \eta = \sum_{m=-F_a}^{F_a} p_m X_{m,1}^2 / \left[\sum_{m=-F_a}^{F_a} \sum_{\alpha=\pm 1} p_m X_{m,\alpha}^2 \right], \quad (3.4)$$

$X_{m,\alpha} = C_{m \alpha_w m + \alpha_w}^{F_a \ 1 \ F_c} C_{m + \alpha_w - \alpha \ m + \alpha_w}^{F_b \ 1 \ F_c}$ is the product of the relevant Clebsch-Gordan coefficients for the transitions, and $\alpha_w = 1$ is the helicity of the *write* field. The collective atomic spin excitation operators $\hat{S}_\alpha^{(i)}$ are given by Eq. (3.55). For weak states of excitation the collective spin operators satisfy bosonic commutation relations correct to $O(1/\sqrt{N})$: $[\hat{S}_\alpha^{(i)}, \hat{S}_\beta^{(i)\dagger}] = \delta_{\alpha,\beta}$. Evaluating the coefficient $\cos^2 \eta$ for the experimental conditions $F_a = F_c = 3$, $F_b = 2$, we find $\eta = 0.81 \times \pi/4$. It is important to realize that the vacuum component in density matrix $\hat{\rho}$ (Eq. (3.1)) has no influence on the fidelity of DLCZ's quantum communication protocols due to built-in purification, even though $\chi \ll 1$ [47].

Detection of a photon by D1 produced by the $|c\rangle \rightarrow |b\rangle$ transition results in the sample of atoms containing, in the ideal case, exactly one excitation in the related collective atomic mode. After a variable delay time Δt (bounded by the lifetime of the ground-state atomic coherences) we convert the atomic excitation into a single photon by illuminating the atomic ensemble with a pulse of light near-resonant with the $|b\rangle \rightarrow |c\rangle$ transition and counter-propagating with respect to the *write* beam (Figure 3.1). For an optically thick atomic sample, the idler photon will be emitted with high probability into the mode determined by the phase-matching condition $\vec{k}_i = \vec{k}_w + \vec{k}_r - \vec{k}_s$, with the atomic qubit state mapped onto a photonic one as discussed in Section 3.2.2. Under the condition of collective enhancement the atomic excitations generated by $\hat{S}_{\pm 1}^{(i)\dagger}$ map to orthogonal idler photon states up to a phase. Assuming equal mapping efficiency, the number of correlated signal-idler counts registered by the detectors can be predicted on the basis of Eq. (3.1). We find, by carefully analyzing

the measurement procedure,

$$C(\theta_s, \theta_i) \propto [(\cos \eta + \sin \eta) \cos(\theta_s - \theta_i) + (\cos \eta - \sin \eta) \cos(\theta_s + \theta_i)]^2, \quad (3.5)$$

where θ_s and θ_i are the orientations of polarizers P_1 and P_2 . Following Clauser-Horne-Shimony-Holt (CHSH) [91, 16], we calculate the correlation function $E(\theta_s, \theta_i)$, given by

$$\frac{C(\theta_s, \theta_i) + C(\theta_s^\perp, \theta_i^\perp) - C(\theta_s^\perp, \theta_i) - C(\theta_s, \theta_i^\perp)}{C(\theta_s, \theta_i) + C(\theta_s^\perp, \theta_i^\perp) + C(\theta_s^\perp, \theta_i) + C(\theta_s, \theta_i^\perp)}, \quad (3.6)$$

where $\theta^\perp = \theta + \pi/2$. The CHSH version of the Bell inequality is then $|S| \leq 2$ where

$$S = E(\theta_s, \theta_i) + E(\theta_s', \theta_i) + E(\theta_s, \theta_i') - E(\theta_s', \theta_i'). \quad (3.7)$$

The maximum violation of the Bell inequality is achieved for a maximally entangled state with the canonical set of angles $\theta_s = -22.5^\circ$, $\theta_i = 0^\circ$, $\theta_s' = 22.5^\circ$ and $\theta_i' = -45^\circ$: $S = 2\sqrt{2} = 2.83$. Based on the value $\eta = 0.81 \times \pi/4$ we find, ideally, $S = 2.77$ which significantly violates the Bell inequality.

In the following sections, we will provide a more detailed analysis of the interaction of the *write* beam with the atomic ensemble. We will show, that due to collective enhancement, the spin waves imprinted on the ensemble by the signal photon emission are independent of those left behind by photons scattered into undetected modes. We will then describe the dynamics of the read process, in which the *read* beam is resonant on the $|b\rangle \leftrightarrow |c\rangle$ transition. We take advantage of the Heisenberg Langevin equations that describe joint photon and spin wave propagation in the presence of a control field that are developed in Appendix C.

3.2.1 The Write Process: Raman Scattering from a Collection of Atoms

In this section, we describe the dynamics of the classical *write* field interacting with an ensemble of N atoms. We describe the *write* and the detected signal fields as distinct narrow bandwidth fields with carrier wave vectors \vec{k}_w and \vec{k}_s respectively.

We follow the conventions introduced in Chapter 2 Section 2.1.4. The *write* beam is detuned from resonance on the $|a\rangle \leftrightarrow |c\rangle$ transition by a frequency Δ_w , so that $ck_w = \omega_c - \omega_a + \Delta_w$, where $\hbar\omega_f$ is the energy of level $|f\rangle$ as described in Chapter 2. The carrier frequency of the signal, $ck_s = \omega_c - \omega_b + \Delta_w$, differs from the *write* beam frequency by the hyperfine splitting between levels $|a\rangle$ and $|b\rangle$. We assume that the propagation direction of the write field \hat{k}_w is nearly parallel to the laboratory fixed angular momentum quantization z -axis, and that the detected signal field propagates along the z -axis; $\hat{k}_s = \hat{z}$. In this limit, we make the paraxial approximation so that the helicities of the fields correspond to the spherical basis vectors (Eq. (2.31)). That is,

$$\vec{e}_\alpha(\hat{k}_w) \approx \vec{e}_\alpha(\hat{k}_s) = \vec{\xi}_\alpha. \quad (3.8)$$

We note that the write and signal fields are not necessarily collinear so that we may allow for the off-axis geometry introduced by Braje *et al* [58]. The positive frequency electric field operators for the write and signal fields are given by

$$\hat{\mathbf{E}}_w^{(+)}(\vec{r}, t) = (2\pi)^{3/2} \mathcal{E}(ck_w) e^{i\vec{k}_w \cdot \vec{r}} e^{-ick_w t} \phi^{(w)}(\vec{r}) \sum_{\alpha=\pm 1} \vec{e}_\alpha(\hat{k}_s) \hat{\varphi}_\alpha^{(w)}(r_\parallel^{(w)}, t) \quad (3.9)$$

and

$$\hat{\mathbf{E}}_s^{(+)}(\vec{r}, t) = (2\pi)^{3/2} \mathcal{E}(ck_s) e^{i\vec{k}_s \cdot \vec{r}} e^{-ick_s t} \phi^{(s)}(\vec{r}) \sum_{\alpha=\pm 1} \vec{e}_\alpha(\hat{k}_s) \hat{\varphi}_\alpha^{(s)}(z, t) \quad (3.10)$$

respectively, where $\phi^{(\iota)}(\vec{r})$ ($\iota \in \{w, s\}$) is the transverse mode function (as discussed in Chapter 2), and $r_\parallel^{(\iota)} \equiv \hat{k}_\iota \cdot \vec{r}$. We assume the collected signal field has a transverse spatial profile much narrower than that of the write beam so that the envelope of the write field is essentially constant over the width of the collected signal mode. The *write* field will be treated classically and is assumed to have a fixed helicity α_w . The expression for the *write* field, therefore, simplifies to

$$\vec{E}_w^{(+)}(\vec{r}, t) = \vec{\xi}_{\alpha_w} e^{i\vec{k}_w \cdot \vec{r}} e^{-ick_w t} E_w(\vec{r}, t) \quad (3.11)$$

where

$$E_w(\vec{r}, t) \equiv (2\pi)^{3/2} \sqrt{n_w} \mathcal{E}(ck_w) \phi^{(w)}(\vec{r}) \varphi(r_{\parallel}^{(w)}, t) \quad (3.12)$$

is the slowly varying electric field amplitude,

$$n_w \equiv \int_{-\infty}^{\infty} c \langle \hat{\varphi}_{\alpha_w}^{\dagger}(z_0, t) \hat{\varphi}_{\alpha_w}(z_0, t) \rangle dt \quad (3.13)$$

is the average number of photons in the write pulse, z_0 is the position at which the pulse enters the atomic sample, and $\varphi(z_0, t)$ is the temporal envelope of the write pulse that satisfies the normalization condition $c \int_{-\infty}^{\infty} dt' |\varphi(z_0, t')|^2 = 1$. We will typically work in the undepleted pump approximation, in which the write beam experiences negligible losses during propagation, i.e. $\varphi(z, t) = \varphi(0, t - z/c)$.

The atoms are assumed to have fixed positions for the duration of the experiment. We treat the atomic positions $\{\vec{r}_{\mu} : \mu = 1 \dots N\}$ as a set of independent identically distributed random variables which are distributed according to the probability density $n(\vec{r})/N$, where $n(\vec{r})$ is the number density of the atomic sample. We assume the atomic density within the sample does not vary over the widths of either the *write* or signal transverse spatial modes. The atomic density is, therefore, taken to be a function only of the propagation distance; $n(\vec{r}) = n(r_{\parallel}^{(s)}) \approx n(r_{\parallel}^{(w)}) \approx n(z)$.

The dynamics of the system are described by the electric dipole interaction discussed in Chapter 2. Because the *write* and signal fields are off resonant on the $|a\rangle \leftrightarrow |c\rangle$ and $|b\rangle \leftrightarrow |c\rangle$ transitions respectively, we may adiabatically eliminate the excited level $|c\rangle$ when Δ_w is much larger than the bandwidth of the write laser pulse Δk_w . We also assume Δ_w is small enough so that the *write* beam is much closer to resonance on the $|a\rangle \leftrightarrow |c\rangle$ transition than on any other electric dipole transition in ^{85}Rb . We show in Appendix B that adiabatic elimination of the excited level yields the effective interaction picture Hamiltonian

$$\hat{V}(t) = \hat{V}_{\text{Stark}}(t) + \hat{V}_{\text{Rayleigh}}(t) + \hat{V}_{\text{Raman}}(t) \quad (3.14)$$

where $\hat{V}_{\text{Stark}}(t)$ accounts for the ac Stark shift, $\hat{V}_{\text{Rayleigh}}(t)$ accounts for Rayleigh scattering of the photon in which an excited atom returns to the initial hyperfine level $|a\rangle$, and $\hat{V}_{\text{Raman}}(t)$ accounts for the dynamics of Raman scattering. It is the Raman scattering that results in the creation of the hyperfine spin wave in which the atomic qubit is encoded.

The Stark shift interaction is given by

$$\hat{V}_{\text{Stark}}(t) = \frac{2}{\hbar\Delta_w} \sum_{\mu=1}^N \left(\hat{\mathbf{d}}_{(a,c)}^{(+)\mu}(t) \cdot \vec{E}_w^{(-)}(\vec{r}_\mu, t) \right) \left(\hat{\mathbf{d}}_{(a,c)}^{(-)\mu}(t) \cdot \vec{E}_w^{(+)}(\vec{r}_\mu, t) \right). \quad (3.15)$$

Substituting the definitions of the dipole operators (Eq. (2.40)) and electric fields (Eqs. (3.10) and (3.11)), the Stark shift interaction simplifies to

$$\hat{V}_{\text{Stark}}^\mu(t) = \sum_{\mu=1}^N \hbar \frac{2|\Omega_w(\vec{r}_\mu, t)|^2}{\Delta_w} \sum_{m=-F_a}^{F_a} |C_{m\alpha_w}^{F_a\ 1\ F_c\ m+\alpha_w}|^2 \tilde{\sigma}_{a,m; a,m}(t), \quad (3.16)$$

where

$$\Omega_w(\vec{r}, t) \equiv \left(c \left\| \hat{\mathbf{d}} \right\| a \right) E_w(\vec{r}, t) \quad (3.17)$$

is the write field Rabi frequency. The Stark shift results in each Zeeman state within ground level $|a\rangle$ being shifted by an energy proportional the square of a corresponding Clebsch-Gordan coefficient. In the nondegenerate three level atomic system treated by Duan, Cirac, and Zoller [92], the ac Stark shift is handled through a trivial unitary transformation. In our degenerate system, however, each Zeeman state is shifted by a different amount. This tends to complicate the dynamics, and its effects on the entanglement generation scheme presented here will be the subject of future investigations. In this work, we will assume that either the detuning is sufficiently large, or the Rabi frequency is sufficiently small so that the ac Stark shift may be neglected. Expressed formally, we assume $\theta_m(\vec{r}, t) \ll 1$ for times after the write pulse interaction, for all $m \in \{m : |m| < F_a\}$ and positions \vec{r} , where the angle $\theta_m(\vec{r}, t)$ is given by

$$\theta_m(\vec{r}, t) \equiv \frac{2}{\Delta_w} |C_{m\alpha_w}^{F_a\ 1\ F_c\ m+\alpha_w}|^2 \int_{-\infty}^t dt' |\Omega_w(\vec{r}, t')|^2. \quad (3.18)$$

The Rayleigh scattering interaction results in the absorption of photons from the *write* beam accompanied by emission of photons of the same frequency. The atom that scatters the photon either returns to its initial state, or possibly a different Zeeman state within the same hyperfine level. The Rayleigh interaction is given by

$$\hat{V}_{\text{Rayleigh}}(t) = \frac{2}{\hbar\Delta_w} \left(\hat{\mathbf{d}}_{(a,c)}^{(+)\mu}(t) \cdot \hat{\mathbf{E}}_R^{(-)}(\vec{r}_\mu, t) \right) \left(\hat{\mathbf{d}}_{(a,c)}^{(-)\mu} \cdot \vec{E}_w^{(+)}(\vec{r}_\mu, t) \right) + h.c. , \quad (3.19)$$

where

$$\hat{\mathbf{E}}_R^{(+)}(\vec{r}, t) = \hat{\mathbf{E}}^{(+)}(\vec{r}, t) - \sum_{\iota \in \{s, w\}} \hat{\mathbf{E}}_\iota^{(+)}(\vec{r}, t) \quad (3.20)$$

is the contribution to the electric field from the reservoir of undetected modes.

It is useful to expand the reservoir field into its constituent plane wave modes as

$$\hat{\mathbf{E}}_R^{(+)}(\vec{r}, t) = i \int d^3k \sum_\lambda \vec{\varepsilon}_\lambda(\hat{k}) \mathcal{E}(ck) e^{i\vec{k} \cdot \vec{r}} e^{-ickt} \delta \hat{a}_\lambda(\vec{k}; \vec{r}, t), \quad (3.21)$$

where $\delta \hat{a}_\lambda(\vec{k}; \vec{r}, t)$ is the contribution of the plane wave annihilation operator $\hat{a}_\lambda(\vec{k})$ to the reservoir field. This operator is given by

$$\begin{aligned} \delta \hat{a}_\lambda(\vec{k}; \vec{r}, t) &= \hat{a}_\lambda(\vec{k}) - \sum_{\iota \in \{s, w\}} \Theta(\Delta k_\iota/2 - |k - k_\iota|) \\ &\quad \times f^{(\iota)}(\vec{k}_\perp^{(\iota)}) e^{ic \frac{|\vec{k}_\perp^{(\iota)}|^2}{2k_\iota} (t - r_\parallel^{(\iota)}/c)} \hat{a}_\lambda^{(\iota)}(k_\parallel^{(\iota)}, t - r_\parallel^{(\iota)}/c), \end{aligned} \quad (3.22)$$

where $\Theta(k)$ is the Heaviside function, $c\Delta k_{w[s]}$, is the maximum bandwidth of the *write* [signal] field as discussed in Chapter 2,

$$f^{(\iota)}(\vec{k}_\perp^{(\iota)}) = -\frac{i}{2\pi} e^{i \frac{|\vec{k}_\perp^{(\iota)}|^2}{2k_\iota} r_\parallel^{(\iota)}} \int d^2r_\perp^{(\iota)} e^{-i\vec{k}_\perp^{(\iota)} \cdot \vec{r}} \phi^{(\iota)}(\vec{r}) \quad (3.23)$$

is the Fourier transform of the transverse mode spatial mode of field ι , and is the inverse of Eq. (2.64), and the operator

$$\hat{a}_\lambda^{(\iota)}(k_\parallel^{(\iota)}, t) \equiv \int d^2k_\perp e^{-ic \frac{|\vec{k}_\perp^{(\iota)}|^2}{2k_\iota} t} f_i^*(\vec{k}_\perp^{(\iota)}) \hat{a}_\lambda(\vec{k}), \quad (3.24)$$

where $\vec{k} = k_\parallel^{(\iota)} \hat{k}_\parallel + \vec{k}_\perp^{(\iota)}$. We note that the time argument of the operator $\delta \hat{a}_\lambda^\dagger(\vec{k}; \vec{r}, t)$ appears as a parameter in the definition (Eq. (3.22)) because we are working in

the interaction picture, and we have included the effects of diffraction of the signal and *write* fields. If one were to neglect diffraction, the operator $\delta\hat{a}_\lambda(\vec{k})$ would be independent of both position \vec{r} and time t .

Expanding the electric field and dipole operators in terms of field mode operators and atomic coherences yields the Rayleigh scattering Hamiltonian

$$\begin{aligned}\hat{V}_{\text{Rayleigh}}(t) = & -2i\hbar \sum_{\alpha=-1}^1 \sum_{m=-F_a}^{F_a} Y_{m,\alpha} \int d^3k \sum_{\lambda} \left(\vec{\xi}_{\alpha} \cdot \vec{\varepsilon}_{\lambda}(\hat{k}) \right) \\ & \times \overline{\mathcal{Z}}'(ck) \sum_{\mu=1}^N \phi^{(w)}(\vec{r}_{\mu}) \varphi(\hat{k}_w \cdot \vec{r}_{\mu}, t) e^{-i(\vec{k}-\vec{k}_w) \cdot \vec{r}_{\mu}} \\ & \times \tilde{\sigma}_{a,m+\alpha_w-\alpha; a,m}^{\mu} e^{ic(k-k_w)t} \delta\hat{a}_{\lambda}^{\dagger}(\vec{k}, \vec{r}, t) + h.c. \quad , \quad (3.25)\end{aligned}$$

where $Y_{m,\alpha} \equiv C_{m+\alpha_w-\alpha}^{F_a \ 1 \ F_c} C_{m \ \alpha_w \ m+\alpha_w}^{F_a \ 1 \ F_c}$,

$$\overline{\mathcal{Z}}'(ck) \equiv \frac{\left| \left(c \left\| \hat{\mathbf{d}} \right\| a \right) \right|^2 \mathcal{E}(ck)}{\hbar^2 \Delta_w} \sqrt{\frac{\hbar c k_w n_w}{2\epsilon_0}} \quad (3.26)$$

is an interaction parameter with units of frequency times volume, $\tilde{\sigma}_{f,m; f',m'}^{\mu} \equiv \exp(i(\omega_{f'} - \omega_f)t) \hat{\sigma}_{f,m; f',m'}^{\mu}(t)$ are the slowly varying atomic coherences for atom μ between states $|f, m\rangle_{\mu}$ and $|f', m'\rangle_{\mu}$. We make the further simplifying assumption that the write electric field spatio-temporal envelope $\varphi(\hat{k}_w \cdot \vec{r}_{\mu}, t)$ does not vary over the length of the ensemble so that it can be taken as independent of the propagation distance, i.e. $\varphi(z, t) = \varphi(0, t)$. The Rayleigh scattering Hamiltonian then simplifies to

$$\begin{aligned}\hat{V}_{\text{Rayleigh}}(t) = & -2i\hbar \varphi(0, t) \sum_{\alpha=-1}^1 \sum_{m=-F_a}^{F_a} Y_{m,\alpha} \int d^3k \sum_{\lambda} \left(\vec{\xi}_{\alpha} \cdot \vec{\varepsilon}_{\lambda}(\hat{k}) \right) \\ & \times \overline{\mathcal{Z}}'(ck) \sum_{\mu=1}^N \phi^{(w)}(\vec{r}_{\mu}) e^{-i(\vec{k}-\vec{k}_w) \cdot \vec{r}_{\mu}} \\ & \times \tilde{\sigma}_{a,m+\alpha_w-\alpha; a,m}^{\mu} e^{ic(k-k_w)t} \delta\hat{a}_{\lambda}^{\dagger}(\vec{k}, t) + h.c. \quad , \quad (3.27)\end{aligned}$$

The Raman scattering interaction involves the absorption of a photon from the *write* laser coupled to the emission of a photon with a frequency near ck_s . This

interaction is given as

$$\hat{V}_{\text{Raman}}(t) = \frac{2}{\hbar \Delta_w} \sum_{\mu=1}^N \left(\hat{\mathbf{d}}_{(b,c)}^{(+)\mu}(t) \cdot \hat{\mathbf{E}}^{(-)}(\vec{r}_\mu, t) \right) \left(\hat{\mathbf{d}}_{(a,c)}^{(-)\mu}(t) \cdot \vec{E}_w^{(+)}(\vec{r}_\mu, t) \right). \quad (3.28)$$

It is convenient to expand this interaction in terms of the plane wave creation and annihilation operators and coherence operators for the individual atoms.

Recalling that we have assumed the write beam does not vary over the length of the ensemble, $\varphi(z, t) \approx \varphi(0, t)$, we find that the Raman scattering interaction can be expressed in terms of products of plane wave operators $\hat{a}_\lambda(\vec{k})$ and hyperfine spin waves $\hat{S}_\alpha(\vec{k} - \vec{k}_w)$, where

$$\hat{S}_\alpha(\vec{q}) \equiv \sum_{m=-F_a}^{F_a} \frac{\sqrt{p_m} X_{m,\alpha}}{\sqrt{\sum_m p_m |X_{m,\alpha}|^2}} \hat{S}_{a,m; b, m+\alpha_w-\alpha}(\vec{q}) \quad (3.29)$$

are hyperfine spin waves with wave vector \vec{q} that are created by emission of a photon with polarization $\vec{\xi}_\alpha$ during the *write* process,

$$\hat{S}_{a,m; b, m'}(\vec{q}) \equiv \sqrt{\frac{\bar{A}^{(w)}}{p_m N}} \sum_{\mu=1}^N \phi^{(w)*}(\vec{r}_\mu) e^{i\vec{q} \cdot \vec{r}_\mu} \tilde{\sigma}_{a,m; b, m'}^\mu, \quad (3.30)$$

where

$$\frac{1}{\bar{A}^{(w)}} \equiv \frac{1}{N} \int dr_\parallel^{(w)} n(r_\parallel^{(w)}) \quad (3.31)$$

is an effective area of the write beam, and p_m is the probability that an atom in the ensemble is initially in the state $|a, m\rangle$. When the total number of scattered photons is much less than the number of atoms, we may neglect any changes in the atomic populations during the *write* process to order $1/N$, and Zeeman coherences can be neglected to order $1/\sqrt{N}$. With this approximation, we find that the spin wave operators obey the following commutation relations:

$$[\hat{S}_{a,m; b, m_b}(\vec{q}), \hat{S}_{a, m'; b, m'_b}(\vec{q}')] = 0 \quad (3.32)$$

$$[\hat{S}_{a,m; b, m_b}(\vec{q}), \hat{S}_{a, m'; b, m'_b}^\dagger(\vec{q}')] = \delta_{m, m'} \delta_{m_b, m'_b} \varrho(\vec{q}' - \vec{q}) + O(1/\sqrt{N}), \quad (3.33)$$

and

$$\left[\hat{S}_\alpha(\vec{q}), \hat{S}_\beta(\vec{q}') \right] = 0 \quad (3.34)$$

$$\left[\hat{S}_\alpha(\vec{q}), \hat{S}_\beta^\dagger(\vec{q}') \right] = \delta_{\alpha\beta} \varrho(\vec{q}' - \vec{q}) + O(1/\sqrt{N}), \quad (3.35)$$

where

$$\varrho(\vec{q}) \equiv \frac{\bar{A}^{(w)}}{N} \sum_{\mu=1}^N \left| \phi^{(w)*}(\vec{r}_\mu) \right|^2 e^{-i\vec{q} \cdot \vec{r}_\mu} \quad (3.36)$$

is the phase matching function. Because the positions of the atoms are random and identically distributed, we take advantage of the central limit theorem and find that

$$\varrho(\vec{q}) = \bar{A}^{(w)} \int d^3r \left| \phi^{(w)}(\vec{r}) \right|^2 \frac{n(\vec{r})}{N} e^{-i\vec{q} \cdot \vec{r}} + O(1/\sqrt{N}) \quad (3.37)$$

is the Fourier transform of an effective atomic density profile interacting with the write beam. The phase matching function takes on its maximum value of one when $\vec{q} = 0$. The Raman scattering potential in terms of these spin waves is given by

$$\begin{aligned} \hat{V}_{\text{Raman}}(t) = & -2i\hbar \sqrt{\frac{N}{\bar{A}^{(w)}}} \sum_{\alpha=-1}^1 \sqrt{\sum_m p_m |X_{m,\alpha}|^2} \\ & \times \varphi(0, t) \int d^3k \, \overline{\mathcal{Z}}(ck) \sum_{\lambda} \left(\vec{\xi}_\alpha \cdot \vec{\varepsilon}_\lambda(\hat{k}) \right) e^{ic(k-k_s)t} \\ & \times \hat{S}_\alpha^\dagger(\vec{k} - \vec{k}_w, t) \hat{a}_\lambda^\dagger(\vec{k}) + h.c. \end{aligned} \quad (3.38)$$

where $X_{m,\alpha} \equiv C_{m\alpha_w}^{F_a \ 1 \ F_c} C_{m+\alpha_w-\alpha}^{F_b \ 1 \ F_c}$, and

$$\overline{\mathcal{Z}}(ck) \equiv \frac{\left(c \left\| \hat{\mathbf{d}} \right\| a \right) \left(c \left\| \hat{\mathbf{d}} \right\| b \right)^* \mathcal{E}(ck)}{\hbar \Delta_w} \sqrt{\frac{ck_w n_w}{2\hbar \epsilon_0}} \quad (3.39)$$

is an interaction parameter with units of frequency times volume. Physically, one interprets the Raman interaction to mean that when a photon of wave vector \vec{k} is scattered, a hyperfine spin wave with wave vector $\vec{k} - \vec{k}_w$ is imprinted on the ensemble.

Let us examine the properties of the phase matching function as it applies to our experimental set up. The *write* beam has a Gaussian profile whose full transverse

width at half its maximum (FWHM) is about $W = 400 \mu\text{m}$. For simplicity, we assume the atomic density has a spherically symmetric Gaussian profile with a FWHM length of $L = 3 \text{ mm} \gg W$. We also assume that the *write* beam and collected signal mode pass through the center of the ensemble. In this case, we find the phase matching function is given by

$$\varrho(\vec{q}) = \exp\left(-\frac{1}{16 \ln 2} (L^2 q_z^2 + W^2 (q_x^2 + q_y^2))\right). \quad (3.40)$$

With this example, let us consider the commutation relations between the spin wave operators that correspond to scattered photons with collinear wave vectors, $\hat{S}_\alpha(k\hat{k} - \vec{k}_w)$ and $\hat{S}_\alpha^\dagger(k'\hat{k} - \vec{k}_w)$. These two operators obey the commutation relation

$$\left[\hat{S}_\alpha(k\hat{k} - \vec{k}_w), \hat{S}_\alpha^\dagger(k'\hat{k} - \vec{k}_w)\right] = \varrho((k' - k)\hat{k}) + \hat{O}(1/\sqrt{N}), \quad (3.41)$$

but $\varrho((k' - k)\hat{k}) \approx 1$ if $|k - k'| \ll 1/L$. This means that if two photons are emitted with collinear wave vectors, the spin waves they leave behind are virtually identical if their frequency difference is much less than $c/(2\pi L) \approx 16.9 \text{ GHz}$. This frequency is about five times greater than the hyperfine splitting between levels $|a\rangle$ and $|b\rangle$, while the bandwidth of the scattered photons is on the order of the spontaneous emission rate, which is nearly three orders of magnitude less than the hyperfine splitting. We may therefore assume that collinearly scattered photons correspond to identical spin waves, and we make the approximation $\hat{S}_\alpha(k\hat{k} - \vec{k}_w) \approx \hat{S}_\alpha(k_s\hat{k} - \vec{k}_w)$. On the other hand, if two photons are emitted in different directions \hat{k} , and \hat{k}' , one can show that the associated spin waves are independent. This is done by evaluating the commutator between the annihilation operator $\hat{S}_\alpha(k_s\hat{k} - \vec{k}_w)$ and the creation operator $\hat{S}_\alpha^\dagger(k_s\hat{k}' - \vec{k}_w)$ and showing that it is zero. We have

$$\left[\hat{S}_\alpha(k_s\hat{k} - \vec{k}_w), \hat{S}_\alpha^\dagger(k_s\hat{k}' - \vec{k}_w)\right] = \varrho(k_s(\hat{k}' - \hat{k})) + \hat{O}(1/\sqrt{N}). \quad (3.42)$$

The phase matching function evaluated at the difference of these two wave vectors, $\varrho(k_s(\hat{k}' - \hat{k})) \approx 0$ when $|\hat{k}' - \hat{k}| \gg \max(1/L, 1/W) = 1/(k_s W) \approx (\pi/180) \times 0.018^\circ$.

Two spin waves are therefore, independent if the angle between their corresponding photon emission directions is greater than a fraction of a degree. For our experiment, we will therefore make the approximation on the phase matching function

$$\varrho(\vec{k} - \vec{k}') \approx \delta^2 \hat{k} \delta(\hat{k} - \hat{k}') \quad (3.43)$$

where

$$\delta^2 \hat{k} \equiv \int d^2 \hat{k}' \rho(k_s(\hat{k}' - \hat{k})) \quad (3.44)$$

is a differential solid angle over which two spin waves cannot be differentiated, and $\delta(\hat{k} - \hat{k}')$ is the delta function with respect to the solid angle measure. Up to a normalization factor, this gives us quasi-bosonic commutation relations for the imprinted spin waves

$$[\hat{S}_{a,m;b,m_b}(k_s \hat{k} - \vec{k}_w), \hat{S}_{a,m';b,m'_b}^\dagger(k_s \hat{k}' - \vec{k}_w)] = \delta^2 \hat{k} \delta_{m,m'} \delta_{m_b,m'_b} \delta(\hat{k} - \hat{k}'). \quad (3.45)$$

Having made the approximation $\hat{S}_\alpha(k\hat{k} - \vec{k}_w) \approx \hat{S}_\alpha(k_s \hat{k} - \vec{k}_w)$, we may further simplify the Raman scattering interaction

$$\begin{aligned} \hat{V}_{\text{Raman}}(t) &= -i \frac{2\hbar k_s \vec{\varepsilon}(ck_s)}{c} \sqrt{\frac{2\pi N}{\bar{A}^{(w)}}} \sum_{\alpha=-1}^1 \sqrt{\sum_m p_m |X_{m,\alpha}|^2} \\ &\times \int d^2 \hat{k} \hat{S}_\alpha^\dagger(k_s \hat{k} - \vec{k}_w, t) \\ &\times \sum_\lambda (\vec{\xi}_\alpha \cdot \vec{\varepsilon}_\lambda(\hat{k})) \sqrt{c} \varphi(0, t) \hat{\psi}_\lambda^\dagger(\hat{k}, t) + h.c. \quad , \end{aligned} \quad (3.46)$$

where

$$\hat{\psi}_\lambda(\hat{k}, t) \equiv \sqrt{\frac{c}{2\pi}} \int_{k_s - \Delta k_s/2}^{k_s + \Delta k_s/2} dk e^{-ic(k-k_s)t} k \hat{a}_\lambda(k\hat{k}), \quad (3.47)$$

is a field annihilation operator for a photon created at the position $\vec{r} = 0$ at time t propagating the direction \hat{k} , and $c\Delta k_s$ is the maximum bandwidth of the signal field. This frequency is chosen to be much larger than the bandwidth of the emitted signal photons, yet much smaller than the detuning Δ_w . The inverse relationship is given by

$$\hat{a}_\lambda(k\hat{k}) \approx \frac{1}{k} \sqrt{\frac{c}{2\pi}} \int_{-\infty}^{\infty} dt' \hat{\psi}_\lambda(\hat{k}, t') e^{ic(k-k_s)t'}. \quad (3.48)$$

These field operators obey the commutation relations

$$\begin{aligned} \left[\hat{\psi}_\lambda(\hat{k}, t), \hat{\psi}_{\lambda'}^\dagger(\hat{k}', t') \right] &= \delta_{\lambda, \lambda'} \delta(\hat{k} - \hat{k}') \frac{c\Delta k_s}{2\pi} \text{sinc}\left(\frac{c\Delta k_s}{2}(t - t')\right) \\ &\approx \delta_{\lambda, \lambda'} \delta(\hat{k} - \hat{k}') \delta(t - t'). \end{aligned} \quad (3.49)$$

We note that the Raman scattering interaction (Eq. (3.46)) results in the emission of photons in all directions. This is in contrast to the results obtained by Duan *et al* [92] for the limit of a “hot” atomic ensemble. In this limit, thermal fluctuations in the atomic positions occur on time scales much faster than the *write* process, resulting in photons being scattered preferentially in the forward direction. In our cold system, however, the atomic positions may be taken as constant for the duration of the experiment, and the effects of the thermal atomic velocity distribution are negligible.

3.2.1.1 The Nondegenerate Parametric Amplifier Model of Collective spontaneous Raman Scattering

In this section, we demonstrate that, when one traces over uncollected modes, the scattering dynamics of the *write* process reduces to those of a single mode nondegenerate parametric amplifier for the signal field and an idler spin wave. This model is used in Chapters 5 and 6 to calculate photo-detection probabilities and correlations for the field-ensemble system, which is essentially a heralded source of nonclassical light [47, 18, 23]. Given the interaction picture Hamiltonian in Eq. (3.14) and its Raman scattering component (Eq. (3.46)), we separate the Hamiltonian into that part that interacts with the signal field $\hat{H}_s(t)$, and that which interacts with the reservoir modes $\hat{V}^{(\text{Res})}(t)$ as follows:

$$\hat{V}(t) = \hat{H}_s(t) + \hat{V}^{(\text{Res})}(t). \quad (3.50)$$

The signal Hamiltonian is given by

$$\begin{aligned} \hat{H}_s(t) \equiv & i\hbar\chi \left(\cos\eta \sqrt{c}\varphi^{(w)}(0,t) \hat{\psi}_{+1}^{(s)\dagger}(t) \hat{S}_{+1}^{(i)\dagger} \right. \\ & \left. + \sin\eta \sqrt{c}\varphi^{(w)}(0,t) \hat{\psi}_{-1}^{(s)\dagger}(t) \hat{S}_{-1}^{(i)\dagger} - h.c. \right), \end{aligned} \quad (3.51)$$

where $0 \leq \eta \leq \pi/2$ and

$$\cos^2\eta = \frac{\sum_{m=-F_a}^{F_a} p_m X_{m,+1}^2}{\sum_{\alpha=\pm 1} \sum_{m=-F_a}^{F_a} p_m X_{m,\alpha}^2}. \quad (3.52)$$

The interaction parameter χ is given by

$$\chi \equiv \frac{2 \left(c \parallel \hat{\mathbf{d}} \parallel b \right)^* \left(c \parallel \hat{\mathbf{d}} \parallel a \right)}{\Delta_w} \frac{\sqrt{k_s k_w n_w N}}{\hbar \epsilon_0 \bar{A}^{(s)}} \sqrt{\sum_{\alpha=\pm 1} \sum_{m=-F_a}^{F_a} p_m X_{m,\alpha}^2}, \quad (3.53)$$

where

$$\bar{A}^{(s)} = \frac{1}{\sqrt{\frac{1}{N} \int dr_{\parallel}^{(s)} |\phi^{(w)}(z)|^2 n(z)}} \quad (3.54)$$

is an effective area of the signal interaction with the ensemble. The spin wave operators are given by

$$\hat{S}_{\alpha}^{(i)} \equiv \sum_{m=-F_a}^{F_a} \frac{\sqrt{p_m} X_{m,\alpha}}{\sqrt{\sum_m p_m |X_{m,\alpha}|^2}} \hat{S}_{a,m; b, m+\alpha_w-\alpha}^{(i)} \quad (3.55)$$

and,

$$\hat{S}_{a,m; b, m'}^{(i)} \equiv i \frac{\bar{A}^{(s)}}{\sqrt{p_m N}} \sum_{\mu=1}^N \tilde{\sigma}_{a,m; b, m+\alpha_w-\alpha}^{\mu}(t) e^{-i(\vec{k}_w - \vec{k}_s) \cdot \vec{r}_{\mu}} \phi^{(s)}(\vec{r}_{\mu}) \phi^{(w)*}(\vec{r}_{\mu}). \quad (3.56)$$

We call $\hat{S}_{\alpha}^{(i)}$ the idler spin wave. The field operator $\hat{\psi}_{\alpha}^{(s)}(t)$ is given by

$$\hat{\psi}_{\alpha}^{(s)}(t) = \sqrt{c} \hat{\varphi}_{\alpha}^{(s)}(0, t), \quad (3.57)$$

where $\hat{\varphi}_{\alpha}(0, t)$ is the linear photon density annihilation operator within the ensemble. One interprets field operator $\hat{\psi}_{\alpha}^{(s)}(t)$ as the annihilation operator for a signal photon created within the ensemble at time t . These field operators obey the standard bosonic field commutation relations

$$\left[\hat{\psi}_{\alpha}^{(s)}(t), \hat{\psi}_{\beta}^{(s)\dagger}(t') \right] = \delta_{\alpha\beta} \delta(t - t'). \quad (3.58)$$

The Interaction Hamiltonian responsible for scattering into the reservoir is given by

$$\begin{aligned}\hat{V}^{(\text{Res})}(t) &= \hat{V}(t) - \hat{H}_s(t) \\ &= \hat{V}_{\text{Rayleigh}}(t) + \left(\hat{V}_{\text{Raman}}(t) - \hat{H}_s(t) \right).\end{aligned}\quad (3.59)$$

We now show that the signal Hamiltonian commutes with $\hat{V}^{(\text{Res})}(t)$ to order $O(1/\sqrt{N})$. Once we show this, we will be able to easily determine the reduced signal-idler density matrix that results from the *write* process. One may express the idler spin wave operators in terms of the constituent directional spin wave operators as

$$\hat{S}_{a,m;b,m'} \approx -\frac{k_s}{\sqrt{\delta^2 \hat{k}_s}} \int d^2 \hat{k} f^{(s)}(k_s \hat{k} - \vec{k}_s) \hat{S}_{a,m;b,m'}(k_s \hat{k} - \vec{k}_w) \quad (3.60)$$

where we have made the following approximations: $d^2 k_{\perp}^{(s)} \approx k_s^2 d^2 \hat{k}$, $\vec{k}_{\perp}^{(s)} \approx k_s (\hat{k} - \hat{k}_s)$, and

$$\begin{aligned}\delta^2 \hat{k}_s &= \int d^2 \hat{k}' \varrho(k_s (\hat{k}' - \hat{k}_s)) \\ &\approx \frac{(2\pi)^2 \bar{A}^{(w)}}{k_s^2 \bar{A}^{(s)2}}.\end{aligned}\quad (3.61)$$

One may also express the directional spin wave operator in terms of the idler spin wave

$$\begin{aligned}\hat{S}_{\alpha}(k_s \hat{k} - \vec{k}_w) &= \left[\hat{S}_{\alpha}^{(i)}, \hat{S}_{\alpha}^{\dagger}(k_s \hat{k} - \vec{k}_w) \right]^* \hat{S}_{\alpha}^{(i)} + \delta \hat{S}_{\alpha}(k_s \hat{k} - \vec{k}_w) \\ &= -k_s \sqrt{\delta^2 \hat{k}_s} f^*(k_s \hat{k} - \vec{k}_s) \hat{S}_{\alpha}^{(i)} + \delta \hat{S}_{\alpha}(k_s \hat{k} - \vec{k}_w),\end{aligned}\quad (3.62)$$

where

$$\delta \hat{S}_{\alpha}(k_s \hat{k} - \vec{k}_w) \equiv \hat{S}_{\alpha}(k_s \hat{k} - \vec{k}_w) - \left[\hat{S}_{\alpha}^{(i)}, \hat{S}_{\alpha}^{\dagger}(k_s \hat{k} - \vec{k}_w) \right]^* \hat{S}_{\alpha}^{(i)} \quad (3.63)$$

The operator $\delta \hat{S}_{\alpha}(k_s \hat{k} - \vec{k}_w)$ is defined such that

$$\left[\hat{S}_{\alpha}^{(i)}, \delta \hat{S}_{\alpha}^{\dagger}(k_s \hat{k} - \vec{k}_w) \right] = 0 + O(1/\sqrt{N}). \quad (3.64)$$

Eq. (3.62) is the decomposition of the directional spin wave into a portion “parallel” to the idler spin wave and a portion orthogonal to the idler spin wave. We may

similarly decompose the directional photon field annihilation operators. The signal field operator is given in terms of the directional field operators by

$$\hat{\psi}_\alpha^{(s)}(t) = k_s \int d^2\hat{k} f^* \left(k_s \hat{k} - \vec{k}_s \right) \hat{\psi}_\alpha \left(\hat{k}, t \right) \quad (3.65)$$

The directional photon field operator can be decomposed as

$$\hat{\psi}_\alpha \left(\hat{k}, t \right) = k_s f \left(k_s \hat{k} - \vec{k}_s \right) \hat{\psi}_\alpha^{(s)}(t) + \delta\hat{\psi}_\alpha \left(\hat{k}, t \right), \quad (3.66)$$

where

$$\delta\hat{\psi}_\alpha \left(\hat{k}, t \right) \equiv \hat{\psi}_\alpha \left(\hat{k}, t \right) - k_s f \left(k_s \hat{k} - \vec{k}_s \right) \hat{\psi}_\alpha^{(s)}(t) \quad (3.67)$$

is defined such that

$$\left[\hat{\psi}_\alpha^{(s)}(t), \delta\hat{\psi}_\alpha^\dagger \left(\hat{k}, t \right) \right] = 0 \quad (3.68)$$

Using the decompositions of fields and spin waves presented above, we may write the portion of the interaction Hamiltonian responsible for scattering into the field reservoir as

$$\hat{V}^{(\text{Res})}(t) = \hat{V}_{\text{Rayleigh}}(t) + \hat{V}_{\text{Raman}}^{(\text{Res})}(t), \quad (3.69)$$

where

$$\begin{aligned} \hat{V}_{\text{Raman}}^{(\text{Res})}(t) &= -i \frac{2\hbar k_s \mathcal{Z}(ck_s)}{c} \sqrt{\frac{2\pi N}{\bar{A}(w)}} \sum_{\alpha=-1}^1 \sqrt{\sum_m p_m |X_{m,\alpha}|^2} \\ &\quad \times \int d^2\hat{k} \delta\hat{S}_\alpha^\dagger \left(k_s \hat{k} - \vec{k}_w, t \right) \\ &\quad \times \sum_\lambda \left(\vec{\xi}_\alpha \cdot \vec{\varepsilon}_\lambda \left(\hat{k} \right) \right) \sqrt{c} \varphi(0, t) \delta\hat{\psi}_\lambda^\dagger \left(\hat{k}, t \right) + h.c. \end{aligned} \quad (3.70)$$

In this form, it is relatively straight forward to show that

$$\left[\hat{H}_s(t), \hat{V}_{\text{Raman}}^{(\text{Res})}(t) \right] = 0 + \hat{O} \left(1/\sqrt{N} \right) \quad (3.71)$$

One may also show that

$$\left[\hat{H}_s(t), \hat{V}_{\text{Rayleigh}}(t) \right] = 0 + \hat{O} \left(1/\sqrt{N} \right) \quad (3.72)$$

For a sufficiently large number of atoms within the ensemble, the signal Hamiltonian commutes with the remainder of the scattering Hamiltonian $\hat{V}(t)$. Therefore, after the interaction of the *write* pulse with the ensemble, one may trace the density matrix for the system over the undetected field modes and arrive at the density matrix for the signal and associated atomic excitation

$$\hat{\rho} = \hat{U}^{(s)}(\chi) \hat{\rho}_0 \hat{U}^{(s)\dagger}(\chi) \quad (3.73)$$

where $\hat{U}^{(s)}(\chi) \equiv \mathcal{T} \exp \left((1/i\hbar) \int_{-\infty}^T dt \hat{H}_s(t) \right)$, is the unitary evolution operator, T is some time after the write beam has interacted with the ensemble, and \mathcal{T} is the time ordering operator. Taking advantage of the algebra of the field operators (Eq. (3.58)), one finds the evolution operator may be expressed as

$$\hat{U}^{(s)}(\chi) = \prod_{\alpha=\pm 1} \hat{U}_{\alpha}^{(s)}(\chi), \quad (3.74)$$

where

$$\hat{U}_1^{(s)}(\chi) = \exp \left(\chi \cos \eta \left(\hat{a}_{+1}^{(s)\dagger} \hat{S}_{+1}^{(i)\dagger} - \hat{a}_{+1}^{(s)} \hat{S}_{+1}^{(i)} \right) \right) \quad (3.75)$$

and

$$\hat{U}_{-1}^{(s)}(\chi) = \exp \left(\chi \sin \eta \left(\hat{a}_{-1}^{(s)\dagger} \hat{S}_{-1}^{(i)\dagger} - \hat{a}_{-1}^{(s)} \hat{S}_{-1}^{(i)} \right) \right). \quad (3.76)$$

The signal operator $\hat{a}_{\alpha}^{(s)}$ represents a single mode of the electromagnetic field, and is given by

$$\hat{a}_{\alpha}^{(s)} \equiv \int dt \sqrt{c} \varphi^{(w)}(0, t) \hat{\psi}_{\alpha}^{(s)}(t). \quad (3.77)$$

The unitary operator $\hat{U}_1(\chi)$ is nothing more than an evolution operator for a two-mode nondegenerate parametric amplifier discussed in Chapter 5 of Walls and Milburn [16]. This is a drastic simplification of the scattering dynamics. With this parametric amplification model, we can easily calculate statistics for correlations between the signal and idler spin wave. We take advantage of this model in Chapters 5 and 6.

3.2.1.2 Entanglement of Photonic and Atomic Qubits

In order probabilistically generate entanglement between photonic and atomic qubits, we assume the interaction parameter $\chi \ll 1$. Expanding the evolution operator $\hat{U}_s(\chi)$ to first order in χ , we find that reduced signal-atomic density matrix

$$\hat{\rho} = \left(1 + \chi \hat{\Psi}^\dagger(\eta)\right) \hat{\rho}_0 \left(1 + \chi \hat{\Psi}(\eta)\right) \quad (3.78)$$

where

$$\hat{\Psi}(\eta) = \cos \eta \hat{S}_{+1}^{(i)} \hat{a}_{+1}^{(s)} + \sin \eta \hat{S}_{-1}^{(i)} \hat{a}_{-1}^{(s)} \quad (3.79)$$

This matches the density matrix predicted by direct perturbation theory in Ref. [17].

3.2.2 The Read Process: Transferring the Spin Wave to the Idler Field

Now that we have demonstrated how the scattering dynamics produces entanglement between a photon emitted into the detected signal mode and the spin wave imprinted onto the atomic ensemble by this emission, we now wish to explore the dynamics of how the spin wave is transferred to the idler electric field so that it can be subsequently detected. We will first present Heisenberg Langevin equations for a detected idler mode. These Heisenberg equations of motion relate the detected idler field operators to its associated collective atomic excitation. We will then choose an optimal transverse spatial profile for the idler mode. Having chosen this transverse profile, we can express the spin wave excitation created by the write process entirely in terms of the collective excitations coupled to the idler field. We will then solve the Heisenberg Langevin equations in the adiabatic limit for the special case of an initially spin polarized ensemble.

The idler spin wave is retrieved from the ensemble by shining a classical *read* pulse resonant on the $|b\rangle \leftrightarrow |c\rangle$ transition on the ensemble with a carrier wave vector \vec{k}_r . We assume the read pulse is traveling anti-parallel to the write pulse; $\hat{k}_r = -\hat{k}_w$. The *read* field has the same helicity as the write field, so that the read field polarization

$\vec{e}_r = \vec{e}_{\alpha_w}(\hat{k}_r) \approx -\vec{\xi}_{-\alpha_w}$, where we have used the polarization conventions introduced in Appendix A. The positive frequency component of the *read* field is given by

$$\vec{E}_r^{(+)}(\vec{r}, t) = -\vec{\xi}_{-\alpha_w} e^{i\vec{k}_r \cdot \vec{r}} e^{-ick_r t} E_r(t) \quad (3.80)$$

where $E_r(t)$ is a time dependent electric field envelope. We assume the field envelope does not vary over the length of the ensemble or over the width of the collected idler, and we have therefore suppressed the position dependence of $E_r(t)$.

We detect the retrieved idler field, resonant on the $|a\rangle \leftrightarrow |c\rangle$ transition, with a transverse spatial envelope $\phi^{(i)}(\vec{r})$ and a carrier wave vector $\vec{k}_i = [(\omega_c - \omega_a)/c]\hat{k}_i$ propagating nearly antiparallel to the z -axis, so that the helicity vectors $\vec{e}_\alpha(\hat{k}_i) \approx -\vec{\xi}_{-\alpha}$. The positive frequency component of the idler field is given by

$$\hat{\mathbf{E}}_i^{(+)}(\vec{r}, t) = (2\pi)^{3/2} \mathcal{E}(ck_i) e^{i\vec{k}_i \cdot \vec{r}} e^{-ick_i t} \phi^{(i)}(\vec{r}) \sum_{\alpha=\pm 1} \vec{e}_\alpha(\hat{k}_i) \hat{\varphi}_\alpha^{(i)}(r_{\parallel}^{(i)}, t) \quad (3.81)$$

where $\hat{\varphi}_\alpha^{(i)}(z, t)$ is the linear density annihilation operator for idler photons at position z and helicity α . These photon density operators obey the bosonic commutation relations

$$\left[\hat{\varphi}_\alpha^{(i)}(z, t), \hat{\varphi}_\beta^{(i)\dagger}(z', t) \right] = \delta_{\alpha, \beta} \delta(z - z'). \quad (3.82)$$

Their definitions in terms of plane wave operators is given Chapter 2. The *read* and *write* fields interact with the atoms *via* the electric dipole interaction.

The interaction Hamiltonian written in the rotating wave approximation is given by

$$\hat{V}_{\text{read}}(t) = \hat{V}_i(t) + \hat{V}_r(t) + \hat{V}_R(t) \quad (3.83)$$

where $\hat{V}_i(t) = -\sum_\mu \hat{\mathbf{d}}_{(a,c)}^{(-)\mu}(t) \cdot \hat{\mathbf{E}}_i^{(+)}(\vec{r}_\mu) + h.c.$ gives the atomic interaction with the idler field, $\hat{V}_r(t) = -\sum_\mu \hat{\mathbf{d}}_{(b,c)}^{(-)\mu}(t) \cdot \vec{E}_r^{(+)}(\vec{r}_\mu, t) + h.c.$ is the interaction with the classical *read* field, and $\hat{V}_R(t) = -\sum_\mu \hat{\mathbf{d}}^{(-)\mu}(t) \cdot \hat{\mathbf{E}}_R^{(+)}(\vec{r}_\mu, t) + h.c.$ is the interaction with the reservoir, where the reservoir field operator is given by

$$\hat{\mathbf{E}}_R^{(+)}(\vec{r}, t) = \hat{\mathbf{E}}^{(+)}(\vec{r}, t) - \sum_{\iota \in \{r, i\}} \hat{\mathbf{E}}_\iota^{(+)}(\vec{r}, t). \quad (3.84)$$

Following the treatment Appendix C, we assume that the number of idler photons in a slice of the ensemble of length dz is always much less than the number of atoms with which it interacts. In this weak idler approximation [69, 75], we arrive at the following Heisenberg Langevin equations describing the propagation and interaction or the idler field with matter excitations within the ensemble:

$$\left(\frac{\partial}{\partial t} + c\hat{k}_i \cdot \nabla\right) \hat{\varphi}_\alpha^{(i)}(r_\parallel^{(i)}, t) = -i\sqrt{n(r_\parallel^{(i)})} p_m \kappa_i^* \sum_{m=-F_b}^{F_b} C_{m-\alpha}^{F_a-1 F_c} \hat{e}_{m; m-\alpha}(r_\parallel^{(i)}, t), \quad (3.85)$$

$$\begin{aligned} \frac{d}{dt} \hat{e}_{m; m-\alpha}(r_\parallel^{(i)}, t) &= -i\kappa_i \sqrt{n(r_\parallel^{(i)})} p_m C_{m-\alpha}^{F_a-1 F_c} \hat{\varphi}_\alpha^{(i)}(r_\parallel^{(i)}, t) \\ &\quad -i\Omega_r(t) C_{m+\alpha_w-\alpha-\alpha_w m-\alpha}^{F_b-1 F_c} \hat{s}_{m; m+\alpha_w-\alpha}(r_\parallel^{(i)}, t) \\ &\quad + \hat{\zeta}_{a,m; c, m-\alpha}(r_\parallel^{(i)}, t) - \frac{1}{2} \Gamma_c \hat{e}_{m; m-\alpha}(r_\parallel^{(i)}, t), \end{aligned} \quad (3.86)$$

and

$$\frac{d}{dt} \hat{s}_{m; m+\alpha_w-\alpha}(r_\parallel^{(i)}, t) = -i\Omega_r^*(t) C_{m+\alpha_w-\alpha-\alpha_w m-\alpha}^{F_b-1 F_c} \hat{e}_{m; m-\alpha}(r_\parallel^{(i)}, t), \quad (3.87)$$

where $\kappa_i = (c \|\hat{\mathbf{d}}\| a) [\hbar c k_i / (2\epsilon_0)]^{1/2}$ is the idler coupling constant, $\Omega_r(t) \equiv (c \|\hat{\mathbf{d}}\| b) E_r(t)$ is the Rabi frequency of the *read* field, Γ_c is the spontaneous emission rate of level $|c\rangle$,

$$\begin{aligned} \hat{e}_{m; m'}(r_\parallel^{(i)}, t) &\equiv \frac{1}{\sqrt{n(r_\parallel^{(i)})} p_m} \sum_{\mu=1}^N e^{-i\vec{k}_i \cdot \vec{r}_\mu} \phi^{(i)*}(\vec{r}_\mu) \\ &\quad \tilde{\sigma}_{a,m; c, m'}^\mu(t) \delta((\vec{r} - \vec{r}_\mu) \cdot \hat{k}_i) \end{aligned} \quad (3.88)$$

is a collective optical coherence at position $r_\parallel^{(i)} = \hat{k}_i \cdot \vec{r}$ between atoms in state $|a, m\rangle$ and those in $|c, m'\rangle$, and

$$\begin{aligned} \hat{s}_{m; m'}(r_\parallel^{(i)}, t) &\equiv \frac{1}{\sqrt{n(r_\parallel^{(i)})} p_m} \sum_{\mu=1}^N \phi^{(i)*}(\vec{r}_\mu) e^{i(\vec{k}_r - \vec{k}_i) \cdot \vec{r}_\mu} \\ &\quad \times \tilde{\sigma}_{a,m; b, m'}^\mu(t) \delta(r_\parallel^{(i)} - r_{\parallel\mu}^{(i)}) \end{aligned} \quad (3.89)$$

is a collective hyperfine coherence (spin wave) at position $r_{\parallel}^{(i)}$. We show in Appendix C, that these collective operators obey the commutation relations

$$\begin{aligned} & \left[\hat{e}_{m_1; m'_1} \left(r_{\parallel}^{(i)}, t \right), \hat{e}_{m_2; m'_2}^{\dagger} \left(\hat{k}_i \cdot \vec{r}', t \right) \right] \\ &= \delta_{m_1, m_2} \delta_{m'_1, m'_2} \delta \left(\hat{k}_i \cdot (\vec{r} - \vec{r}') \right) + \hat{O} \left(1/\sqrt{N_z} \right) \end{aligned} \quad (3.90a)$$

$$\begin{aligned} & \left[\hat{s}_{m_1; m'_1} \left(r_{\parallel}^{(i)}, t \right), \hat{s}_{m_2; m'_2}^{\dagger} \left(\hat{k}_i \cdot \vec{r}', t \right) \right] \\ &= \delta_{m_1, m_2} \delta_{m'_1, m'_2} \delta \left(\hat{k}_i \cdot (\vec{r} - \vec{r}') \right) + \hat{O} \left(1/\sqrt{N_z} \right), \end{aligned} \quad (3.90b)$$

where N_z is the number of atoms within the idler transverse spatial profile in a slice of the ensemble of thickness dz at position $r_{\parallel}^{(i)} = -z$. We assume $N_z \gg 1$ for all positions within the ensemble.

The Heisenberg Langevin equations state how a collected mode from the *read* process is related to a set of collective atomic excitations. We now choose an optimal carrier wave number \vec{k}_i and transverse spatial profile $\phi^{(i)}(\vec{r})$ for the idler mode. We accomplish this by revisiting the expression for the idler spin wave operator, and re-expressing it as

$$\hat{S}_{\alpha}^{(i)} \equiv \sum_{m=-F_a}^{F_a} \frac{\sqrt{p_m} X_{m, \alpha}}{\sqrt{\sum_m p_m |X_{m, \alpha}|^2}} \hat{S}_{a, m; b, m+\alpha_w-\alpha}^{(i)} \quad (3.91)$$

and,

$$\begin{aligned} \hat{S}_{a, m; b, m'}^{(i)} &= i \bar{A}^{(s)} \int dr_{\parallel}^{(i)} \sqrt{\frac{n(r_{\parallel}^{(i)})}{N}} e^{-i((\vec{k}_w - \vec{k}_s + \vec{k}_r - \vec{k}_i) \cdot \hat{k}_i) r_{\parallel}^{(i)}} \phi^{(w)*} \left(r_{\parallel}^{(i)} \right) \\ &\times \frac{1}{\sqrt{n(r_{\parallel}^{(i)}) p_m}} \sum_{\mu=1}^N \tilde{\sigma}_{a, m; b, m+\alpha_w-\alpha}^{\mu}(t) e^{i(\vec{k}_r - \vec{k}_i) \cdot \vec{r}_{\mu}} \\ &\times e^{-i(\vec{k}_w - \vec{k}_s + \vec{k}_r - \vec{k}_i) \cdot \vec{r}_{\perp}^{(i)}} \phi^{(s)}(\vec{r}_{\mu}) \delta \left(\hat{k}_i \cdot (\vec{r} - \vec{r}_{\mu}) \right). \end{aligned} \quad (3.92)$$

We choose the idler direction and the associated transverse profile pair $(\hat{k}_i, \phi^{(i)}(\vec{r}))$ to be the member of the set

$$\left\{ (\hat{k}_i, \phi(\vec{r})) : \left(\hat{k}_i \cdot \nabla \right) \phi(\vec{r}) = i \frac{\nabla_{\perp}^{(i)2}}{2k_i} \phi(\vec{r}) \right\} \quad (3.93)$$

such that

$$\int d^2 r_{\perp}^{(i)} \left| \phi \left(\vec{r}_{\perp}^{(i)}, r_{\parallel}^{(i)} \right) - e^{i(\vec{k}_w - \vec{k}_s + \vec{k}_r - \vec{k}_i) \cdot \vec{r}_{\perp}^{(i)}} \phi^{(s)*}(\vec{r}) \right|^2 \quad (3.94)$$

is minimized. In this way, the overlap between the excitation associated with the detected idler mode and the spin wave imprinted by the detection of the signal is maximized. This overlap is maximized when the phase matching condition $\vec{k}_i = \vec{k}_w - \vec{k}_s + \vec{k}_r$ is satisfied and the transverse mode function is given by

$$\phi^{(i)}(\vec{r}) = \phi^{(s)*}(\vec{r}). \quad (3.95)$$

With this choice, we express the imprinted spin wave as

$$\hat{S}_{m,\alpha}^{(i)} = i \int dr_{\parallel}^{(i)} \bar{A}^{(s)} \phi^{(w)*} \left(r_{\parallel}^{(i)} \hat{k}_i \right) \sqrt{\frac{n(r_{\parallel}^{(i)})}{N}} \hat{s}_{m; m+\alpha_w-\alpha} \left(r_{\parallel}^{(i)} \right). \quad (3.96)$$

Recall that we have chosen to detect the signal whose propagation direction $\hat{k}_s = \hat{z}$. According to the phase matching condition, we will consequently choose the idler propagation direction $\hat{k}_i = -\hat{z}$ anti-parallel to the z -axis.

We see by inspection of the Heisenberg Langevin equations, that under conditions of phase matching, the imprinted idler spin wave $\hat{S}_{\alpha}^{(i)}$, is coupled to the idler field with helicity α by the dipole interaction with the read field. In this way, the polarization information of the idler spin wave can be retrieved and detected. In the absence of decoherence during the storage of the spin wave, the idler can be retrieved after an arbitrary delay simply by activating the *read* field.

The idler retrieval Heisenberg Langevin equations may be solved in the adiabatic limit using the adiabatic dark-state polariton mechanism [69, 75] in the special case of an initially polarized atomic sample. Let us assume the atoms are prepared in the state $|a, 0\rangle$, so that $p_m = \delta_{m,0}$. Using an argument analogous to the one presented in Appendix C, we arrive at the annihilation operator of the dark-state polariton with helicity α , $\hat{\Psi}_{\alpha}^{(i)}$, which is given by

$$\hat{\Psi}_{\alpha}^{(i)}(z, t) \equiv \frac{\Omega_r^*(t) \hat{\varphi}_{\alpha}^{(i)}(z, t) - \kappa_i^* \sqrt{n(z)} \sqrt{p_m} R'_{\alpha}(\alpha_w) \hat{s}_{0; +\alpha_w-\alpha}(z, t)}{\sqrt{|\Omega_r(t)|^2 + n(z) |\kappa_i|^2 |R_{\alpha}|^2}}, \quad (3.97)$$

where

$$R_\alpha(\alpha_w) = \frac{C_{0-\alpha-\alpha}^{F_a \ 1 \ F_c}}{C_{\alpha_w-\alpha-\alpha_w}^{F_b \ 1 \ F_c}} \quad (3.98)$$

is a ratio of Clebsch-Gordan coefficients. This collective matter-field excitation obeys the propagation equation

$$\left(\frac{\partial}{\partial t} - V_\alpha(z, t) \frac{\partial}{\partial z} \right) \hat{\Psi}_\alpha^{(i)}(z, t) = \hat{\Psi}_\alpha(z, t) \frac{1}{2} \frac{\partial V_\alpha(z, t)}{\partial z}, \quad (3.99)$$

where

$$V_\alpha(z, t) = \frac{c |\Omega_r(t)|^2}{|\Omega_r(t)|^2 + |\kappa_i|^2 n(z) |R_\alpha(\alpha_w)|^2} \quad (3.100)$$

is the position dependent group velocity for a dark-state polariton (DSP) of helicity α . Notice that where the atomic density goes to zero, the group velocity approaches the speed of light c , and the polariton consists entirely of the electric field excitation. One can show that, for constant Rabi frequency, the solution of Eq. (3.99) is

$$\hat{\Psi}_\alpha(z, t) = \sqrt{\frac{V_\alpha(z_0)}{V_\alpha(z)}} \hat{\Psi} \left(z_0, t + \int_{z_0}^z \frac{dz'}{V_\alpha(z')} \right), \quad (3.101)$$

where z_0 is some initial position. If, we are given an initial value of the DSP operator at all of space at a fixed time, $t = t_0$, then the solution to the Heisenberg equations is given by

$$\hat{\Psi}_\alpha(z, t) = \sqrt{\frac{V_\alpha(z_0(z, t))}{V_\alpha(z)}} \hat{\Psi}_\alpha(z_0(t, z), 0), \quad (3.102)$$

where $z_0(t, z)$ is the solution to the integral equation

$$\int_z^{z_0} \frac{dz'}{V_\alpha(z')} = t - t_0. \quad (3.103)$$

We therefore see that when the atomic sample is polarized and the *read* field is turned on adiabatically, the idler spin wave would be completely transferred to the detected idler field. We note, however, that because the polarization components propagate at different group velocities, the temporal profiles of the retrieved photons would be different for each helicity. Therefore, if one were to turn on the read field for only a short time, one helicity component would be retrieved with a higher efficiency than

the other. These unequal retrieval efficiencies are manifested when one estimates the *read* process dynamics using time dependent perturbation theory [93]. When one then traces over the atomic degrees of freedom, the two photon component of the signal-idler density matrix would be given in the interaction picture by

$$\hat{\rho}'_{si} = \hat{\Psi}_2^\dagger |vac\rangle \langle vac| \hat{\Psi}_2 \quad (3.104)$$

where

$$\hat{\Psi}_2 = \left(\cos \eta' \hat{a}_1^{(s)} \hat{a}_1^{(i)} + \sin \eta' \hat{a}_{-1}^{(s)} \hat{a}_{-1}^{(i)} \right), \quad (3.105)$$

and the different retrieval frequencies are manifested in the difference between the mixing angle η' and that of the signal-idler spin wave density matrix of Eq. (3.1), η .

When the atoms are unpolarized, the retrieval dynamics are more complex. With the level configuration of this experiment [17], a DSP cannot exist for either helicity of the idler excitation [19, 18] (See Appendix C for more detail.) The retrieval dynamics in this scenario are the subject of further theoretical investigation. The Heisenberg Langevin equations do tell us, however, that the stored atomic spin wave $\hat{S}_\alpha^{(i)}$ couples to the detected idler field of Helicity α . We will therefore model the retrieval process as an effective beam splitter, where an idler field mode $\hat{a}_\alpha^{(i)}$ with some spatio-temporal envelope $\varphi_\alpha^{(i)}(t + z/c)$ is related to $\hat{S}_\alpha^{(i)}$ by

$$\hat{a}_\alpha^{(i)} = \sqrt{\epsilon_\alpha} \hat{S}_\alpha^{(i)} + \sqrt{1 - \epsilon_\alpha} \hat{\zeta}_\alpha^{(in)} \quad (3.106a)$$

$$\hat{\zeta}_\alpha^{(out)} = -\sqrt{1 - \epsilon_\alpha} \hat{S}_\alpha^{(i)} + \sqrt{\epsilon_\alpha} \hat{\zeta}_\alpha^{(in)}, \quad (3.106b)$$

where $\hat{\zeta}^{(in)}$ and $\hat{\zeta}^{(out)}$ are input and output noise operators respectively, and ϵ_α is the retrieval efficiency of the idler spin wave of helicity α . We will assume that the input noise modes are in the vacuum state, and do not influence the photon counting statistics. In this chapter, we assume the retrieval efficiencies for the two idler helicities are equal $\epsilon_1 = \epsilon_{-1}$.

3.3 Experiment

A magneto-optical trap (MOT) of ^{85}Rb is used to provide an optically thick atomic cloud for our experiment (Figure 3.1). The ground levels $\{|a\rangle; |b\rangle\}$ correspond to the $5S_{1/2}, F_{a,b} = \{3, 2\}$ levels, while the excited level $|c\rangle$ represents the $\{5P_{1/2}, F_c = 3\}$ level of the D_1 line at 795 nm. The experimental sequence starts with all of the atoms prepared in level $|a\rangle$. The “dark” period lasts 640 ns, with the whole cycle taking 1.5 μs . All the light responsible for trapping and cooling is shut off during the dark period, with the trapping light shut off about 200 ns before the repumping light to empty the $F = 2$ hyperfine level. The quadrupole magnetic field of the MOT is switched off for the duration of the measurement sequence. The ambient magnetic field is compensated by three pairs of Helmholtz coils.

A 130 ns long *write* pulse tuned to the $|a\rangle \rightarrow |c\rangle$ transition is focused into the MOT with a Gaussian waist of about 400 μm . The light induces spontaneous Raman scattering via the $|c\rangle \rightarrow |b\rangle$ transition. The scattered light goes through the quarter-wave plate to map circular polarizations into linear ones, then passes through polarizer P_1 (set at angle θ_s) and impinges onto a single photon detector D1.

After a user-programmable delay Δt , a 120 ns long *read* pulse, with circular polarization opposite to that of the *write* pulse, tuned to the $|b\rangle \rightarrow |c\rangle$ transition illuminates the atomic ensemble. This accomplishes a transfer of the memory state onto the single photon (idler) emitted by the $|c\rangle \rightarrow |a\rangle$ transition. After passing through the quarter-wave plate and polarizer P_2 set at angle θ_i , the idler photon is directed onto a single-photon detector D2.

Both *write/read* and signal/idler pairs of fields are counter-propagating. The waist of the signal-idler mode in the MOT is about 150 μm . The four-wave mixing signal is used to align the single mode fibers collecting signal and idler photons, and to optimize the overlap between the pump and probe modes [58]. The value of delay Δt between the application of the *write* and *read* pulses is 200 ns. The electronic

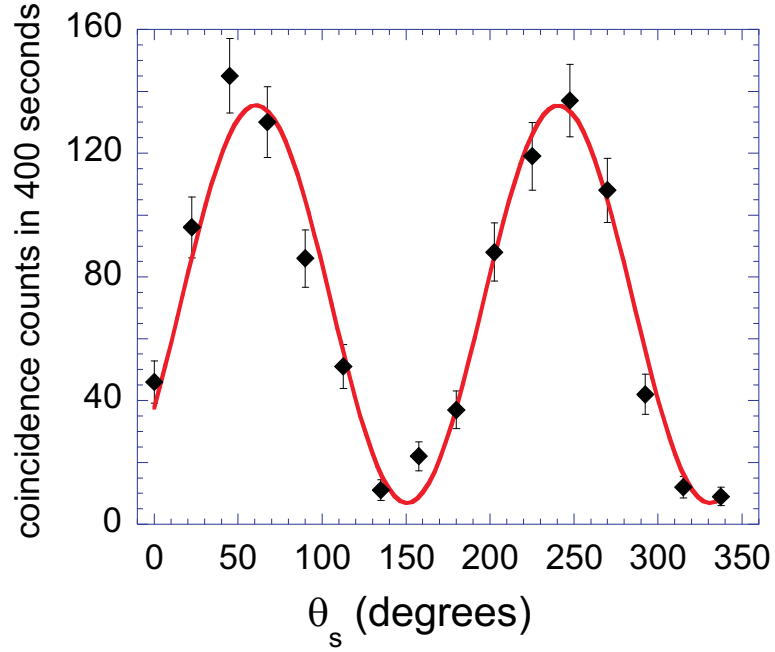


Figure 3.2: Measured coincidence fringe for $\theta_i = 67.5^\circ$. The curve is a fit based on Eq.(3.5), augmented by a background contribution, with $\eta = 0.81 \times \pi/4$, with visibility and amplitude being adjustable parameters. The visibility of the fit is 90%. Uncertainties are based on the statistics of the photon counting events.

Table 3.1: Measured correlation function $E(\theta_s, \theta_i)$ and S for $\Delta t = 200$ ns delay between *write* and *read* pulses; all the errors are based on the statistics of the photon counting events.

θ_s	θ_i	$E(\theta_s, \theta_i)$
-22.5	0	0.641 ± 0.024
-22.5	-45	0.471 ± 0.029
22.5	0	0.587 ± 0.027
22.5	-45	-0.595 ± 0.027
		$S = 2.29 \pm 0.05$

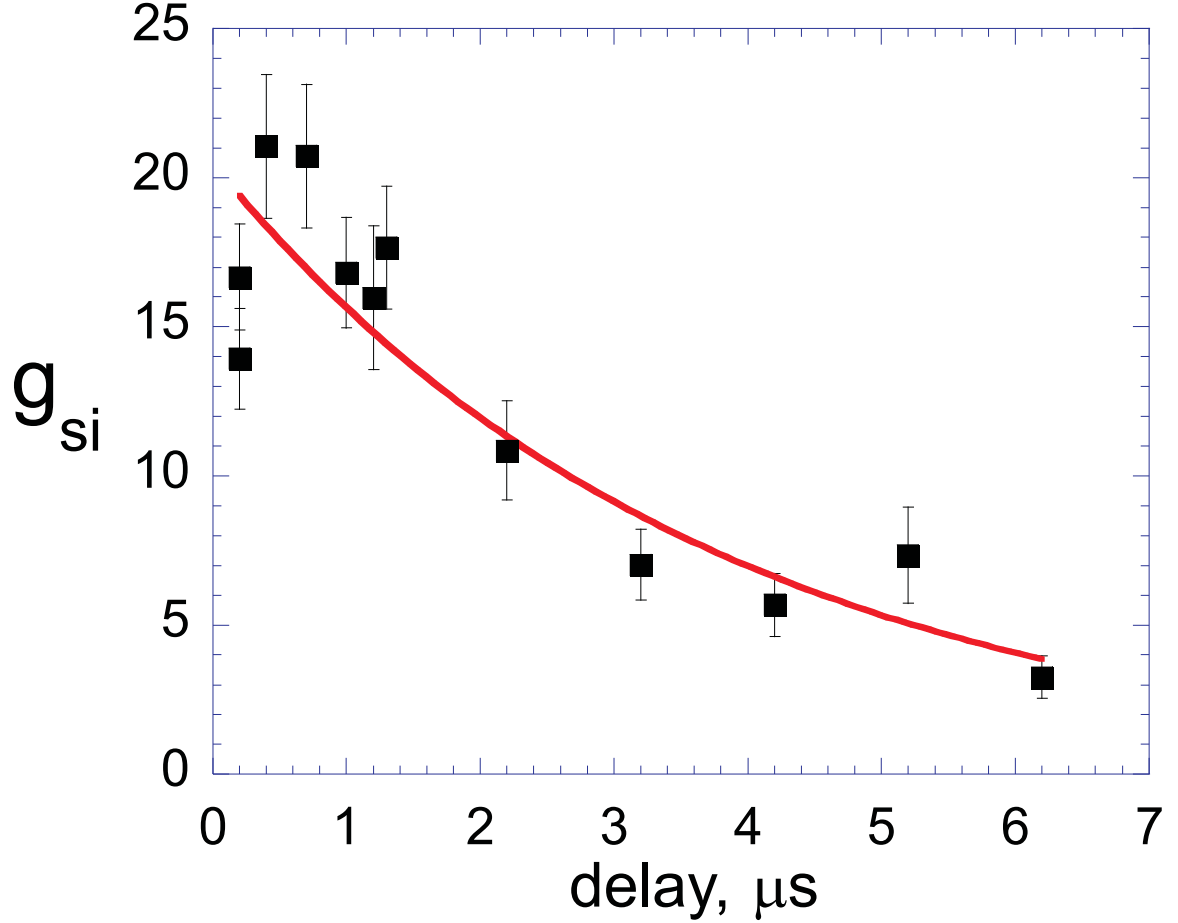


Figure 3.3: Normalized signal-idler intensity correlation function g_{si} as a function of storage time. Uncertainties are based on the statistics of the photon counting events. The full curve is the best exponential fit with time constant $\tau = 3.7\mu\text{s}$.

pulses from the detectors are gated with 140 ns and 130 ns windows centered on the time determined by the *write* and *read* light pulses, respectively. Afterwards, the electronic pulses are fed into a time-interval analyzer (with 2 ns time resolution). In order to measure the correlation between the photons produced by the *write* and *read* pulses, the output of D1 is fed into the “Start” input of a time-interval analyzer, and the output of D2 is fed into the “Stop” input.

A typical interference fringe in the signal-idler coincidence detection is displayed in Figure 3.2. In order to infer probabilistic atom-photon entanglement, we calculate the degree of Bell inequality violation $|S| \leq 2$ [91, 16]. Table 3.1 presents measured

values for the correlation function $E(\theta_s, \theta_i)$ using the canonical set of angles θ_s, θ_i . We find $S = 2.29 \pm 0.05 \not\geq 2$ - a clear violation of the Bell inequality. The value of S is smaller than the ideal value of 2.77 due to experimental imperfections, particularly non-zero counts in the minima of interference curves that arise as the result of the finite value of the normalized signal-idler intensity correlation function g_{si} [90, 51, 54] shown in Figure 3.3. To our knowledge, this is the first observed violation of the Bell inequality involving a collective excitation.

The effective detection efficiencies as determined by the ratios of the coincidence signal-idler count rate R_{si} to singles count rates R_s and R_i are $\alpha_{s,i} = R_{si}/R_{i,s} \simeq 0.02$. In all cold atomic ensemble experiments within the DLCZ program reported to date, the quadrupole magnetic field of the MOT has been the main source of the atomic memory decoherence (limiting storage times on the order of 100 ns [51, 54, 56, 57]). In this work, we have switched off the quadrupole field for the duration of our protocol, and the coherence time has increased to several μs , as is evident from the measured normalized intensity correlation function g_{si} displayed in Figure 3.3 (the length of the dark period was increased up to 7 μs for this measurement at the expense of lower count rate).

The robustness and relative simplicity of probabilistic atom-photon entanglement hold promise for the realization of a distributed quantum network involving the interconnection of several similar elements. We are currently investigating connecting two such quantum nodes.

CHAPTER 4

QUANTUM TELECOMMUNICATION BASED ON ATOMIC CASCADE TRANSITIONS

A quantum repeater at telecommunications wavelengths with long-lived atomic memory is proposed, and its critical elements are experimentally demonstrated using a cold atomic ensemble. Via atomic cascade emission, an entangled pair of $1.53\text{ }\mu\text{m}$ and 780 nm photons is generated. The former is ideal for long-distance quantum communication, and the latter is naturally suited for mapping to a long-lived atomic memory. Together with our demonstration of photonic-to-atomic qubit conversion presented in Chapter 8, both of the essential elements for the proposed telecommunications quantum repeater have now been realized.

4.1 Introduction

A quantum network would use the resources of distributed quantum mechanical entanglement, thus far largely untapped, for the communication and processing of information via qubits [29, 30, 47]. Significant advances in the generation, distribution, and storage of qubit entanglement have been made using laser manipulation of atomic ensembles, including atom-photon entanglement and matter-light qubit conversion [57], Bell inequality violation between a collective atomic qubit and a photon [17], and light-matter qubit conversion and entanglement of remote atomic qubits [21]. In each of these works photonic qubits were generated in the near-infrared spectral region. In related developments, entanglement of an ultraviolet photon with a trapped ion [32, 33] and of a near-infrared photon with a single trapped atom [38] have been demonstrated. Heterogeneous quantum network schemes that combine single-atom

and collective atomic qubits are being actively pursued [48, 49, 50]. However, photons in the ultraviolet to the near-infrared range are not suited for long-distance transmission over optical fibers due to high losses.

In this Chapter, we propose a telecommunications wavelength quantum repeater based on cascade atomic transitions in either (1) a single atom or (2) an atomic ensemble. We will first discuss the latter case, with particular reference to alkali metals. Such ensembles, with long lived ground level coherences can be prepared in either solid [94] or gas [17] phase. For concreteness, we consider a cold atomic vapor confined in high-vacuum. The cascade transitions may be chosen so that the photon (signal) emitted on the upper arm has telecommunication range wavelength, while the second photon (idler), emitted to the atomic ground state, is naturally suited for mapping into atomic memory. Experimentally, we demonstrate phase-matched cascade emission in an ensemble of cold rubidium atoms using two different cascades: (a) at the signal wavelength $\lambda_s = 776$ nm, via the $5S_{1/2} \rightarrow 5D_{5/2}$ two-photon excitation, (b) at $\lambda_s = 1.53$ μm , via the $5S_{1/2} \rightarrow 4D_{5/2}$ two-photon excitation. We observe polarization entanglement of the emitted photon pairs and superradiant temporal profiles of the idler field in both cases.

4.2 *Proposal*

We now outline our approach in detail and at the end we will summarize an alternative protocol for single atoms.

Step (A) - As illustrated in Figure 4.1(a), the atomic sample is prepared in level $|a\rangle$, e.g., by means of optical pumping. It is important to note that, in the case of an atomic ensemble qubit, an incoherent mixture of Zeeman states is sufficient for our realization. The upper level $|d\rangle$, which may be of either *s*- or *d*-type, can be excited either by one- or two-photon transitions, the latter through an intermediate level $|c\rangle$. The advantage of two photon excitation is that it allows for non-collinear

phase matching of signal and idler photons; single photon excitation is forbidden in electric dipole approximation and phase-matched emission is restricted to a collinear geometry (this argument implicitly assumes that the refractive index of the vapor is approximately unity). Ideally the excitation is two-photon detuned from the upper level $|d\rangle$, creating a virtual excitation.

Step (B) - Scattering via the upper level $|d\rangle$ to ground level $|a\rangle$ through the intermediate level $|e\rangle$ (where $|e\rangle$ may coincide with $|c\rangle$) results in the cascaded emission of signal and idler fields. The signal field, which is emitted on the upper arm, has a temporal profile identical to that of the laser excitation as a consequence of the large two photon detuning. As noted earlier, the wavelength of this field lies in the 1.1-1.6 μm range, depending on the alkali metal transition used. The signal field can be coupled to an optical fiber (which may have losses as low as 0.2 dB/km) and transmitted to a remote location.

The temporal profile of the idler field can be much shorter than the single-atom spontaneous decay time t_s of the intermediate level. Under the conditions of a large Fresnel number of the exciting laser fields, the decay time is of order t_s/d_{th} , characteristic of superradiance [95][96][90]. Here $d_{th} \approx 3n\lambda^2l/(8\pi)$ is the optical thickness, where λ is the wavelength, n is the number density and l is the length of the sample.

The direction of the idler field is determined by the phase matching condition $\vec{k}_1 + \vec{k}_2 = \vec{k}_s + \vec{k}_i$, where \vec{k}_1 and \vec{k}_2 are the wavevectors of the laser fields I and II, respectively. Under conditions of phase matching, collective enhancement causes emission of the the idler photon correlated with a return of the atom into the Zeeman state from which it originated [17]. The fact that the atom begins and ends the absorption-emission cycle in the same state is essential for strong signal-idler polarization correlations. The reduced density operator for the field, taking into account collective enhancement, will be shown to be:

$$\hat{\rho}(t) \approx \left(1 + \sqrt{\epsilon}\hat{A}_2^\dagger(t)\right) \hat{\rho}_{vac} \left(1 + \sqrt{\epsilon}\hat{A}_2(t)\right), \quad (4.1)$$

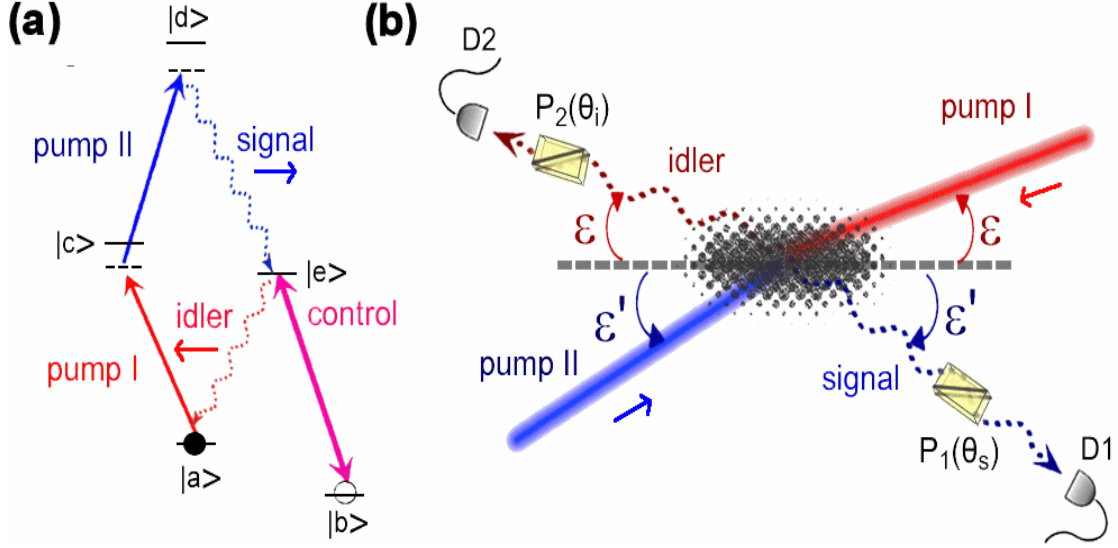


Figure 4.1: (a) The atomic structure for the proposed cascade emission scheme involving excitation by pumps I and II. Pump II and the signal photons lie in the telecommunication wavelength range when a suitable level of orbital angular momentum $L = 0$ or $L = 2$ is used as level $|d\rangle$. For atomic rubidium, the signal wavelength is $1.32\mu\text{m}$ ($6S_{1/2} \rightarrow 5P_{1/2}$ transition), $1.37\mu\text{m}$ ($6S_{1/2} \rightarrow 5P_{3/2}$ transition), $1.48\mu\text{m}$ ($4D_{3/2(5/2)} \rightarrow 5P_{1/2}$ transition), $1.53\mu\text{m}$ ($4D_{3/2(5/2)} \rightarrow 5P_{3/2}$ transition). For atomic cesium, the signal wavelength is $1.36\mu\text{m}$ ($7S_{1/2} \rightarrow 6P_{1/2}$ transition), $1.47\mu\text{m}$ ($7S_{1/2} \rightarrow 6P_{3/2}$ transition). For Na and K the corresponding wavelengths are in the $1.1\text{-}1.4\mu\text{m}$ range. (b) Schematic of experimental setup based on ultra-cold ^{85}Rb atomic gas. For $\lambda_s = 776\text{ nm}$, phase matching results in the angles $\epsilon' \approx \epsilon \approx 1^\circ$, while for $\lambda_s = 1.53\mu\text{m}$, $\epsilon' \approx 2\epsilon \approx 2^\circ$. P_1 and P_2 are polarizers; D1 and D2 are detectors.

where $\hat{\rho}_{vac}$ is the vacuum state of the field, $\hat{A}_2^\dagger(t)$ is a time dependent two photon creation operator for the signal and idler fields, and $\epsilon \ll 1$. For linearly polarized pumps with parallel (vertical) polarizations, we find

$$\hat{A}_2^\dagger = \cos \chi \hat{a}_H^\dagger \hat{b}_H^\dagger + \sin \chi \hat{a}_V^\dagger \hat{b}_V^\dagger \quad (4.2)$$

where χ is determined by Clebsch-Gordan coupling coefficients (Section 4.3), $\hat{a}_{H(V)}^\dagger$ and $\hat{b}_{H(V)}^\dagger$ are creation operators for a horizontally (vertically) polarized signal and idler photon, respectively. For the hyperfine level configuration $F_a = 3 \rightarrow F_c = 4 = F_e \rightarrow F_d = 5$, and for an unpolarized atomic sample, we find $\sin \chi = 2 \cos \chi = 2/\sqrt{5}$.

Step (C) - The photonic qubit is encoded in the idler field polarization. Photonic to atomic qubit conversion was achieved in Ref.[21]. Such conversion can be performed either within the same ensemble or in a suitably prepared adjacent ensemble/pair of ensembles. In either case, a strong laser control beam is required to couple the other ground hyperfine level $|b\rangle$ to the intermediate level $|e\rangle$. Collective excitations involving two orthogonal hyperfine coherences serve as the logical states of the atomic qubit [57, 17, 21].

4.3 Theory

In this section, we go into more theoretical detail regarding the outline of our proposal. We consider an ensemble of N atoms with the level configuration shown in Figure 4.1(a). The atomic hyperfine levels $|a\rangle$, $|b\rangle$, $|c\rangle$, $|d\rangle$, and $|e\rangle$ have energies $\hbar\omega_a \equiv 0$, $\hbar\omega_b$, $\hbar\omega_c$, $\hbar\omega_d$, and $\hbar\omega_e$ respectively. The total angular momentum of a hyperfine level $|f\rangle$ is denoted by F_f . We assume the atoms are prepared in an incoherent mixture of the Zeeman states of level $|a\rangle$. We express the initial atom-field density matrix $\hat{\rho}_0$ as

$$\hat{\rho}_0 \equiv \hat{\rho}_{vac} \otimes \left(\bigotimes_{\mu=1}^N \sum_{m_\mu=-F_a}^{F_a} p_{m_\mu} |a, m_\mu\rangle_\mu \langle a, m_\mu| \right), \quad (4.3)$$

where p_M is the probability of finding an atom in state $|a, M\rangle$.

From time $t = -T$ to time $t = 0$, the pump laser fields are activated. Pump I is tuned to the $|a\rangle \leftrightarrow |c\rangle$ transition with detuning $\Delta_I = ck_1 - \omega_c$, and pump II drives the $|c\rangle \leftrightarrow |d\rangle$ transition with detuning $\Delta_{II} = ck_2 - (\omega_d - \omega_c)$, where \vec{k}_1 and \vec{k}_2 are the wavevectors of pumps I and II, respectively. The pump electric fields are given by

$$\vec{E}_I(\vec{r}, t) = \vec{e}_I e^{i\vec{k}_1 \cdot \vec{r}} e^{-ick_1 t} E_I(\vec{r}, t) \quad (4.4a)$$

$$\vec{E}_{II}(\vec{r}, t) = \vec{e}_{II} e^{i\vec{k}_2 \cdot \vec{r}} e^{-ick_2 t} E_{II}(\vec{r}, t), \quad (4.4b)$$

where $E_{I(II)}(\vec{r}, t)$ is the slowly varying electric field amplitude of pump I (II), and $\vec{e}_{I(II)}$ is the polarization of pump I (II). Since the spatial intensity profiles of the pump lasers are not uniform throughout the atomic sample, we take the Rabi frequencies $\Omega_I(\vec{r}) = E_I(\vec{r}, t) \left(c \|\hat{\mathbf{d}}\|_a \right)$ and $\Omega_{II}(\vec{r}) = E_{II}(\vec{r}, t) \left(d \|\hat{\mathbf{d}}\|_c \right)$ to be spatially dependent. For simplicity, the field and state phases are chosen such that the Rabi frequencies are real; we further assume the fields I and II have polarizations $\vec{e}_I = \vec{\xi}_{\alpha_I}$ and $\vec{e}_{II} = \vec{\xi}_{-\alpha_I}$ respectively, where $\vec{\xi}_\alpha$ are the laboratory fixed spherical basis vectors (Eq. (2.31)). When the pump fields are off single photon and two photon resonance, and the duration of the pump fields T is much less than the decay times in the problem, this process creates the signal photon, as illustrated in Figure 4.1, and leaves behind a collective atomic excitation with one atom in the excited state $|e\rangle$.

In order to estimate the density matrix created by the pump process, we consider the electric dipole interaction picture Hamiltonian (Eq. (2.38)),

$$\hat{V}(t) = \hat{V}_I(t) + \hat{V}_{II}(t) + \hat{V}_s(t) + \hat{V}_i(t) + \hat{V}_R(t), \quad (4.5)$$

where $\hat{V}_I = -\sum_{\mu=1}^N \vec{E}_I^{(+)}(\vec{r}_\mu, t) \cdot \hat{\mathbf{d}}_{(a,c)}^{(-)\mu}(t) + h.c.$ is the interaction of the atoms with pump I, $\hat{V}_{II} = -\sum_{\mu=1}^N \vec{E}_{II}^{(+)}(\vec{r}_\mu, t) \cdot \hat{\mathbf{d}}_{(c,d)}^{(-)\mu}(t) + h.c.$ is the interaction of pump II with the atoms, $\hat{V}_s = -\sum_{\mu=1}^N \hat{\mathbf{E}}^{(+)}(\vec{r}_\mu, t) \cdot \hat{\mathbf{d}}_{(e,d)}^{(-)\mu}(t) + h.c.$ is the interaction of the atoms with the field on the signal ($|e\rangle \leftrightarrow |d\rangle$) transition, $\hat{V}_i = -\sum_{\mu=1}^N \hat{\mathbf{E}}^{(+)}(\vec{r}_\mu, t) \cdot \left(\hat{\mathbf{d}}_{(a,e)}^{(-)\mu}(t) + \right.$

$\hat{\mathbf{d}}_{(b,e)}^{(-)\mu}(t) + h.c.$ is the interaction of the atoms with the field on the idler transitions, and $\hat{V}_R(t)$ is the coupling of the electric field to all other allowed transitions within the atomic sample. We apply third order perturbation theory to the initial system density matrix $\hat{\rho}_0$. When the phases $\Delta_I T$, $\Delta_{II} T$, $(\Delta_I + \Delta_{II}) T \gg 1$, and when one neglects the effects of the ac Stark shift (which becomes relevant in second order perturbation theory), we find that to first order in the interaction time T the only resonant terms of the perturbative expansion (i.e. those terms that do not oscillate with frequencies on the order of the detunings) are those that correspond to emission of a photon with frequency $ck = \Delta + \omega_d - \omega_f$ with an atom being transferred from level $|a\rangle$ to $|f\rangle$, where $|f\rangle$ is some hyperfine level with energy $\omega_f < \omega_d$. In the limit of a dilute atomic gas, where the optical thickness is low, we make the approximation that each atom interacts independently with the quantized electromagnetic field. In this limit, one can determine the state of the system by considering the evolution of a single atom interacting with the field in the Weisskopf-Wigner model of spontaneous emission. For times $t > 0$ this yields the density matrix

$$\hat{\rho}(t) = (1 + \hat{U}_s(t) + \hat{U}_R(t))\hat{\rho}_0(1 + \hat{U}_s^\dagger(t) + \hat{U}_R^\dagger(t)), \quad (4.6)$$

where the first order contribution to the evolution operator leading to emission of a signal photon on the $|d\rangle \leftrightarrow |e\rangle$ transition \hat{U}_s is given by

$$\begin{aligned} \hat{U}_s(t) = & \sum_{\mu=1}^N \frac{\Omega_I(\vec{r}_\mu)\Omega_{II}(\vec{r}_\mu)}{\Delta_I\Delta} \int d^3k_s \sum_{\lambda_s} \kappa_s \sum_{\alpha_s=-1}^1 \left(\vec{\varepsilon}_\lambda^* \left(\hat{k}_s \right) \cdot \vec{\xi}_{\alpha_s} \right) \\ & \times e^{i(\vec{k}_1 + \vec{k}_2 - \vec{k}_s) \cdot \vec{r}_\mu} \frac{1 - e^{i(\delta_s(k_s)T)}}{\delta_s(k_s)} \hat{b}_{\lambda_s}^\dagger(\vec{k}_s) \\ & \times \sum_{M=-F_a}^{F_a} Z_{M,\alpha_s} \hat{\Sigma}_{M,\alpha_s}^{(\mu)\dagger}(t), \end{aligned} \quad (4.7)$$

where $\Delta \equiv \Delta_I + \Delta_{II}$ is the detuning from the two-photon resonance of the pump fields, $\kappa_s = [\hbar(\Delta + \omega_d - \omega_e)/(2\epsilon_0(2\pi)^3)]^{1/2} \left(d \left\| \hat{\mathbf{d}} \right\| e \right)$ is a measure of the signal field coupling strength, \vec{k}_s is the signal wavevector, \vec{r}_μ is the position of atom μ ,

$\delta_s(k_s) \equiv ck_s - (\omega_d - \omega_e + \Delta)$ is the signal photon detuning, $\hat{b}_{\lambda_s}(\vec{k}_s)$ is the annihilation operator for a signal photon of wavevector \vec{k}_s and polarization $\vec{\varepsilon}_{\lambda}(\hat{k}_s)$, and $Z_{M,\alpha_s} \equiv C_{M\alpha_I}^{F_a\ 1\ F_c} C_{M+\alpha_I-\alpha_I}^{F_c\ 1\ F_d} C_{M-\alpha_s\ \alpha_s}^{F_e\ 1\ F_d}$ is the appropriate product of Clebsch-Gordan coefficients. The operator $\hat{\Sigma}_{M,\alpha_s}^{(\mu)\dagger}(t)$ contains the dynamics of atom μ interacting with the idler field, and is given by

$$\begin{aligned} \hat{\Sigma}_{M,\alpha_s}^{(\mu)\dagger}(t) &= e^{-\frac{\Gamma_e}{2}t} \hat{\sigma}_{e,M-\alpha_s;a,M}^{(\mu)} \\ &+ \int d^3k_i \sum_{\lambda_i} \sum_{\alpha_i=-1}^1 e^{-i\vec{k}_i \cdot \vec{r}_\mu} f_{\lambda_i,\alpha_i,M}(\vec{k}_i, t) \\ &\quad \times \hat{a}_{\lambda_i}^\dagger(\vec{k}_i) \hat{\sigma}_{a,M-\alpha_s-\alpha_i;a,M}^{(\mu)} \\ &+ \int d^3k_i \sum_{\lambda_i} \sum_{\alpha_i=-1}^1 e^{-i\vec{k}_i \cdot \vec{r}_\mu} g_{\lambda_i,\alpha_i,M}(\vec{k}_i, t) \\ &\quad \times \hat{a}_{\lambda_i}^\dagger(\vec{k}_i) \hat{\sigma}_{b,M-\alpha_s-\alpha_i;a,M}^{(\mu)}, \end{aligned} \quad (4.8)$$

where Γ_e is the excited state spontaneous emission rate, $\hat{\sigma}_{f,m;f',m'}^{(\mu)} \equiv |f, m\rangle_\mu \langle f', m'|$ is a μ^{th} atom atomic coherence, \vec{k}_i is the idler photon wavevector, $\hat{a}_{\lambda_i}(\vec{k}_i)$ is the idler field annihilation operator for a photon of wavevector \vec{k}_i and polarization $\vec{\varepsilon}_{\lambda_i}(\hat{k}_i)$, and the time dependence of the amplitudes f and g is given by

$$\begin{aligned} f_{\lambda_i,\alpha_i,M}(\vec{k}_i, t) &= i\kappa_i (\vec{\varepsilon}_{\lambda_i}^*(\hat{k}_i) \cdot \vec{\xi}_{\alpha_i}) C_{M-\alpha_s-\alpha_i\ \alpha_i\ M-\alpha_s}^{F_a\ 1\ F_e} \\ &\quad \times \frac{1 - e^{i(ck_i - (\omega_e - i\Gamma_e/2))t}}{ck_i - (\omega_e - i\Gamma_e/2)} \end{aligned} \quad (4.9)$$

$$\begin{aligned} g_{\lambda_i,\alpha_i,M}(\vec{k}_i, t) &= i\kappa' \left(\vec{\varepsilon}_{\lambda_i}^*(\hat{k}_i) \cdot \vec{\xi}_{\alpha_i} \right) C_{M-\alpha_s-\alpha_i\ \alpha_i\ M-\alpha_s}^{F_b\ 1\ F_c} \\ &\quad \times \frac{1 - e^{i(ck_i - (\omega_e - \omega_b - i\Gamma_e/2))t}}{ck_i - (\omega_e - \omega_b - i\Gamma_e/2)}, \end{aligned} \quad (4.10)$$

where $\kappa_i = \left(e \left\| \hat{\mathbf{d}} \right\| a \right) [\hbar c(\omega_e - \omega_a)/(2\epsilon_0(2\pi)^3)]^{1/2}$ is the coupling strength of the field to the $|a\rangle \leftrightarrow |e\rangle$ transition, $\kappa' = \left(e \left\| \hat{\mathbf{d}} \right\| a \right) [\hbar c(\omega_e - \omega_a)/(2\epsilon_0(2\pi)^3)]^{1/2}$ is the coupling strength of the field to the $|b\rangle \leftrightarrow |e\rangle$ transition. The operator $\hat{U}_R(t)$ accounts for the scattering of photons on transitions other than the signal $|d\rangle \leftrightarrow |e\rangle$ transition.

Once the idler photon has been emitted, for $t \gg 1/\Gamma_e$, we can determine the two-photon density matrix by tracing over the atomic components of $\hat{\rho}(t)$ in Eq. (4.6).

When this is done, we find a collective enhancement effect, in which the contributions of density matrix components corresponding to the atom scattering back to its original state dominate. This can be seen by expanding the density matrix (Eq. (4.6)) in terms of the photon creation/annihilation operators and individual atomic coherences between a ground state $|a, m\rangle_\mu$ and an arbitrary atomic state $|f, m'\rangle_\mu$ for atom μ . When tracing over the atomic degrees of freedom, one only needs to consider the following partial traces and their Hermitian conjugates:

$$\text{Tr}_{atoms} \left(\tilde{\sigma}_{f, m'; a, m}^\mu \hat{\rho}_0 \right) = \delta_{f, a} \delta_{m, m'} \hat{\rho}_{vac} \quad (4.11a)$$

and

$$\begin{aligned} & \text{Tr}_{atoms} \left(\tilde{\sigma}_{f_1, m'_1; a, m_1}^\mu \hat{\rho}_0 \tilde{\sigma}_{a, m_2; f_2, m'_2}^\nu \right) \\ &= \left[\left(1 - \delta_{f_1, a} \delta_{m_1, m'_1} \right) p_{m_1} \delta_{m_1, m_2} \delta_{m'_1, m'_2} \delta_{f_1, f_2} \delta_{\mu, \nu} \right. \\ & \quad \left. + p_{m_1} \delta_{f_1, a} \delta_{f_2, a} \delta_{m_1, m'_1} \delta_{m_2, m'_2} [p_{m_2} (1 - \delta_{\mu\nu}) + \delta_{m_1, m_2} \delta_{\mu\nu}] \right] \hat{\rho}_{vac}. \end{aligned} \quad (4.11b)$$

One sees by inspection that the partial trace in Eq. (4.11a), survives only when the atom scatters back to its original state. Furthermore, the trace in Eq. (4.11b) survives only when the atom scatters back to its original state (second term of Eq. (4.11b)) or when the two atomic coherence operators involved correspond to the same atom (first term of Eq. (4.11b)). Because the two-photon portion of the reduced density operator involves a summation over two atomic indices μ and ν , the terms in which an atom returns to its original state dominate, and the others provide a correction of order $1/N$. As a result, the photon pairs scattered in the phase matched directions are polarization entangled. The full two photon density matrix is given in this approximation by

$$\begin{aligned} \hat{\rho}_2(t) &= \left(1 + \sqrt{\epsilon} \hat{A}_2^\dagger \right) \hat{\rho}_{vac} \left(1 + \sqrt{\epsilon} \hat{A}_2 \right) \\ & \quad + \text{Tr} \left(\hat{U}_R(t) \hat{\rho}_0 \hat{U}_R^\dagger(t) \right) \hat{\rho}_{vac} + O(1/N), \end{aligned} \quad (4.12)$$

where $\hat{A}_2^\dagger(t)$ is time dependent two photon creation operator, and $\hat{\rho}_{vac}$ is the vacuum density matrix. The operator \hat{A}_2^\dagger is given by

$$\begin{aligned} \sqrt{\epsilon} \hat{A}_2^\dagger &= i \frac{N \Omega_{eff}}{\Delta} \int d^3 k_s \int d^3 k_i \left(\kappa_s \kappa_i \varrho(\vec{k}_i + \vec{k}_s - \vec{k}_1 - \vec{k}_2) \right. \\ &\quad \times \frac{1 - e^{-i(c k_s - (\omega_d - \omega_e + \Delta))T}}{c k_s - (\omega_d - \omega_e + \Delta)} \\ &\quad \times \frac{1}{c k_i - (\omega_e - i\Gamma_e/2)} \\ &\quad \times \left. \sum_{\alpha_s=-1}^1 X_{\alpha_I, \alpha_s} \hat{a}_{[-\alpha_s]}^\dagger(\vec{k}_i) \hat{b}_{[\alpha_s]}^\dagger(\vec{k}_s) \right), \end{aligned} \quad (4.13)$$

where $\Omega_{eff} \equiv \frac{1}{\Delta_I} \int d^3 r \Omega_I(\vec{r}) \Omega_{II}(\vec{r}) \frac{n(\vec{r})}{N}$ is the effective two photon Rabi frequency, and $n(\vec{r})$ is the atomic density at position \vec{r} . The phase matching function $\varrho(\vec{q})$ is determined by the Fourier transform of the effective single atom density interacting with the pump fields, which is given by

$$\begin{aligned} \varrho(\vec{q}) &\equiv \frac{1}{N} \sum_{\mu} \frac{\Omega_1(\vec{r}_\mu) \Omega_2(\vec{r}_\mu)}{\Delta_I \Omega_{eff}} e^{-i\vec{q} \cdot \vec{r}} \\ &= \left(\int d^3 r \frac{\Omega_1(\vec{r}) \Omega_2(\vec{r})}{\Delta_I \Omega_{eff}} \frac{n(\vec{r})}{N} e^{-i\vec{q} \cdot \vec{r}} \right) + O(1/\sqrt{N}). \end{aligned} \quad (4.14)$$

The weight associated with each pair of polarizations for the signal and idler is given by the product of Clebsch-Gordan coefficients

$$\begin{aligned} X_{\alpha_I, \alpha_s} &\equiv \sum_{M=-F_g}^{F_g} p_M C_{M \alpha_I}^{F_a \ 1 \ F_c} C_{M+\alpha_I -\alpha_I}^{F_c \ 1 \ F_d} \\ &\quad \times C_{M-\alpha_s \alpha_s}^{F_e \ 1 \ F_d} C_{M-\alpha_s}^{F_a \ 1 \ F_e}. \end{aligned} \quad (4.15)$$

The annihilation operators for polarization $\vec{\xi}_\alpha$ are defined as

$$\hat{a}_{[\alpha]}(\vec{k}_i) \equiv \sum_{\lambda} \left(\vec{\varepsilon}_\lambda(\hat{k}_i) \cdot \vec{\xi}_\alpha^* \right) \hat{a}_\lambda(\vec{k}_i) \quad (4.16)$$

$$\hat{b}_{[\alpha]}(\vec{k}_s) \equiv \sum_{\lambda} \left(\vec{\varepsilon}_\lambda(\hat{k}_s) \cdot \vec{\xi}_\alpha^* \right) \hat{b}_\lambda(\vec{k}_s). \quad (4.17)$$

Note, that unless \vec{k} is oriented along the z -axis, the $\hat{a}_{[\alpha]}(\vec{k})$ and $\hat{a}_{[\alpha']}(\vec{k})$ do not obey strict bosonic commutation relations, but, instead satisfy

$$\left[\hat{a}_{[\alpha]}(\vec{k}), \hat{a}_{[\alpha']}^\dagger(\vec{k}') \right] = \delta(\vec{k} - \vec{k}') \left(\delta_{\alpha, \alpha'} - \left(\vec{\xi}_{\alpha'} \cdot \hat{k} \right) \left(\hat{k} \cdot \vec{\xi}_\alpha^* \right) \right), \quad (4.18)$$

with the signal creation and annihilation operators obeying similar commutation relations. We note that this model does not account for propagation effects or for the enhanced idler emission rates associated with superradiance which occur in optically thick media. Since the collective enhancement that produces the desired polarization entanglement does not depend on the atomic decay rate, however, this entanglement should still result when superradiance and propagation effects are significant.

In our experiment both pumps are linearly polarized along the fixed z -axis, i.e. $\alpha_I = 0$, and are counterpropagating along the y -axis. For a field propagating along the direction \hat{k} , we assume the horizontal polarization $\vec{e}_H(\hat{k})$ and vertical polarization vectors $\vec{e}_V(\hat{k})$ are defined such that $\{\vec{e}_H(\hat{k}), \vec{e}_V(\hat{k}), \hat{k}\}$ form a right handed coordinate system. We choose the horizontal and vertical polarization vectors to be consistent with the conventions presented in Appendix A. Signal and idler detectors are placed so as to detect the phase-matched nearly forward scattered signal, $\hat{k}_s \approx \hat{y}$ and the nearly backward scattered idler $\hat{k}_i \approx -\hat{y}$, as illustrated in Figure 4.1(b). By tracing $\hat{\rho}_2$ over the reservoir of undetected modes, we find the effective two-photon state

$$|\Psi_{eff}\rangle = (\cos \chi \hat{a}_H^\dagger \hat{b}_H^\dagger - \sin \chi \hat{a}_V^\dagger \hat{b}_V^\dagger) |vac\rangle, \quad (4.19)$$

where

$$\cos \chi = \frac{Y_{+1} + Y_{-1}}{\sqrt{4Y_0^2 + (Y_{+1} + Y_{-1})^2}} \quad (4.20a)$$

$$\sin \chi = \frac{2Y_0}{\sqrt{4Y_0^2 + (Y_{+1} + Y_{-1})^2}}, \quad (4.20b)$$

and

$$Y_\alpha = \sum_{M=-F_g}^{F_g} p_M C_{M0M}^{F_a1F_c} C_{M0M}^{F_c1F_d} C_{M-\alpha\alpha M}^{F_e1F_d} C_{M-\alpha M-\alpha}^{F_a1F_e}. \quad (4.21)$$

For our level configuration and an unpolarized sample ($p_M = 1/(2F_a + 1)$), we find

$$\tan \chi = 2 \quad (4.22)$$

or

$$|\Psi_{eff}\rangle = \left(\frac{1}{\sqrt{5}} \hat{a}_H^\dagger \hat{b}_H^\dagger - \frac{2}{\sqrt{5}} \hat{a}_V^\dagger \hat{b}_V^\dagger \right) |vac\rangle. \quad (4.23)$$

We could alternatively assume pumps I and II to have opposite circular polarizations (equal helicities) counterpropagating along the z -axis. Let \hat{b}_α^\dagger be the creation operator for the forward scattered signal photon with helicity α , and $\hat{a}_{\alpha_i}^\dagger$ be the creation operator for the phase-matched backward scattered idler photon with helicity α_i . In this case, we find the two photon operator

$$|\Psi_{eff}\rangle = (\cos \eta \hat{a}_{-1}^\dagger \hat{b}_{-1}^\dagger + \sin \eta \hat{a}_{+1}^\dagger \hat{b}_{+1}^\dagger) |vac\rangle. \quad (4.24)$$

where

$$\cos \eta = \frac{X_{+1}}{\sqrt{X_{+1}^2 + X_{-1}^2}} \quad (4.25)$$

and

$$X_\alpha = \sum_{M=-F_g}^{F_g} p_M C_{M-1 M+1}^{F_a-1 F_c} C_{M+1 -1 M}^{F_c-1 F_d} C_{M-\alpha \alpha M}^{F_e-1 F_d} C_{M-\alpha M-\alpha}^{F_a-1 F_e}. \quad (4.26)$$

From symmetry relations for the Clebsch-Gordan coefficients, we find that, for the set of atomic levels used in our experiments, $\eta = \pi/4$, and the thus two-photon state would be a completely symmetric Bell state.

4.4 Experiment

We observe phase-matched cascade emission of entangled photon pairs, using samples of cold ^{85}Rb atoms, for two different atomic cascades: (a) at $\lambda_s = 776$ nm, via the $5s_{1/2} \rightarrow 5d_{5/2}$ two-photon excitation, (b) at $\lambda_s = 1.53$ μm , via the $5s_{1/2} \rightarrow 4d_{5/2}$ two-photon excitation. The investigations are carried out in two different laboratories using similar setups, Figure 4.1(b). A magneto-optical trap (MOT) of ^{85}Rb provides an optically thick cold atomic cloud. The atoms are prepared in an incoherent mixture of the level $|a\rangle$, which corresponds to the $5s_{1/2}$, $F_a = 3$ ground level, by means of optical pumping. The intermediate level $|c\rangle = |e\rangle$ corresponds to the $5p_{3/2}$, $F_c = 4$ level of the D_2 line at 780 nm, and the excited level $|d\rangle$ represents (a) the $5d_{5/2}$ level with $\lambda_s = 776$ nm, or (b) the $4d_{5/2}$ level with $\lambda_s = 1.53$ μm . Atomic level

$|b\rangle$ corresponds to $5s_{1/2}, F_b = 2$, and could be used to implement the light-to-matter qubit conversion [21].

The trapping and cooling light as well as the quadrupole magnetic field of the MOT are switched off for the 2 ms duration of the measurement. The ambient magnetic field is compensated by three pairs of Helmholtz coils. Counterpropagating pumps I (at 780 nm) and II (at 776 nm or $1.53\mu\text{m}$), tuned to two-photon resonance for the $|a\rangle \rightarrow |d\rangle$ transition are focused into the MOT using the off-axis, counter-propagating geometry of Harris and coworkers [59]. This two-photon excitation induces phase-matched signal and idler emission.

With quasi-cw pump fields, we perform photoelectric coincidence detection of the signal and idler fields. The latter are directed onto single photon detectors D1 and D2. For $\lambda_s = 1.53 \mu\text{m}$, the signal field is coupled into 100 m of single-mode fiber, and detector D1 (cooled InGaAs photon counting module) is gated using the output pulse of silicon detector D2. The electronic pulses from the detectors are fed into a time-interval analyzer with 1 ns time resolution.

We measure the stationary signal-idler intensity correlation function $G_{si}(\tau) = \langle \mathcal{T} : \hat{I}_s(t) \hat{I}_i(t + \tau) : \rangle$, where the notation $\mathcal{T} ::$ denotes time and normal ordering of operators, and \hat{I}_s and \hat{I}_i are the signal and idler intensity operators, respectively [90]. Results for (a) $\lambda_s = 776 \text{ nm}$ and (b) $\lambda_s = 1.53 \mu\text{m}$ are presented in Figure 4.2 and Figure 4.3, respectively. In particular, the measured correlation functions are shown in Figure 4.2(a,b) and Figure 4.3(a). The correlation function shown in Figure 4.2(a) exhibits quantum beats due to the two different hyperfine components of the the $5p_{3/2}$ level [97]. The correlation times are consistent with superradiant scaling $\sim t_s/d_{th}$, Figure 4.2(c), where $t_s \approx 27 \text{ ns}$ for the $5p_{3/2}$ level [95].

In order to investigate polarization correlations of the signal and idler fields, they are passed through polarizers P_1 (set at angle θ_s) and P_2 (set at angle θ_i), respectively, as shown in Figure 4.1(b). We integrate the time-resolved counting rate over a window

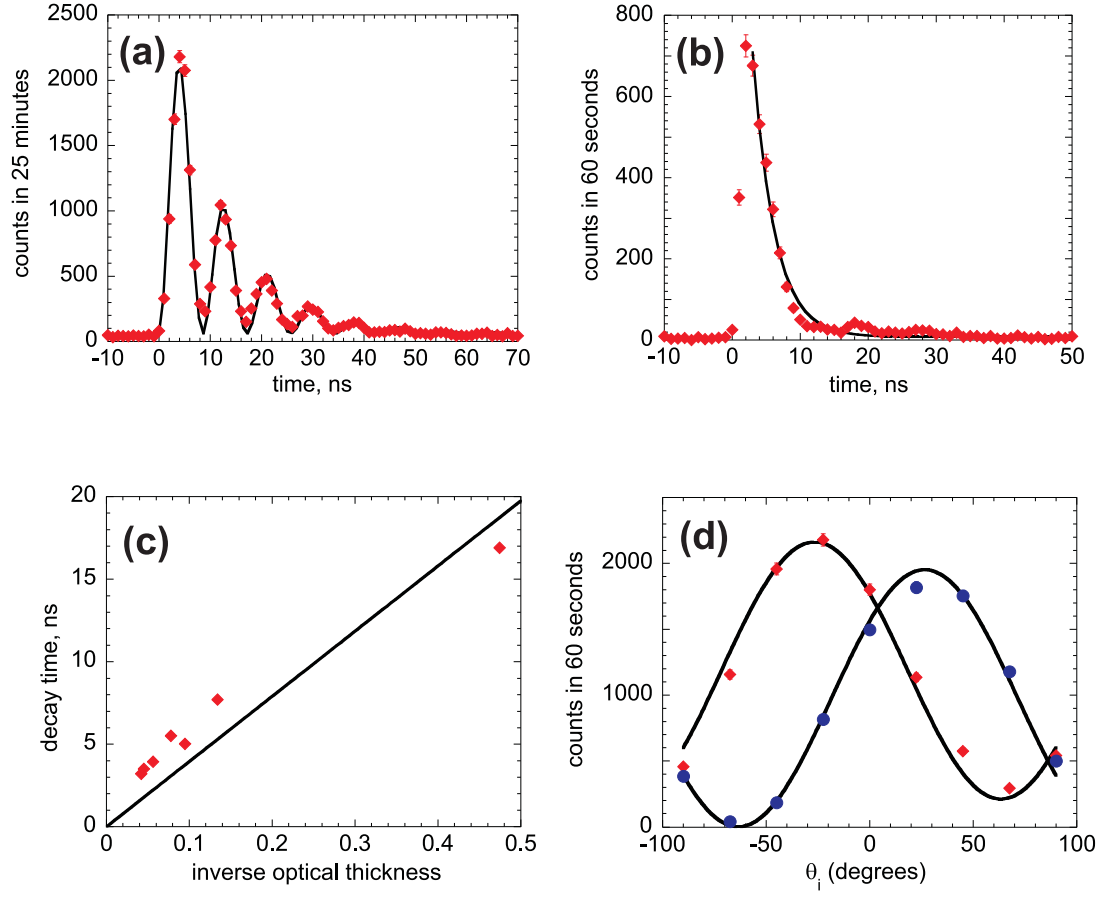


Figure 4.2: (a) Count rate proportional to the signal-idler intensity correlation function G_{si} as a function of signal-idler delay τ , $|d\rangle = |5d_{5/2}, F = 4\rangle$. The quantum beats are associated with 120 MHz hyperfine splitting, $F = 3$ and 4, of the $5p_{3/2}$ level [97]. The solid curve is a fit of the form $\beta + A \exp(-t/\alpha) \sin^2(\pi\Omega t)$, where $\beta = 63$, $A = 2972$, $\alpha = 11$ ns and $\Omega = 117$ MHz are adjustable parameters. (b) Same as (a), but for $|d\rangle = |5d_{5/2}, F = 5\rangle$. Since this state can only decay through the $F = 4$ component of the $5p_{3/2}$ level, there are no quantum beats. The solid curve is an exponential fit with decay time of 3.2 ns. (c) The measured decay time vs the inverse measured optical thickness. (d) Measured coincidence fringes for $\theta_s = 45^\circ$ (red diamonds) and $\theta_s = 135^\circ$ (blue circles). The solid curves are fits based on Eqs. (4.1)(4.2), with $\cos \chi = 1/\sqrt{5}$.

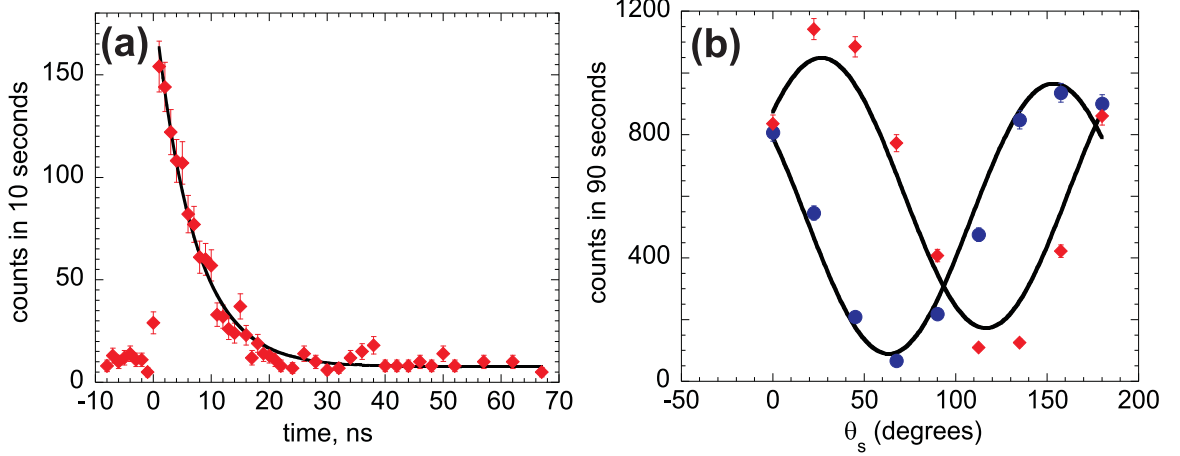


Figure 4.3: (a) Same as Figure 4.2(a,b), but for $|d\rangle = |4d_{5/2}, F = 5\rangle$. The solid curve is an exponential fit with decay time of 6.7 ns. (b) Measured coincidence fringes for $\theta_i = 45^\circ$ (red diamonds) and $\theta_i = 135^\circ$ (blue circles). The solid curves are fits based on Eqs. (4.1)(4.2), with $\cos \chi = 1/\sqrt{5}$.

ΔT centered at the maximum of the signal-idler intensity correlation function $G_{si}(\tau)$, with (a) $\Delta T = 6$ ns for $\lambda_s = 776$ nm, and (b) $\Delta T = 1$ ns for $\lambda_s = 1.53$ μm . The resulting signal-idler coincidence rate $C(\theta_s, \theta_i)$ exhibits sinusoidal variation as a function of the polarizers' orientations, as shown in Figs. 4.2(d) and 4.3(b). In order to verify the predicted polarization entanglement, we check for violation of Bell's inequality $S \leq 2$ [91, 90, 16]. We first calculate the correlation function $E(\theta_s, \theta_i)$, given by

$$\frac{C(\theta_s, \theta_i) + C(\theta_s^\perp, \theta_i^\perp) - C(\theta_s^\perp, \theta_i) - C(\theta_s, \theta_i^\perp)}{C(\theta_s, \theta_i) + C(\theta_s^\perp, \theta_i^\perp) + C(\theta_s^\perp, \theta_i) + C(\theta_s, \theta_i^\perp)}, \quad (4.27)$$

where $\theta^\perp = \theta + \pi/2$, and $S = |E(\theta_s, \theta_i) + E(\theta_s', \theta_i)| + |E(\theta_s, \theta_i') - E(\theta_s', \theta_i')|$.

Measured values of $E(\theta_s, \theta_i)$, using the set of angles θ_s, θ_i , chosen to maximize the violation of Bell's inequality, are presented in Table 4.1. We find (a) $S = 2.185 \pm 0.025$ for $\lambda_s = 776$ nm, and (b) $S = 2.132 \pm 0.036$ for $\lambda_s = 1.53$ μm , consistent with polarization entanglement of signal and idler fields in both cases. The entangled two-photon state of Eqs. (4.1)(4.2), for $\sin \chi = 2/\sqrt{5}$, has a substantial degree of asymmetry. If

Table 4.1: Measured correlation function $E(\theta_s, \theta_i)$ and S for $\lambda_s = 776$ nm and $\lambda_s = 1.53\mu\text{m}$.

λ_s	θ_s	θ_i	$E(\theta_s, \theta_i)$
776 nm	0°	-67.5°	-0.670 ± 0.011
	45°	-22.5°	-0.503 ± 0.013
	0°	-22.5°	0.577 ± 0.012
	45°	-67.5°	-0.434 ± 0.014
			$S = 2.185 \pm 0.025$
$1.53 \mu\text{m}$	22.5°	45°	-0.554 ± 0.027
	67.5°	0°	-0.682 ± 0.027
	22.5°	0°	0.473 ± 0.024
	67.5°	45°	-0.423 ± 0.029
			$S = 2.132 \pm 0.036$

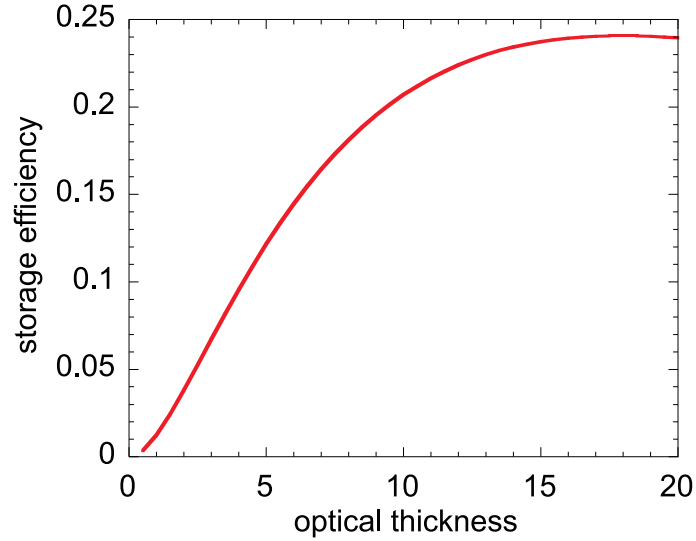


Figure 4.4: Efficiency of storage and subsequent retrieval of a coherent idler field with decay time of 6 ns in an auxiliary atomic ensemble, obtained by numerical integration of the Maxwell-Bloch equations [18, 19] as discussed in the text. The atomic coherence time is assumed to be much longer than the storage time.

oppositely, circularly, polarized pumps I and II were used, the corresponding two-photon state would be symmetric with $\sin \chi = \cos \chi = 1/\sqrt{2}$.

The quantum repeater protocol involves sequential entanglement swapping via Hong-Ou-Mandel (HOM) interference followed by coincidence detection [90, 47]. High-visibility HOM interference requires that the signal and idler photon wave-packets have no entanglement in the time or frequency domains [98, 99, 100]. This may be achieved with excitation pulses that are far detuned from two-photon resonance and with pulse lengths much shorter than the superradiant emission time t_s/d_{th} of level $|e\rangle$.

The idler field qubit is naturally suited for conversion into an atomic qubit encoded into the collective hyperfine coherence of levels $|a\rangle = |5^{1/2}S_{1/2}, F = 3\rangle$ and $|b\rangle = |5^2S_{1/2}, F = 2\rangle$. To perform such conversion, either the same or another similar ensemble/pair of ensembles could be employed [21]. A time-dependent control laser field resonant on the $|b\rangle = |5^2S_{1/2}, F = 2\rangle \leftrightarrow |e\rangle = |5^2P_{3/2}, F = 3\rangle$ transition could selectively convert one of the two frequency components of the idler field, shown in Figure 4.2(a), into a collective atomic qubit. Pulsed excitation should be used in order to enable the synchronization of the idler qubit and the control laser. Numerical simulations show that qubit conversion and subsequent retrieval can be done with good efficiency for moderate optical thicknesses, even though the idler field temporal profile is shorter than those employed in Chapter 8 [21] (compare with Figure 6.3 in Chapter 6 [18]). To demonstrate this, we consider the following scenario in which the idler is stored in an auxiliary ensemble initially polarized in the atomic state $|a, 0\rangle$. The time dependence of the idler field envelope is given by $\varphi^{(i)}(t) \sim \Theta(t) \exp(-t/(2t_s/d_{th}))$ where $\Theta(t)$ is the Heaviside function. A control field of positive helicity (resonant on the $|b\rangle \leftrightarrow |e\rangle$ transition) propagates parallel to the collected idler mode. The control field has an initial Rabi frequency $\Omega_c \equiv \left(e \left\| \hat{\mathbf{d}} \right\| b\right) E_c = 3\Gamma_e$, where E_c is the control electric field amplitude. The control field is smoothly turned off over a period of 20 ns

centered at time $t = 20$ ns, thus storing the idler qubit. We then reactivate the control field at a later time $t = 520$ ns. We numerically calculate the storage and retrieval dynamics using the procedure for solving the Maxwell-Bloch equations outlined in Appendix C. In Figure 4.4, we show the calculated efficiency of storage and subsequent retrieval of a negative helicity idler field with a time constant $t_s/d_{th} = 6$ ns as a function of optical thickness of the auxiliary ensemble. These results indicate that qubit conversion can, indeed, be achieved with reasonable efficiency even though the bandwidth of the idler field is much larger than the spontaneous emission rate of the atoms within the sample.

The basic protocols we have outlined can also be applied to single alkali atom emitters. Similar cascade decays in single atoms were used in early experiments demonstrating violation of local realism [101] and single photon generation [102]. For alkali metal atoms, it is necessary to optically pump the atom into a single Zeeman state, e.g., $m = 0$, of level $|a\rangle$. A virtual excitation of a single Zeeman state of level $|d\rangle$ is created with short laser pulses. Coherent Raman scattering to level $|e\rangle$ results in atom-photon polarization entanglement. In order to prevent spontaneous decay of the level $|e\rangle$, a control field π -pulse is applied immediately after the application of the two-photon excitation, transferring the atomic qubit into the ground state where it could live for a long time. It is important that the π -pulse duration is shorter than the spontaneous lifetime of level $|e\rangle$. Two-photon interference and photoelectric detection of signal photons produced by two remote single atom nodes would result in entanglement of these remote atomic qubits [103]. Qubit detection for single atoms can be achieved with nearly unit efficiency and in a time as short as $50 \mu\text{s}$ [32, 33]. Such high efficiency and speed lead to the possibility of a loophole-free test of Bell's inequality, for atoms separated by about 30 kilometers. Cascaded entanglement swapping between successive pairs of remote entangled atomic qubits may be achieved via local coupling of one of the atoms from the first pair and its neighboring partner

from the the following pair [34].

We also point out that the cascade level scheme employed here can be used to convert a telecommunications photon into a near-infrared photon using four-wave mixing. This could potentially be useful because single-photon detectors for the visible and near-infrared currently have much higher quantum efficiency, and much lower dark count probability, than practically viable (e.g., InGaAs) detectors used at telecommunication wavelengths.

In summary, we have proposed a practical telecommunication quantum repeater scheme based on cascade transitions in alkali metal atoms. We have generated entanglement of a pair of $1.53\text{ }\mu\text{m}$ and 780 nm photons using an ensemble of ultra-cold rubidium atoms. Combined with our recent demonstration of light-to-matter qubit conversion [21], the key steps of our proposal have now been taken.

CHAPTER 5

DETERMINISTIC SINGLE PHOTONS VIA CONDITIONAL QUANTUM EVOLUTION

A source of deterministic single photons is proposed and demonstrated by the application of a measurement-based feedback protocol to a heralded single photon source consisting of an ensemble of cold rubidium atoms. Our source is stationary and produces a photoelectric detection record with sub-Poissonian statistics¹.

5.1 Introduction

Quantum state transfer between photonic- and matter-based quantum systems is a key element of quantum information science, particularly of quantum communication networks. Its importance is rooted in the ability of atomic systems to provide excellent long-term quantum information storage, whereas the long-distance transmission of quantum information is nowadays accomplished using light. Inspired by the work of Duan *et al.* [47], emission of non-classical radiation has been observed in first-generation atomic ensemble experiments [51, 52, 54].

In 2004 the first realization of coherent quantum state transfer from a matter qubit onto a photonic qubit was achieved [57]. This breakthrough laid the groundwork for several further advances towards the realization of a long-distance, distributed network of atomic qubits, linear optical elements and single-photon detectors [17, 18, 20, 19, 21, 22]. A seminal proposal for universal quantum computation with a similar set of physical resources has also been made [104].

¹This chapter is based on Ref. [23]

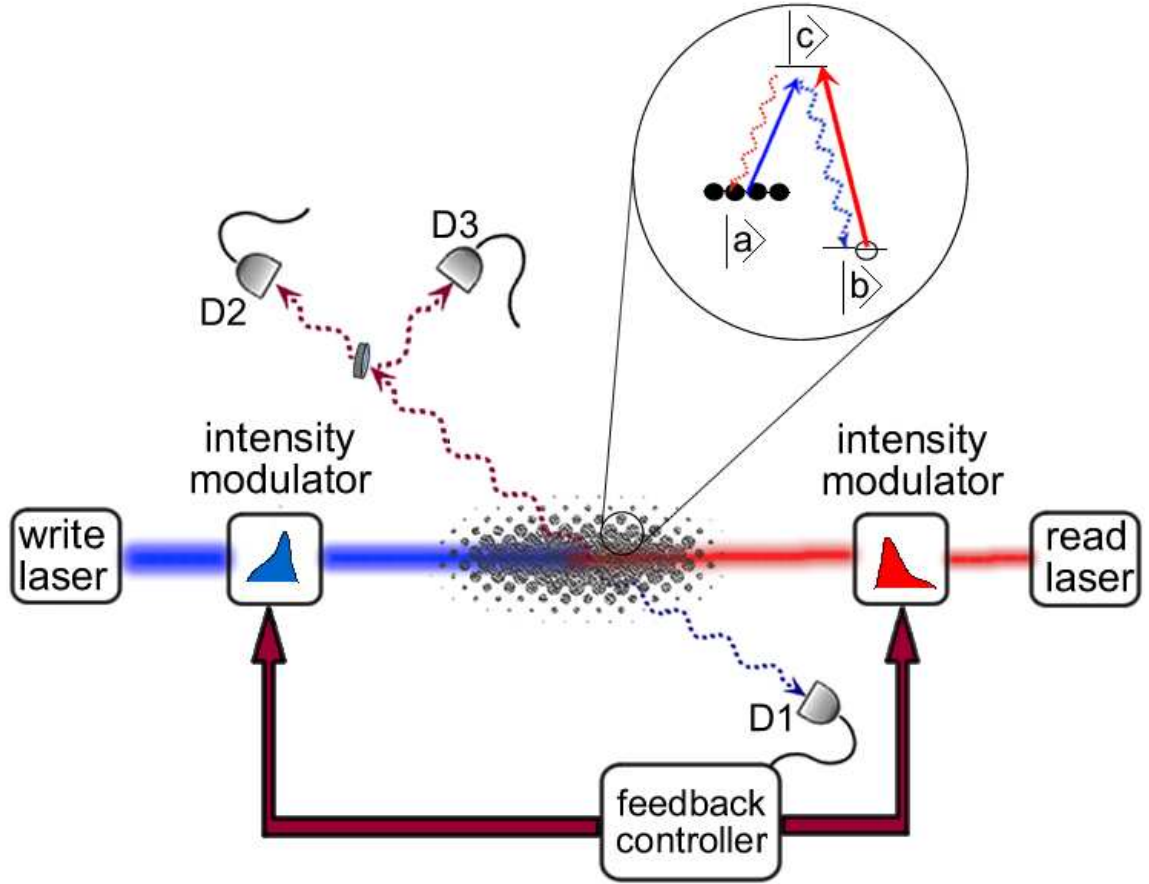


Figure 5.1: Schematic of experimental setup, with the inset showing the atomic level scheme (see text).

An important additional tool for quantum information science is a deterministic source of single photons. Previous implementations of such a source used *single emitters*, such as quantum dots [60, 61, 62], color centers [63, 64], neutral atoms [36, 37, 65], ions [66], and molecules [67]. The measured efficiency η_D to detect a single photon per trial with these sources is typically less than 1%, with the highest reported measured value of about 2.4% [36, 37], to our knowledge.

We propose a deterministic single photon source based on an *ensemble of atomic emitters*, measurement, and conditional quantum evolution. We report the implementation of this scheme using a cold rubidium vapor, with a measured efficiency

$\eta_D \approx 1 - 2\%$. In common with the cavity QED system, our source is suitable for reversible quantum state transfer between atoms and light, a prerequisite for a quantum network. However, unlike cavity QED implementations [36, 37], it is unaffected by intrinsically probabilistic single atom loading. Therefore, it is stationary and produces a photoelectric detection record with truly sub-Poissonian statistics

The key idea of our protocol is that a single photon can be generated at a predetermined time if we know that the medium contains an atomic excitation. The presence of the latter is heralded by the measurement of a scattered photon in a *write* process, such as the collective stimulated Raman scattering process described in Chapter 3. Since this is intrinsically probabilistic, it is necessary to perform independent, sequential *write* trials before the excitation is heralded. After this point one simply waits and reads out the excitation at the predetermined time. The performance of repeated trials and heralding measurements represents a conditional feedback process and the duration of the protocol is limited by the coherence time of the atomic excitation. Our system has therefore two crucial elements: (a) a high-quality probabilistic source of heralded photons, and (b) long atomic coherence times. We note that related schemes using parametric down-conversion have been discussed [105, 106].

Heralded single photon sources are characterized by mean photon number $\langle \hat{n} \rangle \ll 1$, as the unconditioned state consists mostly of vacuum [107, 102]. More importantly, in the absence of the heralding information the reduced density operator of the atomic excitation is thermal [16]. In contrast, its evolution conditioned on the recorded measurement history of the signal field in our protocol, ideally results in a single atomic excitation. However, without exception all prior experiments with atomic ensembles did not have sufficiently long coherence times to implement such a feedback protocol [51, 52, 54, 57, 17, 18, 20, 19, 21, 55, 77, 59, 108]. In earlier work quantum feedback protocols have demonstrated control of non-classical states of light [109] and motion of a single atom [110] in cavity QED.

5.2 *Heralded Single Photon Source*

We first outline the procedure for heralded single photon generation. A schematic of our experiment is shown in Figure 5.1. An atomic cloud of optical thickness ≈ 7 is provided by a magneto-optical trap (MOT) of ^{85}Rb . The ground levels $\{|a\rangle; |b\rangle\}$ correspond to the $5S_{1/2}, F_{a,b} = \{3, 2\}$ hyperfine levels, while the excited level $|c\rangle$ represents the $\{5P_{1/2}, F_c = 3\}$ level of the D_1 line at 795 nm. The experimental sequence starts with all of the atoms prepared in level $|a\rangle$. An amplitude modulator generates a linearly polarized 70 ns long *write* pulse tuned to the $|a\rangle \rightarrow |c\rangle$ transition, and focused into the MOT with a Gaussian waist of about $430\ \mu\text{m}$. We showed in Chapter 3 Section 3.2.1.1 that the *write* process can be described using a simple model based on nondegenerate parametric amplification. The light induces spontaneous Raman scattering via the $|c\rangle \rightarrow |b\rangle$ transition. The annihilation of a *write* photon creates a pair of excitations: namely a signal photon and a quasi-bosonic collective atomic excitation [47]. The scattered light with polarization orthogonal to the *write* pulse is collected by a single mode fiber and directed onto a single photon detector D1, with overall propagation and detection efficiency η_s . When the *write* pulse is sufficiently far detuned from the $|a\rangle \leftrightarrow |c\rangle$ transition, the signal photon has a temporal envelope $\psi_s(t - r_{\parallel}^{(s)}/c)$, where $r_{\parallel}^{(s)} = \hat{k}_s \cdot \vec{r}$ and \hat{k}_s is the signal propagation direction, identical to that of the *write* pulse. The signal envelope satisfies the normalization condition $\int_t^{t+t_0} |\psi_s(t')|^2 dt' = 1$, where t is the time at which the *write* process trial begins, and t_0 is the duration of this trial. By adapting the nondegenerate parametric amplification model of Chapter 3 to the case where only one polarization of the signal is captured, the correlated signal atomic excitation density matrix may be written as [16]

$$\hat{\rho}_{As} = \hat{\Psi}^\dagger(\chi) \hat{\rho}_0 \hat{\Psi}(\chi), \quad (5.1)$$

where

$$\hat{\Psi}(\chi) = \frac{1}{\cosh \chi} \sum_{n=0}^{\infty} \tanh^n \chi \frac{\hat{a}_s^n \hat{A}^n}{n!}, \quad (5.2)$$

$\hat{\rho}_0$ is the signal and atomic vacuum density matrix as given in Eq. (3.2), \hat{a}_s is the annihilation operator for the detected signal photon, and \hat{A} is the atomic excitation annihilation operator.

Starting with the correlated state of signal field and atomic excitation (Eq. (5.1)), we project out the vacuum from the state produced by the *write* pulse using the projection operator : $\hat{1} - e^{-\hat{d}^\dagger \hat{d}}$:, where $\hat{d} = \sqrt{\eta_s} \hat{a}_s + \sqrt{1 - \eta_s} \hat{\xi}_s$, and $\hat{\xi}_s$ is a bosonic operator accounting for degrees of freedom other than those detected. Tracing over the signal and all other undetected modes, we find that the density matrix for the atomic excitation A conditioned on having at least one photoelectric detection event is given by ²

$$\rho_{A|1} = \frac{1}{p_1} \sum_{n=1}^{\infty} \frac{\tanh^{2n} \chi}{\cosh^2 \chi} (1 - (1 - \eta_s)^n) \frac{1}{n!} \hat{A}^{\dagger n} \hat{\rho}_0 \hat{A}^n, \quad (5.3)$$

where $p_1 \ll 1$ is the probability of a signal photoelectric detection event per *write* pulse, and the interaction parameter χ is given in terms of p_1 and η_s by

$$\sinh^2 \chi = p_1 / [\eta_s (1 - p_1)], \quad (5.4)$$

We note that in Eq. (5.3) there is zero probability to find the atomic vacuum $\hat{\rho}_0$.

After a storage time τ , a *read* pulse of length 80 ns containing around 3×10^7 photons, and with polarization orthogonal to that of the *write* pulse, tuned to the $|b\rangle \rightarrow |c\rangle$ transition, illuminates the atomic ensemble (Figure 5.1). Ideally, the *read* pulse converts atomic spin excitations into the idler field emitted on the $|c\rangle \rightarrow |a\rangle$ transition. The elastically scattered light from the *read* beam is filtered out, while the idler field polarization orthogonal to that of the *read* beam is directed into a 50:50 single-mode fiber beamsplitter. Both *write/read* and signal/idler pairs of fields are

²We show in Appendix D that this result can also be derived using arguments based on elementary photon counting probabilities [111].

counter-propagating [59]. The waist of the signal-idler mode in the MOT is about $180 \mu\text{m}$. The two outputs of the fiber beamsplitter are connected to detectors D2 and D3. Electronic pulses from the detectors are gated with 120 ns (D1) and 100 ns (D2 and D3) windows centered on times determined by the *write* and *read* light pulses, respectively. Subsequently, the electronic pulses from D1, D2, and D3 are fed into a time-interval analyzer which records photoelectric detection events with a 2 ns time resolution.

The transfer of atomic excitation to the detected idler field at either Dk ($k=2,3$) is given by a linear optics relation $\hat{a}_k = \sqrt{\eta_i(\tau)/2}\hat{A} + \sqrt{1-\eta_i(\tau)/2}\hat{\xi}_k(\tau)$, where \hat{a}_k depends parametrically on τ and corresponds to a mode with an associated temporal envelope $\phi(t)$, normalized so that $\int_0^\infty dt |\phi(t)|^2 = 1$, and $\hat{\xi}_k(\tau)$ is a bosonic operator which accounts for coupling to degrees of freedom other than those detected. The efficiency $\eta_i(\tau)/2$ is the probability that a single atomic excitation stored for τ results in a photoelectric event at Dk , and includes the effects of idler retrieval and propagation losses, symmetric beamsplitter (factor of 1/2) and non-unit detector efficiency. We start from the elementary probability density $Q_{k|1}(t_c)$ for a count at time t_c and no other counts in the interval $[0, t_c)$, $Q_{k|1}(t_c) = |\phi(t_c)|^2 \langle : \hat{a}_k^\dagger \hat{a}_k \exp(-\int_0^{t_c} dt |\phi(t)|^2 \hat{a}_k^\dagger \hat{a}_k) : \rangle$ [111]. Using Eq. (5.3), we then calculate probability $p_{k|1} \equiv \int_0^\infty dt Q_{k|1}(t)$ that detector Dk registers at least one photoelectric detection event. We similarly calculate the probability $p_{23|1}$ of at least one photoelectric event occurring at both detectors. These probabilities are given by

$$p_{2|1}(\tau) = p_{3|1}(\tau) = \Pi(\eta_i(\tau)/2; p_1, \eta_s), \quad (5.5)$$

$$p_{23|1}(\tau) = p_{2|1}(\tau) + p_{3|1}(\tau) - \Pi(\eta_i(\tau); p_1, \eta_s), \quad (5.6)$$

where we show the explicit dependence on τ . Here $1 - \Pi(\eta; p_1, \eta_s)$ is given by

$$\frac{1}{p_1} \left(\frac{1}{1 + \eta \sinh^2 \chi} - \frac{1}{1 + (\eta_s + \eta(1 - \eta_s)) \sinh^2 \chi} \right). \quad (5.7)$$

These calculations are carried out in more detail in Appendix D.

Our conditional quantum evolution protocol transforms a heralded single photon source into a deterministic one. The critical requirements for this transformation are higher efficiency and longer memory time of the heralded source than those previously reported [17, 18]. In Figure 5.2 we show the results of our characterization of an improved source of heralded single photons. Panel (a) of Figure 5.2 shows the measured intensity cross-correlation function $g_{si} \equiv [p_{2|1} + p_{3|1}]/[p_2 + p_3]$ as a function of p_1 . Large values of g_{si} under conditions of weak excitation - i.e., small p_1 - indicate strong pairwise correlations between signal and idler photons. The efficiency of the signal photon generation and detection is given by $\eta_s \rightarrow g_{si}p_1$, in the limit $\sinh^2 \chi \ll 1$. We have measured $\eta_s \approx 0.08$, which includes the effects of passive propagation and detection losses ϵ_s . It is important to distinguish the *measured* efficiency from the *intrinsic* efficiency which is sometimes employed. The intrinsic efficiency of having a signal photon in a single spatial mode at the input of the single-mode optical fiber $\eta_s^0 \equiv (\eta_s/\epsilon_s) \approx 0.24$. We measure $\epsilon_s \equiv \epsilon_s^f \epsilon_s^t \epsilon_s^d \approx 0.3$ independently using coherent laser light, where the fiber coupling efficiency $\epsilon_s^f \approx 0.7$, optical elements transmission $\epsilon_s^t \approx 0.85$, and the detection efficiency $\epsilon_s^d \approx 0.55$. The measured efficiency of the idler photon detection is $\eta_i \rightarrow g_{si}(p_2 + p_3) \approx 0.075$. Here p_2 and p_3 are defined by expressions analogous to Eq. (5.4). Similarly, the intrinsic efficiency for the idler field $\eta_i^0 \equiv (\eta_i/\epsilon_i) \approx 0.34$, where we measure $\epsilon_i \equiv \epsilon_i^f \epsilon_i^t \epsilon_i^d \approx 0.22$, with $\epsilon_i^f \approx 0.75$, $\epsilon_i^t \approx 0.59$, and $\epsilon_i^d \approx 0.55$. The reported values of $\eta_s \approx 0.08$ and $\eta_i \approx 0.075$ represent slight improvements on the previous highest measured efficiencies in atomic ensemble experiments of $0.04 - 0.07$ [18, 21].

The quality of the heralded single photons produced by our source is assessed using the procedure of Grangier *et al.*, which involves a beamsplitter followed by two single photon counters, as shown in Figure 5.1 [102]. An ideal single-photon input to the beamsplitter results in photoelectric detection at either D2 or D3, but not both. An imperfect single photon input will result in strong anticorrelation of the coincidence

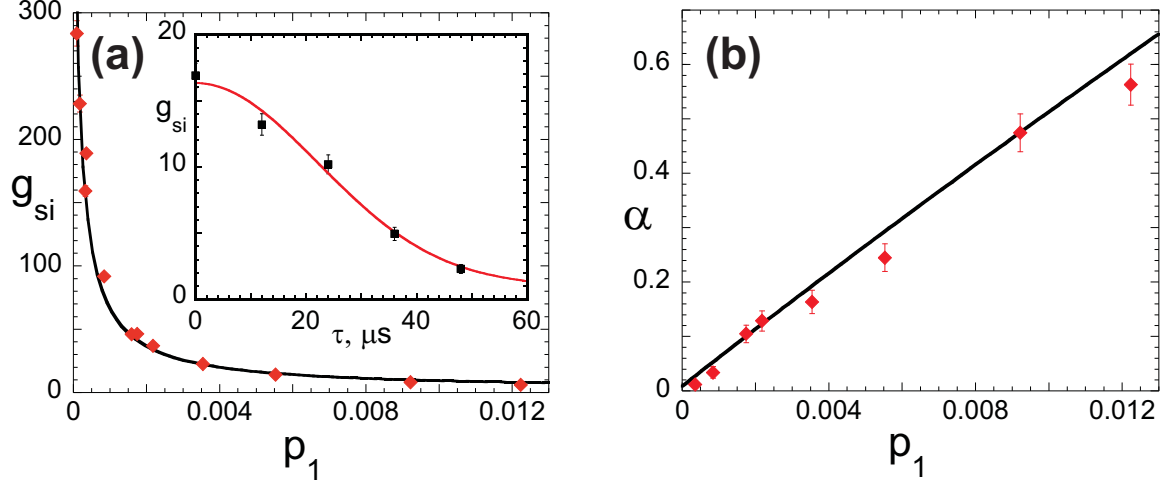


Figure 5.2: Correlation functions g_{si} (panel (a)) and $\bar{\alpha}$ (panel (b)) as a function of p_1 , taken at $\tau = 80$ ns. The solid lines are based on Eq. (5.5,5.6), with addition of a nearly-negligible background contribution, as in Ref. [18]. The inset shows normalized signal-idler intensity correlation function g_{si} as a function of the storage time τ . The full curve is a fit of the form $1 + B \exp(-\tau^2/\tau_c^2)$ with $B = 16$ and the collapse time $\tau_c = 31.5 \mu\text{s}$ as adjustable parameters.

counts. Quantitatively, this is determined by the anticorrelation parameter $\bar{\alpha}$ given by the ratio of various photoelectric detection probabilities measured by the set of detectors D1,D2 and D3: $\bar{\alpha} = p_{23|1}/(p_{2|1}p_{3|1})$. Classical fields must satisfy a criterion $\bar{\alpha} \geq 1$ based on the Cauchy-Schwarz inequality [102]. For an ideally prepared single photon state $\bar{\alpha} \rightarrow 0$. Panel (b) shows the measured values of $\bar{\alpha}$ as a function of p_1 , with $\min\{\bar{\alpha}\} = 0.012 \pm 0.007$ representing a ten-fold improvement on the lowest previously reported value in atomic ensembles [18].

In order to evaluate the atomic memory coherence time τ_c , we measure g_{si} as a function of the storage time τ , inset of Figure 5.2(a). To maximize τ_c , the quadrupole coils of the MOT are switched off, with the ambient magnetic field compensated by three pairs of Helmholtz coils [17]. The measured value of $\tau_c \approx 31.5 \mu\text{s}$, a three-fold improvement over the previously reported value, is limited by dephasing of different Zeeman components in the residual magnetic field [18, 20, 19] as discussed in Chapters 6 and 7.

5.3 Protocol for Generation of Deterministic Single Photons

The long coherence time enables us to implement a conditional quantum evolution protocol. In order to generate a single photon at a predetermined time t_p , we initiate the first of a series of trials at a time $t_p - \Delta t$, where Δt is on the order of the atomic coherence time τ_c . Each trial begins with a *write* pulse. If D1 registers a signal photoelectric event, the protocol is halted. The atomic memory is now armed with an excitation and is left undisturbed until the time t_p when a *read* pulse converts it into the idler field. If D1 does not register an event, the atomic memory is reset to its initial state with a cleaning pulse, and the trial is repeated. The duration of a single trial $t_0 = 300$ ns. If D1 does not register a heralding photoelectric event after N trials, the protocol is halted $1.5 \mu\text{s}$ prior to t_p , and any background counts in the idler channel are detected and included in the measurement record.

Armed with Eqs. (5.5) and (5.6), we can calculate the unconditioned detection and coincidence probabilities for the complete protocol. The probability that the atomic excitation is produced on the j^{th} trial is $p_1 (1 - p_1)^{j-1}$. This excitation is stored for a time $(N - j)t_0$ before it is retrieved and detected, $N = \Delta t/t_0$ is the maximum number of trials that can be performed in the protocol (we ignore the $1.5 \mu\text{s}$ halting period before the read-out).

One can express the probability of a photoelectric event at Dk ($k = 2, 3$), P_k , and the coincidence probabilities P_{23} in terms of the conditional probabilities of Eqs. (5.5) and (5.6),

$$P_\mu = p_1 \sum_{j=1}^N (1 - p_1)^{j-1} p_{\mu|1}(\Delta t - jt_0), \quad (5.8)$$

$\mu = 2, 3, 23$. In the limit of infinite atomic coherence time and $N \rightarrow \infty$, $P_\mu \rightarrow p_{\mu|1}$. Hence, if the memory time is sufficiently long for an adequate number of trials, the protocol ideally results in deterministic preparation of a single atomic excitation,

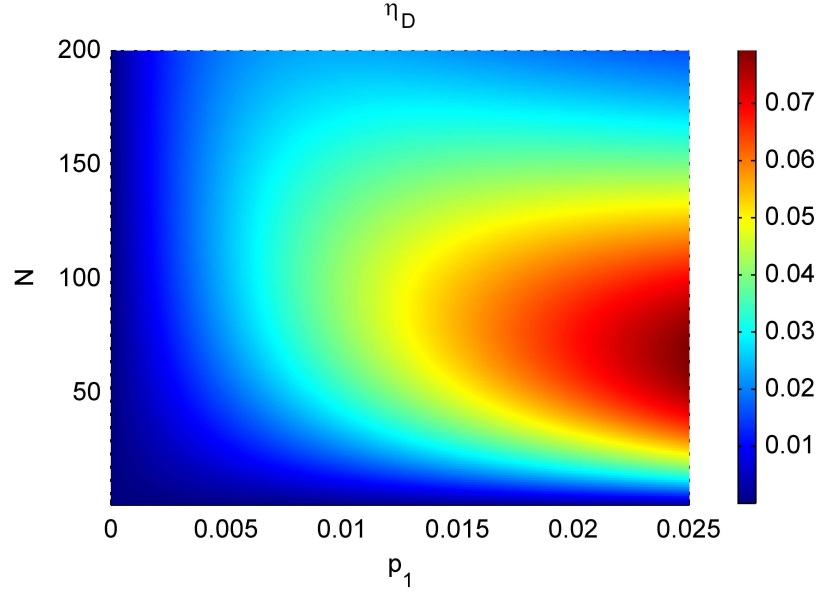


Figure 5.3: Predicted efficiency to generate and detect a single photon η_D as a function of N and p_1 . These predictions are based on Eq. (5.8) with the values of efficiencies and coherence times given in the text.

which can be converted into a single photon at a desired time. Consistent with Figure 5.2(a) inset, we assume a combined retrieval-detection efficiency that decays as a Gaussian function of storage time, $\eta_i(\tau) = \eta_i(0)e^{-(\tau/\tau_c)^2}$, where τ_c is the atomic spin-wave coherence time.

In Figure 5.4 we present the predicted degree of second order coherence for zero time delay $g_D^{(2)}(0) \equiv P_{23}/(P_2P_3)$ [112] as a function of N and p_1 . The corresponding predicted values of efficiency $\eta_D \equiv P_2 + P_3 - P_{23}$ are shown in Figure 5.3. Figure 5.5 shows the measured degree of 2nd order coherence for zero time delay $g_D^{(2)}(0)$ [112] and the measured efficiency η_D as a function of N (panels (a) and (b)), and as a function of p_1 (panels (c) and (d)). The solid curves are based on Eq. (5.8). The dashed lines in panels (a) and (c) show the expected value of $g_D^{(2)}(0) = 1$ for a weak coherent state (as we have confirmed in separate measurements). The particular value of p_1 used in the measurements of Figure 5.5 panels (a) and (b) was chosen with the aid of Figures 5.3 and 5.4 to optimize $g_D^{(2)}(0)$ and η_D . The value of Δt used in panels

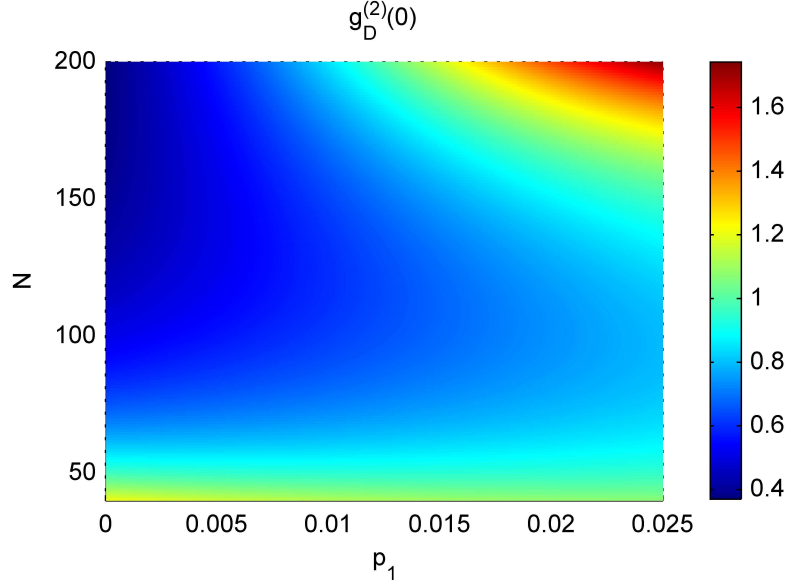


Figure 5.4: Predicted values of η_D as a function of N and p_1 . These predictions are based on Eq. (5.8) with the values of efficiencies and coherence times given in the text.

(c) and (d) was similarly chosen to optimize $g_D^{(2)}(0)$ and η_D . The minimum value of $g_D^{(2)}(0) = 0.41 \pm 0.04$ indicates substantial suppression of two-photon events and under the same conditions $\eta_D = 0.012$ ³. As shown in Figure 5.5(a), when N is small, the protocol does not result in deterministic single photons. Instead, the cleaning pulse-induced vacuum component of the idler field leads to additional classical noise. Large N , and hence long coherence times, are crucial to reduce this noise below the coherent state level and to approach a single photon source. Note, that in the limit of infinite atomic memory and $N \rightarrow \infty$, $g_D^{(2)}(0) \rightarrow \min\{\bar{\alpha}\} \approx 0.012 \pm 0.007$ and $\eta_D \rightarrow \eta_i \approx 0.075$, substantially exceeding the performance of any demonstrated deterministic single photon source.

Moreover, η_D can be further increased by employing atomic sample with larger optical thickness and by optimizing the spatial focusing patterns of the signal and

³The corresponding value of the measured Mandel parameter $Q_D \equiv -\eta_D(1 - g_D^{(2)}(0))$ is $\approx -0.007 \pm 10\%$ and is largely determined by η_D [112].

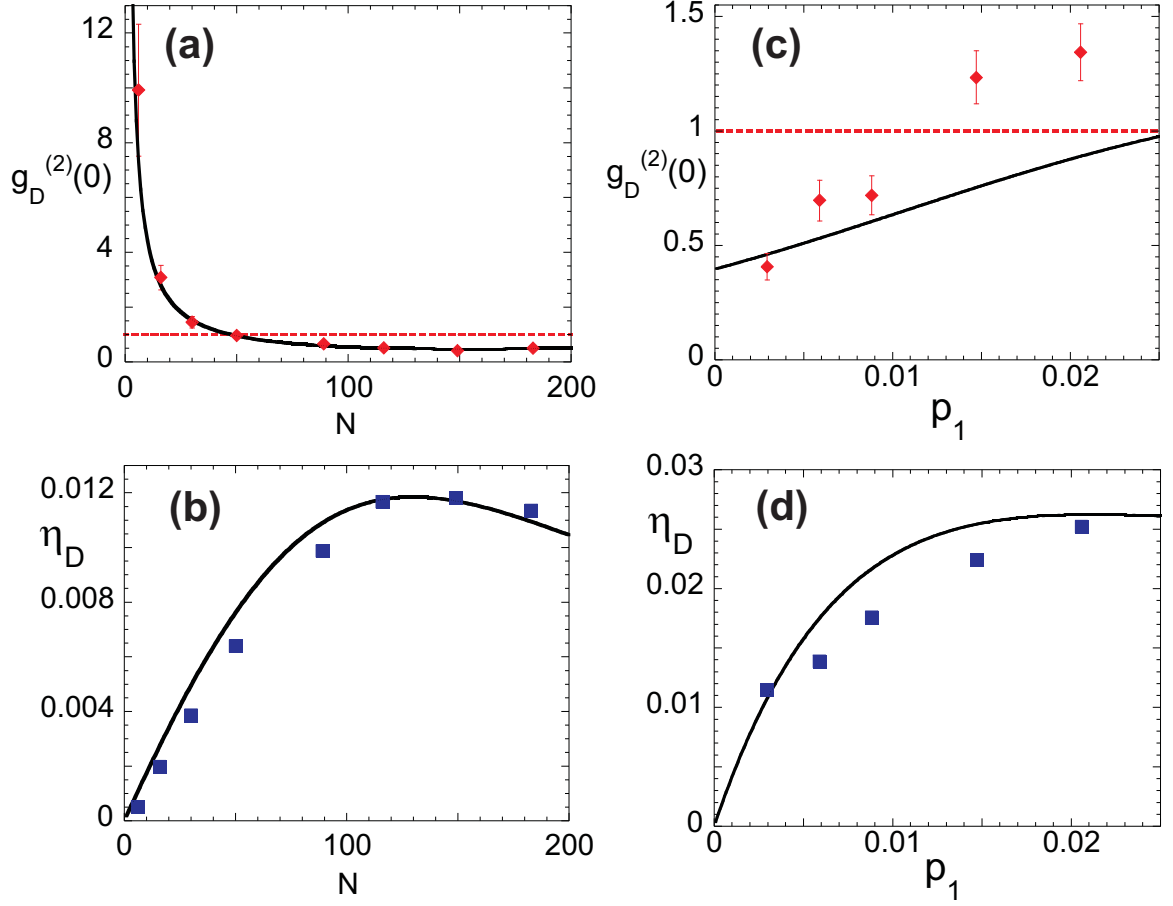


Figure 5.5: $g_D^{(2)}(0)$ as a function of maximum number of trials N (panel (a)) and p_1 (panel (c)); measured efficiency to generate and detect a single photon η_D as a function of N (panel (b)) and p_1 (panel (d)). For panels (a) and (b) $p_1 = 0.003$ (about 6×10^5 photons per *write* pulse were used), whereas for panels (c) and (d) $N = 150$. The full curves are based on Eq. (5.8) with the values of efficiencies and coherence times given in the text, with however η_D multiplied by an empirical factor of $2/3$. We believe this reduced efficiency is due to imperfect switching of the *read* light in the feedback-based protocol (we note that there are no other adjustable parameters in the simple theory presented). Evident deviations from the theory in panels (c) and (d), beyond the statistical uncertainties associated with photoelectric counting events, could be explained either by inadequacies of the theory, or slow systematic drifts in the residual magnetic field and the *read* light leakage.

idler fields⁴. In principle, the spatial signal-idler correlations from an atomic ensemble (and, therefore η_i^0) can also be improved by use of an optical cavity. However, in the absence of special precautions the use of a cavity will itself introduce additional losses associated, e.g., with the mirror coatings or the cavity locking optics [36, 37, 66, 108]. The measured efficiency η_D would involve a trade-off between improved spatial correlations due to the cavity and the concomitant losses that it introduces.

Long atomic coherence time enables a large number of trials N , which is necessary to eliminate the classical fluctuations of the heralded single photon source, and results in sub-Poissonian photon statistics. This can be explained most simply in the limit of infinite atomic memory in which the probability P_k that a detection event at Dk (Figure 5.7) is made after N trials is given by the product of the probability $1 - p_{vac}$ that an atomic excitation has been created (p_{vac} is the probability that the ensemble is in the vacuum state) and $p_{k|1}$ the conditional probability that a photoelectric detection is registered on Dk given that a heralding event was recorded. Likewise, the probability of a coincidence detection at D2 and D3, P_{23} is given in terms of the conditional joint probability $p_{23|1}$ for coincidence given a heralding event has been recorded, i.e.,

$$P_k = (1 - p_{vac})p_{k|1} \quad (5.9a)$$

$$P_{23} = (1 - p_{vac})p_{23|1}, \quad (5.9b)$$

where $p_{vac} = (1 - p_1)^N$ for N trials and $p_1 \ll 1$ is, as defined above, the probability of a signal photoelectric detection in a single write pulse trial. The correlation function $g_D^{(2)}(0)$, is given by

$$\begin{aligned} g_D^{(2)} &\equiv \frac{P_{23}}{P_2 P_3} \\ &= \frac{\bar{\alpha}}{1 - p_{vac}}. \end{aligned} \quad (5.10)$$

⁴In separate sets of measurements, we have observed $\eta_s \approx 0.2$, for the intrinsic signal efficiency $\eta_s^0 \approx 0.6$.

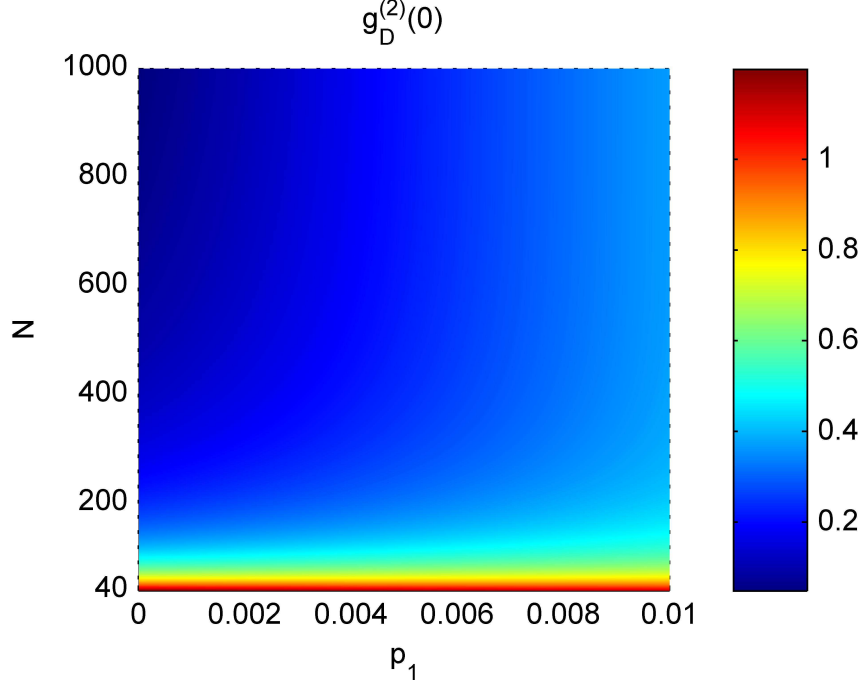


Figure 5.6: $g_D^{(2)}$ as a function of N and p_1 in the limit of infinite atomic memory. The values for the efficiencies η_s and η_i are given in the text.

When the probability p_{vac} is large, as is the case for a small maximum number of trials, N , and since the anti-correlation parameter is by definition positive $\bar{\alpha} > 0$, the presence of multiple atomic excitations combined with the large vacuum component of the detected field gives super-Poissonian statistics. If N is sufficiently large $p_{vac} \rightarrow 0$, however, and we recover a value of $g_D^{(2)}(0)$ identical to the anti-correlation parameter $\bar{\alpha}$, which is less than one for a heralded single photon source. As a consequence the statistics become sub-Poissonian in this limit, and the quality of the protocol is limited by the quality of the single photons produced by the heralded single photon source (Figure 5.6).

We should emphasize that $g_D^{(2)}$ does not tend to $\bar{\alpha}$ in the limit of small N , so the feedback protocol is essential. In the limit of small N one might expect instead that $g_D^{(2)} \rightarrow 2$, consistent with a thermal distribution of atomic excitations. However, this expectation is correct only in the limit of perfect signal propagation and detection

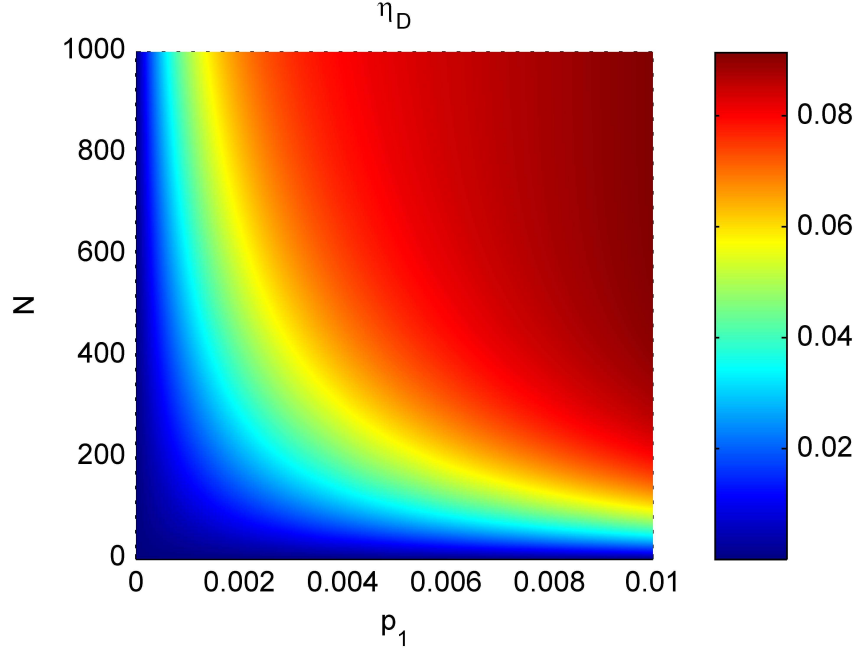


Figure 5.7: η_D as a function of N and p_1 in the limit of infinite atomic memory. The values for the efficiencies η_s and η_i are given in the text.

efficiency $\eta_s \rightarrow 1$. This can be readily demonstrated using the atomic density operator given in Eq. (5.3). However, for $\eta_s \ll 1$ one finds $g_D^{(2)} \gg 2$, as confirmed in our experiments.

In conclusion, we have proposed and demonstrated a stationary source of deterministic photons based on an ensemble of cold rubidium atoms.

CHAPTER 6

STORAGE AND RETRIEVAL OF SINGLE PHOTONS TRANSMITTED BETWEEN REMOTE QUANTUM MEMORIES

In the previous chapters, we have explored the use of atomic ensembles interacting with classical laser fields to produce non-classical states of light. We reported the probabilistic generation of entangled qubits in Chapters 3 and 4. While in Chapter 5, we showed how the heralded (probabilistic) single photon source used to generate entangled qubits in Chapter 3 could be exploited in the generation of deterministic single photons. Here, we demonstrate how the light-ensemble interface and the idea of Electromagnetically Induced Transparency (EIT) [71, 72] is used to implement another essential primitive of a quantum network: a quantum memory element, in which the nonclassical states of light discussed in the earlier chapters can be stored and later retrieved¹.

6.1 Introduction

An elementary quantum network operation involves storing a qubit state in an atomic quantum memory node, and then retrieving and transporting the information through a single photon excitation to a remote quantum memory node for further storage or analysis. Implementations of quantum network operations are thus conditioned on the ability to realize such matter-to-light and/or light-to-matter quantum state mappings. Here, we report generation, transmission, storage and retrieval of single

¹This chapter is based on Ref. [18] and the associated supplementary online information

quanta using two remote atomic ensembles. A single photon is generated from a cold atomic ensemble at Site *A* via the protocol of Duan, Lukin, Cirac, and Zoller (DLCZ) [47] and is directed to Site *B* through a 100 meter long optical fiber. The photon is converted into a single collective excitation via the dark-state polariton approach of Fleischhauer and Lukin [69]. This mechanism is described in detail in Appendix C. After a programmable storage time the atomic excitation is converted back into a single photon. This is demonstrated experimentally, for a storage time of 500 nanoseconds, by measurement of an anticorrelation parameter $\overline{\alpha}$. Storage times exceeding ten microseconds are observed by intensity cross-correlation measurements. The length of the storage period is two orders of magnitude longer than the time to achieve conversion between photonic and atomic quanta. The controlled transfer of single quanta between remote quantum memories constitutes an important step towards distributed quantum networks.

A quantum network, consisting of quantum nodes and interconnecting channels, is an outstanding goal of quantum information science. Such a network could be used for distributed computing or for the secure sharing of information between spatially remote parties [5, 25, 26, 29, 104, 47]. While it is natural that the network’s fixed nodes (quantum memory elements) could be implemented by using matter in the form of individual atoms or atomic ensembles, it is equally natural that light fields be used as carriers of quantum information (flying qubits) using optical fiber interconnects. The matter-light interface seems inevitable since the local storage capability of ground state atomic matter cannot be easily recreated with light fields. Interfacing material quanta and single photons is therefore a basic primitive of a quantum network.

The potential of atomic ensembles to serve as quantum memories has recently attracted considerable attention [68, 41, 69, 47, 13, 70], spawning two distinct lines of research. In one, using the physics of “slow light” propagation in an optically thick atomic ensemble, weak coherent laser pulses have been stopped and retrieved in a

controlled fashion [69, 73, 44, 45]. In the other, motivated by the seminal proposal of Duan, Lukin, Cirac, and Zoller (DLCZ) [47], correlated pairs of photons and single photons have been produced from an atomic ensemble [51, 52, 53, 54, 55, 59]. Collective atomic qubits, atom-photon entanglement, and quantum state transfer from atomic to photonic qubits have also been demonstrated [57]. These initial experimental demonstrations within the DLCZ paradigm were beset by short atomic coherence times, of the order of the laser pulse length. In contrast, recent advances in atomic ensemble research [17, 23] allow for long quantum memory times, in excess of ten microseconds in the present work, more than two orders of magnitude longer than the duration of the laser pulses involved in the protocols. Longer quantum memory times have subsequently been produced and reported in Ref.[23], as discussed in Chapter 5.

6.2 *Experiment*

Here we report the synthesis of these two lines of research by demonstrating the generation, transmission, storage and retrieval of single photons using remote atomic ensembles as quantum memories. The essential ingredient which enables the completion of this synthesis, and which we report here, is the ability to convert single photons into single collective atomic excitations. In our experiment the remote quantum memories are based on cold atomic clouds of ^{85}Rb confined in magneto-optical traps (MOTs) at Sites A and B , as shown in Figure 6.1. Sites A and B are physically located in adjacent laboratories, with a 100 meter long single-mode optical fiber serving as the quantum information channel.

Our protocol begins with the generation of single photons at Site A , using an improved version of the DLCZ approach in the off-axis, counter-propagating geometry [59, 17] (discussed in Chapter 3). The fiber channel directs the signal field to Site B where an optically thick atomic ensemble is prepared in level $|b\rangle$ (right inset in Figure 6.1). The signal field propagation in the atomic medium is controlled by

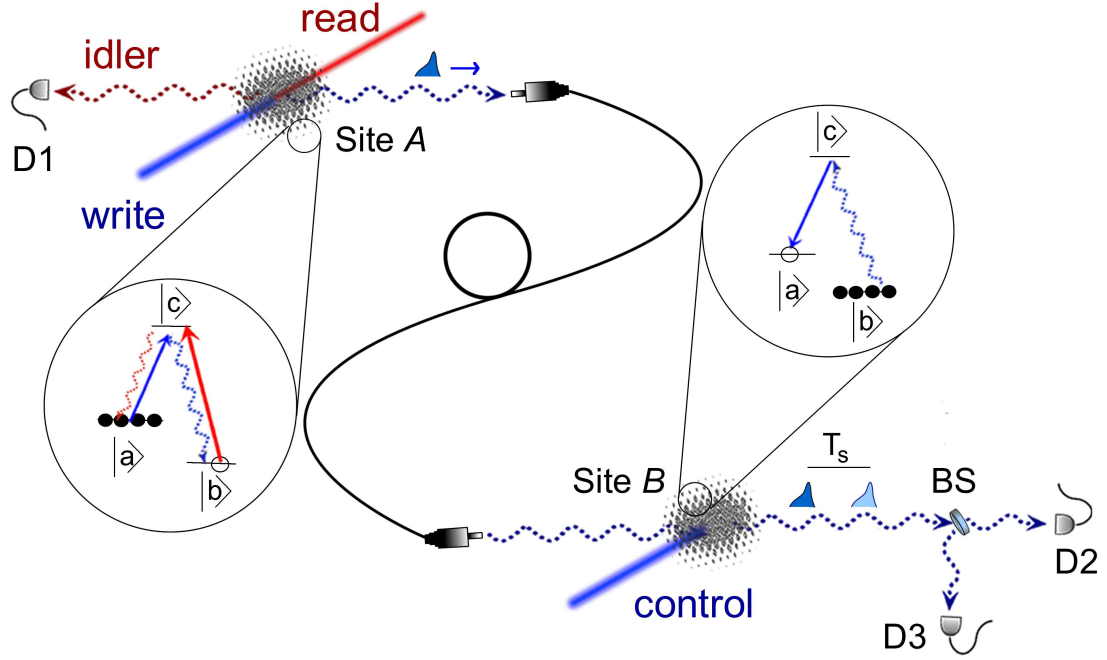


Figure 6.1: A schematic diagram of our experimental setup demonstrating generation, transmission, storage and retrieval of single photon excitations of the electromagnetic field. Two atomic ensembles at Sites *A* and *B* are connected by a single-mode fiber. The insets show the structure and the initial populations of atomic levels for the two ensembles. All the light fields responsible for trapping and cooling, as well as the quadrupole magnetic fields in both MOTs, are shut off during the period of the protocol. The ambient magnetic field at each Site is compensated by three pairs of Helmholtz coils (not shown). Correlated signal and idler fields are generated at Site *A*. The signal field is transmitted via optical fiber from Site *A* to Site *B*, where it is converted to atomic excitation, stored for a duration T_s , and subsequently retrieved. A Hanbury Brown-Twiss setup consisting of a beamsplitter BS and two detectors D2 and D3, together with detector D1 for the idler field, are used to verify the single photon character of the retrieved field.

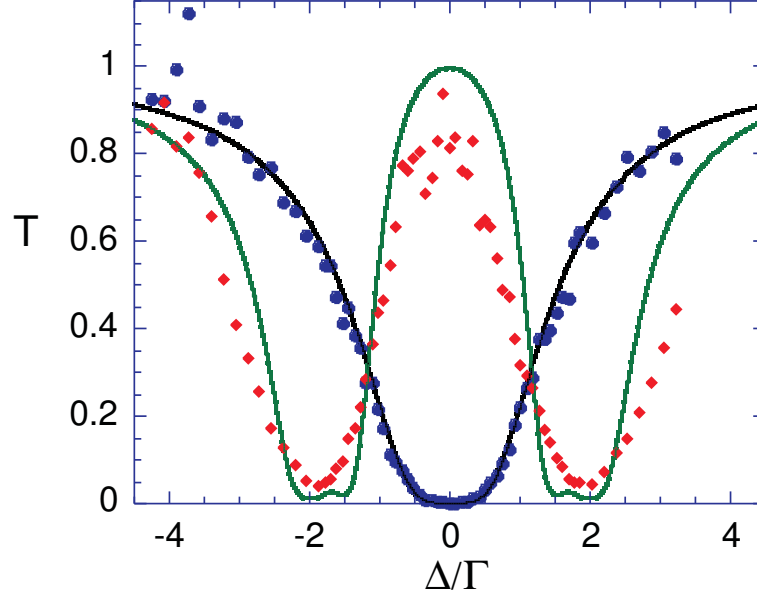


Figure 6.2: Measured transmission spectra of a coherent probe field as the function of probe detuning in the presence of, and absence of, EIT. Data are taken using 700 ns long coherent laser pulses. T is the intensity transmittance, Δ is the probe detuning and Γ is the decay rate of level $|c\rangle$. In the absence of *control* field (circles) the probe is strongly absorbed near resonance, whereas with the *control* field on (diamonds) the medium becomes transparent. Each probe pulse contains on average 0.3 photons. Each data point is an average of 2×10^5 experimental trials. The optical thickness $d = 8$ and the *control* field Rabi frequency $\Omega = 3\Gamma$ are used to obtain the solid curves, based on the theoretical model discussed in Appendix C.

an additional laser field (*control*) through the process of electromagnetically-induced transparency (EIT) [71, 72]. As we deal with an unpolarized atomic ensemble, we must take into account the Zeeman degeneracy of the atomic levels. Choosing the same circular polarizations for both the probe and the *control* fields allows us to retain transparency, as discussed in more detail in Appendix C. In Figure 6.2 we show the EIT transmission spectrum recorded for a coherent laser probe field instead of the signal field. Evidently, in the absence of the *control* light the probe field is absorbed by the optically thick sample. With the addition of the cw *control* field, the medium is rendered transparent around the $|b\rangle \leftrightarrow |c\rangle$ transition resonance $\Delta = 0$.

The *control* field strongly modifies the group velocity of the signal field. For a

time-dependent *control* field, a strong reduction of the group velocity of the propagating signal field can be understood in terms of a coupled matter-light field excitation known as a “dark-state polariton.” By adiabatically switching off the *control* field, the coupled excitation can be converted into a pure atomic excitation, i.e., the signal field is “stopped” [69, 44, 45]. An important condition to achieve storage is a sufficiently large optical thickness of the atomic sample, which enables strong spatial compression of the incident signal field [41]. In our experiment the measured optical thickness $d \simeq 8$, where d is defined such that $\exp(-d)$ is the on-resonance intensity transmittance in the absence of a control field. Figure 6.3 compares our observations with the predictions of a theoretical model of Appendix C. Figure 6.3a compares the propagation of the signal pulse in vacuum and in the atomic medium under conditions of EIT with a cw *control* field. The observed pulse delay under conditions of EIT is about 20 ns, corresponding to more than three orders of magnitude reduction in group velocity. Figure 6.3b shows the effect of turning off the *control-storage* field when the signal pulse is approximately centered in the medium, and the subsequent retrieval of the signal field when the *control-retrieval* field is switched back on after a 500 ns storage time. Figure 6.3c shows retrieval after a storage time of 15 μ s. Qualitative agreement of the pulse shapes has been obtained in our theoretical analysis of the protocol using the full Zeeman structure of the atoms and a classical description of the signal field (Figure 6.3d-f).

In order to verify the single-photon character of the signal field (a) without storage, and (b) with storage and retrieval, we use a Hanbury Brown-Twiss detection scheme, employing a beamsplitter followed by two single photon counters, as shown in Figure 6.1 [102]. To provide such characterization, we note that classical fields must satisfy a criterion $\bar{\alpha} \geq 1$ based on the Cauchy-Schwarz inequality [102, 113]. For an ideally prepared single photon state $\bar{\alpha} \rightarrow 0$. Here the anticorrelation parameter $\bar{\alpha}$ is a function of the storage time T_s , and is given by the ratio of various photoelectric

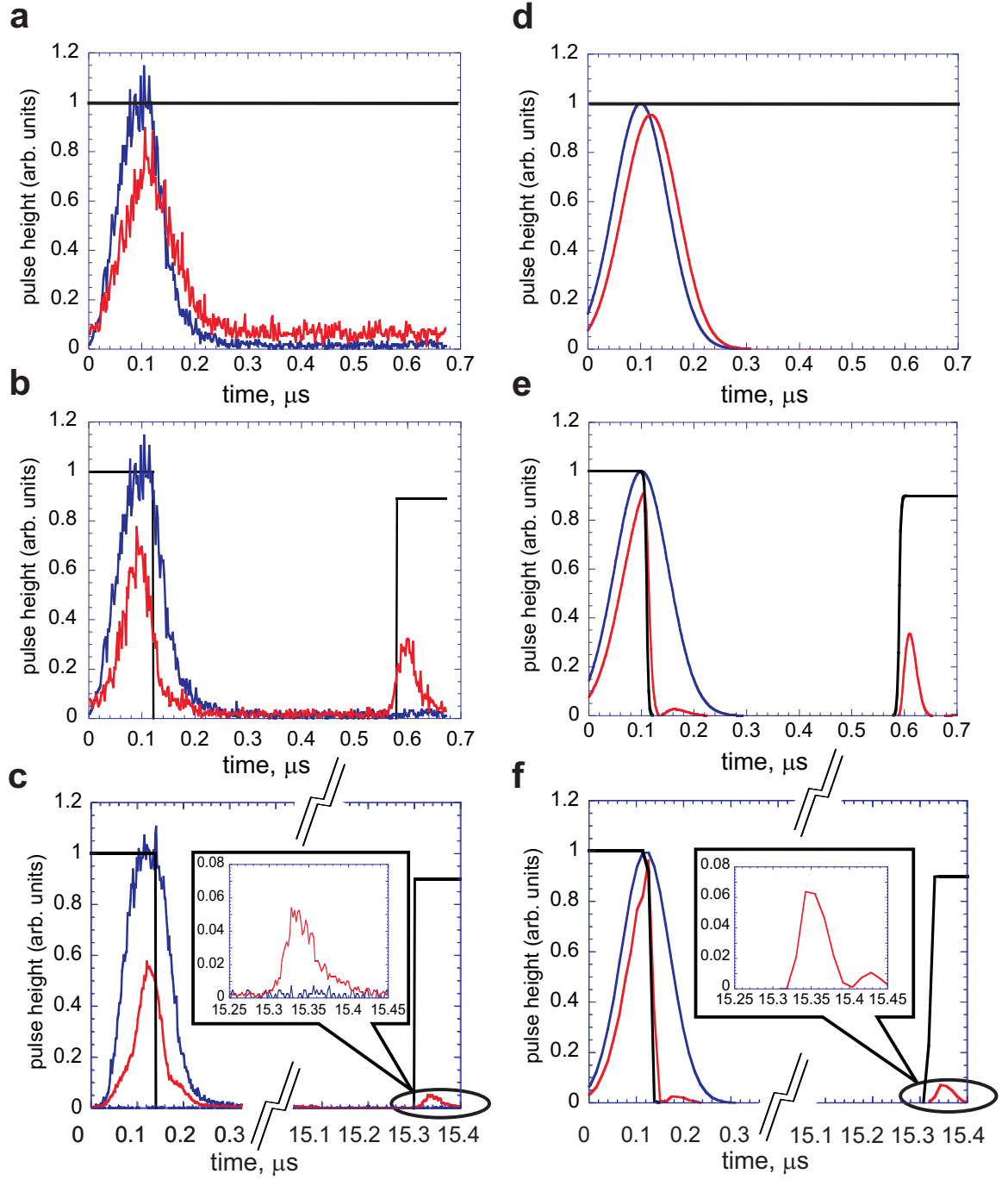


Figure 6.3: Experimental and theoretical pulse shapes as a function of time, showing EIT, storage and retrieval. The color code is: *control* field - black, pulse in vacuum - blue, delayed, stored and retrieved field - red. Panel (a) with a cw *control* field shows EIT pulse delay. In panel (b) the *control* field is switched off and then on again after 500 ns, shows light storage and retrieval. Panel (c) is similar to (b) but with a 15 μ s storage. Panels (d), (e), and (f) are corresponding theoretical plots.

detection probabilities which are measured by the set of detectors D1, D2 and D3 (described in Section 6.3):

$$\overline{\alpha}(T_s) = \frac{p_1 p_{123}}{p_{12} p_{13}}. \quad (6.1)$$

As an auxiliary measure of signal-idler field correlations, and as a way to quantify the quantum memory storage time, we also evaluate the normalized intensity cross-correlation function $g_{si} \equiv (p_{12} + p_{13})/[p_1(p_2 + p_3)]$ [114, 90]. In particular, it serves to estimate the total efficiency and background levels in the experiment, since g_{si} is, by definition, independent of efficiencies whereas p_1 is proportional to the overall idler channel efficiency.

First we measure g_{si} and $\overline{\alpha}$ without storage at Site B (i.e., with no atomic sample in place), and the results are displayed in Figure 6.4, a and b, respectively. Next we add an optically thick atomic sample at Site B , and perform storage of duration $T_s = 500$ ns and subsequent retrieval of the signal field, with results shown in Figure 6.4, c and d, respectively. No correction for background or dark counts were made to any of the experimental counting rates. The curve fits of g_{si} are based on a simple theoretical model, and allow us to obtain the efficiency in the idler channel and the background contributions to p_2 and p_3 for the stored signal field. These same values are used to produce the corresponding theoretical curves in Figure 6.4, b and d. The measured values of $\overline{\alpha} < 1$, displayed in Figure 6.4, b and d, confirm the single-photon character of both the source and retrieved signal fields (with the minimum values of $\overline{\alpha} = 0.14 \pm 0.11$ and $\overline{\alpha} = 0.36 \pm 0.11$, respectively). Overall, we estimate that the probability p_s for successful generation, transmission, storage, retrieval, and detection of a signal photon is approximately $p_s \simeq 10^{-5}$ for each trial. The efficiency of photon storage and retrieval E can be estimated as the ratio of the values of $p_2 + p_3$ with and without storage. We find $E \simeq 0.06$, in agreement with the theoretical result shown in Figure 6.3e.

To investigate the storage capability of our quantum memory at Site B , we measure

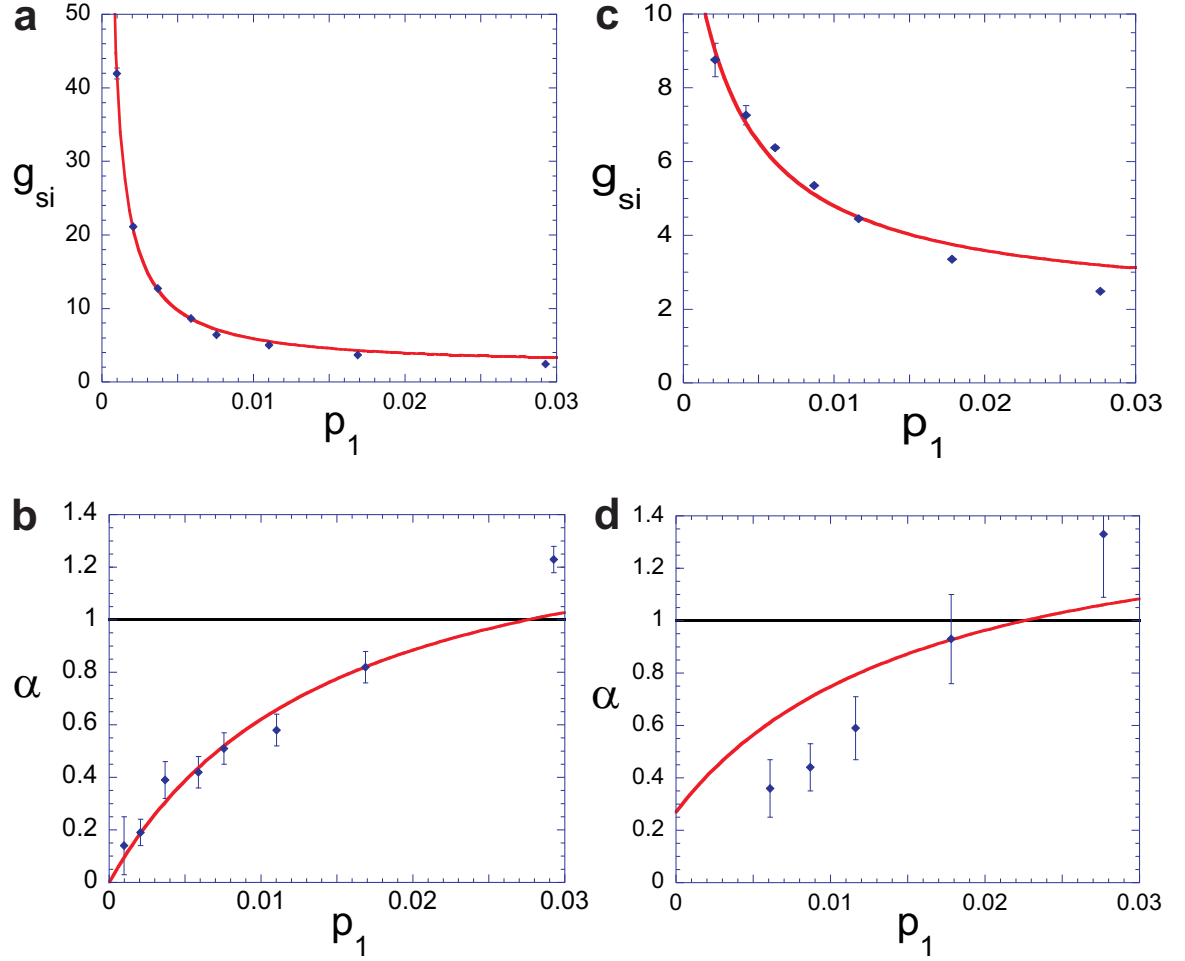


Figure 6.4: Measured intensity cross-correlation function g_{si} and anticorrelation function α as a function of the idler photoelectric detection probability p_1 . Panels (a) and (b) are for the source (propagation in vacuum). Panels (c) and (d) are for stopped, stored for 500 ns, and retrieved signal field. The solid lines are based on a theoretical model that includes losses and background. Error bars represent \pm one standard deviation and are based on the statistics of the photoelectric counting events.

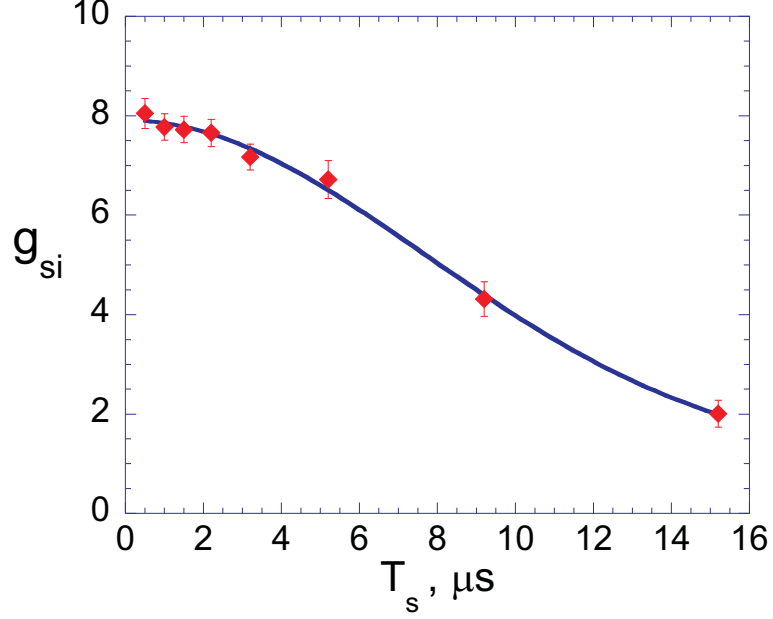


Figure 6.5: Normalized signal-idler intensity correlation function g_{si} as a function of the storage time T_s at Site B . Data (diamonds) are taken for $p_1 = 0.0047$, but with a smaller background contribution than that of Figure 6.4, c and d. The full curve is a fit of the form $1 + B \exp(-t^2/\tau^2)$ with $B = 7$ and the collapse time $\tau = 11 \mu\text{s}$ as adjustable parameters. Error bars represent \pm one standard deviation and are based on the statistics of the photoelectric counting events.

g_{si} as a function of the storage time of the signal field T_s (Figure 6.5). A Gaussian fit provides a time constant $\tau = 11 \mu\text{s}$, which is an estimate of our quantum memory time. The collapse is consistent with the Larmor precession of a dark-state polariton in an unpolarized atomic ensemble in a residual magnetic field [51, 57]. Experimentally we attempt to null the uniform, dc component of the magnetic field. A definitive way to distinguish whether the collapse is due to uniform or non-uniform and ac fields is to measure the damping time of the periodic revivals of the retrieved signal field at longer storage times. In a uniform magnetic field, undamped revivals of the dark-state polariton should occur at times equal to nT_L , where T_L is the Larmor period for level $|a\rangle$ or $|b\rangle$ and n can be either integer or half-integer, depending on the direction of the magnetic field relative to the light beam geometry (a synopsis of these ideas is given in the Appendix C, with the full theory presented in Ref.[19]). We have

conducted separate experiments with an externally applied magnetic field [20], which suggest that the collapse in the present experiment is likely due to magnetic field gradients and/or ac fields at the level of a few tens of mG. However, more extensive investigations to quantitatively determine the temporal and spatial structure of the residual magnetic field, and the various contributions to it, are ongoing.

6.3 *Measurement Procedure*

To generate single photons at Site *A*, we use the DLCZ approach in the off-axis, counter-propagating geometry introduced by Harris and coworkers [59]. The insets in Figure 6.1 indicate schematically the structure of the three atomic levels involved, $|a\rangle$, $|b\rangle$ and $|c\rangle$, where $\{|a\rangle; |b\rangle\}$ correspond to the $5S_{1/2}$, $F = \{3, 2\}$ levels of ^{85}Rb , and $|c\rangle$ represents the $\{5P_{1/2}, F = 3\}$ level associated with the D_1 line at 795 nm. The experimental sequence begins with an unpolarized sample of atoms prepared in level $|a\rangle$ (left inset of Figure 6.1). A 160 ns long *write* laser pulse tuned to the $|a\rangle \rightarrow |c\rangle$ transition is focused into the MOT with a Gaussian waist of about 400 μm . The *write* pulse generates a Raman-scattered signal field via the $|c\rangle \leftrightarrow |b\rangle$ transition. We collect a Gaussian mode centered around the momentum \vec{k}_s that forms an angle of about 2° with the *write* beam. The *write* pulse is so weak that on average less than one photon is scattered into the collected mode for each pulse. The signal field is coupled into the 100 meter long fiber connecting Sites *A* and *B*.

For each signal photon emission event, a correlated collective atomic excitation is created in the atomic ensemble. After a delay $\Delta t = 200$ ns, a 140 ns long counter-propagating *read* laser pulse resonant with the $|b\rangle \rightarrow |c\rangle$ transition illuminates the atomic ensemble and converts the atomic excitation into the idler field. Under the conditions of collective enhancement, the idler field is emitted with high probability into the mode determined by the phase-matching condition $\vec{k}_i = \vec{k}_w + \vec{k}_r - \vec{k}_s$, where \vec{k}_i , \vec{k}_w and \vec{k}_r are the wave vectors of the idler, *write* and *read* fields, respectively.

The waist of the signal-idler mode in the MOT is about $150\text{ }\mu\text{m}$. The idler field is directed onto a single photon counter D1. Ideally, photoelectric detection of the idler field projects the quantum state of the signal field into a single photon state. The repetition rate of the experiment is $2 \cdot 10^5\text{ s}^{-1}$. Each data point in Figure 6.4 involves an average over a time period that varied from several minutes up to 1.5 hours for the data point with the lowest value of p_1 in d.

To measure the photoelectric detection probabilities $p_1, p_2, p_3, p_{13}, p_{12}, p_{23}$, and p_{123} , the outputs of the detectors are fed to three “Stop” inputs of the time-interval analyzer which records the arrival times with a 2 ns time resolution. The electronic pulses from the detectors D1,D2,D3 are gated for periods $[t_0^i, t_0^i + T_g^i]$, with $T_g^1 = 140\text{ ns}$, $T_g^2 = T_g^3 = 240\text{ ns}$, respectively, centered on the times determined by the *write* and *read* (for no storage) or *control-retrieval* (for storage) laser pulses. Counts recorded outside the gating periods are therefore removed from the analysis. The list of recorded events allows us to determine the single-channel photoelectric event probabilities $p_i = N_i/M$, where N_i is the total number of counts in the i -th channel and M is the number of experimental trials, (for D_i , $i = 1, 2, 3$). If photoelectric detections in different channels i, k, m happen within the same gating period, they contribute to the corresponding joint probabilities $p_{ij} = N_{ij}/M$, where N_{ij} is the total number of coincidences between D_i and D_j , $i, j = 1, 2, 3$. The joint probability of all three detectors registering a count is given by $p_{123} = N_{123}/M$.

6.4 Photoelectric counting statistics

In order to take into account the possibility of the creation of multiple signal-idler photon pairs created in the *write-read* processes at site A , we use a theoretical model based on parametric down-conversion derived in Chapter 3, Section 3.2.1.1. The

annihilation operators for the idler and signal field are transformed as [90]:

$$\begin{aligned}\hat{a}_i^{(out)} &= \cosh(\chi)\hat{a}_i^{(in)} + \sinh(\chi)\hat{a}_s^{\dagger(in)}, \\ \hat{a}_s^{(out)} &= \cosh(\chi)\hat{a}_s^{(in)} + \sinh(\chi)\hat{a}_i^{\dagger(in)}.\end{aligned}\tag{6.2}$$

Here χ is the Raman gain at Site A. We also wish to assess the overall efficiencies and the background levels in our experiment. Modeling the background to the signal in terms of a coherent field with average photon number B_s , we find that in the low intensity limit discussed in Appendix D

$$g_{si} \approx \frac{\langle \hat{a}_i^{(out)\dagger} \hat{a}_s^{(out)\dagger} \hat{a}_s^{(out)} \hat{a}_i^{(out)} \rangle}{\langle \hat{a}_s^{(out)\dagger} \hat{a}_s^{(out)} \rangle \langle \hat{a}_i^{(out)\dagger} \hat{a}_i^{(out)} \rangle}\tag{6.3}$$

$$= \frac{(1 + 2 \sinh^2(\chi)) + B_s}{\sinh^2(\chi) + B_s}.\tag{6.4}$$

We also determine the anticorrelation parameter $\bar{\alpha}$ of Grangier *et al.* (in the weak intensity limit of Appendix D) [102]:

$$\bar{\alpha} \approx \frac{\langle \hat{a}_s^{(out)\dagger 2} \hat{a}_i^{(out)\dagger} \hat{a}_i^{(out)} \hat{a}_s^{(out) 2} \rangle \langle \hat{a}_i^{(out)\dagger} \hat{a}_i^{(out)} \rangle}{\langle \hat{a}_i^{(out)\dagger} \hat{a}_s^{(out)\dagger} \hat{a}_s^{(out)} \hat{a}_i^{(out)} \rangle^2}\tag{6.5}$$

$$= \frac{\sinh^2(\chi)(4 + 6 \sinh^2(\chi)) + 4B_s(1 + 2 \sinh^2(\chi))}{(1 + 2 \sinh^2(\chi) + B_s)^2}.\tag{6.6}$$

Using the treatment of Appendix D, we find that in the low intensity limit, the singles count rates at detectors D1, D2, and D3 are given by $R_1 = \epsilon_1 \sinh^2(\chi)$, $R_2 = |T|^2 \epsilon_2 \sinh^2(\chi)$ and $R_3 = |R|^2 \epsilon_3 \sinh^2(\chi)$ (assuming that $R_i \ll W$, where W is the repetition rate of the experiment); T and R are the transmission and reflection coefficients of the beamsplitter BS, shown in Figure 6.6.

In the absence of the medium we empirically find negligible background B_s . The solid curve in Figure 6.4A is based on this model, setting $B_s = 0$. We find that the best fit to the data in Figure 6.4A is given by $\epsilon_1 \approx 0.039$. The solid line in Figure 6.4B is based on Eq. (6.6) with this value of ϵ_1 .

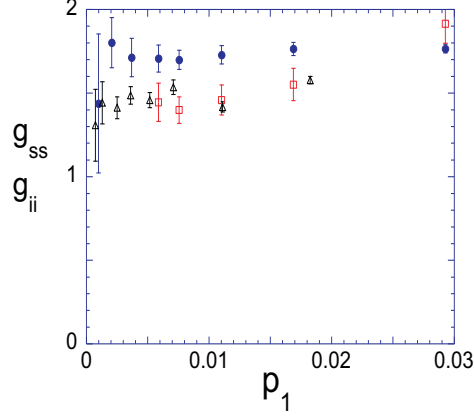


Figure 6.6: Normalized intensity autocorrelation functions g_{ii} (triangles) and g_{ss} (circles for the source, squares for the stored and retrieved field). Uncertainties are based on the statistics of the photon counting events.

For the stored light, we have to account for the fact that a significant fraction of detected signal photons are due to background associated with the *control-retrieval* pulse. By fitting the data of Figure 6.4C to Eq. (6.4), we find $B_s \approx 0.08$. Substituting this value into Eq. (6.6), we obtain the solid curve in Figure 6.4D. In order to reduce this background, we have performed initial investigations using an optically pumped Rb cell to filter out light at the frequency of the control field. In this case we found increased non-classical correlations between the idler and the stored and retrieved signal photon, e.g., for $T_s = 500$ ns g_{si} increased from 8 ± 0.2 to 15.6 ± 1.4 .

In addition, we measure the intensity autocorrelation functions $g_{ss} = p_{23}/[p_2 p_3]$ and g_{ii} . These are shown in Figure 6.1. In order to evaluate the latter, we insert a beamsplitter and additional detector D_a into the path of the idler photon, so that $g_{ii} = p_{1a}/[p_1 p_a]$. Using these together with the measured values of g_{si} shown in Figure 6.4 of Ref.[18], one can evaluate Clauser's parameter $R = g_{si}^2/[g_{ss} g_{ii}]$. For classical fields $R \leq 1$, whereas we observe strong violation of this inequality.

The total measured transmission and detection efficiencies for the idler and signal fields respectively are $w_i = 0.25 \pm 0.03$ and $w_s = 0.15 \pm 0.02$, consisting of the quantum efficiencies of the detectors 0.55 ± 0.05 and the passive transmission losses accounting

for the rest. The ratio of $h \equiv \epsilon_i/w_i = 0.16$ indicates the strength of the spatial signal-idler correlations in our source of conditional single photons at Site A , with $h \rightarrow 1$ for the ideal case.

6.5 *Conclusion*

We have demonstrated generation, storage and retrieval of single quanta transmitted between two remote atomic ensembles serving as quantum memory elements. The control of the matter-field interface at the level of single quanta, and at remote sites, is encouraging for further developments and applications in quantum information science. In particular, the storage of a photonic qubit, with two logical states, would represent a crucial advance. In order to achieve this, the quantum memory at Site B would likewise need a second logical state, so as to realize a collective atomic qubit. Two different approaches for such qubits have already been demonstrated [57, 17]. If a second logical state were added to both quantum memories at Sites A and B , generation of remote entanglement of two atomic qubits would be possible.

CHAPTER 7

DARK-STATE POLARITON COLLAPSES AND REVIVALS

In this chapter¹, we investigate the dynamics of dark-state polaritons in an atomic ensemble with ground-state degeneracy. A signal light pulse may be stored and retrieved from the atomic sample by adiabatic variation of the amplitude of a control field. This procedure was used to obtain the results of the previous chapter in which single photons were stored and retrieved from an atomic medium. During the storage process, a magnetic field causes rotation of the atomic hyperfine coherences, leading to collapses and revivals of the dark-state polariton number. In Section 7.2, we predict that these collapses and revivals are observable in measurements of the retrieved signal field, as a function of storage time and magnetic field orientation.

We test this prediction in the experiments reported in Section 7.3. Both coherent and single photon states of light are stored in, and retrieved from a cold atomic gas by time dependent variation of a control field. The observed series of collapses and revivals of measured retrieval efficiency as a function of storage time agrees very well with our theoretical predictions.

This strong agreement lends credence to the proposition that the quantum memory coherence times in the previous chapters are limited by the presence of ambient magnetic fields.

¹This chapter is based on Refs. [19, 20]

7.1 *Introduction*

A quantum memory element consisting of an ensemble of atoms, with efficient coupling to a signal light field, represents a node in several quantum network architectures [69, 47, 41, 48, 49]. A dark-state polariton (DSP) is a collective excitation, with light field and atomic spin wave parts, in which the relative size of the light and matter contributions can be varied by changing the amplitude of a control laser field [69]. In connection with atomic memories, DSPs offer the possibility for efficient transfer of information between a light carrier and an atomic medium, with programmable storage of the excitation in the atomic spin coherence. The storage and subsequent retrieval of the signal field component of the DSP can be achieved by the extinction and subsequent reactivation of the control field after a given storage time. Experimental demonstrations of “stopped-light” can be understood in terms of the concept of DSP in just this way [44, 45, 74].

In Chapter 6 the storage and retrieval of single photons using an atomic ensemble based quantum memory was reported, with a storage time conjectured to be limited by inhomogeneous broadening in the ambient magnetic field [18]. During the storage, the DSP consists entirely of atomic spin-wave, and in order to understand its dynamics in a magnetic field it is necessary to properly account for the atomic level degeneracy and the signal and control field polarizations. In particular for alkali atoms, which have non-zero nuclear spin, the electronic levels have hyperfine structure (see Chapter 2). In this case we must define a more general form of DSP field operator than that of a simple lambda configuration, in which the atomic spin-wave part corresponds to a particular superposition of hyperfine coherences of the ground electronic level. These coherences are, in turn, intimately related to the phenomenon of electromagnetically-induced transparency (EIT) [71, 72, 115, 116].

The remarkable protocol of Duan, Lukin, Cirac, and Zoller (DLCZ) provides a

measurement-based scheme for the creation of atomic spin excitations [47]. In systems where EIT is operative, these excitations will in general contain a dark-state polariton component. The orthogonal contribution may be regarded as a bright-state polariton in that it couples dissipatively to the excited atomic level in the presence of the control field [75]. Observation of the retrieved signal field, however, picks out the dark state polariton part, while the orthogonal component is converted into spontaneous emission [19]. A number of previous works reported generation and subsequent retrieval of DLCZ collective excitations [51, 52, 53, 55, 54, 57, 59, 17, 117]. Several of these studies investigated the decoherence of these excitations in cold atomic samples [51, 54, 57, 17, 117]. It has been similarly conjectured in these works that the decay of the coherence was due to spin precession in the ambient magnetic field. While the observed decoherence times are consistent with the residual magnetic fields believed to be present, the observation of revivals predicted in Section 7.2 [19] would be solid proof that Larmor precession is indeed the current limitation on the quantum memory lifetime. Moreover, controlled revivals could provide a valuable tool for quantum network architectures that involve collective atomic memories.

We shall see that in a magnetic field the temporal evolution of the DSP reveals a series of collapses and revivals due to the evolution of its spin-wave component during the storage phase of the process. In Section 7.2, we predict that the collapses and revivals should be directly observable in measurements of the retrieved signal field as a function of storage time. This prediction is then verified experimentally in Section 7.3.

7.2 Theory

We develop the theory of EIT in a degenerate atomic medium with ground levels $|b\rangle$ and $|a\rangle$ and excited level $|c\rangle$, which have energies $\hbar\omega_b \equiv 0$, $\hbar\omega_a$ and $\hbar\omega_c$, respectively (Figure 7.1). The Zeeman states of level $|b\rangle$ are written $|b, m\rangle$, where $-F_b \leq m \leq F_b$;

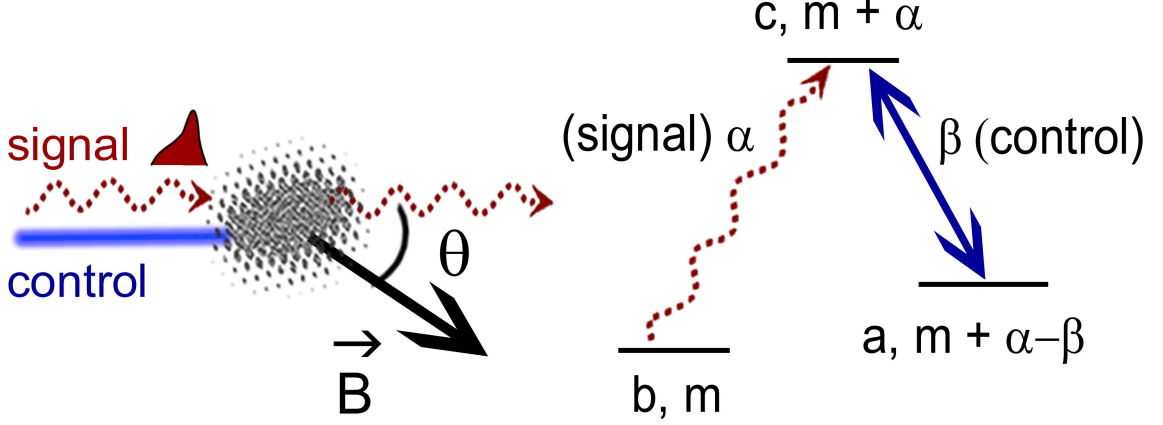


Figure 7.1: On the left, a diagram shows an atomic ensemble interacting with copropagating signal and control fields. The signal (helicity α), resonant on the $|b\rangle \leftrightarrow |c\rangle$ transition, is stored and subsequently retrieved by variation of a control field (helicity β), which resonantly couples levels $|a\rangle$ and $|c\rangle$. A constant magnetic field \vec{B} , oriented at an angle θ from the propagation axis, rotates the atomic coherences during the storage. For each state $|b, m\rangle$ in level $|b\rangle$, there is either an associated Λ configuration, as shown on the right, or an unconnected one, as discussed in the text. The signal connects the states $|b, m\rangle$ and $|c, m + \alpha\rangle$, while the control field drives transitions between $|c, m + \alpha\rangle$ and $|a, m + \alpha - \beta\rangle$.

similar definitions hold for the other levels. All N atoms are assumed to be initially prepared in level $|b\rangle$ without polarization, i.e., the density matrix of atom μ is $\hat{\rho}_\mu = \sum_m p |b, m\rangle_\mu \langle b, m|$ where we write $p = 1/(2F_b + 1)$. The atoms experience a uniform magnetic field \vec{B} oriented at an angle θ with respect to the light propagation z axis. The magnetic field-atom interaction $\hat{V}_B = \mu_B \vec{B} \cdot \sum_{s=b,a,c} g_s \sum_{\mu=1}^N \hat{\mathbf{F}}_s^\mu$, where $\hat{\mathbf{F}}_s^\mu$ is the projection of the atomic angular momentum operator for atom μ onto level $|s\rangle$ and g_s is the corresponding Landé g factor. The magnetic field induces a Larmor spin precession which is primarily important in the storage phase, when the signal field amplitude is zero. In a pure three state system, a magnetic field has been used to manipulate the phase of a stored light pulse [74]. We note that in prior work collapses and revivals of single-atom Zeeman coherences have been observed[118, 119].

We assume the signal field has a carrier wave vector $\vec{k}_s = [(\omega_c - \omega_b)/c]\hat{z}$, a time

independent transverse spatial profile $\phi^{(s)}(\vec{r})$, which satisfies the normalization condition $\int d^2 r_{\perp}^{(s)2} |\phi^{(s)}(\vec{r})|^2 = 1$, where for a vector \vec{v} , $\vec{v}_{\perp}^{(s)} \equiv \vec{v} - \hat{k}_s \cdot \vec{v}$. The positive frequency component of the signal electric field is given in the interaction picture by

$$\hat{\mathbf{E}}_s^{(+)}(\vec{r}, t) = (2\pi)^{3/2} \mathcal{E}(ck_s) e^{i\vec{k}_s \cdot \vec{r}} e^{-ick_s t} \phi^{(s)}(\vec{r}) \sum_{\alpha=\pm 1} \vec{\xi}_{\alpha} \hat{\varphi}_{\alpha}^{(s)}(z, t), \quad (7.1)$$

where $\hat{\varphi}_{\alpha}^{(s)}(z, t)$ is the linear photon density annihilation operator for signal photons at position $z = \vec{r} \cdot \hat{z}$ and helicity α . These photon density operators obey the bosonic equal time commutation relations

$$\left[\hat{\varphi}_{\alpha}^{(s)}(z, t), \hat{\varphi}_{\beta}^{(s)\dagger}(z', t) \right] = \delta_{\alpha, \beta} \delta(z - z'). \quad (7.2)$$

Their definitions in terms of plane wave operators is given in Eq. (2.63) of Chapter 2.

A control field of helicity β propagates nearly parallel to the z -axis with a wave vector $\vec{k}_c = [(\omega_c - \omega_a)/c] \hat{k}_c$. We will make the paraxial approximation on the control field helicities $\vec{e}_{\beta}(\hat{k}_c) \approx \vec{\xi}_{\beta}$, where $\vec{\xi}_{\alpha}$ are the laboratory fixed spherical basis vectors (Eq. (2.31)). We allow the freedom in the choice of control field propagation direction so that we may adequately describe the off axis configuration used in the experiments described in Section 7.3. The positive frequency component of the classical control field is given by

$$\vec{E}_c^{(+)}(\vec{r}, t) \equiv \vec{e}_{\beta}(\hat{k}_c) e^{i\vec{k}_c \cdot \vec{r}} e^{-ick_c t} E_c(t), \quad (7.3)$$

where $E_c(t)$ is the slowly varying control electric field. We assume E_c is constant over the width of the transverse spatial profile of the signal. Furthermore, we assume $E_c(t)$ varies sufficiently slowly that we may consider it constant over the length of the ensemble.

We proceed by generalizing the perturbative treatment of Fleischhauer and Lukin [75] to include the degenerate atomic level scheme and the presence of a magnetic field. We assume the number of photons contained in the signal pulse is much less than the number of atoms in the sample, and we retain only terms up to first order in

the signal field amplitude. In this limit, we can neglect the populations of levels $|c\rangle$ and $|a\rangle$, as well as the coherences between these levels. Furthermore, for an initially unpolarized sample in level $|b\rangle$, the ground state populations and *Zeeman* coherences, as opposed to hyperfine coherences, are unaffected by the signal, control and magnetic fields. Our treatment can be extended to an initially spin-polarized atomic sample, as we will report in a separate publication. We show in Appendix C that in this weak signal limit [69, 75], the signal field, which we assume propagates in the positive z direction, and collective atomic coherence operators satisfy the quantum Langevin equations

$$\left(\frac{\partial}{\partial t} + c\frac{\partial}{\partial z}\right) \hat{\varphi}_\alpha^{(s)}(z, t) = i\sqrt{n(z)} p \kappa_s^* \sum_{m=-F_b}^{F_b} C_{m\alpha} \hat{e}_{m; m+\alpha}(z, t), \quad (7.4a)$$

$$\frac{d}{dt} \hat{s}_{m; m'}(z, t) = i\Omega_c(t) C'_{m'\beta} \hat{e}_{m; m'+\beta}(z, t), \quad (7.4b)$$

and

$$\begin{aligned} \left(\frac{d}{dt} + \frac{\Gamma_c}{2}\right) \hat{e}_{m; m'}(z, t) &= i\kappa_s \sqrt{n(z)} p \sum_{\alpha=-1}^1 C_{m\alpha} \delta_{m'; m+\alpha} \hat{\varphi}_\alpha^{(s)}(z, t) \\ &+ i\Omega_c(t) C'_{m'-\beta, \beta} \hat{s}_{m; m'-\beta}(z, t) \\ &+ \delta_{m', m+\alpha} \hat{\zeta}_{b, m; c, m+\alpha}(z, t), \end{aligned} \quad (7.4c)$$

where the atomic number density $n(z)$ is assumed to be a function only of the propagation distance z , κ_s is the signal field coupling constant on the probe transition, and $\Omega_c(t) = E_c(t) \left(c \left\| \hat{\mathbf{d}} \right\| a\right)$ is the control field Rabi frequency which we assume is real. We adopt the shorthand for the Clebsch-Gordan coefficients $C_{m\alpha} \equiv C_{m \alpha}^{F_b \ 1 \ F_c}$ and $C'_{m\beta} \equiv C_{m \beta}^{F_a \ 1 \ F_c}$; it is useful to define $R_{m\alpha}(\beta) = C_{m\alpha}/C'_{m+\alpha-\beta, \beta}$. The collective optical coherence is defined

$$\hat{e}_{m; m'}(z, t) \equiv \frac{1}{\sqrt{n(z)} p} \sum_{\mu=1}^N e^{-ik_s z_\mu} \phi^{(s)*}(\vec{r}_\mu) \tilde{\sigma}_{b, m; c, m'}^\mu(t) \delta(z - z_\mu), \quad (7.5)$$

and the collective hyperfine coherences are given by

$$\hat{s}_{m; m'}(z, t) \equiv \frac{1}{\sqrt{n(z)} p} \sum_{\mu=1}^N \phi^{(s)*}(\vec{r}_\mu) e^{i(\vec{k}_c - \vec{k}_s) \cdot \vec{r}_\mu} \tilde{\sigma}_{b, m; a, m'}^\mu(t) \delta(z - z_\mu). \quad (7.6)$$

It is shown in Appendix C, that, in the weak signal limit, these collective coherence operators obey the quasi-bosonic commutation relations

$$[\hat{e}_{m_1; m'_1}(z, t), \hat{e}_{m_2; m'_2}(z', t)] = [\hat{e}_{m_1; m'_1}(z, t), \hat{s}_{m_2; m'_2}(z', t)] = 0, \quad (7.7a)$$

$$[\hat{s}_{m_1; m'_1}(z, t), \hat{s}_{m_2; m'_2}(z', t)] = [\hat{s}_{m_1; m'_1}(z, t), \hat{e}_{m_2; m'_2}^\dagger(z', t)] = 0, \quad (7.7b)$$

$$[\hat{e}_{m_1; m'_1}(z, t), \hat{e}_{m_2; m'_2}^\dagger(z', t)] = \delta_{m_1, m'_1} \delta_{m_2, m'_2} \delta(z - z') + \hat{O}(1/\sqrt{N}), \quad (7.7c)$$

and

$$[\hat{s}_{m_1; m'_1}(z, t), \hat{s}_{m_2; m'_2}^\dagger(z', t)] = \delta_{m_1, m'_1} \delta_{m_2, m'_2} \delta(z - z') + \hat{O}(1/\sqrt{N}). \quad (7.7d)$$

The decay rate of level $|c\rangle$ is denoted by Γ_e and $\hat{\zeta}_{b, m; c, m'}$ is a corresponding quantum noise operator. The coupling of the atoms to the uniform magnetic field can be taken into account by the addition of appropriate commutators with the interaction \hat{V}_B in the atomic equations.

We first establish some standard features of EIT with our model. The propagation of a classical (coherent) signal through the medium is found by dropping the quantum noise operator, and replacing the field and coherence operators with their respective expectation values. For a constant amplitude control field, the linear susceptibility for the signal field of angular frequency ω is found to be

$$\chi_\alpha(\Delta) \approx \frac{c}{2\omega_c} d'(z) \sum_m \frac{\Gamma_c \Delta X_{m\alpha}^2 (\Omega_c^2 C_{m+\alpha-\beta, \beta}^2 - \Delta^2 + i\Delta\Gamma_c/2)}{(\Omega_c^2 C_{m+\alpha-\beta, \beta}^2 - \Delta^2)^2 + (\Delta\Gamma_c/2)^2}, \quad (7.8)$$

where $\Delta \equiv \omega - \omega_c$ is the detuning of the signal from atomic resonance, $X_{m\alpha} \equiv C_{m\alpha}/\sqrt{(2F_c + 1)/3}$, and $d'(z) = dd(z)/dz$. The dimensionless quantity $d(z)$ is the optical thickness, which is defined such that $\exp(-d)$ is the on-resonance intensity transmittance in the absence of a control field, and can be expressed as

$$d(z) = 2\pi w \left(\int_{-\infty}^z dz' n(z') \right) \left(\frac{c}{\omega_e} \right)^2 \frac{2F_c + 1}{2F_b + 1} \quad (7.9)$$

where w is the fraction of atoms in excited level $|c\rangle$ that spontaneously decay into ground level $|b\rangle$. When a control field is present, an EIT window exists provided that

the Clebsch-Gordan coefficients $C'_{m+\alpha-\beta,\beta}$ do not vanish for any $-F_b \leq m \leq F_b$ for which $C_{m\alpha} \neq 0$. If, however, $C'_{m+\alpha-\beta,\beta} = 0$, and $C_{m\alpha} \neq 0$, it means that there is an excited state $|c, m + \alpha\rangle$ not coupled by the control field to a state in the ground level $|a\rangle$, i.e., there is an unconnected lambda configuration. The subset of atoms initially in the state $|b, m\rangle$ would absorb the signal field and spontaneously emit radiation as if there were no control field present. In order for EIT to exist, one must make a judicious choice of atomic levels and signal and control field polarizations.

Assuming a choice of polarizations that supports EIT, we are able to generalize the adiabatic treatment of Ref. [69] to Eq. (7.4) to derive the DSP operator for helicity α , with control field polarization β (see Appendix C)

$$\hat{\Psi}_\alpha(z, t) = \frac{\Omega_c^*(t) \hat{\varphi}_\alpha^{(s)}(z, t) - \sqrt{n(z) p \kappa_s^*} \sum_m R_{m\alpha}(\beta) \hat{s}_{m; m+\alpha-\beta}(z, t)}{\sqrt{|\Omega_c(t)|^2 + n(z) p |\kappa_s|^2 \sum_m |R_{m,\alpha}(\beta)|^2}}. \quad (7.10)$$

As in Ref.[69], this operator obeys the simple propagation equation $(\partial/\partial t + v_g \partial/\partial z) \hat{\Psi}_\alpha(z, t) = -(1/2) \hat{\Psi}_\alpha(\partial/\partial z) v_g$ with the reduced group velocity $v_g = c\Omega_c^2/(\Omega_c^2 + Np|\kappa_s|^2 \sum_m |R_{m\alpha}(\beta)|^2)$ which can be adiabatically controlled by time dependent variation of $\Omega_c(t)$. From the definition of $\hat{\Psi}$, we see that as Ω_c goes to zero, the wave excitation stops propagating and transforms into a particular linear combination of hyperfine coherences $\sim \sum_m R_{m\alpha}(\beta) \hat{s}_{m; m+\alpha-\beta}(z, t)$. This nontrivial result arises from the treatment of the full degeneracy of the atomic ensemble; only this combination of hyperfine coherences is adiabatically transformed into the signal field *via* the control field retrieval process. Orthogonal combinations of hyperfine coherences couple to optical coherences in the presence of the control field and result in excited state spontaneous emission; we will refer to these as the bright-state polariton (BSP) component. It is also possible that some population of atoms remains trapped in the ground states, and is unaffected by the control field.

One can also show that the DSP behaves like a bosonic field. When the DSP operator exists for polarizations α and β , the DSP operators obey the commutation

relations

$$\left[\hat{\Psi}_\alpha(z, t), \hat{\Psi}_\beta(z', t) \right] = 0 \quad (7.11)$$

$$\left[\hat{\Psi}_\alpha(z, t), \hat{\Psi}_\beta^\dagger(z', t) \right] = \delta_{\alpha, \beta} \delta(z - z') + \hat{O}(1/\sqrt{N}). \quad (7.12)$$

In order to demonstrate the importance of the dark state polariton in the signal storage and retrieval process in a magnetic field, we numerically solve Eqs. (7.4) for a coherent signal field using the Fourier space propagation equation (Eq. (C.51)) of Section C.5 in Appendix C. We thus calculate the expectation values of the spin wave coherences $\langle \hat{s}_{m; m+\alpha-\beta}(z, t) \rangle$ and the signal field, allowing us to determine the DSP and BSP components. This is accomplished by defining a vector space of $2F_b + 2$ dimensions, with orthonormal basis vectors \mathbf{e}_m , each corresponding to a hyperfine coherence $\hat{s}_{m; m+\alpha-\beta}$, and \mathbf{e}_φ corresponding to the signal field. We define the coherence “vector” $\mathbf{v} \equiv \langle \hat{\varphi}_\alpha^{(s)} \rangle \mathbf{e}_\varphi + \sum_m \langle \hat{s}_{m; m+\alpha-\beta}(z, t) \rangle \mathbf{e}_m$. We note that this is not normalized since its magnitude is dependent on both the time dependent signal and control fields. Associated with the DSP we define a vector $\mathbf{u}_\Psi \equiv \Omega_c \mathbf{e}_\varphi + \sqrt{Np}\kappa_s \sum_m R_{m\alpha}(\beta) \mathbf{e}_m$ and the corresponding unit vector $\mathbf{e}_\Psi = \mathbf{u}_\Psi / \|\mathbf{u}_\Psi\|$. We then determine the DSP component $p_D = |\mathbf{e}_\Psi^* \cdot \mathbf{v}|^2$, and BSP component $p_B = \|\mathbf{v} - \mathbf{e}_\Psi \mathbf{e}_\Psi^* \cdot \mathbf{v}\|^2$.

As an example of signal storage and retrieval we consider an atomic sample of ^{85}Rb , in which the control field and signal field polarizations are chosen equal $\alpha = \beta = 1$, and the optical thickness $d = 8$, Figure 7.2. The atomic levels $|b\rangle$, $|a\rangle$ and $|c\rangle$ correspond to the $5^2S_{1/2} F = 2, 3$ and $5^2P_{3/2} F = 3$ levels of the D_2 line, respectively. The spontaneous decay rate $\Gamma_c/(2\pi) = 5.98$ MHz. The incident signal field has a Gaussian envelope of full width half maximum 120 ns, and the peak enters the 3 mm long sample at $t = -60$ ns. The control field has a constant Rabi frequency $\Omega_c = 1.5\Gamma_c$ until it is smoothly turned off at $t = 0$ over a period of 20 ns, when a fraction of the signal field is converted into hyperfine coherences of the atomic spin wave. The excitation is stored from $0 \leq t \leq 2 \mu\text{s}$ in the presence of the magnetic field,

before the control field is reactivated, and the signal field retrieved. In Figure 7.2, panels (A) and (B), the magnetic field is chosen so that the storage time corresponds to a quarter of a Larmor period $T_L \equiv 2\pi\hbar/|g_g\mu_B\vec{B}|$, while in panels (C) and (D), the storage time is $T_L/2$. In panel (A) p_D grows as the signal pulse arrives at the point of observation, and reaches a peak when the control field is switched off. It then decays during the storage phase, due to Larmor precession of the hyperfine coherences in the applied magnetic field, which causes the corresponding growth of p_B . When the control field is reactivated, p_B decays rapidly due excited level coupling and subsequent spontaneous emission, though p_D remains finite as the spin wave coherence of the DSP is converted into the forward propagating signal field; the retrieved signal field intensity is illustrated in panel(B). In panel (C), where the storage time is $T_L/2$, p_D undergoes a complete revival. The energy of the retrieved signal field shown in panel (D) is therefore much larger, by a factor of 5.73, than that in panel (B). This is in good agreement with the DSP theory for retrieval efficiency discussed later, which predicts that the retrieved signal energy of panel (D) should be 5.53 times that in panel (B). These results demonstrate the importance of the adiabatic concept of DSP for a realistic experimental scenario. The retrieved signal field directly reflects the DSP dynamics in the magnetic field.

We can predict the retrieval efficiency of a stored signal pulse by tracking the population of the DSP as it evolves under the influence of the magnetic field. During the storage, the evolution of the spin wave operators is given by $\hat{s}_{m; m+\alpha-\beta}(z, t) = \sum_{m_1=-F_g}^{F_g} \sum_{m_2=-F_{g'}}^{F_{g'}} \mathcal{D}_{m_1 m}^{(b)\dagger}(t) \mathcal{D}_{m+\alpha-\beta, m_2}^{(a)}(t) \hat{s}_{m_1; m_2}(z, 0)$, where $\mathcal{D}_{m, m'}^{(s)}(t) \equiv \langle s, m | \exp(-ig_s \vec{\Omega}_B \cdot \hat{\mathbf{F}} t) | s, m' \rangle$ is the matrix element of the rotation operator for states in hyperfine level $|s\rangle$, and $\vec{\Omega}_B \equiv \mu_B \vec{B} / \hbar$. Using the bosonic commutation relations for the spin wave operators, we can calculate the number of polaritons $\langle \hat{N}_\alpha(t_s) \rangle = \int dz \langle \hat{\Psi}_\alpha^\dagger(z, t_s) \hat{\Psi}_\alpha(z, t_s) \rangle$ as a function of storage time t_s for an arbitrary DSP quantum state created in the storage process. In the limit of infinite control field amplitude, this converts into

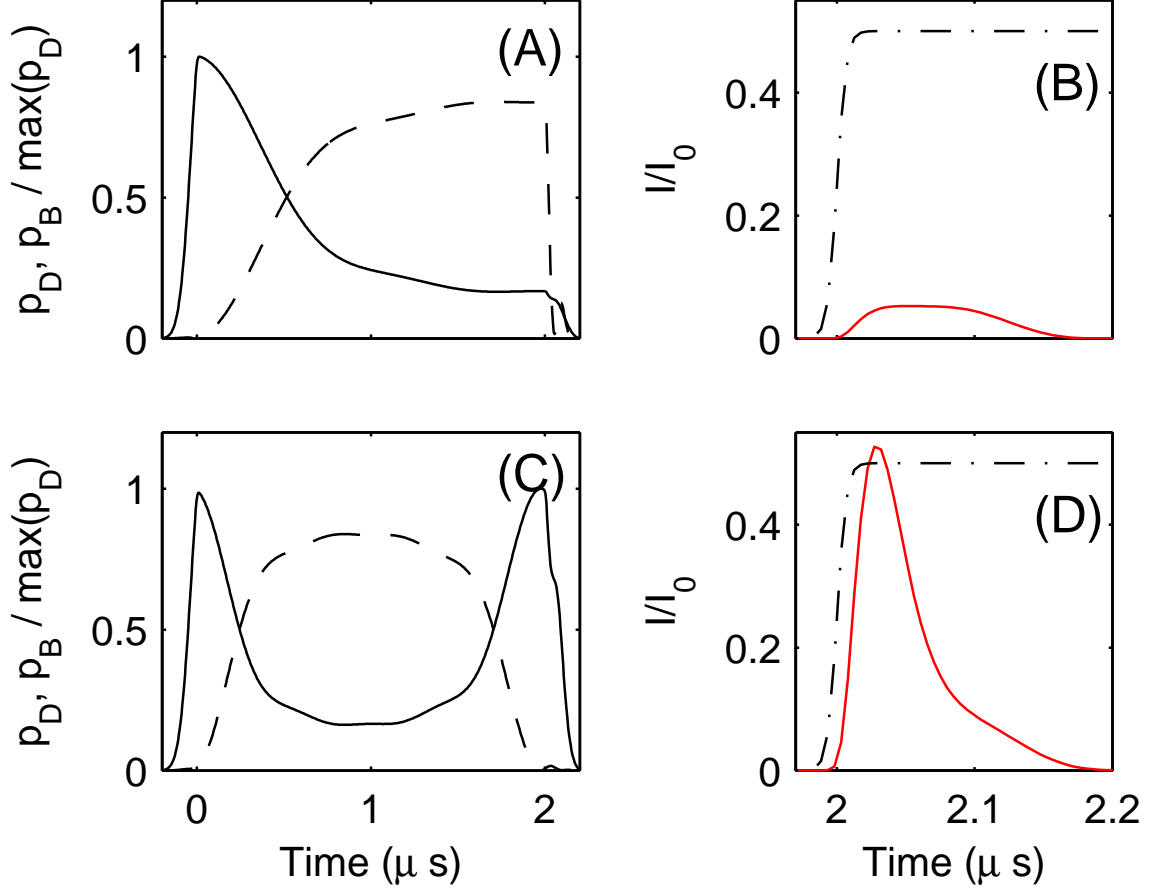


Figure 7.2: Numerical results illustrate the storage and retrieval of a signal pulse from an atomic ensemble as described in the text. We show results for two values of the magnetic field oriented along the z axis. Panels (A) and (B) correspond to a magnetic field $B = 0.267$ G, so that the signal is stored for $T_L/4$, where $T_L = 8 \mu\text{s}$ is the Larmor period. Panels (C) and (D) show results for $B = 0.535$ G, corresponding to a signal storage time of $T_L/2$, where $T_L = 4 \mu\text{s}$. The signal field intensity transmittance $I(t)/I_0$ (Solid line) and control field Rabi frequency (dot-dashed line), displayed in arbitrary units, are shown in panels (B) and (D). Panels (A) and (C) display scaled dark state p_D (solid line) and bright state p_B (dashed line) polariton components, as explained in the text. In panel (B) the ratio of retrieved to input signal pulse energy is 4.38% while in (D) the ratio is 25.09%.

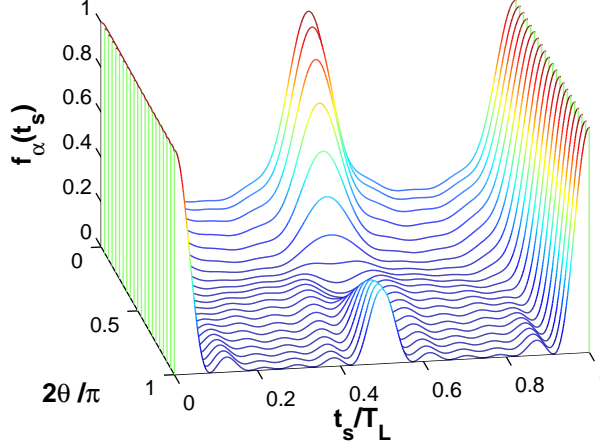


Figure 7.3: The DSP population fraction $f_\alpha(t_s)$ calculated for orientations of the magnetic field $0 \leq \theta \leq \pi/2$ over one Larmor period. These results illustrate collapses and revivals whose features are dependent on θ . The atomic configuration and field polarizations α and β are described in the text.

the total number of photons in the retrieved signal field $\int dz \langle \hat{\varphi}_\alpha^{(s)\dagger}(z, t) \hat{\varphi}_\alpha^{(s)}(z, t) \rangle$.

We therefore derive an expression for the signal retrieval efficiency as the fraction

$f_\alpha(t_s) \equiv \langle \hat{N}_\alpha(t_s) \rangle / \langle \hat{N}_\alpha(0) \rangle$:

$$f_\alpha(t_s) = \left| \sum_{m_1 m_2} \frac{R_{m_1 \alpha}(\beta) R_{m_2 \alpha}(\beta)}{\sum_m |R_{m \alpha}(\beta)|^2} \mathcal{D}_{m_2 m_1}^{(g)}(t_s) \times \mathcal{D}_{m_1 + \alpha - \beta, m_2 + \alpha - \beta}^{(g')\dagger}(t_s) \right|^2. \quad (7.13)$$

In Figure 7.3, we display the $f_\alpha(t_s)$ as a function of t_s for a variety of magnetic field orientations. We again consider an ensemble of ^{85}Rb atoms with the same choice of atomic configuration and field polarizations discussed earlier. For $t_s \ll T_L$, we observe a collapse in the polariton population, yielding an approximate retrieval efficiency of $f_\alpha(t_s) \approx \exp(-\Upsilon_\alpha^2 (\Omega_L t_s)^2 / 2)$, where the collapse rate Υ_α depends on the angle, θ , between the magnetic field and the propagation axis. For $\theta = 0$, we find

$$\Upsilon_\alpha^2(\theta = 0) = 4 \sum_{m_1, m_2} \frac{|R_{m_1 \alpha}(\beta) R_{m_2 \alpha}(\beta)|^2}{(\sum_m |R_{m \alpha}(\beta)|^2)^2} (m_1 - m_2)^2. \quad (7.14)$$

With the approximation $g_b = -g_a$, valid for ground level alkalis, it is clear that the system undergoes a revival to the initial state after a complete Larmor period,

and thus the signal retrieval efficiency should equal the zero storage time value. Depending on the orientation of the magnetic field, we observe also a partial revival at half the Larmor period. For a magnetic field oriented along the z axis, the system dynamics are relatively simple. Each hyperfine coherence $\hat{s}_{m; m+\alpha-\beta}$ merely picks up a phase factor that oscillates at $m + (\alpha - \beta)/2$ times twice the Larmor frequency, thus returning the system to its initial state at half the Larmor period. In this case, the partial revival is actually a full revival. On the other hand, for $\theta = \pi/2$, a rotation through half the Larmor period causes the coherence transformation $\hat{s}_{m; m+\alpha-\beta} \rightarrow \hat{s}_{-m; -(m+\alpha-\beta)}$ up to an overall phase factor. As a result, for the choice of equal field polarizations ($\alpha = \beta$), the retrieval efficiency at half the Larmor period simplifies to $(\sum_m R_{m\alpha}(\alpha)R_{-m,\alpha}(\alpha)/\sum_m |R_{m\alpha}(\alpha)|^2)^2$, resulting in a partial revival. For other orientations of the magnetic field, particularly for $\theta = \pi/4$, the revival at half the Larmor period is suppressed. This reflects the more complicated dynamics of the individual spin coherences $\hat{S}_{g' m'}^{g m}$, each of which transform into a superposition of all $(2F_b + 1)(2F_a + 1)$ spin coherences, with complex time dependent coefficients governed by the rotation matrices. Stated physically, there is a strong destructive interference between the various spin coherences when $\theta \approx \pi/4$.

7.3 *Experimental Observation*

In this section, we report observations of collapses and revivals of dark-state polaritons in agreement with the theoretical predictions [19] of the previous section. In our experiment, we employ two different sources for the signal field, a coherent laser output and a conditional source of single photons [47]. The latter is achieved by using a cold atomic cloud of ^{85}Rb at Site A in the off-axis geometry pioneered by Harris and coworkers [59]. Another cold atomic cloud of ^{85}Rb at Site B serves as the atomic quantum memory element, as shown in Figure 7.4. Sites A and B are physically located in adjacent laboratories connected by a 100 meter long single-mode optical

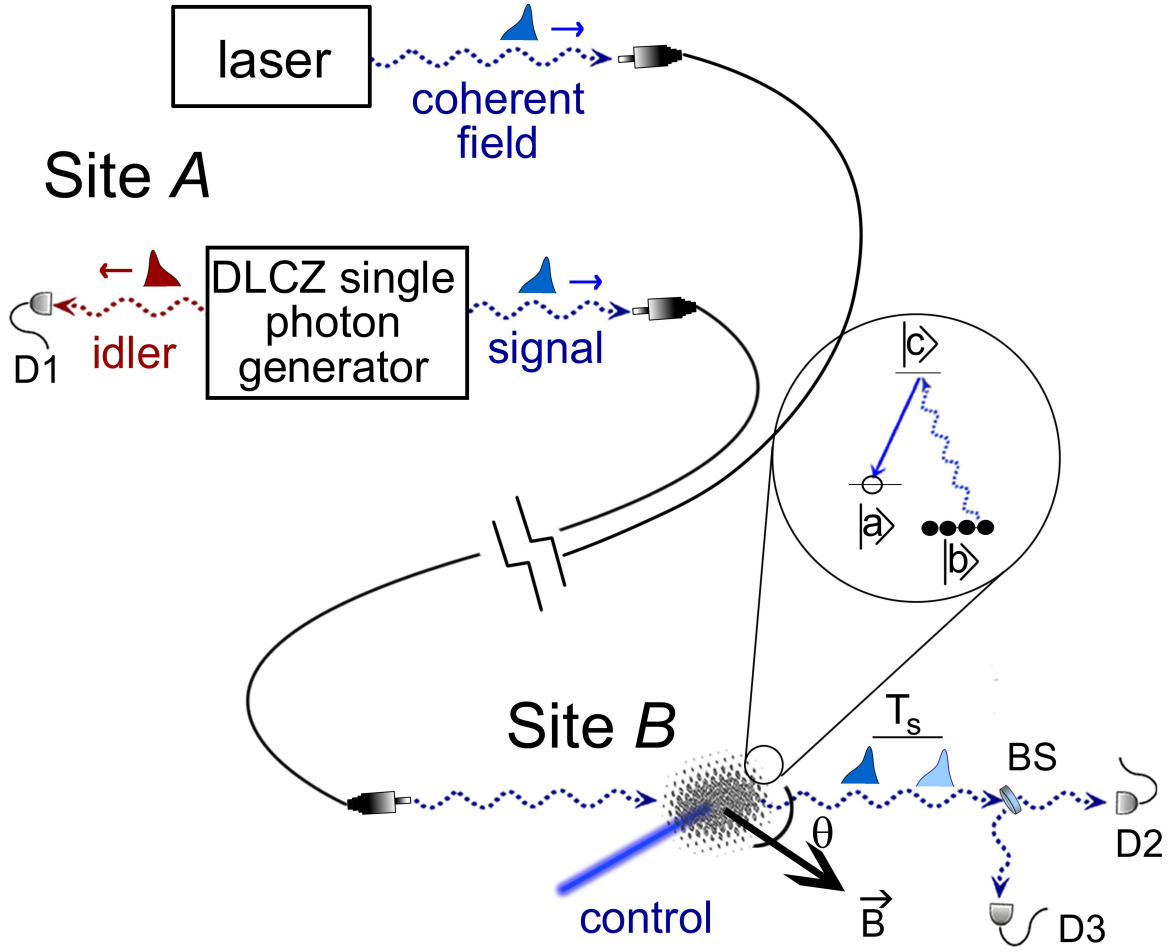


Figure 7.4: A schematic diagram illustrates our experimental setup. A signal field from either a laser, or a DLCZ source of conditional single photons at Site A is carried by a single-mode fiber to an atomic ensemble at Site B, where it is resonant on the $|b\rangle \leftrightarrow |c\rangle$ transition. The signal field is stored, for a duration T_s , and subsequently retrieved by time-dependent variation of a control field resonant between levels $|a\rangle$ and $|c\rangle$. All the light fields responsible for trapping and cooling, as well as the quadrupole magnetic field in the MOT, are shut off during the period of the storage and retrieval process. An externally applied magnetic field created by three pairs of Helmholtz coils (not shown) makes an angle θ with the signal field wavevector. The inset shows the structure and the initial populations of atomic levels involved. The signal field is measured by detectors D2 and D3, while detector D1 is used in the conditional preparation of single photon states of the signal field at Site A.

fiber. The fiber channel directs the signal field to the optically thick atomic ensemble prepared in level $|b\rangle$. The inset in Figure 7.4 indicates schematically the structure of the three atomic levels involved, $|a\rangle$, $|b\rangle$ and $|c\rangle$, where $\{|a\rangle; |b\rangle\}$ correspond to the $5^2S_{1/2}, F_a = 3, F_b = 2$ levels of ^{85}Rb , and $|c\rangle$ represents the $5^2P_{1/2}, F_c = 3$ level associated with the D_1 line at 795 nm. The signal field is resonant with the $|b\rangle \leftrightarrow |c\rangle$ transition and the control field with the $|a\rangle \leftrightarrow |c\rangle$ transition.

When the signal field enters the atomic ensemble at Site B , its group velocity is strongly modified by the control field. By switching off the control field within about 100 ns, the coupled excitation is converted into a spin wave excitation with a dominant dark state polariton component, i.e., the signal field is “stored” [69, 44, 45, 74]. An important condition to achieve this storage is a sufficiently large optical thickness of the atomic sample, which enables strong spatial compression of the incident signal field [41]. In our experiment the measured optical thickness $d \simeq 8$. The subsequent evolution of a dark state polariton in an external magnetic field is predicted to reveal a series of collapses and revivals whose structure is sensitive to the magnitude and orientation θ of the field relative to the signal wavevector, as discussed in the previous section [19].

As we deal with an unpolarized atomic ensemble, we must take into account the Zeeman degeneracy of the atomic levels. Choosing the same circular polarizations for both the probe and the control fields allows us to retain transparency [18, 19]. For a signal field of positive helicity, the dark state polariton annihilation operator for position z is given by [19]

$$\hat{\Psi}_+(z, t) = \frac{\Omega_c^*(t) \hat{\varphi}_+^{(s)}(z, t) - \sqrt{n(z) p \kappa_s^*} \sum_m R_{m,+}(1) \hat{s}_{m;m}(z, t)}{\sqrt{|\Omega_c(t)|^2 + n(z) p |\kappa_s|^2 \sum_m |R_{m,+}(+1)|^2}}. \quad (7.15)$$

As discussed in the previous section, the signal is stored in the form of spin wave excitations associated with the dark state polaritons $\sim \sum_m R_{m,+} \hat{S}_{m;m}(z)$ for some range of positions z within the sample. During the storage phase, and in the presence

of the magnetic field \vec{B} , the atomic hyperfine coherences rotate according to the transformation

$$\hat{s}_{m;m}(z, t) = \sum_{m_1=-F_b}^{F_b} \sum_{m_2=-F_a}^{F_a} \mathcal{D}_{m_1 m_2}^{(b)\dagger}(t) \mathcal{D}_{m, m_2}^{(a)}(t) \hat{s}_{m_1; m_2}(z, 0), \quad (7.16)$$

For ^{85}Rb , ignoring the nuclear magnetic moment, $g_a = -g_b$. This rotation dynamically changes the dark state polariton population during storage.

The measured signal retrieved after a given storage time T_s is determined by the remaining dark state polariton population. Stated differently, only the linear combination of hyperfine coherences $\sim \sum_m R_{m,+1}(1) \hat{s}_{m;m}(z, T_s)$ contributes to the retrieved signal. We calculate the number of dark state polariton excitations as a function of T_s using Eqs. (7.15) and (7.16), $\langle \hat{N}(T_s) \rangle = \int dz \langle \hat{\Psi}_{+1}^\dagger(z, T_s) \hat{\Psi}_{+1}(z, T_s) \rangle$, and find

$$\frac{\langle \hat{N}(T_s) \rangle}{\langle \hat{N}(0) \rangle} = \left| \sum_{m_1 m_2} \frac{R_{m_1,+1}(1) R_{m_2,+1}(1)}{\sum_m |R_{m,+1}(1)|^2} \mathcal{D}_{m_2 m_1}^{(b)\dagger}(T_s) \mathcal{D}_{m_1 m_2}^{(a)}(T_s) \right|^2. \quad (7.17)$$

In Figure 7.5, panels (f) through (j), we show the retrieval efficiency for various orientations of a magnetic field of magnitude 0.47 G, corresponding to the Larmor period of 4.6 μs . With the approximation $g_a = -g_b$ it is clear that the system undergoes a revival to the initial state after one Larmor period ($2\pi/|g_b \vec{\Omega}_B|$), and thus the signal retrieval efficiency equals the zero storage time value. Depending on the orientation of the magnetic field, a partial revival at half the Larmor period is also observed. For a magnetic field oriented along the z axis (Figure 7.5(f)), the polariton dynamics is relatively simple. Each hyperfine coherence $\hat{s}_{m;m}$ merely picks up a phase factor that oscillates at frequency $2m|g_b \vec{\Omega}|$, thus returning the system to its initial state at half the Larmor period. In this case, the partial revival is actually a full revival. On the other hand, for $\theta = \pi/2$ (Figure 7.5(j)), a rotation through half the Larmor period causes the coherence transformation $\hat{s}_{m;m} \rightarrow -\hat{s}_{-m;-m}$, and as a result, the retrieval efficiency is reduced to $(\sum_m R_{m,+1}(1) R_{-m,+1}(1) / \sum_m R_{m,+1}^2)^2$. The

substructure within a half Larmor period is associated with interference of different hyperfine coherences contributing to the dark-state polariton [19].

To test these predictions, we apply a uniform dc magnetic field of magnitude 0.5 ± 0.05 G to the atomic ensemble using three pairs of Helmholtz coils. In our first set of measurements, 150 ns long coherent laser pulses containing on average $\simeq 5$ photons serve as the signal field. The outputs of the single-photon detectors D2 and D3 are fed into two “Stop” inputs of a time-interval analyzer which records the arrival times with a 2 ns time resolution. The electronic pulses from the detectors are gated for the period $[t_0, t_0 + T_g]$, with $T_g = 240$ ns, centered on the time determined by the control laser pulse during the retrieval stage. Counts recorded outside the gating period are therefore removed from the analysis. The recorded data allows us to determine the number of photoelectric events $N_2 + N_3$, where N_i is the total number of counts in the i -th channel ($i = 1, 2, 3$).

By measuring the retrieved field for different storage times and orientations of the magnetic field, we obtain the collapse and revival signals shown in Figure 7.5, (a) through (e). As expected, we observe revivals at integer multiples of the Larmor period. In addition, we see partial revivals at odd multiples of half the Larmor period, except in the vicinity of $\theta = \pi/4$. The measured substructures within a single revival period are in good agreement with the theory (cf., insets of Figure 7.5, (e) and (j)). We attribute the overall damping of the revival signal in the experimental data to the magnetic field gradients. The evident decrease of this damping while θ is varied from 0 to $\pi/2$ suggests that such gradients are predominantly along the direction of the signal field wavevector. Similarly, we attribute the additional broadening of the revival peaks at longer times to inhomogeneous magnetic fields, possibly ac fields, not included in the theoretical description. We are pursuing additional investigations to determine the temporal and spatial characteristics of the residual magnetic fields [76].

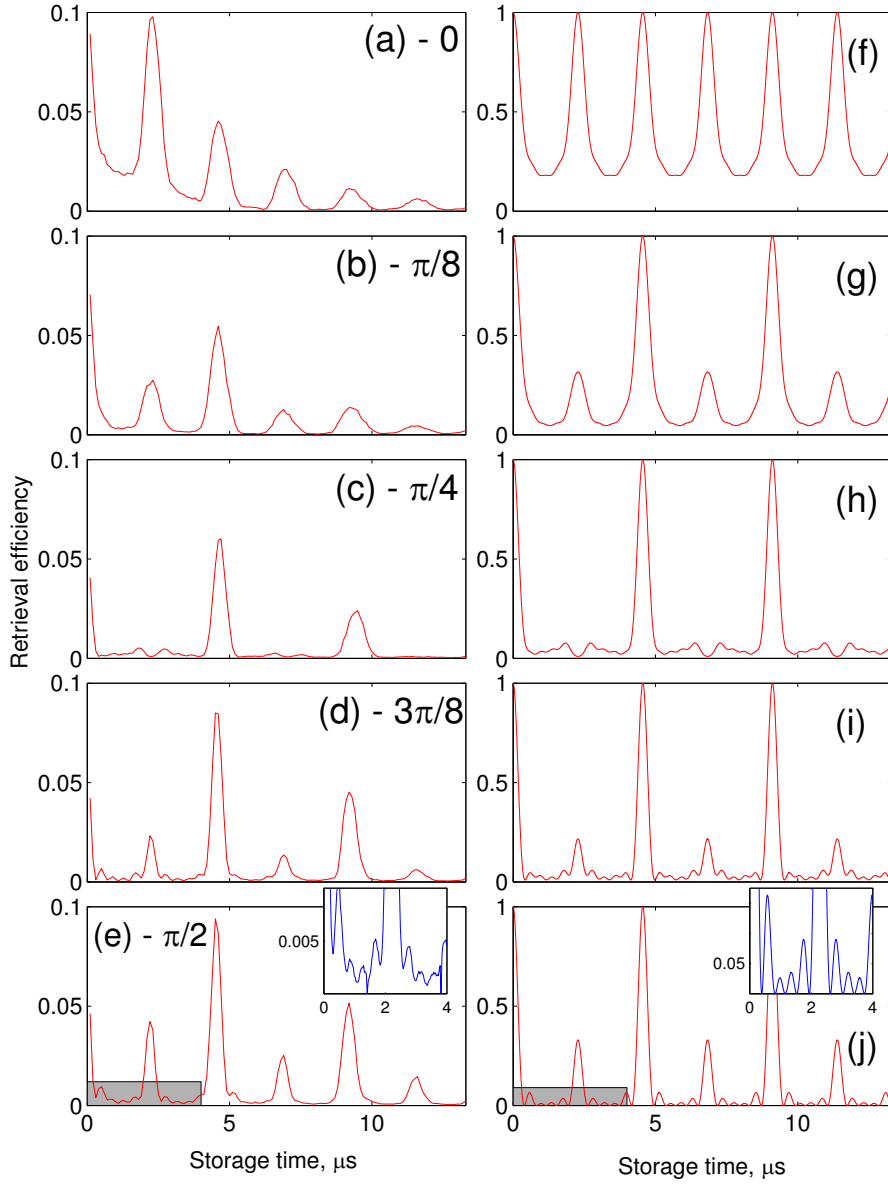


Figure 7.5: Panels (a)-(e) show the ratio of the number of photoelectric detection events for the retrieved and incident signal fields for various orientations, $\theta = 0, \pi/8, \pi/4, 3\pi/8, \pi/2$, of the applied magnetic field, and as a function of storage time. The incident signal field is a weak coherent laser pulse. In all cases the control pulse is switched off at $T_s = 0$. We observe a series of collapses and revivals at multiples of the half Larmor period of $2.3 \mu\text{s}$. The observed damping over several Larmor periods is likely caused by residual magnetic field gradients. The inset in Panel (e) demonstrates the observed substructure within the first Larmor period. Panels (f) through (j) are corresponding theoretical plots of the dark-state polariton number calculated using Eq. (7.17).

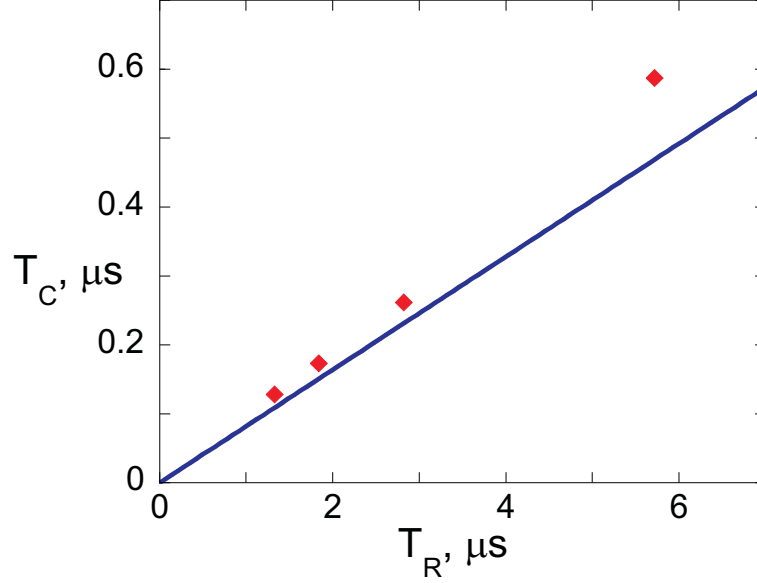


Figure 7.6: Diamonds show the measured collapse time T_C of the first revival at half the Larmor period as a function of the measured revival time T_R , for magnetic field values of 0.8, 0.6, 0.4, and 0.2 G, respectively, and for fixed orientation $\theta = \pi/2$. The line shows the corresponding theoretical prediction $T_C \approx 0.082T_R$ from Eq. (7.17).

Theory predicts that both the collapse and the revival times (T_C and T_R , respectively) scale inversely with the magnetic field [19]. In Figure 7.6 the theoretical prediction $T_C \approx 0.082T_R$ (solid line) is compared with the experimentally measured values. We find very good agreement except for the lowest value of magnetic field $B = 0.2$ G which may be explained by the presence of residual magnetic field gradients.

In the measurements presented above, classical, coherent laser light was used as the signal field [90]. We have also investigated the revival dynamics of our atomic memory with the signal field in a single photon state, as shown in Figure 7.4. The procedure for production of a single photon state of the signal field at Site A is conditioned on the detection of an idler photon by D1 (see Refs.[17, 18] for further details). If photoelectric detections in different channels 1, 2 or 1, 3 happen within the same gating period, they contribute to the corresponding coincidence counts between D1 and D j , N_{1j} , $j = 2, 3$. We evaluate the α parameter of Grangier *et al.* [102], given

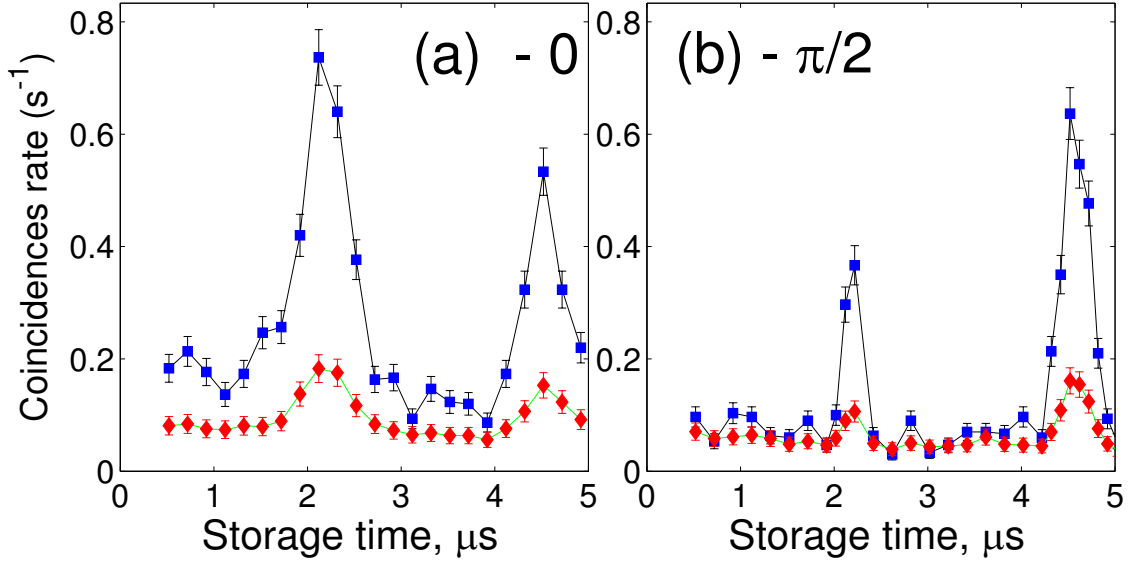


Figure 7.7: Squares show the measured rate of coincidence detections between D1 and D2,3, $N_{si} = N_{12} + N_{13}$ as a function of the storage time. Diamonds show the measured level of random coincidences N_R . The ratio of squares to diamonds gives g_{si} . Uncertainties are based on the statistics of the photoelectric counting events.

by the ratio of various photoelectric detection probabilities which are measured by the set of detectors D1,D2 and D3. For an ideal single-photon state $\alpha = 0$, whereas for coherent fields $\alpha = 1$. We have experimentally determined $\alpha = 0.51 \pm 0.06$, without any correction for background or dark counts.

The normalized intensity cross-correlation function $g_{si} \equiv (N_{12} + N_{13})/N_R$ may be employed as a measure of non-classical signal-idler field correlations [90, 16], as discussed in detail in Ref.[51]. Here $N_R \equiv N_1 \cdot (N_2 + N_3) \cdot R_{rep}$ is the level of random coincidences, where R_{rep} is the repetition rate of the experimental protocol. The values of g_{si} are obtained by the ratio of the upper and lower traces in Figure 7.7. The measurements presented there give values of g_{si} well in excess of two at the revival times, suggesting the dark-state polaritons have a non-classical nature. One could further evaluate self-correlations for the idler field g_{ii} , and for the signal field g_{ss} , and confirm that the Cauchy-Schwarz inequality $g_{si}^2 \leq g_{ss}g_{ii}$ is indeed violated [51, 90, 16].

We have measured, by adding a beamsplitter and an additional detector, the value $g_{ii} = 1.42 \pm 0.03$. When the signal field is stored and retrieved 500 ns later, we find that both $g_{ss} \leq 2$ [18]. While the total number of recorded coincidences between detectors D2 and D3 is not high enough to evaluate g_{ss} for the revived polariton, it is also expected to be less than two, leading to a substantial violation of the Cauchy-Schwarz inequality.

7.4 *Conclusion*

We have developed a theory of the DSP as a mechanism to store and retrieve light pulses in a degenerate unpolarized atomic medium. The role of the DSP and its connection to storage retrieval efficiency have been verified by full numerical solutions of the propagation equations for a classical incident signal field. In the presence of a magnetic field, we have demonstrated that the DSP population undergoes collapses and revivals during the pulse storage time. We predict that this polariton dynamics is directly reflected in the signal pulse retrieval efficiency. These predictions have been verified by experimental observation. Our results may find applications in quantum communication and computation approaches that utilize quantum memories [47, 29, 104, 120]

CHAPTER 8

ENTANGLEMENT OF REMOTE ATOMIC QUBITS

This chapter presents a synthesis of the protocol for generating probabilistic entanglement between the polarization of a photon and a collective atomic excitation of Chapter 3 and the ability to store nonclassical states of the light field demonstrated in Chapter 6.¹ We report observations of entanglement of two remote atomic qubits, achieved by generating an entangled state of an atomic qubit and a single photon at Site *A*, transmitting the photon to Site *B* in an adjacent laboratory through an optical fiber, and converting the photon into an atomic qubit. Entanglement of the two remote atomic qubits is inferred by performing, locally, quantum state transfer of each of the atomic qubits onto a photonic qubit and subsequent measurement of polarization correlations in violation of the Bell inequality $|S| \leq 2$. We experimentally determine $S_{exp} = 2.16 \pm 0.03$. Entanglement of two remote atomic qubits, each qubit consisting of two independent spin wave excitations, and reversible, coherent transfer of entanglement between matter and light, represent important advances in quantum information science.

8.1 *Introduction*

Realization of massive qubits, and their entanglement, is central to practical quantum information systems [29, 47, 5]. Remote entanglement of photons can now be achieved in a robust manner using the well-developed technology of spontaneous parametric

¹This chapter is based on Ref.[21].

down-conversion [25, 26, 27], with propagation to remote locations by means of optical fibers. Photons, however, are difficult to store for any appreciable period of time, whereas qubits based on ground-state atoms have long lifetimes. Local entanglement of massive qubits has been observed between adjacent trapped ions [121] and between pairs of Rydberg atoms in a collimated beam [31]. In order to entangle qubits at remote locations the use of photons as an intermediary seems essential [103, 122, 123, 124]. Photons also offer some flexibility as information carriers as they can propagate in optical fiber with low losses. The creation, transport, storage, and retrieval of single photons between remote atomic ensembles located in two different laboratories was recently reported [18]. The first step in creating remote entanglement between massive qubits is to entangle one such qubit with the mediating light field, which is then directed towards the second qubit via an optical fiber. There have recently been important advances towards this goal by demonstrating entanglement of a photon with a trapped ion [32], with a collective atomic qubit [57, 17], and with a single trapped atom [38, 125].

A promising route towards the creation and application of long-lived qubit entanglement in scalable quantum networks was proposed by Duan, Lukin, Cirac, and Zoller [47, 124]. These atomic qubits rely on collective atomic states containing exactly one spin excitation. For useful quantum information processing two orthogonal spin wave excitation states $\hat{S}_+^\dagger |0\rangle_a, \hat{S}_-^\dagger |0\rangle_a$ are needed for the logical states of a qubit [47], where $|0\rangle_a$ represents the collective atomic ground state. We note that the two states $|0\rangle_a$ and $\hat{S}^\dagger |0\rangle_a$, do not appear to constitute a practically useful qubit [126]. In the experiment of Chapter 6 [18] each of the two remote ensembles only contained one logical state, since the atomic ground state component does not serve this purpose. Entanglement of continuous atomic variables in two separate atomic ensembles has been reported [127], as appropriate for continuous-variable quantum information processing, but not for qubit entanglement.

In two recent experiments, collective atomic qubits were generated using cold atomic ensembles [57, 17]. In the first of these the logical states were single spin wave excitations (ideally, $\hat{s}_+^\dagger|0\rangle_a, \hat{s}_-^\dagger|0\rangle_a$), in either one of two distinct atomic ensembles inside a high vacuum chamber. In the second experiment, two orthogonal spin waves of a single cold ensemble represented the logical qubit states [17]. The experiments [57, 17] realized a single atomic qubit system, but did not address the issue of entanglement of atomic qubits.

While remote entanglement of atomic qubits has not been previously demonstrated, Refs. [57, 17] realized two basic primitives of a quantum network: (a) entanglement of photonic and atomic qubits, and (b) quantum state transfer from an atomic to a photonic qubit. The crucial additional ingredient is the reverse operation, the conversion of a photonic qubit into an atomic qubit. This enables the transfer of atom-photon entanglement into remote atomic qubit entanglement.

8.2 *Theory and Experiment*

Here we report remote atomic qubit entanglement using cold atomic clouds of ^{85}Rb confined at Sites A and B , as shown in Figure 8.1. These sites are situated in separate laboratories and linked by an optical fiber. A notable distinction between the two nodes is that the qubit generated at Site A is written on an unpolarized atomic ensemble, as in Chapter 3 [17], whereas at Site B the atomic ensemble is prepared, ideally, in the ($m = 0$) Zeeman state of the $F = 2$ ground level by optical pumping. All the light fields responsible for trapping and cooling of the atoms, as well as the quadrupole magnetic fields at both sites, are shut off during the period of the protocol. The ambient magnetic field at each site is compensated by three pairs of Helmholtz coils, and a bias field of 0.2G is added at Site B for the purpose of optical pumping.

Our protocol starts with the generation of an entangled state of a signal photon and a collective atomic qubit at Site A , achieved through Raman scattering of a

classical laser write pulse as discussed in Chapter 3. The state can be represented schematically as

$$\begin{aligned} |\Psi\rangle &= |0\rangle_a |0\rangle_f + \chi(\cos\eta |+\rangle_a |+\rangle_f + \sin\eta |-\rangle_a |-\rangle_f) \\ &\equiv |0\rangle_a |0\rangle_f + \chi |\psi\rangle, \end{aligned} \quad (8.1)$$

where $|+\rangle_f \equiv \hat{a}_+^\dagger |0\rangle_f$ and $|-\rangle_f \equiv \hat{a}_-^\dagger |0\rangle_f$ are the normalized states of positive and negative helicity of the signal photon, $|0\rangle_f$ is the field vacuum state, $|\pm\rangle_a \equiv \hat{S}_\pm^\dagger |0\rangle_a$ describes the two logical qubit states, corresponding to non-symmetric collective atomic modes [13], and $\chi \ll 1$. The asymmetry angle $\eta = 0.81\pi/4$ [17]. Eq. (8.1) represents probabilistic entanglement generation, where ideally for each signal photon emission event, an entangled atomic qubit is created in the atomic ensemble [47, 32]. Since we deal with an unpolarized atomic ensemble, the state of the system is more rigorously described by a density operator as discussed in Chapter 3 [17].

The orthogonal polarization modes of the signal field produced at Site *A* are directed along the optical fiber to Site *B*. As the signal field propagates from Site *A* to Site *B*, it passes through two quarter wave plates, causing the transformation of the signal field operators $\hat{a}_\pm \rightarrow \pm\hat{a}_\mp$. The signal field propagation in the atomic medium at Site *B* is controlled by an additional laser field (control) through the process of electromagnetically-induced transparency (EIT) [72, 71, 73, 69, 44, 45].

We implement the storage phase at Site *B*, by adiabatically reducing the control field amplitude to zero, while the signal pulse lies within the cloud. The orthogonal atomic spin wave excitations thereby created in the spin-polarized gas constitute the logical states of the atomic qubit. In order to convert the signal field qubit into a collective atomic qubit, it is necessary that the optically thick atomic sample supports EIT for both field helicities [69, 19]. To this end, we optically pump the atomic cloud at Site *B* using a linearly polarized field resonant to the $F = 2 \leftrightarrow F' = 2$ transition of the D_1 -line, and an additional repumping field resonant to the $F = 3 \leftrightarrow F' = 3$

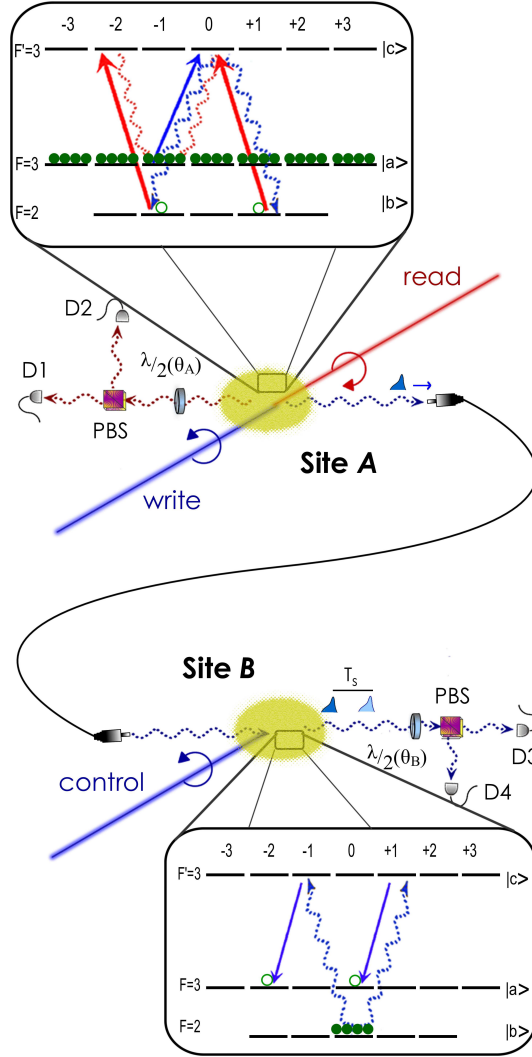


Figure 8.1: A schematic diagram of our experimental setup. Two cold atomic ensembles of ^{85}Rb , an unpolarized sample at Site A, and a spin-polarized sample at Site B, separated by 5.5 m, are connected by a single-mode fiber. The insets show the structure and the initial populations of the atomic levels for the two ensembles. An entangled state of a collective atomic qubit and a signal field is generated at Site A by Raman scattering of the write laser field. The orthogonal helicity states of the generated signal field are transmitted via optical fiber from Site A to Site B, where they are converted to orthogonal collective atomic excitations, stored for a duration T_s , and subsequently converted into an idler field by adiabatic variation of the control field amplitude. The atomic qubit at Site A is similarly converted into an idler field by a read laser pulse, counterpropagating with respect to the write pulse. For polarization analysis, each idler field propagates through a quarter-wave plate (not shown), a half-wave plate ($\lambda/2$) and a polarizing beamsplitter (PBS). Polarization correlations of the idler fields are recorded by photoelectric detection using the single photon detectors D1-D4.

transition of the D_2 -line. We measured the optical thickness $d \simeq 8$ for both circular components of the signal field.

In the adiabatic limit, the propagation, storage, and retrieval of the signal within Site B is well described by the dark-state polariton mechanism [69, 75, 19, 20] discussed in Section C.5 of Appendix C. When the atomic sample at Site B is spin polarized, a dark-state polariton operator exists for each polarization of the signal. These polaritons are orthogonal, allowing each polarization to be stored independently. The dark-state polariton operator of helicity $\alpha = \pm 1$ at Site B is given by Eq. (C.66) with $p_m = \delta_{m,0}$ and $\beta = 1$.

By switching off the control field over a period of about 20 ns, the photonic qubit is converted into an atomic qubit. At this stage remote atomic qubits should have been created at Sites A and B . Atoms at Site B should, ideally, be prepared in a single Zeeman $m = 0$ state of the $F = 2$ hyperfine ground level (lower inset in Figure 8.1). In practice the pumping is not perfect, possibly due to radiation trapping in the optically thick atomic medium [128]. We measure lower storage and retrieval efficiency for the negative helicity signal component compared with that of the positive helicity component (3% vs 8%). Numerical simulations indicate that the discrepancy between the efficiencies is consistent with a residual population in the $|F = 2, m = -2\rangle$ atomic state at the 10% level. This results in undesirable absorption of the signal field with negative helicity. These simulations were performed using the propagation equation (C.51) derived in Section C.4.1.

The signal photon of helicity $\alpha = \pm 1$ is stored in the ensemble at Site B with efficiency ϵ_α . After a storage time T_s , the non-vacuum component of the state of the two ensembles is given by the following density operator: $\hat{\rho} = (1 - \epsilon)\hat{\rho}_A + \epsilon\hat{\rho}_{AB}$, where the component $\hat{\rho}_A$ describes the state of single excitation at Site A , and is expressed by

$$\hat{\rho}_A = \frac{1 - \epsilon_-}{1 - \epsilon} \cos^2 \eta \hat{s}_{A+}^\dagger \hat{\rho}_{vac} \hat{s}_{A+} + \frac{1 - \epsilon_+}{1 - \epsilon} \sin^2 \eta \hat{s}_{A-}^\dagger \hat{\rho}_{vac} \hat{s}_{A-}, \quad (8.2)$$

where $\hat{\rho}_{vac}$ is the product of the ground state atomic density operators for the ensembles at Sites A and B . The density operator $\hat{\rho}_{AB} = \hat{\Psi}_{AB}^\dagger(T_s)\hat{\rho}_{vac}\hat{\Psi}_{AB}(T_s)$ in the two-qubit sub-space represents an entangled atomic state where

$$\hat{\Psi}_{AB}^\dagger(T_s) = e^{i\phi(T_s)} \cos \eta' \hat{s}_{A+}^\dagger \hat{s}_{B-}^\dagger - \sin \eta' \hat{s}_{A-}^\dagger \hat{s}_{B+}^\dagger \quad (8.3)$$

with $\cos \eta' = \sqrt{\epsilon_-/\epsilon} \cos \eta$, and $\epsilon = \epsilon_- \cos^2 \eta + \epsilon_+ \sin^2 \eta$ is the average efficiency of photon storage at Site B . The phase $\phi(t) = -2(g\mu_B/\hbar)B_0t$ is induced by the applied magnetic field $B_0 = 0.2\text{G}$ oriented along the propagation axis at Site B , where g is the Landé g-factor for hyperfine level with $F = 3$.

Ideally, entanglement should have been created between the collective atomic qubits at Sites A and B . After a storage time T_s , the remote collective atomic excitations are converted by quantum state transfer into idler fields emanating from Sites A and B , using a read laser pulse at Site A and by reactivating the control field at Site B [57, 17]. The resulting idler-idler photoelectric correlations may be calculated using the effective two-photon state

$$|\Psi_2\rangle = \cos \eta_f |HV\rangle + e^{i\phi_f} \sin \eta_f |VH\rangle \quad (8.4)$$

where $|HV\rangle = \hat{a}_{A,H}^\dagger \hat{a}_{B,V}^\dagger |0\rangle_f$ and $|VH\rangle = \hat{a}_{A,V}^\dagger \hat{a}_{B,H}^\dagger |0\rangle_f$, and the subscripts A and B indicate the idler mode at the respective site. We omit higher-order terms in photon number [18].

The phase ϕ_f , which includes the contributions due to the Larmor precession $\phi(T_s)$, the light phase shifts in the atomic media, and various optical elements, is introduced as an adjustable parameter. The mixing angle η_f is determined by the relative efficiencies with which the two qubit states are transferred from the atomic ensembles to the idler fields. If we assume equal transfer efficiencies at Site A , we find $\cos \eta_f = \sqrt{\epsilon_{B-}/\epsilon_B} \cos \eta$, where $\epsilon_B = \epsilon_{B-} \cos^2 \eta + \epsilon_{B+} \sin^2 \eta$ and $\epsilon_{B\pm}$ is the combined storage and retrieval efficiency for a photon of helicity \pm at Site B . Measurements of these efficiencies give $\epsilon_{B+} = 0.08$, and $\epsilon_{B-} = 0.03$. With $\eta = 0.81\pi/4$ fixed by

the atom-photon entanglement process at Site A [17] we get $\eta_f = 1.12\pi/4$. Our experimental data, including those displayed in Figure 8.3, are consistent with this value of η_f and $\phi_f \ll 1$.

The above arguments are clearly conditional on the generation of the signal qubit. According to Eq. (8.1), the corresponding probability scales as χ^2 , and this determines the efficiency of the probabilistic entanglement generation. However, as Duan *et al.* point out [47], quantum network protocols eliminate the vacuum component of Eq. (8.1) and only the entanglement characteristics of $|\psi\rangle$ are relevant [129, 130]. In our experiment, atomic qubits were stored for a time 500 ns at Site A and 200 ns at Site B . It should be possible to extend the qubit storage times to longer than 10 μ s, as the single-quanta storage results suggest [18].

The measurement of the atomic qubits is performed by quantum state transfer onto the idler fields at both sites using the read laser pulse at Site A and the control laser pulse at Site B . The polarization state of either idler field is measured using a polarizing beamsplitter and two single photon detectors, D1, D2 for Site A and D3, D4 for Site B (additional technical details are given in Refs.[57, 17, 18]). Polarization correlations between the idler fields produced at the remote sites are recorded and analyzed for the presence of entanglement. The contributions of the vacuum and single photon idler excitations are excluded in the observed photoelectric coincidences between the remote sites [129, 130]. Since quantum state transfer is a local process, it cannot generate entanglement. Hence, observation of idler field entanglement confirms probabilistic entanglement of the two remote atomic qubits. We denote the number of such coincidences between detector Dn , $n = 1, 2$ at Site A and detector Dm , $m = 3, 4$ at Site B by $C_{nm}(\theta_A, \theta_B)$. Here θ_A and θ_B are the angles by which polarization is rotated by the half-waveplates at these Sites.

The two-particle interference produces a high-visibility sinusoidal fringe pattern for the coincidence rates $C_{nm}(\theta_A, \theta_B)$, which is characteristic of entangled particles.

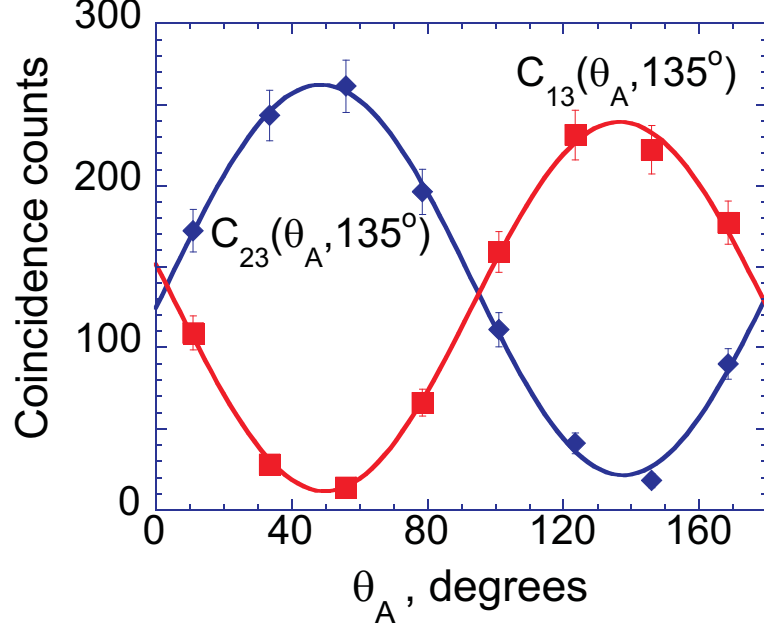


Figure 8.2: Measured coincidence fringes $C_{n3}(\theta_A, \theta_B)$ as a function of θ_A , for $\theta_B = 135^\circ$, $n = 1$, diamonds, $n = 2$, squares. The curves are sinusoidal fits to the data. Each point is acquired for 15 minutes. The effective repetition rate is 108 kHz, each trial takes $1.1 \mu s$.

Figure 8.2 shows measured coincidence fringes for some representative angles. We calculate the coincidence rates $C_{nm}(\theta_A, \theta_B)$ to be

$$\begin{aligned}
C_{13}(\theta_A, \theta_B) &\propto \epsilon_1 \epsilon_3 |(\cos \eta_f + e^{i\phi_f} \sin \eta_f) \sin(\theta_B + \theta_A) \\
&\quad + (\cos \eta_f - e^{i\phi_f} \sin \eta_f) \sin(\theta_B - \theta_A)|^2, \quad (8.5a)
\end{aligned}$$

$$\begin{aligned}
C_{24}(\theta_A, \theta_B) &\propto \epsilon_2 \epsilon_4 |(\cos \eta_f + e^{i\phi_f} \sin \eta_f) \sin(\theta_B + \theta_A) \\
&\quad - (\cos \eta_f - e^{i\phi_f} \sin \eta_f) \sin(\theta_B - \theta_A)|^2, \quad (8.5b)
\end{aligned}$$

$$\begin{aligned}
C_{14}(\theta_A, \theta_B) &\propto \epsilon_1 \epsilon_4 |(\cos \eta_f - e^{i\phi_f} \sin \eta_f) \cos(\theta_B - \theta_A) \\
&\quad + (\cos \eta_f + e^{i\phi_f} \sin \eta_f) \cos(\theta_B + \theta_A)|^2, \quad (8.5c)
\end{aligned}$$

$$\begin{aligned}
C_{23}(\theta_A, \theta_B) &\propto \epsilon_2 \epsilon_3 |(\cos \eta_f - e^{i\phi_f} \sin \eta_f) \cos(\theta_B - \theta_A) \\
&\quad - (\cos \eta_f + e^{i\phi_f} \sin \eta_f) \cos(\theta_B + \theta_A)|^2, \quad (8.5d)
\end{aligned}$$

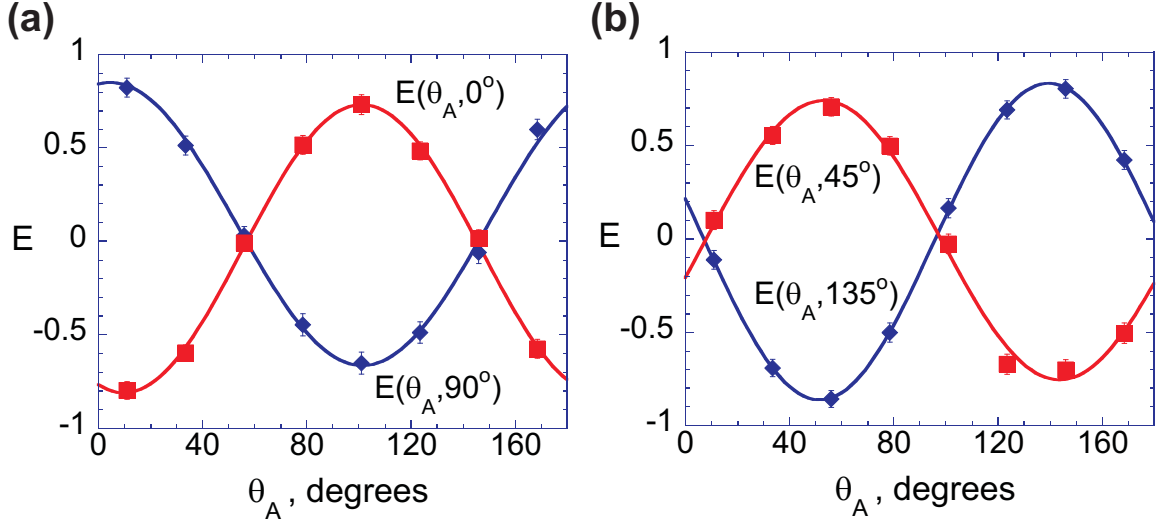


Figure 8.3: Measured correlation function $E(\theta_A, \theta_B)$ as a function of θ_A . (a), $\theta_B = 0^\circ$, squares, and 90° , diamonds. (b), $\theta_B = 45^\circ$, squares, and 135° , diamonds. The curves are sinusoidal fits to the data.

where ϵ_m is the overall efficiency (including propagation losses) for detector D_m , and similar expressions for the other three rates.

8.3 Measurement of Bell's Inequality Violation

Observation of Bell inequality violation is one method to confirm two-particle entanglement, by way of measurement of discrete values of $C_{nm}(\theta_A, \theta_B)$ at polarization settings which lie on the slopes of the fringe pattern. Explicitly, following Clauser-Horne-Shimony-Holt (CHSH) [91], we calculate the correlation function $E(\theta_A, \theta_B)$, given by

$$\frac{C_{13}(\theta_A, \theta_B) + C_{24}(\theta_A, \theta_B) - C_{14}(\theta_A, \theta_B) - C_{23}(\theta_A, \theta_B)}{C_{13}(\theta_A, \theta_B) + C_{24}(\theta_A, \theta_B) + C_{14}(\theta_A, \theta_B) + C_{23}(\theta_A, \theta_B)}. \quad (8.6)$$

In Figure 8.3 we display $E(\theta_A, \theta_B)$ as a function of θ_A , for four values of θ_B . By fitting the correlation functions in Figure 8.3 with sinusoids, we determine a set of four pairs of angles $\theta_A = 78.5^\circ$, $\theta_B = 45^\circ$, $\theta'_A = 33.5^\circ$ and $\theta'_B = 0^\circ$ that should maximize the Bell inequality violation. We acquire data for two hours at each of these four points (Table 8.1). In order to account for unequal efficiencies of the detectors $D1, D2$ and

Table 8.1: Measured values of the correlation function $E(\theta_A, \theta_B)$ at particular polarization settings and the Bell parameter S .

θ_A	θ_B	$E(\theta_A, \theta_B)$
78.5	45	0.447 ± 0.017
33.5	45	0.640 ± 0.014
78.5	0	0.572 ± 0.015
33.5	0	-0.504 ± 0.016
		$S = 2.16 \pm 0.03$

$D3, D4$, each correlation measurement consisted of four runs, flipping polarization of either one of the idler fields by 90 degrees between the runs. As a result, the products $\epsilon_m \epsilon_n$ are effectively replaced by the symmetric factor $\frac{1}{4}(\epsilon_1 + \epsilon_2)(\epsilon_3 + \epsilon_4)$ in Eq. (8.5a). In this case the correlation function $E(\theta_A, \theta_B)$ becomes independent of these efficiencies:

$$\begin{aligned}
 E(\theta_A, \theta_B) = & -\frac{1}{2}[\cos(2(\theta_A - \theta_B))(1 - \cos \phi_f \sin 2\eta_f) \\
 & + \cos(2(\theta_A + \theta_B))(1 + \cos \phi_f \sin 2\eta_f)].
 \end{aligned} \tag{8.7}$$

The CHSH version of the Bell inequality is then $|S| \leq 2$, where

$$S = E(\theta_A, \theta_B) + E(\theta'_A, \theta_B) + E(\theta_A, \theta'_B) - E(\theta'_A, \theta'_B). \tag{8.8}$$

We find $S = 2.16 \pm 0.03 \not\leq 2$, in clear violation of the Bell inequality. No corrections for background or dark counts were made to any of the experimental counting rates, and these are chiefly responsible for the reduction in the observed value of S from the ideal value of 2.60 predicted by our theoretical model.

8.3.1 Fidelity of entanglement between remote Sites A and B

An alternative method to characterize entanglement of the ensemble of detected idler-idler photoelectric correlations is to determine the fidelity with respect to the maximally entangled state [131, 121, 32, 130]

$$|\Psi\rangle_M = (|V_A, H_B\rangle + |H_A, V_B\rangle)/\sqrt{2} \tag{8.9}$$

Table 8.2: Inferred density matrix elements ρ_{ij} . Error bars represent \pm one standard deviation and are based on the statistics of the photoelectric counting events.

θ_A	θ_B	HH	HV	VH	VV
11°	0°	0.086 ± 0.007	0.315 ± 0.012	0.565 ± 0.013	0.034 ± 0.005
56°	45°	0.275 ± 0.012	0.055 ± 0.006	0.060 ± 0.006	0.610 ± 0.013

and this is given by

$$F = \frac{1}{2}(\rho_{VH,VH} + \rho_{HV,HV} + \rho_{HV,VH} + \rho_{VH,HV}). \quad (8.10)$$

We can write a lower bound on F in terms of the diagonal matrix elements of the two-photon component of the density matrix in the original and rotated basis as follows [32],

$$F \geq \frac{1}{2}(\rho_{HV,HV} + \rho_{VH,VH} - 2\sqrt{\rho_{HH,HH}\rho_{VV,VV}} + \bar{\rho}_{HH,HH} + \bar{\rho}_{VV,VV} - \bar{\rho}_{HV,HV} - \bar{\rho}_{VH,VH}). \quad (8.11)$$

The diagonal density matrix elements are proportional to the joint two-photon photoelectric detection probabilities, and can be expressed in terms of the coincidence counts in the original $C_{ij}(11^\circ, 0^\circ)$, and rotated, $C_{ij}(56^\circ, 45^\circ)$, bases as follows

$$\rho_{ij,ij} = \frac{C_{ij}(11^\circ, 0^\circ)}{C_{13}(11^\circ, 0^\circ) + C_{23}(11^\circ, 0^\circ) + C_{14}(11^\circ, 0^\circ) + C_{24}(11^\circ, 0^\circ)} \quad (8.12)$$

$$\bar{\rho}_{ij,ij} = \frac{C_{ij}(56^\circ, 45^\circ)}{C_{13}(56^\circ, 45^\circ) + C_{23}(56^\circ, 45^\circ) + C_{14}(56^\circ, 45^\circ) + C_{24}(56^\circ, 45^\circ)}. \quad (8.13)$$

As usual, normalization by the total number of coincidences here accounts for finite measurement efficiency due to field propagation and detection losses.

Having measured each data point for one hour (Table 8.2), we found $F = 0.77 \pm 0.01$, whereas the classical limit corresponds to $F = 0.5$.

8.4 Conclusion

In conclusion, we have demonstrated entanglement of two remote atomic qubits, based on collective atomic states. By photoelectric detection of polarization correlations of

the idler fields we have also confirmed the mapping of atomic qubit entanglement onto photonic qubits. Long-lived entanglement of remote massive qubits and entanglement transfer between matter and light are important prerequisites for realization of a scalable quantum information network.

CHAPTER 9

CONCLUSION

In this thesis, we have provided theoretical descriptions of several recent experiments which implement basic quantum network operations using light interactions with cold atomic ensembles. We have examined how collective Raman scattering of a classical laser field can be modeled as a nondegenerate parametric amplifier involving a single mode of the detected signal field and an associated idler collective excitation. When the classical *write* pulse is sufficiently weak, this collective Raman scattering results in the entanglement between a qubit encoded in the polarization of the photon and the imprinted atomic excitation. The entanglement is inferred by transferring the idler spin wave to an associated idler electromagnetic field mode and subsequently measuring the correlations between the signal and idler fields. This retrieval process can be understood through the dark-state polariton mechanism when EIT is operative. When EIT is not possible, as in the experiment of Chapter 3, however, the retrieval process is not as well understood; the dynamics of the retrieval process are the subject of future investigations.

We also demonstrated that entanglement between the polarizations of two photons can be achieved using atomic cascade transitions. The cascade scheme has the advantage that the atomic transitions can be chosen such that one of the photons is emitted in the telecom range, making it ideal for long distance transmission through optical fibers. The second photon, on the other hand, lies in a frequency band that is ideal for storage within an atomic ensemble. In the experimental demonstration of this entanglement, superradiant time scales were observed in the temporal correlations of the emitted quantum fields. A detailed theoretical description of the superradiant

behavior in this system is currently under development [132].

The collective Raman scattering process that generates probabilistic entanglement between the scattered photons and an associated atomic excitation was also exploited to produce a source of deterministic single photons. The experimental advances that lead to increased quantum memory lifetime (e.g. better isolation from ambient magnetic fields that lead to Larmor collapse of the dark-state polariton) have allowed us to implement a measurement-based quantum feedback protocol that arms the atomic ensemble with a single collective excitation with high probability. The excitation state of atomic ensemble is then mapped to a detected mode of the electromagnetic field at a predetermined time.

We also extended the theory of dark-state polaritons introduced in Ref. [69] to treat collections of atoms with nuclear spin degeneracy. This development allowed us to theoretically describe the storage and retrieval of single photon states within an atomic ensemble reported in Chapter 6. We further predicted, that in the presence of a uniform magnetic field, Larmor precession induces collapses and revivals of the dark-state polariton population and, therefore, of the retrieval efficiency as a function of storage time. These predictions were confirmed by experimental observations. It will be shown in a separate work [76] that magnetic field gradients explain the observed reduction of revival amplitudes (Figure 7.5), and are responsible for the current limitation of quantum memory lifetimes.

Finally, the primitive operations of probabilistic entanglement generation between a photon and quantum memory element and the mapping of a photonic state to a collective atomic excitation were synthesized to produce entanglement of two remote atomic qubits.

APPENDIX A

POLARIZATION CONVENTIONS

In the thesis, whenever I am constrained to choose the polarization vectors $\vec{\varepsilon}_\lambda$ ($\lambda \in \{H, V\}$) for a propagation direction \hat{k} , they are chosen according to the convention presented here. Let us express the propagation direction \hat{k} in terms of the angles $\theta_{\hat{k}}$ and $\phi_{\hat{k}}$ as

$$\hat{k} = \cos \theta_{\hat{k}} \hat{x} - \sin \theta_{\hat{k}} \sin \phi_{\hat{k}} \hat{y} + \sin \theta_{\hat{k}} \cos \phi_{\hat{k}} \hat{z}. \quad (\text{A.1})$$

We then choose the horizontal polarization

$$\vec{\varepsilon}_H(\hat{k}) = -\hat{\theta}_{\hat{k}} = \sin \theta_{\hat{k}} \hat{x} + \cos \theta_{\hat{k}} \sin \phi_{\hat{k}} \hat{y} - \cos \theta_{\hat{k}} \cos \phi_{\hat{k}} \hat{z}, \quad (\text{A.2})$$

and the “vertical” polarization

$$\vec{\varepsilon}_V(\hat{k}) = -\hat{\phi}_{\hat{k}} = \cos \phi_{\hat{k}} \hat{y} + \sin \phi_{\hat{k}} \hat{z} \quad (\text{A.3})$$

Notice that these vectors are orthonormal and the set $\{\vec{\varepsilon}_H, \vec{\varepsilon}_V, \hat{k}\}$ form a right handed coordinate system.

We note that in the most common situations, where the signal of interest propagates along the $\hat{k} = \hat{z}$ axis, our convention the “expected” definitions for horizontal and vertical polarization vectors:

$$\vec{\varepsilon}_H(\hat{z}) = \hat{x} \quad (\text{A.4})$$

$$\vec{\varepsilon}_V(\hat{z}) = \hat{y}. \quad (\text{A.5})$$

We also note that when we perform a reflection $\hat{k} \rightarrow -\hat{k}$, we have the following transformations for the linear polarizations in this particular convention:

$$\vec{\varepsilon}_H(-\hat{k}) = \vec{\varepsilon}_H(\hat{k}) \quad (\text{A.6})$$

$$\vec{\varepsilon}_V(-\hat{k}) = -\vec{\varepsilon}_V(\hat{k}). \quad (\text{A.7})$$

We also adopt the following convention for the spherical helicity vectors. Let $\vec{e}_\alpha(\hat{k})$ be the spherical vector of helicity $\alpha \in \{-1, 0, 1\}$ with respect to the direction \hat{k} . The helicity vectors are given by

$$\vec{e}_0(\hat{k}) = \hat{k} \quad (\text{A.8a})$$

$$\vec{e}_{\pm 1}(\hat{k}) = \mp \frac{1}{\sqrt{2}} \left(\vec{e}_H(\hat{k}) \pm i \vec{e}_V(\hat{k}) \right). \quad (\text{A.8b})$$

The spherical basis vectors satisfy the orthogonality relations

$$\vec{e}_\alpha^*(\hat{k}) \cdot \vec{e}_\beta(\hat{k}) = \delta_{\alpha\beta} \quad (\text{A.9a})$$

$$\vec{e}_\alpha(\hat{k}) \cdot \vec{e}_\beta(\hat{k}) = (-1)^\alpha \delta_{\alpha, -\beta} \quad (\text{A.9b})$$

Since the z axis serves as the typical quantization axis for angular momentum, we define the “laboratory fixed” circular polarization vectors as the spherical basis vectors, $\vec{\xi}_\alpha \equiv \vec{e}_\alpha(\hat{z})$.

We note the following symmetry relationships among helicity vectors:

$$\vec{e}_\alpha^*(\hat{k}) = (-1)^\alpha \vec{e}_{-\alpha}(\hat{k}) \quad (\text{A.10a})$$

$$\vec{e}_\alpha(-\hat{k}) = -\vec{e}_{-\alpha}(\hat{k}) \quad (\text{A.10b})$$

$$= (-1)^{\alpha+1} \vec{e}_\alpha^*(\hat{k}). \quad (\text{A.10c})$$

APPENDIX B

DERIVATION OF THE EFFECTIVE HAMILTONIAN FOR SCATTERING FROM ATOMIC ENSEMBLES

In this Appendix, we show how one can adiabatically eliminate the excited state in a three level atom and arrive at the effective Hamiltonian for stimulated Raman scattering used to describe the Raman scattering from atomic ensembles, which can result in the generation of entangled qubits.

We consider a collection of N three level atom with two levels $|a\rangle$ and $|b\rangle$ in the ground state hyperfine manifold and an excited level $|c\rangle$ that may be coupled to ground levels $|a\rangle$ and $|b\rangle$ *via* an electric dipole transition. Levels $|a\rangle$, $|b\rangle$, and $|c\rangle$ have total atomic angular momenta F_a , F_b , and F_c respectively.

These atoms interact with a pump, or *write*, field and the electromagnetic reservoir. The *write* field has the properties of a narrow bandwidth *system* field described in Chapter 2. The positive frequency electric *write* field operator can be expressed in terms of the slowly varying photon density operators $\hat{\phi}(z, t)$ and their transverse spatial profile $\phi^{(w)}(\vec{r})$ as

$$\hat{\mathbf{E}}_w^{(+)}(\vec{r}, t) = (2\pi)^{3/2} \mathcal{E}(ck_w) e^{i\vec{k}_w \cdot \vec{r}} e^{-ick_w t} \phi^{(w)}(\vec{r}) \sum_{\alpha=\pm 1} \vec{\xi}_\alpha \hat{\phi}_\alpha^{(w)}(z, t) \quad (\text{B.1})$$

The *write* beam carrier frequency $ck_w = (\omega_c - \omega_a) + \Delta_w$ is detuned from resonance on the $|a\rangle \leftrightarrow |c\rangle$ transition by the frequency Δ_w . We assume, however, that Δ_w is small enough that the pump field is much closer to resonance on the $|a\rangle \leftrightarrow |c\rangle$ transition than to any other electric dipole transition in the chosen atom (^{85}Rb in

our experiments). Furthermore, the bandwidth of the pump field has a bandwidth $c\Delta k_w \ll \Delta_w$.

The positive frequency component of the electric reservoir field is given by

$$\hat{\mathbf{E}}_R^{(+)}(\vec{r}, t) = \hat{\mathbf{E}}(\vec{r}, t) - \hat{\mathbf{E}}_w(\vec{r}, t) \quad (\text{B.2})$$

with the total positive frequency electric field expressed in the interaction picture in terms of plane wave annihilation operators as

$$\hat{\mathbf{E}}^{(+)}(\vec{r}, t) = i \int d^3k \sum_{\lambda} \vec{\varepsilon}_{\lambda}(\hat{k}) \mathcal{E}(ck) e^{i\vec{k} \cdot \vec{r}} e^{-ickt} \hat{a}_{\lambda}(\vec{k}) \quad (\text{B.3})$$

The atom field interaction in the interaction picture is given in the electric dipole and rotating wave approximations by

$$\hat{V}(t) = - \sum_{\mu} \left(\hat{\mathbf{d}}_{(a,c)}^{(-)\mu}(t) \cdot \hat{\mathbf{E}}^{(+)}(\vec{r}_{\mu}, t) + \hat{\mathbf{d}}_{(b,c)}^{(-)\mu}(t) \cdot \hat{\mathbf{E}}^{(+)}(\vec{r}_{\mu}, t) \right) + h.c. , \quad (\text{B.4})$$

where $\hat{\mathbf{d}}_{(f,f')}^{(-)}(t)$ is the negative frequency component of the dipole operator coupling levels $|f\rangle$ and $|f'\rangle$. These dipole operators may be expressed in terms of atomic coherences as in Eq. (2.39) in Chapter 2.

From the interaction picture Hamiltonian, we arrive at the Heisenberg equation of motion for the slowly varying write field envelope

$$\left(\frac{\partial}{\partial t} + c \frac{\partial}{\partial z} \right) \hat{\varphi}_{\alpha}^{(w)}(z, t) = i \sqrt{\frac{ck_w}{2\hbar\epsilon_0}} e^{-ik_w z} e^{i\Delta_w t} \tilde{\mathcal{P}}_{(a,c)\alpha}^{(+)}(z, t), \quad (\text{B.5})$$

where

$$\tilde{\mathcal{P}}_{(f,f')\alpha}^{(+)}(z, t) \equiv \sum_{\mu=1}^N \vec{\xi}_{\alpha}^* \cdot \tilde{\mathbf{d}}_{(f,f')}^{(+)(\mu)}(t) \phi^{(w)*}(\vec{r}_{\mu}) \delta\left(r_{\parallel}^{(w)} - \hat{k}_w \cdot \vec{r}_{\mu}\right), \quad (\text{B.6})$$

is the slowly varying positive frequency linear polarization density interacting with the *write* field component with helicity α , and $\tilde{\mathbf{d}}_{(f,f')}^{(+)(\mu)}(t) = \exp i((\omega_{f'} - \omega_f)t) \hat{\mathbf{d}}_{(f,f')}^{(+)(\mu)}(t)$ is the slowly varying dipole operator connecting levels $|f\rangle$ and $|f'\rangle$.

B.1 Atomic Coherence Equations of Motion

In this Section we write the equations of motion for the individual atomic coherences.

For a general slowly varying coherence between states $|f_1, m_1\rangle$ and $|f_2, m_2\rangle$, we have the Heisenberg equation of motion,

$$\begin{aligned} \frac{d\tilde{\sigma}_{f_1, m_1; f_2, m_2}^{(\mu)}(t)}{dt} &= \frac{i}{\hbar} \left[\tilde{\sigma}_{f_1, m_1; f_2, m_2}(t), \hat{\mathbf{d}}^{(+)\mu}(t) \right] \cdot \left(\hat{\mathbf{E}}_w^{(-)}(\vec{r}_\mu, t) + \hat{\mathbf{E}}_R^{(-)}(\vec{r}_\mu, t) \right) \\ &+ \frac{i}{\hbar} \left[\tilde{\sigma}_{f_1, m_1; f_2, m_2}(t), \hat{\mathbf{d}}^{(-)\mu}(t) \right] \\ &\cdot \left(\hat{\mathbf{E}}_w^{(+)}(\vec{r}_\mu, t) + \hat{\mathbf{E}}_R^{(+)}(\vec{r}_\mu, t) \right). \end{aligned} \quad (\text{B.7})$$

Below, we write the equations of motion for the slowly varying Zeeman coherences, optical coherences, and the hyperfine coherences between levels $|a\rangle$ and $|b\rangle$. The Heisenberg equations of motion for the Zeeman coherences are as follows:

$$\begin{aligned} \frac{d\tilde{\sigma}_{a, m_1; a, m_2}^{(\mu)}(t)}{dt} &= \\ &ie^{ik_w z_\mu} \sum_{\alpha=-1}^1 C_{m_2 \alpha}^{F_a \ 1 \ F_c} e^{i\Delta t} \tilde{\sigma}_{a, m_1; c, m_2 + \alpha}(t) \hat{\Omega}_{(a, c) \alpha}^{(w) \dagger}(\vec{r}, t) \\ &- ie^{ik_w z_\mu} \sum_{\alpha=-1}^1 C_{m_1 \alpha}^{F_a \ 1 \ F_c} e^{-i\Delta t} \tilde{\sigma}_{c, m_1 + \alpha; a, m_2}(t) \hat{\Omega}_{(a, c) \alpha}(\vec{r}_\mu, t) \\ &+ \sum_{\alpha=-1}^1 C_{m_2 \alpha}^{F_a \ 1 \ F_c} \tilde{\sigma}_{a, m_1; c, m_2 + \alpha}(t) \\ &\times \int d^3k \sum_{\lambda} \left(\vec{\xi}_\alpha \cdot \vec{\varepsilon}_\lambda(\hat{k}) \right) \mathcal{G}_{(a, c)}^*(ck) e^{-i\vec{k} \cdot \vec{r}_\mu} e^{i(ck - (\omega_c - \omega_a))t} \tilde{a}_\lambda^\dagger(\vec{k}, t) \\ &+ \sum_{\alpha=-1}^1 C_{m_1 \alpha}^{F_a \ 1 \ F_c} \tilde{\sigma}_{c, m_1 + \alpha; a, m_2}(t) \\ &\times \int d^3k \sum_{\lambda} \left(\vec{\xi}_\alpha^* \cdot \vec{\varepsilon}_\lambda(\hat{k}) \right) \mathcal{G}_{(a, c)}(ck) e^{i\vec{k} \cdot \vec{r}_\mu} e^{-i(ck - (\omega_c - \omega_a))t} \tilde{a}_\lambda(\vec{k}, t), \end{aligned} \quad (\text{B.8})$$

$$\begin{aligned}
& \frac{d\tilde{\sigma}_{b,m_1; b,m_2}^\mu(t)}{dt} \\
&= \sum_{\alpha=-1}^1 C_{m_2 \alpha}^{F_b \ 1 \ F_c} \tilde{\sigma}_{b,m_1; c,m_2+\alpha}(t) \\
&\quad \times \int d^3k \sum_{\lambda} \left(\vec{\xi}_{\alpha} \cdot \vec{\varepsilon}_{\lambda}(\hat{k}) \right) \mathcal{G}_{(b,c)}^*(ck) e^{-i\vec{k} \cdot \vec{r}_{\mu}} e^{i(ck - (\omega_c - \omega_b))t} \tilde{a}_{\lambda}^{\dagger}(\vec{k}, t) \\
&+ \sum_{\alpha=-1}^1 C_{m_1 \alpha}^{F_b \ 1 \ F_c} \tilde{\sigma}_{c,m_1+\alpha; b,m_2}(t) \\
&\quad \times \int d^3k \sum_{\lambda} \left(\vec{\xi}_{\alpha}^* \cdot \vec{\varepsilon}_{\lambda}(\hat{k}) \right) \mathcal{G}_{(b,c)}(ck) e^{i\vec{k} \cdot \vec{r}_{\mu}} e^{-i(ck - (\omega_c - \omega_b))t} \tilde{a}_{\lambda}(\vec{k}, t), \quad (\text{B.9})
\end{aligned}$$

and

$$\begin{aligned}
& \frac{d\tilde{\sigma}_{c,m_1; c,m_2}^\mu(t)}{dt} \\
&= \sum_{\alpha} C_{m_1-\alpha}^{F_a \ 1 \ F_c} e^{i\Delta_w t} \tilde{\sigma}_{a,m_1-\alpha; c,m_2}(t) \\
&\quad \times \left[\int d^3k \sum_{\lambda} \left(\vec{\xi}_{\alpha} \cdot \vec{\varepsilon}_{\lambda}(\hat{k}) \right) \mathcal{G}_{(a,c)}^*(ck) e^{-i\vec{k} \cdot \vec{r}_{\mu}} e^{ic(k-k_w)t} \tilde{a}_{\lambda}^{\dagger}(\vec{k}, t) \right. \\
&\quad \left. - i e^{-ik_w z} \hat{\Omega}_{(a,c)\alpha}^{(w)\dagger}(\vec{r}, t) \right] \\
&+ \sum_{\alpha=-1}^1 C_{m_1-\alpha}^{F_b \ 1 \ F_c} e^{i\Delta_w t} \tilde{\sigma}_{b,m_1-\alpha; c,m_2}(t) \\
&\quad \times \int d^3k \sum_{\lambda} \left(\vec{\xi}_{\alpha} \cdot \vec{\varepsilon}_{\lambda}(\hat{k}) \right) \mathcal{G}_{(b,c)}^*(ck) e^{-i\vec{k} \cdot \vec{r}_{\mu}} e^{i(ck - (\Delta_w + \omega_c - \omega_b))t} \tilde{a}_{\lambda}^{\dagger}(\vec{k}, t) \\
&- \sum_{\alpha=-1}^1 C_{m_2-\alpha}^{F_a \ 1 \ F_c} e^{-i\Delta_w t} \tilde{\sigma}_{c,m_1; a,m_2-\alpha}(t) \\
&\quad \times \left[\int d^3k \sum_{\lambda} \left(\vec{\xi}_{\alpha}^* \cdot \vec{\varepsilon}_{\lambda}(\hat{k}) \right) \mathcal{G}_{(a,c)}(ck) e^{i\vec{k} \cdot \vec{r}_{\mu}} e^{-ic(k-k_w)t} \tilde{a}_{\lambda}(\vec{k}, t) \right. \\
&\quad \left. - i e^{ik_w z} \hat{\Omega}_{(a,c)\alpha}^{(w)}(\vec{r}, t) \right] \\
&- \sum_{\alpha=-1}^1 C_{m_2-\alpha}^{F_b \ 1 \ F_c} e^{-i\Delta_w t} \tilde{\sigma}_{c,m_1; b,m_2-\alpha}(t) \\
&\quad \times \int d^3k \sum_{\lambda} \left(\vec{\xi}_{\alpha}^* \cdot \vec{\varepsilon}_{\lambda}(\hat{k}) \right) \mathcal{G}_{(b,c)}(ck) e^{i\vec{k} \cdot \vec{r}_{\mu}} \\
&\quad \times e^{-i(ck - (\Delta_w + \omega_c - \omega_b))t} \tilde{a}_{\lambda}(\vec{k}, t), \quad (\text{B.10})
\end{aligned}$$

where $\tilde{a}_\lambda(\vec{k}, t) \equiv e^{ickt} \hat{a}_\lambda(\vec{k}, t)$ is the slowly varying annihilation operator for a photon of wave vector \vec{k} and polarization $\vec{\epsilon}_\lambda(\hat{k})$,

$$\hat{\Omega}_{(a,c)\alpha}^{(w)}(\vec{r}, t) \equiv \left(c \left\| \hat{\mathbf{d}} \right\| a \right) \sqrt{\frac{ck_w}{2\hbar\epsilon_0}} \phi^{(w)}(\vec{r}) \hat{\varphi}_\alpha^{(w)}(z, t) \quad (\text{B.11})$$

is the Rabi frequency operator of the pump field of helicity α on the $|a\rangle \leftrightarrow |c\rangle$ transition, and $\mathcal{G}_{(f,f')}(ck) \equiv \left(f' \left\| \hat{\mathbf{d}} \right\| f \right) \mathcal{E}(ck)/\hbar$, is the coupling constant between the quantum field and on the $|f\rangle \leftrightarrow |f'\rangle$ transition.

The Heisenberg equations for the optical coherences between the ground levels $|a\rangle, |b\rangle$ and the excited level $|c\rangle$ are given by

$$\begin{aligned} & e^{i\Delta_w t} \frac{d\tilde{\sigma}_{a,m_1; c, m_2}^{(\mu)}(t)}{dt} \\ &= - \sum_{\alpha=-1}^1 C_{m_2-\alpha \alpha m_2}^{F_b \ 1 \ F_c} \tilde{\sigma}_{a, m_1; b, m_2-\alpha}(t) \\ & \quad \times \int d^3k \sum_{\lambda} \left(\vec{\xi}_\alpha^* \cdot \vec{\epsilon}_\lambda(\hat{k}) \right) \mathcal{G}_{(b,c)}(ck) e^{i\vec{k} \cdot \vec{r}_\mu} e^{-i(ck - (\Delta_w + \omega_c - \omega_b))t} \tilde{a}_\lambda(\vec{k}, t) \\ &+ \sum_{\alpha=-1}^1 \left(C_{m_2-\alpha \alpha m_2}^{F_a \ 1 \ F_c} \tilde{\sigma}_{a, m_1; a, m_2-\alpha}(t) - C_{m_1 \alpha m_1+\alpha}^{F_a \ 1 \ F_c} \tilde{\sigma}_{c, m_1+\alpha; c, m_2}(t) \right) \\ & \quad \times \left[i e^{ik_w z} \hat{\Omega}_{(a,c)\alpha}^{(w)}(\vec{r}_\mu, t) \right. \\ & \quad \left. - \int d^3k \sum_{\lambda} \left(\vec{\xi}_\alpha^* \cdot \vec{\epsilon}_\lambda(\hat{k}) \right) \mathcal{G}_{(a,c)}(ck) e^{i\vec{k} \cdot \vec{r}_\mu} e^{-ic(k-k_w)t} \tilde{a}_\lambda(\vec{k}, t) \right], \quad (\text{B.12}) \end{aligned}$$

and

$$\begin{aligned}
& e^{i\Delta_w t} \frac{d\tilde{\sigma}_{b,m_1; c,m_2}^\mu(t)}{dt} \\
&= \sum_{\alpha=-1}^1 C_{m_2-\alpha \alpha m_2}^{F_a \ 1 \ F_c} \tilde{\sigma}_{b,m_1; a,m_2-\alpha}(t) \\
&\quad \times \left[i e^{ik_w z_\mu} \hat{\Omega}_{(a,c)\alpha}^{(w)}(\vec{r}_\mu, t) \right. \\
&\quad \left. - \int d^3k \sum_{\lambda} \left(\vec{\xi}_\alpha^* \cdot \vec{\varepsilon}_\lambda(\hat{k}) \right) \mathcal{G}_{(a,c)}(ck) e^{i\vec{k} \cdot \vec{r}_\mu} e^{ic(k-k_w)t} \tilde{a}_\lambda(\vec{k}, t) \right] \\
&\quad - \sum_{\alpha=-1}^1 \left(C_{m_2-\alpha \alpha m_2}^{F_b \ 1 \ F_c} \tilde{\sigma}_{b,m_1; b,m_2-\alpha}(t) - C_{m_1 \alpha m_1+\alpha}^{F_b \ 1 \ F_c} \tilde{\sigma}_{c,m_1+\alpha; c,m_2}(t) \right) \\
&\quad \times \int d^3k \sum_{\lambda} \left(\vec{\xi}_\alpha^* \cdot \vec{\varepsilon}_\lambda(\hat{k}) \right) \mathcal{G}_{(b,c)}(ck) e^{i\vec{k} \cdot \vec{r}_\mu} e^{-i(ck-(\Delta_w+\omega_c-\omega_b))t} \tilde{a}_\lambda(\vec{k}, t) \quad (\text{B.13})
\end{aligned}$$

Finally, the hyperfine coherences between levels $|a\rangle$ and $|b\rangle$ obey the equation of motion

$$\begin{aligned}
& \frac{d\tilde{\sigma}_{a,m_1; b,m_2}^\mu(t)}{dt} \\
&= \sum_{\alpha=-1}^1 C_{m_2 \alpha m_2+\alpha}^{F_b \ 1 \ F_c} e^{i\Delta_w t} \tilde{\sigma}_{a,m_1; c,m_2+\alpha}^\mu(t) \\
&\quad \times \int d^3k \sum_{\lambda} \left(\vec{\xi}_\alpha \cdot \vec{\varepsilon}_\lambda(\hat{k}) \right) \mathcal{G}_{(b,c)}^*(ck) e^{-i\vec{k} \cdot \vec{r}_\mu} e^{i(ck-(\Delta_w+\omega_c-\omega_b))t} \tilde{a}_\lambda^\dagger(\vec{k}, t) \\
&\quad - \sum_{\alpha=-1}^1 C_{m_1 \alpha m_1+\alpha}^{F_a \ 1 \ F_c} e^{-i\Delta_w t} \tilde{\sigma}_{c,m_1+\alpha; b,m_2}(t) \\
&\quad \times \left[i e^{ik_w z_\mu} \hat{\Omega}_{(a,c)\alpha}^{(w)}(\vec{r}, t) \right. \\
&\quad \left. - \int d^3k \sum_{\lambda} \left(\vec{\xi}_\alpha^* \cdot \vec{\varepsilon}_\lambda(\hat{k}) \right) \mathcal{G}_{(a,c)}(ck) e^{i\vec{k} \cdot \vec{r}_\mu} e^{-ic(k-k_w)t} \hat{a}_\lambda(\vec{k}, t) \right]. \quad (\text{B.14})
\end{aligned}$$

B.2 Adiabatic Elimination of the Optical Coherences

In this section, we give an overview of the argument allowing one to adiabatically eliminate the optical coherences and populations of level $|c\rangle$ from the dynamics. We

begin by examining the equations of motion for the coherences within the ground state manifold and the pump field envelope. We identify the conditions under which these variables are time independent, i.e., are in a steady state. This steady state is parameterized by the controlled variables of the system, such as the pump field intensity. According to the principle of adiabaticity, provided the controlled system variables vary sufficiently slowly, the system variables should follow the steady state corresponding to those changing parameters.

For the ground level coherences and pump field to remain time independent, it is necessary that the optical coherences satisfy the following conditions:

$$\frac{d}{dt} \left(e^{i\Delta_w t} \tilde{\sigma}_{a,m_1; c,m_2}^\mu(t) \right) = 0, \quad (\text{B.15})$$

and

$$\frac{d}{dt} \left(e^{i\Delta_w t} \tilde{\sigma}_{b,m_1; c,m_2}^\mu(t) \right) = 0. \quad (\text{B.16})$$

From these conditions and the above equations of motion for the optical coherences, we may express the optical coherences in terms of the hyperfine coherences and electric field. These optical coherences are given in the adiabatic limit by

$$\begin{aligned} & \tilde{\sigma}_{a,m_a; c,m_c}^\mu(t) \\ &= -\frac{1}{\hbar\Delta_w} \left[\tilde{\sigma}_{a,m_a; c,m_c}^\mu(t), \hat{\mathbf{d}}^{(-)\mu}(t) \cdot \left(\hat{\mathbf{E}}_w^{(+)}(\vec{r}_\mu, t) + \hat{\mathbf{E}}_R^{(+)}(\vec{r}_\mu, t) \right) \right] \\ &= -\frac{1}{\hbar\Delta_w} \left[\tilde{\sigma}_{a,m_a; c,m_c}^{(\mu)}(t), \hat{\mathbf{d}}_{(a,c)}^{(-)\mu} \right] \cdot \left(\hat{\mathbf{E}}_w^{(+)}(\vec{r}_\mu, t) + \hat{\mathbf{E}}_R^{(+)}(\vec{r}_\mu, t) \right) \\ &\quad - \frac{1}{\hbar\Delta_w} \tilde{\sigma}_{a,m_a; c,m_c}^\mu(t) \left(\hat{\mathbf{d}}_{(b,c)}^{(-)\mu} \cdot \hat{\mathbf{E}}_R^{(+)}(\vec{r}_\mu, t) \right) \end{aligned} \quad (\text{B.17})$$

and

$$\begin{aligned} & \tilde{\sigma}_{b,m_b; c,m_c}^\mu(t) \\ &= -\frac{1}{\hbar\Delta_w} e^{i(\omega_c - \omega_a)t} \tilde{\sigma}_{b,m_b; c,m_c}^\mu(t) \left(\hat{\mathbf{d}}_{(a,c)}^{(-)\mu} \cdot \left(\hat{\mathbf{E}}_w^{(+)}(\vec{r}_\mu, t) + \hat{\mathbf{E}}_R^{(+)}(\vec{r}_\mu, t) \right) \right) \\ &\quad - \frac{1}{\hbar\Delta_w} \left[\tilde{\sigma}_{b,m_b; c,m_c}^\mu(t), \left(\hat{\mathbf{d}}_{(b,c)}^{(-)\mu} \cdot \hat{\mathbf{E}}_R^{(+)}(\vec{r}_\mu, t) \right) \right]. \end{aligned} \quad (\text{B.18})$$

Substituting Eqs. (B.17) and (B.18) into the dipole interaction Hamiltonian (Eq. (B.4)), we arrive at an effective Hamiltonian for the dynamics of the field interacting with levels $|a\rangle$ and $|b\rangle$. We write the effective Hamiltonian as

$$\begin{aligned}\hat{V}(t) = & \sum_{\mu=1}^N \left[\frac{1}{\hbar\Delta_w} \left(\hat{\mathbf{d}}_{(a,c)}^{(+)\mu}(t) \cdot \left(\hat{\mathbf{E}}_w^{(-)}(\vec{r}_\mu, t) + \hat{\mathbf{E}}_R^{(-)}(\vec{r}_\mu, t) \right) \right) \right. \\ & \times \left(\hat{\mathbf{d}}_{(a,c)}^{(-)\mu}(t) \cdot \left(\hat{\mathbf{E}}_w^{(+)}(\vec{r}_\mu, t) + \hat{\mathbf{E}}_R^{(+)}(\vec{r}_\mu, t) \right) \right) \\ & + \frac{2}{\hbar\Delta_w} \left(\hat{\mathbf{d}}_{(a,c)}^{(+)\mu}(t) \cdot \left(\hat{\mathbf{E}}_w^{(-)}(\vec{r}_\mu, t) + \hat{\mathbf{E}}_R^{(-)}(\vec{r}_\mu, t) \right) \right) \\ & \times \left(\hat{\mathbf{d}}_{(b,c)}^{(-)\mu}(t) \cdot \hat{\mathbf{E}}_R^{(+)}(\vec{r}_\mu, t) \right) \\ & \left. + \frac{1}{\hbar\Delta_w} \left(\hat{\mathbf{d}}_{(b,c)}^{(+)}(t) \cdot \hat{\mathbf{E}}_R^{(-)}(\vec{r}_\mu, t) \right) \left(\hat{\mathbf{d}}_{(b,c)}^{(-)\mu}(t) \cdot \hat{\mathbf{E}}_R^{(+)}(\vec{r}_\mu, t) \right) \right] + h.c.. \quad (\text{B.19})\end{aligned}$$

We may neglect terms in which only the reservoir field operators $\hat{\mathbf{E}}_R^{(\pm)}(\vec{r}_\mu, t)$ appear since these terms contribute to the Lamb shift, or radiation shift, which has already been included in the bare atomic Hamiltonian in Chapter 2 Section 2.1.1. We then arrive at the final effective Hamiltonian describing off resonant light scattering from a cold atomic gas

$$\hat{V}(t) = \hat{V}_{Stark}(t) + \hat{V}_{Rayleigh}(t) + \hat{V}_{Raman}(t), \quad (\text{B.20})$$

where

$$\hat{V}_{Stark}(t) = \sum_{\mu=1}^N \frac{2}{\hbar\Delta_w} \left(\hat{\mathbf{d}}_{(a,c)}^{(+)\mu}(t) \cdot \hat{\mathbf{E}}_w^{(-)}(\vec{r}_\mu, t) \right) \left(\hat{\mathbf{d}}_{(a,c)}^{(-)\mu}(t) \cdot \hat{\mathbf{E}}_w^{(+)}(\vec{r}_\mu, t) \right) \quad (\text{B.21})$$

describes the ac Stark shift, an effective shift of the energies of the states in ground level $|a\rangle$ resulting from interaction with the *write* field,

$$\hat{V}_{Rayleigh}(t) = \frac{2}{\hbar\Delta_w} \sum_{\mu=1}^N \left(\hat{\mathbf{d}}_{(a,c)}^{(+)\mu}(t) \cdot \hat{\mathbf{E}}_R^{(-)}(\vec{r}_\mu, t) \right) \left(\hat{\mathbf{d}}_{(a,c)}^{(-)\mu}(t) \cdot \hat{\mathbf{E}}_w^{(+)}(\vec{r}_\mu, t) \right) + h.c. \quad (\text{B.22})$$

describes Rayleigh scattering from the ensemble, and

$$\hat{V}_{Raman}(t) = \frac{2}{\hbar\Delta_w} \sum_{\mu=1}^N \left(\hat{\mathbf{d}}_{(b,c)}^{(+)\mu}(t) \cdot \hat{\mathbf{E}}_R^{(-)}(\vec{r}_\mu, t) \right) \left(\hat{\mathbf{d}}_{(a,c)}^{(-)\mu}(t) \cdot \hat{\mathbf{E}}_w^{(+)}(\vec{r}_\mu, t) \right) + h.c. \quad (\text{B.23})$$

is the Raman scattering interaction, in which a scattered photon results in an atom being transferred from level $|a\rangle$ to level $|b\rangle$.

APPENDIX C

DYNAMICS OF LIGHT PROPAGATION IN A GAS OF THREE-LEVEL ATOMS

In this appendix, we provide additional information on the theory of electromagnetically induced transparency (EIT) for atoms with Zeeman degeneracy. We begin by deriving a set of Heisenberg Langevin equations that describe the propagation of a quantized signal field through an atomic sample in the presence of a control field. To account for stray magnetic fields in the system, we include a interaction with a constant, dc, magnetic field. We then describe how the equations of motion can be solved numerically in the limit of a classical signal field. These simulations were used to produce the numerical predictions made in Chapters 6 and 7. When a judicious choice of atomic levels and field polarizations is made, we show that the medium supports EIT for the signal field. We then show that in an adiabatic limit, the propagation, storage, and retrieval dynamics of the quantum field within the atomic sample is well described by the dark state polariton mechanism [19]. The dark state polariton was first introduced in the context of electromagnetically induced transparency in nondegenerate three-level atoms by Fleischhauer and Lukin [69, 75].

C.1 Model Description

In this Section, we introduce the model used in Chapters 6 and 7 to characterize the signal propagation dynamics leading to EIT in a collection of atoms with Zeeman degeneracy.

We consider an ensemble of N atoms with three hyperfine levels in a Λ configuration labeled by $|a\rangle$, $|b\rangle$, and $|c\rangle$ with total angular momenta F_a , F_b , and F_c and energies $\hbar\omega_a$, $\hbar\omega_b$, and $\hbar\omega_c$, respectively. An atom, labeled by index μ ($\mu = 1 \dots N$), rests at position \vec{r}_μ . We assume the atomic velocities are sufficiently low that we may take the atoms to be stationary. The atomic positions $\{\vec{r}_\mu\}$ are treated as classical independent identically distributed random variables with an associated probability density $n(\vec{r})/N$, where $n(\vec{r})$ is the atomic number density. The atoms interact with a classical control field resonant on the $|a\rangle \leftrightarrow |c\rangle$ transition and a quantized signal field resonant on the $|b\rangle \leftrightarrow |c\rangle$ transition. The signal and control fields both satisfy the properties of narrow bandwidth *system* fields discussed in Chapter 2. We assume the signal field has a carrier wave vector $\vec{k}_s = [(\omega_c - \omega_b)/c]\hat{z}$. The signal field has the time independent transverse spatial profile $\phi^{(s)}(\vec{r})$, which satisfies the normalization condition $\int d^2k_\perp^{(s)2} |\phi^{(s)}(\vec{r})|^2 = 1$, where for a vector \vec{v} , $\vec{v}_\perp^{(s)} \equiv \vec{v} - \hat{k}_s \cdot \vec{v}$. The positive frequency component of the signal electric field is given in the interaction picture by

$$\hat{\mathbf{E}}_s^{(+)}(\vec{r}, t) = (2\pi)^{3/2} \mathcal{E}(ck_s) e^{i\vec{k}_s \cdot \vec{r}} e^{-ick_s t} \phi^{(s)}(\vec{r}) \sum_{\alpha=\pm 1} \vec{\xi}_\alpha \hat{\varphi}_\alpha^{(s)}(z, t), \quad (\text{C.1})$$

where $\hat{\varphi}_\alpha^{(s)}(z, t)$ is the linear photon density annihilation operator for signal photons at position $z = \vec{r} \cdot \hat{z}$ and helicity α . These photon density operators obey the bosonic equal time commutation relations

$$\left[\hat{\varphi}_\alpha^{(s)}(z, t), \hat{\varphi}_\beta^{(s)\dagger}(z', t) \right] = \delta_{\alpha,\beta} \delta(z - z'). \quad (\text{C.2})$$

Their definitions in terms of plane wave operators is given in Eq. (2.63) of Chapter 2.

The control field propagates nearly parallel to the z -axis with a wave vector $\vec{k}_c = [(\omega_c - \omega_a)/c]\hat{k}_c$. We will make the paraxial approximation on the control field helicities $\vec{e}_\alpha(\hat{k}_s) \approx \vec{\xi}_\alpha$, where $\vec{\xi}_\alpha$ are the laboratory fixed spherical basis vectors (Eq. (2.31)). We allow the freedom in the choice of control field propagation direction so that we may adequately describe the off axis configuration used in the experiments described

in Chapters 6 through 8. The positive frequency component of the classical control field is given by

$$\vec{E}_c^{(+)}(\vec{r}, t) \equiv \vec{e}_c e^{i\vec{k}_c \cdot \vec{r}} e^{-ick_c t} E_c(t), \quad (\text{C.3})$$

where \vec{e}_c is the control field polarization, and $E_c(t)$ is the slowly varying control electric field. We assume E_c is constant over the width of the transverse spatial mode of the signal. Furthermore, we assume $E_c(t)$ varies sufficiently slowly that we may consider it constant over the length of the ensemble.

The dynamics of the field-ensemble system are governed by the interaction picture Hamiltonian

$$\hat{V}(t) = \hat{V}_{AS}(t) + \hat{V}_{AC}(t) + \hat{V}_{AR}(t) + \hat{V}_{AB}(t), \quad (\text{C.4})$$

where $\hat{V}_{AS} = -\sum_{\mu=1}^N \hat{\mathbf{d}}^\mu(t) \cdot (\hat{\mathbf{E}}_s^{(+)}(\vec{r}_\mu, t) + \hat{\mathbf{E}}_s^{(-)}(\vec{r}_\mu, t))$ is the interaction of the atoms with the signal field, $\hat{\mathbf{d}}^\mu(t)$ is the electric dipole operator of atom μ (Eq. (2.39)), $\hat{V}_{AC}(t) = -\sum_{\mu=1}^N \hat{\mathbf{d}}^\mu(t) \cdot (\vec{E}_c^{(+)}(\vec{r}_\mu, t) + \vec{E}_c^{(-)}(\vec{r}_\mu, t))$ is the interaction of the atoms with the control field,

$$\hat{V}_{AB}(t) = \sum_{f \in \{a,b,c\}} g_f \mu_B \vec{B} \cdot \left(\sum_{\mu=1}^N \hat{\mathbf{F}}_f^\mu \right) \quad (\text{C.5})$$

is the interaction of the atoms with the constant magnetic field \vec{B} , \vec{F}_f^μ is the projection of the total angular momentum operator of atom μ onto level $|f\rangle$, g_f is the corresponding Landé g factor, and μ_B is the Bohr magneton. As we shall demonstrate later, the associated Larmor precession serves as a possible explanation for the reduction of retrieval efficiency of stored photons over long storage times reported in Chapter 6[22]. The uniform magnetic field also leads to the subsequent revivals in retrieval efficiency discussed in Chapter 7[19, 20]. The interaction of the ensemble with the reservoir of undetected electromagnetic field modes is given by

$$\hat{V}_{AR}(t) = -\frac{1}{\epsilon_0} \sum_{\mu=1}^N \hat{\mathbf{d}}^\mu(t) \cdot \hat{\mathbf{D}}_R(\vec{r}_\mu, t), \quad (\text{C.6})$$

where $\hat{\mathbf{D}}_R(\vec{r}, t) = \epsilon_0(\hat{\mathbf{E}}_R^{(+)}(\vec{r}, t) + h.c.)$ is the electric displacement field of the reservoir, as described in Section 2.1.4 of Chapter 2, the positive frequency electric field operator of the reservoir is given by

$$\hat{\mathbf{E}}_R^{(+)}(\vec{r}, t) = \hat{\mathbf{E}}^{(+)}(\vec{r}, t) - \hat{\mathbf{E}}_s^{(+)}(\vec{r}, t) - \vec{E}_c^{(+)}(\vec{r}, t), \quad (\text{C.7})$$

and $\hat{\mathbf{E}}^{(+)}(\vec{r}, t)$ is the total positive frequency electric field operator (Eq. (2.42)). The reservoir electric field operator can be expanded in terms of plane wave modes as

$$\hat{\mathbf{E}}_R^{(+)}(\vec{r}, t) = i \int d^3k \sum_{\lambda} \vec{\epsilon}_{\lambda}(\hat{k}) \mathcal{E}(ck) e^{i\vec{k} \cdot \vec{r}} e^{-ickt} \delta \hat{a}_{\lambda}(\vec{k}; \vec{r}, t), \quad (\text{C.8})$$

where $\delta \hat{a}_{\lambda}(\vec{k}; \vec{r}, t)$ is the contribution of the plane wave annihilation operator $\hat{a}_{\lambda}(\vec{k})$ to the reservoir field. This operator is given by

$$\begin{aligned} \delta \hat{a}_{\lambda}(\vec{k}; \vec{r}, t) &\equiv \hat{a}_{\lambda}(\vec{k}) - \sum_{\iota \in \{s, c\}} \Theta(\Delta k_{\iota}/2 - |k - k_{\iota}|) \\ &\times f^{(\iota)}(\vec{k}_{\perp}^{(\iota)}) e^{ic \frac{|\vec{k}_{\perp}^{(\iota)}|^2}{2k_{\iota}}} (t - \hat{k}_{\iota} \cdot \vec{r}/c) \hat{a}_{\lambda}^{(\iota)}(k_{\parallel}^{(\iota)}, t - r_{\parallel}^{(\iota)}/c), \end{aligned} \quad (\text{C.9})$$

where $\Theta(k)$ is the Heaviside function, $c\Delta k_{s[c]}$, is the maximum bandwidth of the signal [control] field as discussed in Section 2.1.4 of Chapter 2,

$$f^{(\iota)}(\vec{k}_{\perp}^{(\iota)}) = -\frac{i}{2\pi} e^{i \frac{|\vec{k}_{\perp}^{(\iota)}|^2}{2k_{\iota}}} r_{\parallel}^{(\iota)} \int d^2 r_{\perp} e^{-i\vec{k}_{\perp} \cdot \vec{r}} \phi^{(\iota)}(\vec{r}) \quad (\text{C.10})$$

is the Fourier transform of the transverse mode spatial mode of field $\iota \in \{s, c\}$, $\phi^{(\iota)}(\vec{r})$, and the operator

$$\hat{a}_{\lambda}^{(\iota)}(k_{\parallel}^{(\iota)}, t) \equiv \int d^2 k_{\perp} e^{-ic \frac{|\vec{k}_{\perp}^{(\iota)}|^2}{2k_{\iota}}} t f^{(\iota)*}(\vec{k}_{\perp}^{(\iota)}) \hat{a}_{\lambda}(\vec{k}), \quad (\text{C.11})$$

where, for a vector \vec{v} , $\vec{v} = v_{\parallel}^{(\iota)} \hat{v}_{\iota} + \vec{v}_{\perp}^{(\iota)}$.

Before the signal field interacts with the ensemble each atom μ is prepared in the mixed state

$$\hat{\rho}_0^{\mu} = \sum_{m=-F_b}^{F_b} p_m |b, m\rangle_{\mu} \langle b, m| \quad (\text{C.12})$$

where p_m is the probability that atom μ is in the Zeeman state $|b, m\rangle$. This model of the initial atomic state allows us to account for the two initial conditions considered in this thesis: an unpolarized sample in which $p_m = (2F_b + 1)^{-1}$, and a polarized sample in which atoms are prepared in an initial Zeeman state $|b, M\rangle$, with $p_m = \delta_{mM}$. We will refer to the density matrix

$$\hat{\rho}_{A,vac} = \bigotimes_{\mu=1}^N \hat{\rho}_0^\mu \quad (\text{C.13})$$

as the “atomic vacuum”.

In the remainder of this appendix, we will provide an analysis of this model leading to the phenomenon of EIT and the dark-state polariton mechanism for signal storage within the atomic ensemble. In the next section, we consider the interaction of the atoms in the reservoir, and derive the contribution of this interaction to the atomic coherence equations of motion. Section C.3 presents the Heisenberg Langevin equations describing the evolution of the atomic variables as the atoms interact with the signal and *control* fields. We pay particular attention to the limit of a weak signal field, where the atomic level populations remain essentially unchanged. With the weak signal limit, we arrive at the coupled equations between for the signal field and collective atomic excitations presented in Section C.4. From these equations, we will examine the dynamics of signal field propagation in the classical limit, and derive the conditions for EIT. The dark-state polariton mechanism for storage and retrieval of the signal then arises from the adiabatic treatment of Section C.5.

C.2 Interaction of the Atoms with the Reservoir: Spontaneous Emission

In this section, we will provide a review of the dynamics of spontaneous decay of atomic excitations. The decay of optical atomic coherences results from an interaction of the atomic variables with the reservoir of undetected field modes. In the absence of

the control field in our system, it is this spontaneous emission that causes the atomic medium to be opaque to the propagating signal, as observed in Figure 6.2.

Let us consider the Heisenberg equation of motion for the slowly varying atomic coherences $\tilde{\sigma}_{f_1, m_1; f_2, m_2}(t) = \exp(i(\omega_{f_2} - \omega_{f_1})t) \hat{\sigma}_{f_1, m_1; f_2, m_2}(t)$,

$$\begin{aligned} \frac{d\tilde{\sigma}_{f_1, m_1; f_2, m_2}^\mu}{dt} &= \frac{1}{i\hbar} \left[\tilde{\sigma}_{f_1, m_1; f_2, m_2}^\mu(t), \hat{V}_{AS}(t) + \hat{V}_{AC}(t) + \hat{V}_{AB}(t) \right] \\ &\quad + \frac{1}{i\hbar} \left[\tilde{\sigma}_{f_1, m_1; f_2, m_2}^\mu(t), \hat{V}_{AR}(t) \right] \end{aligned} \quad (\text{C.14})$$

with the contribution of the reservoir interaction given by

$$\begin{aligned} &\frac{1}{i\hbar} \left[\tilde{\sigma}_{f_1, m_1; f_2, m_2}^\mu(t), \hat{V}_{AR}(t) \right] \\ &= \frac{i}{\hbar} \sum_{\mu=1}^N \left[\tilde{\sigma}_{f_1, m_1; f_2, m_2}(t), \hat{\mathbf{d}}^\mu(t) \right] \cdot \left(\hat{\mathbf{E}}_R^{(+)}(\vec{r}_\mu, t) + \hat{\mathbf{E}}_R^{(-)}(\vec{r}_\mu, t) \right), \end{aligned} \quad (\text{C.15})$$

where $\hat{\mathbf{E}}_R^{(-)}(\vec{r}, t) = \hat{\mathbf{E}}_R^{(+)\dagger}(\vec{r}, t)$ is the negative frequency component of the reservoir field.

The equation of motion for the coherence (Eq. (C.14)) depends on both the system fields (signal and control) and the reservoir field modes. Ideally, we would like the atomic coherences and system fields to form a closed set of equations so that either analytic or numerical solutions become more tractable. To accomplish this, we approximate the solutions of the reservoir fields, and substitute these solutions into Eq. (C.14). First, we consider the equation of motion for the slowly varying plane wave operator $\tilde{a}_\lambda(\vec{k}, t) \equiv e^{ickt} \hat{a}_\lambda(\vec{k}, t)$. We note that in the interaction picture, $\tilde{a}_\lambda(\vec{k}, t) = \hat{a}_\lambda(\vec{k})$. This operator evolves in the Heisenberg picture according to

$$\frac{d\tilde{a}_\lambda(\vec{k}, t)}{dt} = \frac{\mathcal{E}(ck)}{\hbar} \sum_{\mu=1}^N e^{-i\vec{k} \cdot \vec{r}_\mu} \sum_{\{f, f': \omega_{f'} > \omega_f\}} \vec{\varepsilon}_\lambda(\hat{k}) \cdot \left(\hat{\mathbf{d}}_{(f, f')}^{(+)\mu}(t) + \hat{\mathbf{d}}_{(f, f')}^{(-)\mu}(t) \right). \quad (\text{C.16})$$

Solving Eq. (C.16), we find

$$\begin{aligned}
\tilde{a}_\lambda(\vec{k}, t) &= \tilde{a}_\lambda(\vec{k}, 0) \\
&+ \frac{\mathcal{E}(ck)}{\hbar} \sum_{\mu=1}^N e^{-i\vec{k} \cdot \vec{r}_\mu} \sum_{\{f, f': \omega_{f'} > \omega_f\}} e^{i[ck - (\omega_{f'} - \omega_f)]t} \\
&\times \int_0^t d\tau e^{-i(ck - (\omega_{f'} - \omega_f))\tau} \vec{\varepsilon}_\lambda(\hat{k}) \cdot \tilde{\mathbf{d}}_{(f, f')}^{(+)\mu}(t - \tau) \\
&+ \frac{\mathcal{E}(ck)}{\hbar} \sum_{\mu=1}^N e^{-i\vec{k} \cdot \vec{r}_\mu} \sum_{\{f, f': \omega_{f'} > \omega_f\}} e^{i[ck + (\omega_{f'} - \omega_f)]t} \\
&\times \int_0^t d\tau e^{-i(ck + (\omega_{f'} - \omega_f))\tau} \vec{\varepsilon}_\lambda(\hat{k}) \cdot \tilde{\mathbf{d}}_{(f, f')}^{(-)\mu}(t - \tau), \quad (C.17)
\end{aligned}$$

where, again, $\tilde{\mathbf{d}}_{(f, f')}^{(+)\mu}(t) \equiv \exp(i(\omega_{f'} - \omega_f)t) \hat{\mathbf{d}}_{(f, f')}^{(+)\mu}(t)$ is the slowly varying dipole operator connecting levels $|f\rangle$ and $|f'\rangle$. When we substitute Eq. (C.17) into the equation of motion for the atomic coherence (Eq. (C.16)), we find that the equation of motion contains integrals of the form

$$\begin{aligned}
\hat{\mathbf{G}}_{\mu, \nu}^{s_1, s_2}(t; f, f') &\equiv \sum_\lambda \int d^3k \left(\frac{\mathcal{E}(ck)}{\hbar} \right)^2 e^{is_1\vec{k} \cdot (\vec{r}_\mu - \vec{r}_\nu)} \vec{\varepsilon}_\lambda(\hat{k}) \\
&\times \int_0^t d\tau e^{-i(s_1ck - s_2(\omega_{f'} - \omega_f))\tau} \left(\vec{\varepsilon}_\lambda(\hat{k}) \cdot \tilde{\mathbf{d}}_{(f, f')}^{(s_2)\nu}(t - \tau) \right), \quad (C.18)
\end{aligned}$$

where $s_1, s_2 \in \{\pm 1\}$, and $\mu, \nu \in \{\mu \in \mathbb{N} : \mu \leq N\}$ are atomic indices. These integrals that appear in the equation of motion not only account for the dynamics of a single atom in the reservoir, but also result in an effective interaction between neighboring atoms. It is this interaction that leads to cooperative effects such as superradiance [95, 96, 133, 134, 90], or multiple photon scattering events within the ensemble. In this thesis, however, we assume the atomic gas is sufficiently dilute that we can neglect these multiple scattering effects so that, in essence, each atom sees an independent

reservoir of field modes. The operator quantity $\hat{\mathbf{G}}$ is then approximately

$$\begin{aligned} \hat{\mathbf{G}}_{\mu,\nu}^{s_1,s_2}(t; f, f') &= \delta_{\mu,\nu} \sum_{\lambda} \int d^3k \left(\frac{\mathcal{E}(ck)}{\hbar} \right)^2 \vec{\varepsilon}_{\lambda}(\hat{k}) \\ &\times \int_0^t d\tau e^{-i(s_1ck - s_2(\omega_{f'} - \omega_f))\tau} \left(\vec{\varepsilon}_{\lambda}(\hat{k}) \cdot \tilde{\mathbf{d}}_{(f,f')}^{(s_2)\mu}(t - \tau) \right). \end{aligned} \quad (\text{C.19})$$

This quantity involves an integration of the complex exponential $e^{-i(s_1ck - s_2(\omega_{f'} - \omega_f))\tau}$ over a broad band of wave numbers k . For nonzero delays τ , the wavenumber contributions tend to destructively interfere. As a result, we may make the Markov approximation, assuming that the equation of motion for the coherence at time t depends only on the values of the system variables at that time. We then write

$$\begin{aligned} \hat{\mathbf{G}}_{\mu,\nu}^{s_1,s_2}(t; f, f') &= \delta_{\mu,\nu} \sum_{\lambda} \int d^3k \left(\frac{\mathcal{E}(ck)}{\hbar} \right)^2 \vec{\varepsilon}_{\lambda}(\hat{k}) \left(\vec{\varepsilon}_{\lambda}(\hat{k}) \cdot \tilde{\mathbf{d}}_{(f,f')}^{(s_2)\mu}(t) \right) \\ &\times \int_0^t d\tau e^{-i(s_1ck - s_2(\omega_{f'} - \omega_f))\tau}. \end{aligned} \quad (\text{C.20})$$

Furthermore, we make the approximation on the time integral [16],

$$\begin{aligned} &\int_0^t d\tau e^{-i(s_1ck - s_2(\omega_{f'} - \omega_f))\tau} \\ &\approx \int_0^{\infty} d\tau e^{-i(s_1ck - s_2(\omega_{f'} - \omega_f))\tau} \\ &= \pi\delta(s_1ck - s_2(\omega_{f'} - \omega_f)) - i\text{P.V.} \frac{1}{s_1ck - s_2(\omega_{f'} - \omega_f)} \end{aligned} \quad (\text{C.21})$$

where *P.V.* indicates that the integration over k should be the Cauchy principal value integral.

The final approximation we make in determining the dynamics of an atom interacting with the reservoir is the rotating wave approximation. We assume that we are only interested in time scales much longer than

$$\tau_{RWA} = \frac{2\pi}{\min\{(\omega_f - \omega_{f'}) : f \neq f'\}}, \quad (\text{C.22})$$

and neglect any terms in the equations of motion involving complex exponentials with periods shorter than τ_{RWA} . In the three level system we consider in this appendix,

the minimum energy spacing is the hyperfine splitting of the ground levels: $(\omega_a - \omega_b)/(2\pi) = 3.04 \text{ GHz}$ for ^{85}Rb . This energy splitting is much larger than both the bandwidths of the system fields and the spontaneous emission rate (Eq. (C.25)) [81]. Therefore, we may safely set $\tau_{RWA} = 0.33 \text{ ns} > 2\pi/|\omega_a - \omega_b|$.

In the rotating wave and Markov approximations, we find the contribution of the reservoir interaction to the atomic coherence equations of motion is given by

$$\begin{aligned} & \frac{1}{i\hbar} \left[\tilde{\sigma}_{f,m; f',m'}^\mu, \hat{V}_{AR}(t) \right] \\ & \approx \hat{\zeta}_{f_1,m_1; f_2,m_2}^\mu(t) - \left(\frac{1}{2} (\Gamma_{f_1} + \Gamma_{f_2}) + i(\Delta_{f_1} - \Delta_{f_2}) \right) \tilde{\sigma}_{f_1,m_1; f_2,m_2}(t) \\ & + \sum_{\{f: \omega_{f_1} < \omega_f\}} \delta_{f_1,f_2} \Gamma_{f_1}^f \sum_{\alpha=-1}^1 C_{m_1 \alpha}^{F_{f_1} 1 F_f} C_{m_2 \alpha}^{F_{f_1} 1 F_f} \tilde{\sigma}_{f,m_1+\alpha; f,m_2+\alpha}(t), \quad (\text{C.23}) \end{aligned}$$

where $\hat{\zeta}_{f_1,m_1; f_2,m_2}^\mu(t)$ is the quantum noise operator,

$$\Gamma_{f_1}^f \equiv \frac{4}{3} \frac{(\omega_f - \omega_{f_1})^3}{4\pi\epsilon_0\hbar c^3} \left| \left(f \left\| \hat{\mathbf{d}} \right\| f_1 \right) \right|^2 \quad (\text{C.24})$$

is the spontaneous decay rate from level f to level f_1 ,

$$\Gamma_f \equiv \sum_{\{f': \omega_{f'} < \omega_f\}} \Gamma_{f'}^f \quad (\text{C.25})$$

is the spontaneous emission rate of level f ,

$$\Delta_f \equiv \sum_{f' \neq f} \Delta_{f'}^{f'} \quad (\text{C.26})$$

accounts for a portion of the radiation shift of level $|f\rangle$, and

$$\Delta_{f'}^{f'} \equiv \frac{2}{3\pi} \frac{1}{4\pi\epsilon_0\hbar} \left| \left(f' \left\| \hat{\mathbf{d}} \right\| f \right) \right|^2 \text{P.V.} \int_0^\infty dk \frac{ck^3}{(ck - (\omega_{f'} - \omega_f))} \quad (\text{C.27})$$

is the contribution to the energy shift of level $|f\rangle$ from the level $|f'\rangle$. The noise operator $\hat{\zeta}_{f_1,m_1; f_2,m_2}^\mu(t)$ is given in the rotating wave approximation by

$$\hat{\zeta}_{f_1,m_1; f_2,m_2}^\mu(t) = \sum_{j=1}^4 \hat{\zeta}_{f_1,m_1; f_2,m_2}^{(j)\mu}(t), \quad (\text{C.28})$$

where

$$\begin{aligned}
\hat{\xi}_{f_1, m_1; f_2, m_2}^{(1)\mu}(t) &\equiv \sum_{\{f': \omega_{f_2} < \omega_{f'}\}} \sum_{\alpha=-1}^1 C_{m_2-\alpha}^{F_{f_2} 1 F_{f'}} \\
&\times \left(\int d^3k \sum_{\lambda} \left(\vec{\xi}_{\alpha} \cdot \vec{\varepsilon}_{\lambda}(\hat{k}) \right) \mathcal{G}_{(f_2, f')}^*(ck) e^{-i\vec{k} \cdot \vec{r}} e^{i(ck - (\omega_{f'} - \omega_{f_2}))t} \tilde{a}_{\lambda}^{\dagger}(\vec{k}, 0) \right) \\
&\times \tilde{\sigma}_{f_1, m_1; f', m_2 + \alpha}(t), \tag{C.29a}
\end{aligned}$$

$$\begin{aligned}
\hat{\xi}_{f_1, m_1; f_2, m_2}^{(2)\mu}(t) &\equiv - \sum_{\{f: \omega_f < \omega_{f_2}\}} \sum_{\alpha=-1}^1 C_{m_2-\alpha}^{F_f 1 F_{f_2}} \tilde{\sigma}_{f_1, m_1; f, m_2 - \alpha}(t) \\
&\times \left(\int d^3k \sum_{\lambda} \left(\vec{\xi}_{\alpha}^* \cdot \vec{\varepsilon}_{\lambda}(\hat{k}) \right) \mathcal{G}_{(f, f_2)}(ck) \right. \\
&\quad \left. \times e^{i\vec{k} \cdot \vec{r}} e^{-i[ck - (\omega_{f_2} - \omega_f)]t} \tilde{a}_{\lambda}(\vec{k}, 0) \right), \tag{C.29b}
\end{aligned}$$

$$\begin{aligned}
\hat{\xi}_{f_1, m_1; f_2, m_2}^{(3)\mu}(t) &= \sum_{\{f': \omega_{f_1} < \omega_{f'}\}} \sum_{\alpha=-1}^1 C_{m_1-\alpha}^{F_{f_1} 1 F_{f'}} \tilde{\sigma}_{f', m_1 + \alpha; f_2, m_2}(t) \\
&\times \left(\int d^3k \sum_{\lambda} \left(\vec{\xi}_{\alpha}^* \cdot \vec{\varepsilon}_{\lambda}(\hat{k}) \right) \mathcal{G}_{(f_1, f')}(ck) \right. \\
&\quad \left. \times e^{i\vec{k} \cdot \vec{r}} e^{-i[ck - (\omega_{f'} - \omega_{f_1})]t} \tilde{a}_{\lambda}(\vec{k}, 0) \right), \tag{C.29c}
\end{aligned}$$

and

$$\begin{aligned}
\hat{\xi}_{f_1, m_1; f_2, m_2}^{(4)\mu}(t) &\equiv - \sum_{\{f: \omega_f < \omega_{f_1}\}} \sum_{\alpha=-1}^1 C_{m_1-\alpha}^{F_f 1 F_{f_1}} \\
&\times \left(\int d^3k \sum_{\lambda} \left(\vec{\xi}_{\alpha} \cdot \vec{\varepsilon}_{\lambda}(\hat{k}) \right) \mathcal{G}_{(f, f_1)}^*(ck) e^{-i\vec{k} \cdot \vec{r}} e^{i[ck - (\omega_{f_1} - \omega_f)]t} \tilde{a}_{\lambda}^{\dagger}(\vec{k}, 0) \right) \\
&\times \tilde{\sigma}_{f, m_1 - \alpha; f_2, m_2}(t), \tag{C.29d}
\end{aligned}$$

where $\mathcal{G}_{(f, f')}(ck) \equiv \mathcal{E}(ck) \left(f' \left\| \hat{\mathbf{d}} \right\| f \right) / \hbar$.

We note that we have already included the radiation shift in the bare atomic Hamiltonian \hat{H}_0^{μ} (Eq. (2.18)) in Chapter 2. The inclusion of the energy shifts in the

equation of motion is, therefore, redundant. Removing these energy shifts gives us

$$\begin{aligned}
& \frac{1}{i\hbar} \left[\tilde{\sigma}_{f,m; f',m'}^\mu, \hat{V}_{AR}(t) \right] \\
&= \hat{\zeta}_{f_1,m_1; f_2,m_2}^\mu(t) - \frac{1}{2} (\Gamma_{f_1} + \Gamma_{f_2}) \tilde{\sigma}_{f_1,m_1; f_2,m_2}(t) \\
&+ \sum_{\{f: \omega_{f_1} < \omega_f\}} \delta_{f_1,f_2} \Gamma_{f_1}^f \sum_{\alpha=-1}^1 C_{m_1 \alpha}^{F_{f_1} \ 1 \ F_f} C_{m_2 \alpha}^{F_{f_1} \ 1 \ F_f} \tilde{\sigma}_{f,m_1+\alpha; f',m_2+\alpha}(t). \quad (\text{C.30})
\end{aligned}$$

This equation is valid for describing the interaction of any multi-level atom with the reservoir in which all of the atomic energy levels are well separated.

In deriving the contribution of the reservoir interactions to the equations of motion, one notices that had a rotating wave approximation been made on the initial Hamiltonian, the only consequence would have been that the radiation shifts would have been different. Since these shifts were already redundant, however, delaying the application of the rotating wave approximation does not have any effect when each atom interacts with an independent reservoir.

C.3 Heisenberg Langevin Equations for the Atomic Coherences

In this section, we write the Heisenberg-Langevin equations for the coherences of individual atoms in our atomic ensemble. We will then make the low-intensity approximation, in which one can neglect all coherences except the populations of ground level $|b\rangle$, the optical coherences between levels $|b\rangle$ and $|c\rangle$ and the hyperfine coherences between levels $|b\rangle$ and $|a\rangle$. A similar low-intensity approximation was used in the context of EIT in nondegenerate three-level atoms by Fleischhauer and Lukin [69, 75].

From Eqs. (C.14) and (C.30), we write the Heisenberg Langevin equations of motion for the Zeeman coherences and populations within the initially populated level $|b\rangle$. When we make the rotating wave approximation on these equations of

motion, we have

$$\begin{aligned}
\frac{d\tilde{\sigma}_{b,m; b,m'}(t)}{dt} = & -i(2\pi)^{3/2} \mathcal{G}_{(b,c)}(ck_s) e^{ik_s z_\mu} \phi^{(s)}(\vec{r}_\mu) \\
& \times \sum_{\alpha=-1}^1 C_{m\alpha m+\alpha}^{F_b 1 F_c} \tilde{\sigma}_{c,m+\alpha; b,m'}^\mu(t) \hat{\varphi}_\alpha^{(s)}(z_\mu, t) \\
& + i(2\pi)^{3/2} \mathcal{G}_{(b,c)}^*(ck_s) e^{-ik_s z_\mu} \phi^{(s)*}(\vec{r}_\mu) \\
& \times \sum_{\alpha=-1}^1 C_{m'\alpha m'+\alpha}^{F_b 1 F_c} \tilde{\sigma}_{b,m; c,m'+\alpha}^\mu(t) \hat{\varphi}_\alpha^{(s)\dagger}(z_\mu, t) \\
& + \hat{\zeta}_{b,m; b,m'}^\mu(t) \\
& + \Gamma_b^c \sum_{\alpha=-1}^1 C_{m\alpha m+\alpha}^{F_b 1 F_c} C_{m'\alpha m'+\alpha}^{F_b 1 F_c} \tilde{\sigma}_{c,m+\alpha; c,m'+\alpha}^\mu(t). \quad (\text{C.31})
\end{aligned}$$

Similarly, for the Zeeman coherences and populations within level $|a\rangle$ we have the equation of motion

$$\begin{aligned}
\frac{d\tilde{\sigma}_{a,m; a,m'}^\mu(t)}{dt} = & -i\Omega_c(t) e^{i\vec{k}_c \cdot \vec{r}_\mu} \sum_{\alpha=-1}^1 \left(\vec{\xi}_\alpha^* \cdot \vec{e}_c \right) C_{m\alpha m+\alpha}^{F_a 1 F_c} \tilde{\sigma}_{c,m+\alpha; a,m'}^\mu(t) \\
& + i\Omega_c^*(t) e^{-i\vec{k}_c \cdot \vec{r}_\mu} \sum_{\alpha=-1}^1 \left(\vec{\xi}_\alpha \cdot \vec{e}_c^* \right) C_{m'\alpha m'+\alpha}^{F_a 1 F_c} \tilde{\sigma}_{a,m; c,m'+\alpha}^\mu(t) \\
& + \hat{\zeta}_{a,m; a,m'}^\mu(t) \\
& + \Gamma_a^c \sum_{\alpha=-1}^1 C_{m\alpha m+\alpha}^{F_a 1 F_c} C_{m'\alpha m'+\alpha}^{F_a 1 F_c} \tilde{\sigma}_{c,m+\alpha; c,m'+\alpha}^\mu(t), \quad (\text{C.32})
\end{aligned}$$

where $\Omega_c(t) \equiv \left(c \left\| \hat{\mathbf{d}} \right\| a \right) E_c(t)/\hbar$ is the control field Rabi frequency. The Zeeman

coherences and populations within excited level $|c\rangle$ evolve according to

$$\begin{aligned}
\frac{d\tilde{\sigma}_{c,m; c,m'}^\mu(t)}{dt} = & i(2\pi)^{3/2} \mathcal{G}_{(b,c)}(ck_s) \phi^{(s)}(\vec{r}_\mu) e^{ik_s z_\mu} \\
& \times \sum_{\alpha=-1}^1 C_{m'-\alpha}^{F_b} C_{\alpha m'}^{F_c} \tilde{\sigma}_{c,m; b,m'-\alpha}^\mu(t) \hat{\varphi}_\alpha^{(s)}(z_\mu, t) \\
& - i(2\pi)^{3/2} \mathcal{G}_{(b,c)}^*(ck_s) \phi^{(s)*}(\vec{r}_\mu) e^{-ik_s z_\mu} \\
& \times \sum_{\alpha=-1}^1 C_{m-\alpha}^{F_b} C_{\alpha m}^{F_c} \tilde{\sigma}_{b,m-\alpha; c,m'}^\mu(t) \hat{\varphi}_\alpha^{(s)\dagger}(z_\mu, t) \\
& + ie^{i\vec{k}_c \cdot \vec{r}_\mu} \Omega_c(t) \sum_{\alpha=-1}^1 \left(\vec{\xi}_\alpha^* \cdot \vec{e}_c \right) C_{m'-\alpha}^{F_a} C_{\alpha m'}^{F_c} \tilde{\sigma}_{c,m; a,m'-\alpha}^\mu(t) \\
& - ie^{-ik_c \cdot \vec{r}_\mu} \Omega_c^*(t) \sum_{\alpha=-1}^1 \left(\vec{\xi}_\alpha \cdot \vec{e}_c^* \right) C_{m-\alpha}^{F_a} C_{\alpha m}^{F_c} \tilde{\sigma}_{a,m-\alpha; c,m'}^\mu(t) \\
& + \hat{\zeta}_{c,m; c,m'}^\mu(t) - \Gamma_c \tilde{\sigma}_{c,m; c,m'}^\mu(t). \tag{C.33}
\end{aligned}$$

The optical coherences evolve according to

$$\begin{aligned}
\frac{d\tilde{\sigma}_{a,m; c,m'}^\mu(t)}{dt} = & ie^{ik_s z_\mu} (2\pi)^{3/2} \mathcal{G}_{(b,c)}(ck_s) \phi^{(s)}(\vec{r}_\mu) \\
& \times \sum_{\alpha=-1}^1 C_{m'-\alpha}^{F_b} C_{\alpha m'}^{F_c} \tilde{\sigma}_{a,m; b,m'-\alpha}^\mu(t) \hat{\varphi}_\alpha^{(s)}(z_\mu, t) \\
& + ie^{i\vec{k}_c \cdot \vec{r}_\mu} \Omega_c(t) \sum_{\alpha=-1}^1 \left(\vec{\xi}_\alpha^* \cdot \vec{e}_c \right) \\
& \times \left(C_{m'-\alpha}^{F_a} C_{\alpha m'}^{F_c} \tilde{\sigma}_{a,m; a,m'-\alpha}^\mu(t) - C_{m-\alpha}^{F_a} C_{\alpha m+\alpha}^{F_c} \tilde{\sigma}_{c,m+\alpha; c,m'}^\mu(t) \right) \\
& + \hat{\zeta}_{a,m; c,m'}^\mu(t) - \frac{1}{2} \Gamma_c \tilde{\sigma}_{a,m; c,m'}^\mu(t), \tag{C.34}
\end{aligned}$$

and

$$\begin{aligned}
\frac{d\tilde{\sigma}_{b,m; c,m'}^\mu(t)}{dt} = & ie^{ik_s z_\mu} (2\pi)^{3/2} \mathcal{G}_{(b,c)}(ck_s) \phi^{(s)}(\vec{r}_\mu) \\
& \times \sum_{\alpha=-1}^1 \left(C_{m'-\alpha}^{F_b} C_{\alpha m'}^{F_c} \tilde{\sigma}_{b,m; b,m'-\alpha}^\mu(t) - C_{m-\alpha}^{F_b} C_{\alpha m+\alpha}^{F_c} \tilde{\sigma}_{c,m+\alpha; c,m'}^\mu(t) \right) \hat{\varphi}_\alpha^{(s)}(z_\mu, t) \\
& + ie^{i\vec{k}_c \cdot \vec{r}_\mu} \Omega_c(t) \sum_{\alpha=-1}^1 C_{m'-\alpha}^{F_a} C_{\alpha m'}^{F_c} \tilde{\sigma}_{b,m; a,m'-\alpha}^\mu(t) \left(\vec{\xi}_\alpha^* \cdot \vec{e}_c \right) \\
& + \hat{\zeta}_{b,m; c,m'}^\mu(t) - \frac{1}{2} \Gamma_c \tilde{\sigma}_{b,m; c,m'}^\mu(t). \tag{C.35}
\end{aligned}$$

Finally, the hyperfine coherences between levels $|a\rangle$ and $|b\rangle$ evolve according to

$$\begin{aligned}
\frac{d\tilde{\sigma}_{b,m; a,m'}^\mu(t)}{dt} = & -ie^{ik_s z_\mu} (2\pi)^{3/2} \mathcal{G}_{(b,c)}(ck_s) \phi^{(s)}(\vec{r}_\mu) \\
& \times \sum_{\alpha=-1}^1 C_{m\alpha m+\alpha}^{F_b-1 F_c} \tilde{\sigma}_{c,m+\alpha; a,m'}^\mu(t) \hat{\varphi}_\alpha^{(s)}(z_\mu, t) \\
& + ie^{-i\vec{k}_c \cdot \vec{r}_\mu} \Omega_c^*(t) \sum_{\alpha=-1}^1 \left(\vec{\xi}_\alpha \cdot \vec{e}_c^* \right) C_{m'\alpha m'+\alpha}^{F_a-1 F_c} \tilde{\sigma}_{b,m; c,m'+\alpha}^\mu(t) \\
& + \hat{\zeta}_{b,m; a,m'}^\mu(t). \tag{C.36}
\end{aligned}$$

The interaction with the magnetic field is included in the dynamics of an atomic coherence $\tilde{\sigma}_{f,m; f',m'}^\mu(t)$ can be accounted for by the addition of the term $[\tilde{\sigma}_{f,m; f',m'}^\mu(t), \hat{V}_{AB}(t)]/(i\hbar)$ to the corresponding equation of motion.

C.3.1 Weak Signal Approximation

Here, we follow the treatment of Fleischhauer and Lukin [69, 75] in performing a weak signal approximation. This approximation allows us to neglect many of the coherences whose dynamics are governed by Eqs. (C.31) through (C.36) when considering the propagation of the signal field through the ensemble. We assume the number of signal photons in the slice of the ensemble between z and $z + dz$, given by $\sum_{\alpha=\pm 1} \langle \hat{\varphi}_\alpha^\dagger(z, t) \hat{\varphi}_\alpha(z, t) \rangle dz$, is always much less than the number of atoms with which the signal mode interacts within that slice. That is, in the most extreme of scenarios, where all of the photons have been absorbed and transformed into atomic excitations, only a small fraction of atoms ($O(1/N)$ for single photon pulses) will have been displaced from their original state $\hat{\rho}_0^\mu$ (Eq. (C.12)). To determine whether an atomic coherence should be retained in this weak field approximation, we perform a perturbative expansion in $\hat{\varphi}_\alpha(z, t)$ of that slowly varying atomic coherence using Eqs. (C.31) to Eq. (C.36), and keep coherences to first order in the photon density operator $\hat{\varphi}_\alpha(z, t)$. We note, that to zero order in $\hat{\varphi}_\alpha$, only the populations within level $|b\rangle$ are non-zero (i.e. $\tilde{\sigma}_{b,m; b,m'}^\mu = p_m \delta_{m,m'}$), and all other coherences are significant only to first order or greater in $\hat{\varphi}_\alpha$. In the presence of a magnetic field, we

make the further assumption that either the magnetic field is parallel to the z -axis or that the sample is initially unpolarized (i.e. $p_m = 1/(2F_b + 1)$). Otherwise, the Larmor precession of the atoms within the field would produce macroscopic Zeeman coherences during a storage process regardless of the intensity of the signal field. The effects of macroscopic Zeeman coherences on the propagation of the signal field is the subject of future investigations.

Aside from the populations of level $|b\rangle$, only the optical coherences $\tilde{\sigma}_{b,m; c,m'}^\mu(t)$ and hyperfine coherences $\tilde{\sigma}_{b,m; a,m'}^\mu(t)$ and their Hermitian conjugates survive the weak signal approximation. To first order in the signal field, these operators obey the simplified equations of motion

$$\frac{d\tilde{\sigma}_{b,m; b,m}^\mu(t)}{dt} = 0, \quad (\text{C.37})$$

$$\begin{aligned} & \left(\frac{d}{dt} + \frac{\Gamma_c}{2} \right) \tilde{\sigma}_{b,m; c,m'}^\mu(t) \\ &= ie^{ik_s z_\mu} (2\pi)^{3/2} \mathcal{G}_{(b,c)}(ck_s) \phi^{(s)}(\vec{r}_\mu) \\ & \quad \times \sum_{\alpha=\pm 1} \left(p_m C_{m\alpha}^{F_b-1 F_c} \delta_{m',m+\alpha} \right) \hat{\varphi}_\alpha^{(s)}(z_\mu, t) \\ &+ ie^{i\vec{k}_c \cdot \vec{r}_\mu} \Omega_c(t) \sum_{\beta=-1}^1 C_{m'-\beta}^{F_a-1 F_c} \tilde{\sigma}_{b,m; a,m'-\beta}^\mu(t) \left(\vec{\xi}_\beta^* \cdot \vec{e}_c \right) \\ &+ \delta_{m',m+\alpha} \hat{\zeta}_{b,m; c,m'}^\mu(t) + \frac{1}{i\hbar} \left[\tilde{\sigma}_{b,m; c,m'}^\mu(t), \hat{V}_{AB}(t) \right], \end{aligned} \quad (\text{C.38})$$

and

$$\begin{aligned} \frac{d\tilde{\sigma}_{b,m; a,m'}^\mu(t)}{dt} &= ie^{-i\vec{k}_c \cdot \vec{r}_\mu} \Omega_c^*(t) \sum_{\alpha=-1}^1 \left(\vec{\xi}_\alpha \cdot \vec{e}_c^* \right) C_{m'\alpha}^{F_a-1 F_c} \tilde{\sigma}_{b,m; c,m'+\alpha}^\mu(t) \\ &+ \frac{1}{i\hbar} \left[\tilde{\sigma}_{b,m; c,m'}^\mu(t), \hat{V}_{AB}(t) \right]. \end{aligned} \quad (\text{C.39})$$

The only noise term to survive the weak field approximation is that associated with the optical coherence $\tilde{\sigma}_{b,m; c,m'}^\mu(t)$. This noise operator is given for atom μ by

$$\begin{aligned} \hat{\zeta}_{b,m; c,m+\alpha}^\mu(t) &= -p_m C_{m\alpha}^{F_b-1 F_c} \int d^3k \sum_\lambda \left(\vec{\xi}_\alpha^* \cdot \vec{\varepsilon}_\lambda(\hat{k}) \right) \mathcal{G}_{(b,c)}(ck) \\ & \quad \times e^{i\vec{k} \cdot \vec{r}_\mu} e^{-i[ck - (\omega_c - \omega_b)]t} \tilde{a}_\lambda(\vec{k}, 0). \end{aligned} \quad (\text{C.40})$$

C.4 *Field Propagation and Electromagnetically induced transparency*

The response of the atomic sample to the time dependent control field allows the storage of the signal field within the medium. In this section, we examine the propagation dynamics that results from the interaction of the signal field within the ensemble in the presence of the control field. Beginning from the Heisenberg equation of motion for the linear photon density operator in a general atomic medium (Eq. (2.71)), we arrive at the following signal propagation equation for three-level model we consider in this appendix:

$$\left(\frac{\partial}{\partial t} + c \frac{\partial}{\partial z} \right) \hat{\varphi}_{\alpha}^{(s)}(z, t) = i \sqrt{n(z)} p_m \kappa_s^* \sum_{m=-F_b}^{F_b} C_{m \alpha}^{F_b 1 F_c} \hat{e}_{m; m+\alpha}(z, t), \quad (\text{C.41})$$

where $n(z)$ is the atomic number density as a function of z , $\kappa_s \equiv (2\pi)^{3/2} \mathcal{G}_{(b,c)}(ck_s)$ is the signal coupling strength, and

$$\hat{e}_{m; m'}(z, t) \equiv \frac{1}{\sqrt{n(z)} p_m} \sum_{\mu=1}^N e^{-ik_s z_{\mu}} \phi^{(s)*}(\vec{r}_{\mu}) \tilde{\sigma}_{b, m; c, m'}^{\mu}(t) \delta(z - z_{\mu}) \quad (\text{C.42})$$

when $p_m \neq 0$ and zero otherwise. In the weak signal approximation, these collective optical coherences obey the equal time commutation relations

$$[\hat{e}_{m_1; m'_1}(z, t), \hat{e}_{m_2; m'_2}(z', t)] = 0 \quad (\text{C.43a})$$

$$\begin{aligned} [\hat{e}_{m_1; m'_1}(z, t), \hat{e}_{m_2; m'_2}^{\dagger}(z', t)] &= \frac{\delta_{m_1, m'_1} \delta_{m_2, m'_2}}{n(z)} \sum_{\mu} |\phi^{(s)}(\vec{r}_{\mu})|^2 \delta(z - z_{\mu}) \\ &\times \delta(z' - z_{\mu}). \end{aligned} \quad (\text{C.43b})$$

Because the atomic positions are independent identically distributed random variables with a probability density $n(\vec{r})/N$, we may take advantage of the central limit theorem, and approximate the sum appearing in the commutator as

$$\begin{aligned} &\frac{1}{N} \sum_{\mu} |\phi^{(s)}(\vec{r}_{\mu})|^2 \delta(z - z_{\mu}) \delta(z' - z_{\mu}) \\ &= \int d^3 r'' \frac{n(z'')}{N} |\phi^{(s)}(\vec{r}'')|^2 \delta(z - z'') \delta(z' - z'') + O(1/\sqrt{N}). \end{aligned} \quad (\text{C.44})$$

Because we assume the atomic density is constant over the width of the transverse signal mode $\phi^{(s)}$ and because $\phi^{(s)}$ satisfies the normalization condition, $\int d^2 r_{\perp}^{(s)} |\phi^{(s)}(\vec{r}_{\perp}^{(s)}, z)|^2 = 1$, we may say the collective optical excitations $\hat{e}_{m;m'}(z, t)$ obey approximate bosonic commutation relations

$$\left[\hat{e}_{m_1;m'_1}(z, t), \hat{e}_{m_2;m'_2}^{\dagger}(z', t) \right] = \delta_{m_1,m'_1} \delta_{m_2,m'_2} \delta(z - z') + O(1/\sqrt{N}). \quad (\text{C.45})$$

We similarly define the collective hyperfine excitations

$$\hat{s}_{m;m'}(z, t) \equiv \frac{1}{\sqrt{n(z) p_m}} \sum_{\mu=1}^N \phi^{(s)*}(\vec{r}_{\mu}) e^{i(\vec{k}_c - \vec{k}_s) \cdot \vec{r}_{\mu}} \tilde{\sigma}_{b,m; a,m'}^{\mu}(t) \delta(z - z_{\mu}) \quad (\text{C.46})$$

when $p_m \neq 0$ and zero otherwise. Like the collective optical coherences, these collective hyperfine coherences obey approximate bosonic commutation relations in the weak signal limit:

$$\left[\hat{s}_{m_1;m'_1}(z, t), \hat{s}_{m_2;m'_2}(z', t) \right] = 0 \quad (\text{C.47a})$$

$$\begin{aligned} \left[\hat{s}_{m_1;m'_1}(z, t), \hat{s}_{m_2;m'_2}^{\dagger}(z', t) \right] &= \delta_{m_1,m'_1} \delta_{m_2,m'_2} \delta(z - z') \\ &+ O(1/\sqrt{N}). \end{aligned} \quad (\text{C.47b})$$

The collective coherences obey the Heisenberg-Langevin equations

$$\frac{d}{dt} \hat{s}_{m;m'}(z, t) \equiv i\Omega_c^*(t) \sum_{\alpha=-1}^1 \left(\vec{\xi}_{\alpha} \cdot \vec{e}_c^* \right) C_{m' \alpha m'+\alpha}^{F_a \ 1 \ F_c} \hat{e}_{m;m'+\alpha}(z, t), \quad (\text{C.48})$$

and

$$\begin{aligned} \left(\frac{d}{dt} + \frac{\Gamma_c}{2} \right) \hat{e}_{m;m'}(z, t) &= i\kappa_s \sqrt{n(z) p_m} \sum_{\alpha=-1}^1 C_{m \alpha m+\alpha}^{F_b \ 1 \ F_c} \delta_{m'; m+\alpha} \hat{\varphi}_{\alpha}^{(s)}(z, t) \\ &+ i\Omega_c(t) \sum_{\beta=-1}^1 C_{m'-\beta \beta m'}^{F_a \ 1 \ F_c} \left(\vec{\xi}_{\beta}^* \cdot \vec{e}_c \right) \hat{s}_{m;m'-\beta}(z, t) \\ &+ \delta_{m', m+\alpha} \hat{\zeta}_{b,m; c, m+\alpha}(z, t), \end{aligned} \quad (\text{C.49})$$

where

$$\hat{\zeta}_{b,m; c, m'}(z, t) \equiv \frac{1}{\sqrt{n(z) p_m}} \sum_{\mu=1}^N e^{-i\vec{k}_s \cdot \vec{r}_{\mu}} \phi^{(s)*}(\vec{r}_{\mu}) \hat{\zeta}_{b,m; c, m'}^{\mu}(t) \delta(z - z_{\mu}) \quad (\text{C.50})$$

In the remainder of this appendix, we make the simplifying assumption that the control field has a fixed helicity β ; $\vec{e}_c = \vec{e}_\beta(\hat{k}_c) \approx \vec{\xi}_\beta$.

Once again, the effects of the magnetic field interaction can be accounted for by the addition of the appropriate commutators with the interaction $\hat{V}_{AB}(t)$ in the atomic equations. We note, however, that the bosonic commutation relations of Eqs. (C.45) and (C.47), the collective atomic equations (Eqs. (C.48) and (C.49)), and the signal propagation equation (Eq. (C.41)) are only valid under either the following conditions: the magnetic field is parallel to the quantization z -axis, or the sample is unpolarized. Otherwise the Larmor precession induced by the magnetic field would result in macroscopic Zeeman coherences in level $|b\rangle$.

C.4.1 Propagation of a Classical Signal

To better understand the storage and retrieval dynamics of the signal field described in Chapter 6, we consider the propagation of the signal in the classical limit. In this section, we outline the procedure used to solve the coupled propagation and matter excitation equations (Eqs. (C.41), (C.48), and (C.49)) numerically. The dynamics of classical propagation are described by Eqs. (C.41), (C.48), and (C.49) where the quantum operators have been replaced by their expectation values, and the quantum noise $\hat{\zeta}_{m,m'}(z, t)$ is neglected. In this section, when the magnetic field is present, we consider only the case in which it is oriented along the z -axis; $\vec{B} = B\hat{z}$.

We first decompose the fields and collective excitations into their temporal frequency components, Fourier transforming Eqs. (C.41), (C.48), and (C.49) in time. This transforms the collective excitation equations (Eqs. (C.48) and (C.49)) into coupled algebraic equations, allowing one to express the Fourier components of the matter excitations in terms of the Fourier components of the signal field. One then finds that the signal's frequency components obey the propagation equation

$$\frac{\partial}{\partial z}\varphi_\alpha(z, \Delta) = i\frac{\Delta}{c} \int d\Delta' \left(\delta(\Delta - \Delta') + \frac{1}{2} \frac{\omega_c}{\Delta} \chi_\alpha(\Delta, \Delta', z) \right) \varphi_\alpha(z, \Delta'), \quad (\text{C.51})$$

where

$$\varphi_\alpha(z, \Delta) \equiv \frac{1}{\sqrt{2\pi}} \int_{-\infty}^{\infty} dt \exp(i\Delta t) \varphi_\alpha(z, t), \quad (\text{C.52})$$

and the non-local linear susceptibility is given by

$$\chi_\alpha(\Delta, \Delta') = - \left(\frac{c}{\omega_c - \omega_b} \right) d'_\alpha(z) \sum_{m=-F_b}^{F_b} X_{m,\alpha}^2 \frac{(\Gamma_c/2) K_{m,\alpha}^{-1}(\Delta, \Delta')}{\Delta' + i\Gamma_c/2}, \quad (\text{C.53})$$

where $d'_\alpha(z)$ is the spatial derivative of the optical thickness d_α , which is defined as the negative logarithm of the on resonance intensity transmittance of a signal with polarization α , in the absence of the control field. Here Δ is the frequency space Fourier variable, with $\Delta = 0$ corresponding to a signal component resonant with the $|b\rangle \leftrightarrow |c\rangle$ transition. Explicitly, d_α is given by the dimensionless quantity

$$d_\alpha(z) = 6\pi w \left(\frac{c}{\omega_c - \omega_b} \right)^2 \int_0^z dz' n(z') \sum_m p_m \left| C_{m\alpha m+\alpha}^{F_b 1 F_c} \right|^2, \quad (\text{C.54})$$

$X_{m,\alpha} \equiv \sqrt{p_m} C_{m\alpha m+\alpha}^{F_b 1 F_c} / \sqrt{\sum_{m_b} p_{m_b} \left| C_{m_b\alpha m_b+\alpha}^{F_b 1 F_c} \right|^2}$, and $w = \left| \left(c \left\| \hat{\mathbf{d}} \right\| b \right) \right|^2 / \left(\left| \left(c \left\| \hat{\mathbf{d}} \right\| b \right) \right|^2 + \left| \left(c \left\| \hat{\mathbf{d}} \right\| a \right) \right|^2 \right)$ is the fraction of atoms in the excited level $|c\rangle$ that spontaneously decays into the ground level $|b\rangle$. Furthermore,

$$K_{m,\alpha} = \left(\delta(\Delta - \Delta') - \frac{1}{\sqrt{2\pi}} \frac{L_{m,\alpha}(\Delta, \Delta')}{(\Delta + \delta_c + m\Delta_{cb} + i\Gamma_{cb})} \right) \quad (\text{C.55})$$

is a kernel whose inverse satisfies the property $\int d\Delta'' K(\Delta, \Delta'') K^{-1}(\Delta'', \Delta') = \int d\Delta'' K^{-1}(\Delta, \Delta'') K(\Delta'', \Delta') = \delta(\Delta - \Delta')$. The frequencies $\delta_c \equiv \alpha(\mu_B g_c B/\hbar)$ and $\Delta_{cb} \equiv (g_c - g_b)(\mu_B B/\hbar)$ account for the energy splitting of the Zeeman states resulting from the interaction with the magnetic field $\vec{B} = B\hat{z}$. We also have

$$L_{m,\alpha}(\Delta, \Delta') = \left| C_{m+\alpha-\beta\beta m+\alpha}^{F_a 1 F_c} \right|^2 \frac{1}{\sqrt{2\pi}} \int d\Delta'' \Omega_c(\Delta - \Delta'') \frac{1}{(\Delta'' + (\delta_a + m\Delta_{ab}))} \Omega_c^*(\Delta' - \Delta''), \quad (\text{C.56})$$

where

$$\Omega_c(\Delta) \equiv \frac{1}{\sqrt{2\pi}} \int_{-\infty}^{\infty} dt \exp(i\Delta t) \Omega_c(t), \quad (\text{C.57})$$

$\delta_a = (\alpha - \beta)g_a(\mu_B B/\hbar)$, and $\Delta_{ab} = (g_a - g_b)(\mu_B B/\hbar)$.

With this propagation equation (Eq. (C.51)), we are able to numerically calculate the propagation of the signal field leading to the various features shown in Figures 6.3 and 7.2 (we assume equal signal and control polarizations $\alpha = \beta$ in order to have EIT for the atomic level configurations of Chapters 6 and 7), including group delay, pulse storage and retrieval. The numerical solution of Eq. (C.51) may be obtained by assuming periodic boundary conditions for the signal and control fields on the time interval $[0, T)$, where T is some time much longer than that in which the storage and propagation dynamics occur within the ensemble. Additionally, we sample the signal and control fields on a grid of \mathcal{N} equidistant time points $\{t_j = jT/\mathcal{N} : 0 \leq j < \mathcal{N}\}$. Imposing periodic boundary conditions discretizes the set of available detunings $\{\Delta_j = j(2\pi/T) : -\mathcal{N}/2 \leq j < \mathcal{N}/2\}$. (For a more detailed discussion of discrete spectral decomposition, see Ref. [135].) Having chosen the grid in time and frequency space, we estimate the integrals of Eqs. (C.52) and (C.57) by making the substitution $\int_{-\infty}^{\infty} dt \rightarrow (T/\mathcal{N}) \sum_{j=0}^{\mathcal{N}}$, transforming the integral into a summation. Similarly, in the frequency integrals of Eqs. (C.51) and (C.56), we make the substitution $\int d\Delta \rightarrow (2\pi/T) \sum_{j=-\mathcal{N}/2}^{\mathcal{N}/2-1}$. We further replace the Dirac δ -function with its discrete version: $\delta(\Delta - \Delta') \rightarrow (T/(2\pi))\delta_{\Delta, \Delta'}$. These substitutions transform Eq. (C.51) into a finite set of coupled linear differential equations of the form $(d/dz)\varphi_{\alpha}(z, \Delta_i) = \sum_j \mathcal{L}_{i,j}^{(\alpha)}(z)\varphi_{\alpha}(z, \Delta_j)$. Therefore, given the signal frequency profile $\varphi_{\alpha}(z_0, \Delta)$ (related to the temporal profile through the Fourier transform) as it enters the atomic ensemble at position z_0 , the frequency profile at position z is given by $\varphi_{\alpha}(z, \Delta_i) = \sum_j \left[\exp \left(\int_{z_0}^z dz' \mathcal{L}^{(\alpha)}(z') \right) \right]_{i,j} \varphi_{\alpha}(z_0, \Delta_j)$. The exponentiation of the matrix $\int_{z_0}^z dz' \mathcal{L}^{(\alpha)}(z')$ may be performed by a numerical linear algebra package such as MATLAB.

C.4.2 Linear Susceptibility for Constant Control Field and Electromagnetically Induced Transparency

In the limit of constant control field, the susceptibility reduces to the form

$$\chi_\alpha(\Delta, z) \approx \frac{c}{2(\omega_c - \omega_b)} d'_\alpha(z) \times \sum_m \frac{\Gamma_c \Delta X_{m\alpha}^2 \left(|\Omega_c|^2 |C_{m+\alpha-\beta}^{F_a \ 1 \ F_c}{}_{\beta \ m+\alpha}|^2 - \Delta^2 + i\Delta\Gamma_c/2 \right)}{\left(|\Omega_c|^2 |C_{m+\alpha-\beta}^{F_a \ 1 \ F_c}{}_{\beta \ m+\alpha}|^2 - \Delta^2 \right)^2 + (\Delta\Gamma_c/2)^2}, \quad (\text{C.58})$$

Since the Zeeman shifts are small compared to the spontaneous emission rate, they have been ignored in the above expression. The intensity transmittance of a cw signal of helicity α with detuning Δ is given in terms of the susceptibility by

$$T_\alpha(\Delta) = \exp \left(-\frac{\omega_c - \omega_b}{c} \int dz \operatorname{Im}(\chi_\alpha(\Delta, z)) \right) \quad (\text{C.59})$$

$$= \exp \left(-d_\alpha \sum_m \frac{X_{m\alpha}^2 (\Delta\Gamma_c/2)^2}{\left(|\Omega_c|^2 |C_{m+\alpha-\beta}^{F_a \ 1 \ F_c}{}_{\beta \ m+\alpha}|^2 - \Delta^2 \right)^2 + (\Delta\Gamma_c/2)^2} \right), \quad (\text{C.60})$$

where $d_\alpha \equiv \lim_{z \rightarrow \infty} d_\alpha(z)$ is the total optical thickness of the sample. From Eq. (C.58), one can see that in the presence of the control field, the imaginary part of the susceptibility potentially goes to zero when the signal field is on resonance. When this happens, Eq. (C.60) indicates there is a transparency window for signal frequencies near resonance. The width of this electromagnetically induced transparency window is determined by the intensity of the *control* field. Notice that the medium will only exhibit EIT with a judicious choice of atomic hyperfine levels and field polarizations. If one of the Clebsch-Gordan coefficients multiplying the Rabi frequency Ω_c vanishes (i.e. there is an excited state $|c, m + \alpha\rangle$ not coupled by the control field to the corresponding ground state $|a, m + \alpha - \beta\rangle$), then a fraction of the atoms will simply absorb the signal light as if there is no control field present. We point out that for the level scheme used in the experiments of Chapters 6 and 7, EIT is achieved only

when the signal and control field polarizations are equal ($\alpha = \beta$). The solid curves in Figure 6.2 are based on Eq.(C.58).

C.5 The Adiabatic Limit: Dark State Polaritons

Assuming a choice of polarizations and initial atomic populations p_m that supports EIT, we are able to generalize the adiabatic treatment of Fleischhauer and Lukin to the propagation equations (Eqs. (C.41), (C.48), and (C.49)). This adiabatic approximation results in a simplification of the equations in which the system dynamics can be described by a single propagation equation for a collective excitation known as the dark state polariton. The dark state polariton is composed of an electric field excitation and a particular linear combination of collective hyperfine coherences.

We begin by recognizing that when the medium supports EIT (i.e. $C_{m+\alpha-\beta}^{F_a \ 1 \ F_c} \neq 0$ for all m for which $p_m \neq 0$), we can express $\hat{e}_{m; \ m+\alpha}(z, t)$ as

$$\hat{e}_{m; \ m+\alpha}(z, t) = \frac{1}{i\Omega_c^*(t)C_{m+\alpha-\beta}^{F_a \ 1 \ F_c}} \frac{\partial}{\partial t} \hat{s}_{m; \ m+\alpha-\beta}(z, t) \quad (\text{C.61})$$

This yields the modified propagation equation

$$\begin{aligned} \Omega_c^*(t) \left(\frac{\partial}{\partial t} + c \frac{\partial}{\partial z} \right) \hat{\varphi}_\alpha^{(s)}(z, t) \\ = \sqrt{n(z) p_m} \kappa_s^* \sum_{m=-F_b}^{F_b} R_{m,\alpha}(\beta) \frac{\partial}{\partial t} \hat{s}_{m; \ m+\alpha-\beta}(z, t). \end{aligned} \quad (\text{C.62})$$

where

$$R_{m\alpha}(\beta) \equiv \frac{C_{m \ \alpha \ m+\alpha}^{F_b \ 1 \ F_c}}{C_{m+\alpha-\beta}^{F_a \ 1 \ F_c}} \quad (\text{C.63})$$

is a ratio of Clebsch-Gordan coefficients. Substituting Eq. (C.61) into Eq. (C.49) for $\vec{e}_c = \vec{\xi}_\beta$, we find

$$\begin{aligned} \left(\frac{d}{dt} + \frac{\Gamma_c}{2} \right) \left(\frac{1}{i\Omega_c^*(t)C_{m+\alpha-\beta}^{F_a \ 1 \ F_c}} \frac{\partial}{\partial t} \hat{s}_{m; \ m+\alpha-\beta}(z, t) \right) \\ = i\kappa_s \sqrt{n(z) p_m} C_{m \ \alpha \ m+\alpha}^{F_b \ 1 \ F_c} \hat{\varphi}_\alpha^{(s)}(z, t) + i\Omega_c(t) C_{m+\alpha-\beta}^{F_a \ 1 \ F_c} \hat{s}_{m; \ m+\alpha-\beta}(z, t) \\ + \hat{\zeta}_{b,m; \ c,m+\alpha}(z, t). \end{aligned} \quad (\text{C.64})$$

As in Ref. [75], we normalize t to some characteristic time scale T_a , and express Eq. (C.64) in terms of the dimensionless time $\tilde{t} = t/T_a$. We recognize that $\langle \hat{\zeta}_{b,m; c,m+\alpha}^\dagger(z, t) \hat{\zeta}_{b,m; c,m+\alpha}(z, t') \rangle \sim \delta(t - t') = (1/T_a)\delta(\tilde{t} - \tilde{t}')$ [69, 75]. In the Adiabatic limit, we keep terms to lowest order in $1/T_a$, and therefore derive from (Eq. (C.64)) a necessary condition for adiabaticity

$$\hat{s}_{m; m+\alpha-\beta}(z, t) = -\frac{\kappa_s \sqrt{n(z) p_m}}{\Omega_c(t)} R_{m,\alpha}(\beta) \hat{\varphi}_\alpha^{(s)}(z, t). \quad (\text{C.65})$$

This condition for adiabaticity not only ties the hyperfine coherence to the field, as in Refs. [69, 75], but also ties the values of the hyperfine coherences to each other.

The conditions for adiabaticity (Eq. (C.65)) suggest the form for the dark state polariton of helicity α ,

$$\hat{\Psi}_\alpha(z, t) = \frac{\Omega^*(t) \hat{\varphi}_\alpha(z, t) - \sqrt{n(z)} \kappa_s^* \sum_m \sqrt{p_m} R_{m\alpha}(\beta) \hat{s}_{m; m+\alpha-\beta}(z, t)}{\sqrt{|\Omega_c(t)|^2 + n(z) |\kappa_s|^2 \sum_m p_m |R_{m,\alpha}(\beta)|^2}}. \quad (\text{C.66})$$

This polariton operator, like the collective hyperfine coherences, is quasi-bosonic and satisfies the equal time commutation relations

$$[\hat{\Psi}_\alpha(z, t), \hat{\Psi}_\beta(z', t)] = 0 \quad (\text{C.67})$$

$$[\hat{\Psi}_\alpha(z, t), \hat{\Psi}_\beta^\dagger(z', t)] = \delta(z - z') + \hat{O}(1/\sqrt{N}). \quad (\text{C.68})$$

The operator $\hat{\Psi}_\alpha^\dagger(z, t) \hat{\Psi}_\alpha(z, t)$ may be interpreted as the polariton linear density. From the field propagation equation (Eq. (C.62)), and the condition for adiabaticity (Eq. (C.65)), one can show that in the adiabatic limit, the dark-state polariton satisfies the propagation equation

$$\left(\frac{\partial}{\partial t} + V_\alpha(z, t) \frac{\partial}{\partial z} \right) \hat{\Psi}_\alpha(z, t) = -\frac{1}{2} \hat{\Psi}_\alpha(z, t) \frac{\partial}{\partial z} V_\alpha(z, t) \quad (\text{C.69})$$

where

$$V_\alpha(z, t) = \frac{|\Omega_c(t)|^2}{|\Omega_c(t)|^2 + |\kappa_s|^2 n(z) \sum_m p_m |R_{m,\alpha}(\beta)|^2} \quad (\text{C.70})$$

is the helicity dependent group velocity at position z corresponding to the control field Rabi frequency $\Omega_c(t)$. When the control field intensity is constant, the dark

state polariton at position z is given in terms of the polariton operator at an initial position z_0 by

$$\hat{\Psi}_\alpha(z, t) = \sqrt{\frac{V_\alpha(z_0)}{V_\alpha(z)}} \hat{\Psi}_\alpha\left(z_0, t - \int_{z_0}^z \frac{dz'}{V_\alpha(z')}\right). \quad (\text{C.71})$$

On the other hand, if one has the knowledge of the state of the system or dark-state polariton operator at a specific time t_0 , one may modify the above solution to find

$$\hat{\Psi}_\alpha(z, t) = \sqrt{\frac{V_\alpha(z_0(z, t))}{V_\alpha(z)}} \hat{\Psi}_\alpha(z_0(z, t), t_0), \quad (\text{C.72})$$

where the initial position z_0 is the solution to the integral equation

$$\int_{z_0(z, t)}^z \frac{dz'}{V_\alpha(z')} = t - t_0. \quad (\text{C.73})$$

From Eq. (C.71), one sees that as a signal pulse propagates into the medium, the reduction in group velocity associated with the increasing atomic density causes the spatial profile of the pulse to compress. At the same time, the polariton density $\langle \hat{\Psi}_\alpha^\dagger(z, t) \hat{\Psi}_\alpha(z, t) \rangle$ increases in proportion to $1/V_\alpha(z)$. This trade off between spatial compression of the pulse and increase in polariton density leaves the total polariton population unchanged [75].

The group velocity's dependence on the control field Rabi frequency allows one to manipulate the propagation dynamics of the dark state polariton provided that the Rabi frequency is changed sufficiently slowly. If the control field is turned off when the signal pulse overlaps with the ensemble, a portion of this signal pulse will be stored as the group velocity goes to zero. At this point, the dark state polariton consists entirely of a particular linear combination of hyperfine coherences. In the ideal case, one is able to store and retrieve the quantum state of the field with unit efficiency. In practice, however, there are two competing limitations which limit storage efficiency: the optical depth of the sample is not sufficient to contain the entire profile of the signal, or the finite width of the transparency window causes absorption of the off resonant frequency components. This absorption and the nonadiabatic effects of a

time varying control field are discussed in the context of a nondegenerate three level system in Ref. [75].

In addition, the magnetic field causes a reduction in retrieval efficiency for variable storage times. As discussed in Chapter 7, the Larmor precession of the spin wave causes the stored dark-state polariton into orthogonal bright state polariton [75] components. When the control field is turned on, these bright state components couple to the collective optical coherences, leading to spontaneous emission. In the next section, we will show how, in the simple case of a magnetic field along the quantization axis, the magnetic field induces a Larmor collapse of the dark-state polariton population for short storage times. The dynamics of storage in a uniform magnetic field along an arbitrary direction, leading to collapses and revivals of the storage efficiency, is discussed in Chapter 7.

C.5.1 Larmor collapse

In the presence of a magnetic field, a stored atomic collective excitation Larmor precesses out of the dark-state polariton mode into orthogonal collective excitations. This causes an apparent decoherence which can be calculated by evaluating the number of dark-state polaritons as a function of time. Assuming that there are initially $N_\alpha(0) = \int dz \langle \hat{\Psi}_\alpha^\dagger(z, 0) \hat{\Psi}_\alpha(z, 0) \rangle$ dark-state polaritons, and for a magnetic field oriented in the z -direction, we find the number of dark state polaritons in an unpolarized sample ($p_m = 1/(2F_b + 1)$) is given by

$$N_\alpha(t) = N_\alpha(0) \sum_m \sum_{m'} \frac{|R_{m,\alpha}(\beta) R_{m',\alpha}(\beta)|^2}{(\sum_m |R_{m,\alpha}(\beta)|^2)^2} \cos((m - m') \Delta_{ab} t) \quad (\text{C.74})$$

where again $\Delta_{ab} = (\frac{\mu_B}{\hbar} B_z) (g_a - g_b)$. For short storage times, we find

$$N_\alpha(t) \approx N_\alpha(0) \exp\left(-\frac{1}{2} \Upsilon_\alpha^2 (\Delta_{ab} t)^2\right) \quad (\text{C.75})$$

where

$$\Upsilon^2 = \sum_m \sum_{m'} \frac{|R_{m,\alpha}(\beta) R_{m',\alpha}(\beta)|^2}{(\sum_m |R_{m,\alpha}(\beta)|^2)^2} (m - m')^2 \quad (\text{C.76})$$

For the level scheme used in the experiment of Chapter 6 (with $\alpha = \beta$), $\Upsilon_\alpha^2 \approx 2.1$. We have used this model to estimate the strength of the magnetic field (assuming it is oriented along the z direction), given the time constant τ measured experimentally in Figure 6.5. We find the frequency to be

$$\frac{\Delta_{ab}}{2\pi} \approx 14 \text{ kHz} . \quad (\text{C.77})$$

We have used this value in obtaining the theoretical panels in Figure 6.3 and find good agreement with the experimental observations. Clearly from Eq. (C.74), we can predict the revival of dark-polariton number when $\Delta_{ab}t$ is a multiple of 2π . The revivals occur at $t_n^\parallel = 2\pi n / [(\frac{\mu_B}{\hbar} B_z) |g_a - g_b|] \approx \pi / [(\frac{\mu_B}{\hbar} B_z) |g_a|]$. By contrast, for a magnetic field perpendicular to the z axis, we find $t_n^\perp = 2\pi / [(\frac{\mu_B}{\hbar} B_z) |g_a|] = 2\pi / [(\frac{\mu_B}{\hbar} B_z) |g_b|]$, i.e., $t_n^\perp = 2t_n^\parallel$. The prediction and observation of revivals in retrieval efficiency is discussed in detail in Chapter 7.

APPENDIX D

PHOTON COUNTING STATISTICS FOR A PAIR OF CORRELATED SINGLE MODE FIELDS

In Chapters 5 and 6, we were concerned with photon counting statistics of two electromagnetic fields (the signal and idler) emitted from an atomic ensemble during a *write/read* process. The *write* laser beam probabilistically Raman scatters a photon into a detected signal mode. We showed in Chapter 3 that this process can be modeled as an effective nondegenerate parametric amplifier with the signal consisting of excitations of a single mode of the electromagnetic field. The idler is similarly described by a excitations of a hyperfine spin wave with a spatial profile determined by that of the collected signal mode. The read process then transfers the idler atomic excitation to a single mode of the idler electromagnetic field.

In this Appendix, we describe the details of the photodetection processes. By considering a general correlated state between signal and idler photons, we show how one arrives at photodetection probabilities from the elementary probability densities of a photoelectric detection event (PEDE) occurring at a specific time. In the systems we consider in this thesis, the dead time of the detector, i.e. the time the detector cannot register a PEDE after one has been registered previously, is on the order of the signal and idler mode durations. We account for this limitation by only calculating the elementary probability density for the first photoelectric detection time and neglecting all subsequent photon arrivals. Section D.2 describes how the state of the idler field is conditioned on a PEDE in the signal detector. In Section D.3, we apply these results

specifically to the nondegenerate parametric amplifier model.

Before examining the photodetection process, we define the general correlated signal-idler state. The results of this appendix can be readily generalized to statistical mixtures of correlated signal-idler states. We express the state produced by a generic *write* process in the interaction picture by the Schmidt decomposition

$$|\Psi\rangle_{si} = \sum_j g_j |\psi_j\rangle_s \otimes |\phi_j\rangle_i, \quad (\text{D.1})$$

where $\{|\psi_j\rangle_s\}$ and $\{|\phi_j\rangle_i\}$ are orthogonal sets of state vectors in the signal and idler Hilbert spaces respectively. We expand the states $|\psi_j\rangle_s$ and $|\phi_j\rangle_i$ in terms of Fock states of the single mode fields as

$$|\psi_j\rangle_s = \sum_{n=0}^{\infty} c_{n,j} \frac{\hat{a}^{\dagger n}}{\sqrt{n!}} |vac\rangle \quad (\text{D.2a})$$

$$|\phi_j\rangle_i = \sum_{n=0}^{\infty} d_{n,j} \frac{\hat{b}^{\dagger n}}{\sqrt{n!}} |vac\rangle, \quad (\text{D.2b})$$

where \hat{a} and \hat{b} are the signal and idler annihilation operators respectively. These operators are, in turn, given by

$$\hat{a}^{\dagger} \equiv \int_{-\infty}^{\infty} dt \psi_s(t) \hat{\psi}_s^{\dagger}(t) \quad (\text{D.3a})$$

$$\hat{b}^{\dagger} \equiv \int_{-\infty}^{\infty} dt \psi_i(t) \hat{\psi}_i^{\dagger}(t), \quad (\text{D.3b})$$

where $\psi_{\iota}(t)$ is the temporal envelope of field ι ($\iota = s, i$) which satisfies the normalization condition $\int_{-\infty}^{\infty} dt |\psi_{\iota}(t)|^2 = 1$, and $\hat{\psi}_{\iota}(t)$ is a field operator that annihilates a photon from field ι at time t and a position \vec{r} such that $r_{\parallel}^{(\iota)} = \hat{k}_{\iota} \cdot \vec{r} = 0$; \hat{k}_{ι} is the propagation direction of field ι . Neglecting diffraction, and following the treatment of Chapter 2 Section 2.1.4, we express the field operators in terms of plane wave annihilation operators as

$$\begin{aligned} \hat{\psi}_{\iota}(t) &\equiv \sqrt{c} \hat{\varphi}_{\lambda}^{(\iota)}(0, t) \\ &= \sqrt{\frac{c}{2\pi}} \int dk_{\parallel}^{(\iota)} e^{-ic(k_{\parallel}^{(\iota)} - k_{\iota})t} \hat{a}_{\lambda}^{(\iota)}(k_{\parallel}^{(\iota)}), \end{aligned} \quad (\text{D.4})$$

and

$$\hat{a}_\lambda^{(\iota)} \left(k_\parallel^{(\iota)} \right) = \int d^2 k_\perp f^{(\iota)*}(\vec{k}_\perp^{(\iota)}) \hat{a}_\lambda(\vec{k}), \quad (\text{D.5})$$

where $f^{(\iota)} \left(\vec{k}_\perp^{(\iota)} \right)$ is the transverse mode distribution of field ι as discussed in Chapter 2. The field operators $\hat{\psi}_\iota(t)$ and $\hat{\psi}_\iota^\dagger(t')$ satisfy the bosonic field commutation relations

$$\left[\hat{\psi}_\iota(t), \hat{\psi}_{\iota'}(t') \right] = 0 \quad (\text{D.6})$$

$$\left[\hat{\psi}_\iota(t), \hat{\psi}_{\iota'}^\dagger(t') \right] = \delta(t - t'). \quad (\text{D.7})$$

We find that it is useful to decompose the field operator $\hat{\psi}_{s[i]}(t)$ into a signal [idler] mode component and a component consisting of modes orthogonal to the signal [idler]; i.e.

$$\hat{\psi}_s(t) = \psi_s(t) \hat{a} + \delta \hat{\psi}_s(t) \quad (\text{D.8a})$$

$$\hat{\psi}_i(t) = \psi_i(t) \hat{b} + \delta \hat{\psi}_i(t). \quad (\text{D.8b})$$

In this Appendix, we assume the detectors D1, D2, and D3 are arranged to collect the signal and idler fields as illustrated in Figure 5.1. Detector D1 is placed so that it detects the signal field, and detectors D2 and D3 are placed after a 50:50 beam splitter, and detect the idler field. We model the non-unit detector efficiency η_k of detector Dk as a hypothetical detector of unit efficiency preceded by a beam-splitter, where the field arriving at the detector is described by the field operator $\hat{\psi}_{Dk}(t)$ which is related to the signal and idler fields by the effective beam-splitter relations

$$\hat{\psi}_{D1}(t) = \sqrt{\eta_1} \hat{\psi}_s(t) + \sqrt{1 - \eta_1} \hat{\zeta}_s(t) \quad (\text{D.9a})$$

$$\hat{\psi}_{D2}(t) = \sqrt{\eta_2/2} \hat{\psi}_i(t) + \sqrt{1 - \eta_2/2} \hat{\zeta}_2(t) \quad (\text{D.9b})$$

$$\hat{\psi}_{D3}(t) = \sqrt{\eta_3/2} \hat{\psi}_i(t) + \sqrt{1 - \eta_3/2} \hat{\zeta}_3(t) \quad (\text{D.9c})$$

where $\hat{\zeta}_k(t)$ are bosonic operators that account for coupling to degrees of freedom other than those detected. We assume that the modes associated with these noise

operators are in the vacuum state. As in Chapter 5, the detector efficiencies η_k include the effects of propagation losses, which for the idler, may occur before the beam splitter. Because of this, the noise operators $\hat{\zeta}_2(t)$ and $\hat{\zeta}_3(t)$ are not necessarily independent. This added complication will not have any effect on our calculations, however, since the noise modes are assumed to be in the vacuum state and we calculate only normally ordered expectation values.

D.1 Elementary Photon Counting Probability Densities and

In this section, we find an expression for the probability that a detector D_k registers a photoelectric detection event by considering the elementary probability density for the registration of the first PEDE occurring at time t_c . The elementary probability density for detecting a photon at time t_c with zero PEDE's prior to t_c is given by [111]

$$Q_k(t_c) = \langle \hat{Q}_k(t_c) \rangle \quad (\text{D.10})$$

where $\hat{Q}_k(t_c)$ is the projection operator

$$\begin{aligned} \hat{Q}_k(t_c) = & : \hat{\psi}_{Dk}^\dagger(t_c - z_k/c) \hat{\psi}_{Dk}(t_c - z_k/c) \\ & \times \exp \left(- \int_{-\infty}^{t_c - z_k/c} dt \hat{\psi}_{Dk}^\dagger(t) \hat{\psi}_{Dk}(t) \right) : , \end{aligned} \quad (\text{D.11})$$

z_k is an effective propagation distance for the origin, where the correlated state is created, and detector D_k , and $: \quad :$ denotes time and normal ordering. The operator $\hat{Q}_k(t_c)$ projects on to the subspace in which zero photons arrive at the hypothetical detector of unit efficiency D_k prior to t_c , with one arriving at t_c .

We calculate the elementary probability densities and total detection probabilities at detector D1; similar results will be true at detectors D2 and D3. In order to evaluate the elementary probability density $Q_1(t_c)$, it is necessary to evaluate the matrix element $\langle \psi_{j_2} | \hat{Q}_1(t_c) | \psi_{j_1} \rangle$. By exploiting Eqs. (D.8) and (D.9) and the assumption

that only the signal and idler modes are not in a vacuum state, we find that this matrix element is given by

$$\left\langle \psi_{j_2} \left| \hat{Q}_s(t_c) \right| \psi_{j_1} \right\rangle = \frac{d\varsigma_1(t_c)}{dt_c} \langle \psi_{j_2} | : \hat{a}^\dagger \hat{a} \exp(-\eta_1 \varsigma_s(t_c)) : | \psi_{j_1} \rangle, \quad (\text{D.12})$$

where $\varsigma_1(t_c) \equiv \int_{-\infty}^{t_c - z_1/c} dt |\psi_s(t)|^2$ is the fraction of the signal envelope that has arrived at detector D1 prior to t_c . We similarly define $\varsigma_k(t_c)$ ($k \in \{2, 3\}$) as $\varsigma_k(t_c) \equiv \int_{-\infty}^{t_c - z_k/c} dt |\psi_i(t)|^2$. By Taylor expanding the normally ordered exponential and substituting the expansion of the signal basis states in terms of Fock states (Eq. (D.2)), we find

$$\begin{aligned} \left\langle \psi_{j_2} \left| \hat{Q}_1(t_c) \right| \psi_{j_1} \right\rangle &= \frac{d\varsigma_1(t_c)}{dt_c} \sum_{n=1}^{\infty} n c_{n,j_2}^* c_{n,j_1} \\ &\times \sum_{\ell=0}^{n-1} (-\eta_1 \varsigma_1(t_c))^\ell \frac{(n-1)!}{\ell! (n-1-\ell)!} \end{aligned} \quad (\text{D.13})$$

$$= \frac{d\varsigma_1(t_c)}{dt_c} \sum_{n=1}^{\infty} n c_{n,j_2}^* c_{n,j_1} (1 - \eta_1 \varsigma_1(t_c))^{n-1}. \quad (\text{D.14})$$

Using the matrix elements of Eq. (D.14), we arrive at the elementary probability density

$$Q_1(t_c) = \text{Tr} \left(\hat{Q}_s(t_c) |\Psi\rangle_{si} \langle \Psi| \right) \quad (\text{D.15})$$

$$= \frac{d\varsigma_1(t_c)}{dt_c} \sum_j |g_j|^2 \sum_{n=1}^{\infty} n |c_{n,j}|^2 (1 - \eta_1 \varsigma_1(t_c))^{n-1} \quad (\text{D.16})$$

From $Q_k(t_c)$, we can calculate the total probability p_1 that at least one photoelectric detection event is registered at Dk;

$$p_k = \int_{-\infty}^{\infty} dt_c Q_k(t_c). \quad (\text{D.17})$$

The probability that a PEDE is registered at detector D1, is given by

$$p_1 = \sum_j |g_j|^2 \sum_{n=1}^{\infty} |c_{n,j}|^2 (1 - (1 - \eta_1)^n) \quad (\text{D.18})$$

It is straightforward to show that this result is equivalent to that which one would derive when the detection probability is calculated by

$$p_1 = \left\langle \Psi \left| \hat{P}_1 \right| \Psi \right\rangle_{si}, \quad (\text{D.19})$$

where

$$\hat{P}_k \equiv : \hat{1} - \exp(-\hat{d}_k^\dagger \hat{d}_k) : \quad (\text{D.20})$$

$$= \sum_{\ell=1}^{\infty} \frac{(-1)^{\ell-1}}{\ell!} : (\hat{d}_k^\dagger \hat{d}_k)^\ell :. \quad (\text{D.21})$$

The annihilation operator of the single populated mode of the field arriving at Dk \hat{d}_k is given by

$$\hat{d}_k = \begin{cases} \sqrt{\eta_k} \hat{a} + \sqrt{1-\eta_k} \hat{\xi}_k & : k = 1 \\ \sqrt{\eta_k/2} \hat{b} + \sqrt{1-\eta_k/2} \hat{\xi}_k & : k \in \{2, 3\} \end{cases}, \quad (\text{D.22})$$

where $\hat{\xi}_k$ are bosonic noise operators that account for the contributions from undetected modes. The operator $:\exp(-\hat{d}_k^\dagger \hat{d}_k):$ represents the projection onto the vacuum state of the detected mode \hat{d}_k [136]. The operator \hat{P}_k , therefore, represents the projection onto the subspace in which at least one PEDE is registered at Dk. This can be verified by direct calculation and comparison to Eq. (D.17). For the probability of registering a PEDE at D1, we have

$$\left\langle \hat{P}_1 \right\rangle = \text{Tr} \left(\hat{P}_1 |\Psi\rangle_{si} \langle \Psi| \right) \quad (\text{D.23})$$

$$= \sum_j |g_j|^2 \sum_{n=1}^{\infty} |c_{n,j}|^2 \sum_{\ell=1}^{\infty} (-1)^{\ell-1} \eta_1^\ell \frac{n!}{\ell!(n-\ell)!} \quad (\text{D.24})$$

$$= \sum_j |g_j|^2 \sum_{n=1}^{\infty} |c_{n,j}|^2 (1 - (1 - \eta_1)^n) \quad (\text{D.25})$$

$$= p_1. \quad (\text{D.26})$$

Since this is true for an arbitrary state $|\Psi\rangle_{si}$, we must also have the probability of a PEDE at any detector Dk given by

$$\begin{aligned} p_k &\equiv \int_{-\infty}^{\infty} dt_k Q(t_k) \\ &= \left\langle \hat{P}_k \right\rangle. \end{aligned} \quad (\text{D.27})$$

By generalizing the above arguments, one can calculate the probability of coincidences at detectors Dk_1 and Dk_2 ($k_1 \neq k_2$), i.e. the probability that at least one PEDE is registered at Dk_1 and Dk_2 . These probabilities are given by

$$p_{k_1 k_2} \equiv \int_{-\infty}^{\infty} dt_1 \int_{-\infty}^{\infty} dt_2 \left\langle \hat{Q}_{k_1}(t_1) \hat{Q}_{k_2}(t_2) \right\rangle \quad (\text{D.28})$$

$$= \left\langle \hat{P}_{k_1} \hat{P}_{k_2} \right\rangle. \quad (\text{D.29})$$

Similarly, the probability that at least one photoelectric detection event is registered at all three detectors is given by

$$p_{123} \equiv \int_{-\infty}^{\infty} dt_1 \int_{-\infty}^{\infty} dt_2 \int_{-\infty}^{\infty} dt_3 \left\langle \hat{Q}_1(t_1) \hat{Q}_2(t_2) \hat{Q}_3(t_3) \right\rangle \quad (\text{D.30})$$

$$= \left\langle \hat{P}_1 \hat{P}_2 \hat{P}_3 \right\rangle. \quad (\text{D.31})$$

D.1.1 The Low Intensity Limit

In this section, we show that when the probability of detecting a photon from the correlated state is sufficiently low, we recover the relationships between the field correlation functions and the probabilities p_k , the coincidences $p_{k_1 k_2}$, and p_{123} that were used in calculating correlation functions in Ref.[18].

In the limit of low intensity, the detection probabilities p_k provide good approximations for the mean number of photons in the signal or idler fields. For example, when $\eta_1 \langle \hat{a}^\dagger \hat{a} \rangle \ll 1$, the probability of detecting a photon at D1 is given by

$$p_1 = \left\langle : \hat{1} - \exp \left(-\hat{d}_1^\dagger \hat{d}_1 \right) : \right\rangle \quad (\text{D.32})$$

$$= \left\langle : \hat{1} - \exp \left(-\eta_1 \hat{a}^\dagger \hat{a} \right) : \right\rangle \quad (\text{D.33})$$

$$= \eta_1 \langle \hat{a}^\dagger \hat{a} \rangle + O \left(\left\langle : (\eta_1 \hat{a}^\dagger \hat{a})^2 : \right\rangle \right). \quad (\text{D.34})$$

Similar relationships exist for p_2 and p_3 when $\eta_k \langle \hat{b}^\dagger \hat{b} \rangle \ll 1$. In this limit, we may approximate the mean number of photons in a field using the measured detection

probabilities as

$$\langle \hat{a}^\dagger \hat{a} \rangle \approx \frac{p_1}{\eta_1} \quad (\text{D.35})$$

$$\begin{aligned} \langle \hat{b}^\dagger \hat{b} \rangle &\approx \frac{2p_2}{\eta_2} \\ &= \frac{2p_3}{\eta_3}. \end{aligned} \quad (\text{D.36})$$

In the low intensity limits considered above, one may also use the coincidence probability to estimate higher order moments of the fields. For instance, because the operators associated with the fields arriving at each detector commute, $[\hat{d}_2, \hat{d}_3^\dagger] = 0$, the coincidence between detectors D2 and D3 gives

$$\begin{aligned} p_{23} &= \left\langle : \left(\hat{1} - \exp \left(\hat{d}_2^\dagger \hat{d}_2 \right) \right) \right. \\ &\quad \times \left. \left(\hat{1} - \exp \left(\hat{d}_3^\dagger \hat{d}_3 \right) \right) : \right\rangle \end{aligned} \quad (\text{D.37})$$

$$= \frac{\eta_2 \eta_3}{4} \left\langle : \left(\hat{b}^\dagger \hat{b} \right)^2 : \right\rangle + O \left(\left\langle : \left(\eta \hat{b}^\dagger \hat{b} \right)^3 : \right\rangle \right). \quad (\text{D.38})$$

Similarly, the coincidence between detectors D1 and Dk ($k \in \{2, 3\}$) is

$$p_{1k} \approx \frac{\eta_1 \eta_k}{2} \left\langle : \hat{b}^\dagger \hat{b} \hat{a}^\dagger \hat{a} : \right\rangle. \quad (\text{D.39})$$

We therefore have the approximate expressions for second order correlation functions

$$\langle \hat{b}^{\dagger 2} \hat{b}^2 \rangle \approx \frac{4p_{23}}{\eta_2 \eta_3} \quad (\text{D.40})$$

$$\langle \hat{a}^\dagger \hat{b}^\dagger \hat{b} \hat{a} \rangle \approx \frac{2p_{12}}{\eta_2} \quad (\text{D.41})$$

$$\approx \frac{2p_{13}}{\eta_3}. \quad (\text{D.42})$$

Similarly, with the three detector configuration we consider in this appendix, we may approximate the third order correlation function

$$\langle \hat{b}^{\dagger 2} \hat{a}^\dagger \hat{a} \hat{b}^2 \rangle \approx \frac{4p_{123}}{\eta_1 \eta_2 \eta_3} \quad (\text{D.43})$$

Similar approximations were used to calculate the normalized second order correlation functions g_{si} and the anti-correlation parameter $\bar{\alpha}$ in Chapter 6.

D.2 Conditioning of the Idler Field by Detection of the Signal

Here, we determine how the detection of a signal photon at detector D1 conditions the state of the idler field. This is accomplished by modifying the above treatment to calculate detection probabilities using the elementary probability densities $Q_k(t_c)$. This procedure can be used to determine the conditioned atomic density matrix given the detection of the a signal (Eq. (5.3)) in Chapter 5. It will be shown that this procedure is equivalent to the application of the projection operator : $\hat{1} - \exp(-\hat{d}_1^\dagger \hat{d}_1)$: followed by a partial trace over the signal degrees of freedom.

We begin by determining how the state of the idler field is conditioned on the detection of the signal at a time t_s . This is accomplished by applying the projection operator $\hat{Q}_1(t_s)$ to the state $|\Psi\rangle_{si}$ and performing a partial trace over the signal degrees of freedom. This yields the conditioned density matrix $\hat{w}_{i|1}(t_s)$

$$\hat{w}_{i|1}(t_s) = \text{Tr}_s \left(\hat{Q}_s(t_c) |\Psi\rangle_{si} \langle \Psi| \right) \quad (\text{D.44})$$

$$= \frac{1}{Q_1(t_s)} \sum_{j_1, j_2} g_{j_1} g_{j_2}^* \langle \psi_{j_2} | \hat{Q}_1(t_s) | \psi_{j_1} \rangle_s | \phi_{j_1} \rangle_i \langle \phi_{j_2} | \quad (\text{D.45})$$

$$= \frac{1}{Q_1(t_s)} \frac{d\varsigma_1(t_s)}{dt_s} \sum_{j_1, j_2} g_{j_1} g_{j_2}^* | \phi_{j_1} \rangle_i \langle \phi_{j_2} | \\ \times \sum_{n=1}^{\infty} n c_{n,j_1} c_{n,j_2}^* (1 - \eta_1 \varsigma_1(t_s))^{n-1} \quad (\text{D.46})$$

If one does not have, or chooses to ignore, the arrival time of the signal photon, the conditioned state of the idler becomes a statistical mixture of the density matrices $\hat{w}_{i|1}(t_s)$. This statistical mixture is given by

$$\hat{\rho}_{i|1} = \int_{-\infty}^{\infty} dt_s \frac{Q_1(t_s)}{p_1} \hat{w}_{i|1}(t_s) \quad (\text{D.47})$$

$$= \frac{1}{p_1} \sum_{j_1, j_2} g_{j_1} g_{j_2}^* | \phi_{j_1} \rangle_i \langle \phi_{j_2} | \\ \times \sum_{n=1}^{\infty} c_{n,j_1} c_{n,j_2}^* (1 - (1 - \eta_1)^n). \quad (\text{D.48})$$

The density operator $\hat{\rho}_{i|1}$ represents the state of the idler given that at least one PEDE has been registered by the signal detector. This can be verified by applying the projection operator \hat{P}_1 to the original state $|\Psi\rangle_{si}$ and performing a partial trace over the signal Hilbert space. We have

$$\begin{aligned} \text{Tr}_s \left(\hat{P}_1 |\Psi\rangle_{si} \langle\Psi| \right) &= \sum_{j_1, j_2} g_{j_1} g_{j_2}^* |\phi_{j_1}\rangle_i \langle\phi_{j_2}| \\ &\times \sum_{n=1}^{\infty} c_{n,j_1} c_{n,j_2}^* \sum_{\ell=1}^{\infty} (-1)^{\ell-1} \eta_1^\ell \frac{n!}{\ell!(n-\ell)!} \end{aligned} \quad (\text{D.49})$$

$$= \sum_{j_1, j_2} g_{j_1} g_{j_2}^* |\phi_{j_1}\rangle_i \langle\phi_{j_2}| \sum_{n=1}^{\infty} c_{n,j_1} c_{n,j_2}^* (1 - (1 - \eta_1)^n) \quad (\text{D.50})$$

$$= \hat{\rho}_{i|1}. \quad (\text{D.51})$$

The conditioned density matrix $\hat{\rho}_{i|1}$ may readily be used to calculate the statistics of the idler field given that a signal had been detected. For example, we have the conditioned detection probabilities $p_{k|1} \equiv \text{Tr}(\hat{P}_k \hat{\rho}_{i|1})$ ($k \in \{2, 3\}$). Similarly, the conditioned coincidence probability $p_{23|1} = \text{Tr}(\hat{P}_2 \hat{P}_3 \hat{\rho}_{i|1})$.

D.3 Application to the Degenerate Parametric Amplifier

In this section, we apply the above treatment to the nondegenerate parametric amplifier. The state created by the two-mode nondegenerate parametric amplifier is given by Eq. (D.1) with

$$g_j = \frac{\tanh^j \chi}{\cosh \chi} \quad (\text{D.52a})$$

$$c_{n,j} = \delta_{n,j}, \quad (\text{D.52b})$$

where the parametric amplification process is parameterized by the dimensionless interaction strength χ . By applying Eq. (D.27), we arrive at the detection probabilities

for the parametric amplification process

$$p_k(\chi, \eta_k) = \begin{cases} \frac{\eta_k \sinh^2 \chi}{1 + \eta_k \sinh^2 \chi} & : k = 1 \\ \frac{\eta_k \sinh^2 \chi}{2(1 + (\eta_k/2) \sinh^2 \chi)} & : k = 2, 3 \end{cases}. \quad (\text{D.53})$$

If the state is conditioned on the detection of a signal photon at detector D1, the idler is described by the density matrix

$$\hat{\rho}_{i|1} = \frac{1}{p_1} \sum_{n=1}^{\infty} \frac{\tanh^{2n} \chi}{\cosh^2 \chi} (1 - (1 - \eta_1)^n) \frac{\hat{b}^{\dagger n} |vac\rangle \langle vac| \hat{b}^n}{n!}. \quad (\text{D.54})$$

Notice that if the signal detection process had unit efficiency $\eta_1 = 1$, then the conditioned density matrix is a thermal state with the vacuum component removed. With a non unit efficiency, however, the contributions from the higher photon number components $\frac{\hat{b}^{\dagger n} |vac\rangle \langle vac| \hat{b}^n}{n!}$ are more heavily weighted than they would be in a thermal state. It is this feature that leads to the large classical fluctuations in the protocol for generating deterministic single photons discussed in Chapter 5 for small maximum number of trials.

The conditioned density matrix (Eq. (D.54)) can be used to calculate the conditional detection probabilities $p_{k|1}$ ($k \in \{2, 3\}$), which are given by

$$p_{k|1} = \Pi(\eta_k/2; p_1, \eta_1), \quad (\text{D.55})$$

where

$$\Pi(\eta; p_1, \eta_1) = 1 - \frac{1}{p_1} \left(\frac{1}{1 + \eta \sinh^2 \chi} - \frac{1}{1 + (\eta_1 + \eta(1 - \eta_1)) \sinh^2 \chi} \right). \quad (\text{D.56})$$

Furthermore, one finds that the conditioned coincidence probability is given by

$$p_{23|1} = p_{2|1} + p_{3|1} - \Pi(\eta_k; p_1, \eta_1). \quad (\text{D.57})$$

REFERENCES

- [1] I. Chuang and M. Nielsen, *Quantum Computation and Quantum Information* (Cambridge University Press, 2000).
- [2] P. W. Shor, “Polynomial-Time Algorithms for Prime Factorization and Discrete Logarithms on a Quantum Computer,” *SIAM J. Comput.* **26**, 1484 (1997).
- [3] L. K. Grover, “Quantum Mechanics Helps in Searching for a Needle in a Haystack,” *Phys. Rev. Lett.* **79**, 325 (1997).
- [4] C. H. Bennett and G. Brassard, in *Proceedings of the International Conference on Computers, Systems and Signal Processing* (Indian Institute of Science, Bangalore, India, 1984).
- [5] A. K. Ekert, “Quantum Cryptography Based on Bell’s Theorem,” *Phys. Rev. Lett.* **67**, 661 (1991).
- [6] M. Kitagawa and M. Ueda, “Squeezed Spin States,” *Phys. Rev. A* **47**, 5138 (1993).
- [7] D. J. Wineland, W. M. Itano, F. L. Moore, and D. J. Heinzen, “Spin Squeezing and Reduced Quantum Noise in Spectroscopy,” *Phys. Rev. A* **46**, 6797(R) (1992).
- [8] W. M. Itano, J. C. Bergquist, J. J. Bollinger, J. M. Gilligan, D. J. Heinzen, F. L. Moore, M. G. Raizen, and D. J. Wineland, “Quantum Projection Noise: Population Fluctuations in Two-Level Systems,” *Phys. Rev. A* **47**, 3554 (1993).
- [9] D. J. Wineland, J. J. Bollinger, W. M. Itano, and D. J. Heinzen, “Squeezed Atomic States and Projection Noise in Spectroscopy,” *Phys. Rev. A* **50**, 67 (1994).
- [10] V. Meyer, M. A. Rowe, D. Kielpinski, C. A. Sackett, W. M. Itano, C. Monroe, and D. J. Wineland, “Experimental Demonstration of Entanglement-Enhanced Rotation Angle Estimation Using Trapped Ions,” *Phys. Rev. Lett.* **86**, 5870 (2001).
- [11] A. Kuzmich, N. Bigelow, and L. Mandel, “Atomic Quantum Non-Demolition Measurements and Squeezing,” *Europhys. Lett.* **42**, 481 (1998).
- [12] A. Kuzmich, L. Mandel, and N. P. Bigelow, “Generation of Spin Squeezing via Continuous Quantum Nondemolition Measurement,” *Phys. Rev. Lett.* **85**, 1594 (2000).

- [13] A. Kuzmich and T. A. B. Kennedy, “Nonsymmetric Entanglement of Atomic Ensembles,” *Phys. Rev. Lett.* **92**, 030407 (2004).
- [14] A. Sørensen, L.-M. Duan, J. I. Cirac, and P. Zoller, “Many-Particle Entanglement with Bose-Einstein Condensates,” *Nature* **409**, 63 (2001).
- [15] S. D. Jenkins and T. A. B. Kennedy, “Spin Squeezing in a Driven Bose-Einstein Condensate,” *Phys. Rev. A* **66**, 043621 (2002).
- [16] D. F. Walls and G. J. Milburn, *Quantum Optics* (Springer-Verlag, Berlin, 1994).
- [17] D. N. Matsukevich, T. Chanelière, M. Bhattacharya, S.-Y. Lan, S. D. Jenkins, T. A. B. Kennedy, and A. Kuzmich, “Entanglement of a Photon and a Collective Atomic Excitation,” *Phys. Rev. Lett.* **95**, 040405 (2005).
- [18] T. Chanelière, D. N. Matsukevich, S. D. Jenkins, S.-Y. Lan, T. A. B. Kennedy, and A. Kuzmich, “Storage and Retrieval of Single Photons Transmitted Between Remote Quantum Memories,” *Nature* **438**, 833 (2005), and accompanying Supplementary Information.
- [19] S. D. Jenkins, D. N. Matsukevich, T. Chanelière, A. Kuzmich, and T. A. B. Kennedy, “Theory of Dark-State Polariton Collapses and Revivals,” *Phys. Rev. A* **73**, 021803(R) (2006).
- [20] D. N. Matsukevich, T. Chanelière, S. D. Jenkins, S.-Y. Lan, T. A. B. Kennedy, and A. Kuzmich, “Observation of Dark State Polariton Collapses and Revivals,” *Phys. Rev. Lett.* **96**, 033601 (2006).
- [21] D. N. Matsukevich, T. Chanelière, S. D. Jenkins, S.-Y. Lan, T. A. B. Kennedy, and A. Kuzmich, “Entanglement of Remote Atomic Qubits,” *Phys. Rev. Lett.* **96**, 030405 (2006).
- [22] T. Chanelière, D. N. Matsukevich, S. D. Jenkins, T. A. B. Kennedy, M. S. Chapman, and A. Kuzmich, “Quantum Telecommunication Based on Atomic Cascade Transitions,” *Phys. Rev. Lett.* **96**, 093604 (2006).
- [23] D. N. Matsukevich, T. Chanelière, S. D. Jenkins, S.-Y. Lan, T. A. B. Kennedy, and A. Kuzmich, “Deterministic Single Photons via Conditional Quantum Evolution,” *Phys. Rev. Lett.* **97**, 013601 (2006).
- [24] C. H. Bennett, G. Brassard, C. Crépeau, R. Jozsa, A. Peres, and W. K. Wootters, “Teleporting an Unknown Quantum State via Dual Classical and Einstein-Podolsky-Rosen Channels,” *Phys. Rev. Lett.* **70**, 1895 (1993).
- [25] D. Bouwmeester, J.-W. Pan, K. Mattle, M. Eible, H. Weinfurter, and A. Zeilinger, “Experimental Quantum Teleportation,” *Nature* **390**, 575 (1997).
- [26] D. Boschi, S. Branca, F. De Martini, L. Hardy, and S. Popescu, “Experimental Realization of Teleporting an Unknown Pure Quantum State via Dual Classical and Einstein-Podolsky-Rosen Channels,” *Phys. Rev. Lett.* **80**, 1121 (1998).

- [27] M. Aspelmeyer, H. R. Böhm, T. Gyatso, T. Jennewein, R. Kaltenbaek, M. Lindenthal, G. Molina-Terriza, A. Poppe, K. Resch, M. Taraba, R. Ursin, P. Walther, and A. Zeilinger, “Long-Distance Free-Space Distribution of Quantum Entanglement,” *Science* **301**, 621 (2003).
- [28] N. A. Peters, J. T. Barreiro, M. E. Goggin, T.-C. Wei, and P. G. Kwiat, “Remote State Preparation: Arbitrary Remote Control of Photon Polarization,” *Phys. Rev. Lett.* **94**, 150502 (2005).
- [29] H.-J. Briegel, W. Dür, J. I. Cirac, and P. Zoller, “Quantum Repeaters: The Role of Imperfect Local Operations in Quantum Communication,” *Phys. Rev. Lett.* **81**, 5932 (1998).
- [30] W. Dür, H.-J. Briegel, J. I. Cirac, and P. Zoller, “Quantum Repeaters Based on Entanglement Purification,” *Phys. Rev. A* **59**, 169 (1999).
- [31] E. Hagley, X. Maître, G. Nogues, C. Wunderlich, M. Brune, J. M. Raimond, and S. Haroche, “Generation of Einstein-Podolsky-Rosen Pairs of Atoms,” *Phys. Rev. Lett.* **79**, 1 (1997).
- [32] B. B. Blinov, D. L. Moehring, L.-M. Duan, and C. Monroe, “Observation of Entanglement Between a Single Trapped Atom and a Single Photon,” *Nature* **428**, 153 (2004).
- [33] D. L. Moehring, M. J. Madsen, B. B. Blinov, and C. Monroe, “Experimental Bell Inequality Violation with an Atom and a Photon,” *Phys. Rev. Lett.* **93**, 090410 (2004).
- [34] L.-M. Duan, B. B. Blinov, D. L. Moehring, and C. Monroe, “Scalable Trapped Ion Quantum Computation with a Probabilistic Ion-Photon Mapping,” *Quantum Inf. Comput.* **4**, 165 (2004).
- [35] S. Lloyd, M. S. Shahriar, J. H. Shapiro, and P. R. Hemmer, “Long Distance, Unconditional Teleportation of Atomic States via Complete Bell State Measurements,” *Phys. Rev. Lett.* **87**, 167903 (2001).
- [36] A. Kuhn, M. Hennrich, and G. Rempe, “Deterministic Single-Photon Source for Distributed Quantum Networking,” *Phys. Rev. Lett.* **89**, 067901 (2002).
- [37] J. McKeever, A. Boca, A. D. Boozer, R. Miller, J. R. Buck, A. Kuzmich, and H. J. Kimble, “Deterministic Generation of Single Photons from One Atom Trapped in a Cavity,” *Science* **303**, 1992 (2004).
- [38] J. Volz, M. Weber, D. Schlenk, W. Rosenfeld, J. Vrana, K. Saucke, C. Kursiefer, and H. Weinfurter, “Observation of Entanglement of a Single Photon with a Trapped Atom,” *Phys. Rev. Lett.* **96**, 030404 (2006), quant-ph/0511183.

- [39] L. Childress, J. M. Taylor, A. S. Sørensen, and M. D. Lukin, “Fault-Tolerant Quantum Communication Based on Solid-State Photon Emitters,” *Phys. Rev. Lett.* **96**, 070504 (2006).
- [40] A. Kuzmich and E. S. Polzik, in *Quantum information with continuous variables*, eds S. L. Braunstein and A. K. Pati, Kluwer, 2003.
- [41] M. D. Lukin, “Colloquium: Trapping and Manipulating Photon States in Atomic Ensembles,” *Rev. Mod. Phys.* **75**, 457 (2003).
- [42] M. Bajcsy, A. S. Zibrov, and M. D. Lukin, “Stationary Pulses of Light in an Atomic Medium,” *Nature* **426**, 638 (2003).
- [43] A. S. Zibrov, A. B. Matsko, O. Kocharovskaya, Y. V. Rostovtsev, G. R. Welch, and M. O. Scully, “Transporting and Time Reversing Light via Atomic Coherence,” *Phys. Rev. Lett.* **88**, 103601 (2002).
- [44] D. F. Phillips, A. Fleischhauer, A. Mair, R. L. Walsworth, and M. D. Lukin, “Storage of Light in Atomic Vapor,” *Phys. Rev. Lett.* **86**, 783 (2001).
- [45] C. Liu, Z. Dutton, C. H. Behroozi, and L. V. Hau, “Observation of Coherent Optical Information Storage in an Atomic Medium Using Halted Light Pulses,” *Nature* **409**, 490 (2001).
- [46] M. Johnsson and K. Mølmer, “Storing Quantum Information in a Solid Using Dark-State Polaritons,” *Phys. Rev. A* **70**, 032320 (2004).
- [47] L.-M. Duan, M. D. Lukin, J. I. Cirac, and P. Zoller, “Long-Distance Quantum Communication with Atomic Ensembles and Linear Optics,” *Nature* **414**, 413 (2001).
- [48] M. Saffman and T. J. Walker, “Entangling Single- and N-Atom Qubits for Fast Quantum State Detection and Transmission,” *Phys. Rev. A* **72**, 042302 (2005).
- [49] M. Saffman and T. J. Walker, “Publisher’s Note: Entangling Single- and N-Atom Qubits for Fast Quantum State Detection and Transmission [Phys. Rev. A **72**, 042302 (2005)],” *Phys. Rev. A* **72**, 049903(E) (2005).
- [50] D. D. Yavuz, P. B. Kulatunga, E. Urban, T. A. Johnson, N. Proite, T. Henage, T. G. Walker, and M. Saffman, “Fast Ground State Manipulation of Neutral Atoms in Microscopic Optical Traps,” *Phys. Rev. Lett.* **96**, 063001 (2006).
- [51] A. Kuzmich, W. P. Bowen, A. D. Boozer, A. Boca, C. W. Chou, L. M. Duan, and H. J. Kimble, “Generation of Nonclassical Photon Pairs for Scalable Quantum Communication with Atomic Ensembles,” *Nature* **423**, 731 (2003).
- [52] C. H. van der Wall, M. D. Eisaman, A. André, R. L. Walsworth, D. F. Phillips, A. S. Zibrov, and M. D. Lukin, “Atomic Memory for Correlated Photon States,” *Science* **301**, 196 (2003).

- [53] W. Jiang, C. Han, P. Xue, L.-M. Duan, and G.-C. Guo, “Nonclassical Photon Pairs Generated from a Room-Temperature Atomic Ensemble,” *Phys. Rev. A* **69**, 043819 (2004).
- [54] C. W. Chou, S. V. Polyakov, A. Kuzmich, and H. J. Kimble, “Single-Photon Generation from Stored Excitation in an Atomic Ensemble,” *Phys. Rev. Lett.* **92**, 213601 (2004).
- [55] M. D. Eisaman, L. Childress, A. André, F. Massou, A. S. Zibrov, and M. D. Lukin, “Shaping Quantum Pulses of Light Via Coherent Atomic Memory,” *Phys. Rev. Lett.* **93**, 233602 (2004).
- [56] S. V. Polyakov, C. W. Chou, D. Felinto, and H. J. Kimble, “Temporal Dynamics of Photon Pairs Generated by an Atomic Ensemble,” *Phys. Rev. Lett.* **93**, 263601 (2004).
- [57] D. N. Matsukevich and A. Kuzmich, “Quantum State Transfer Between Matter and Light,” *Science* **306**, 663 (2004), similar results were reported a year later in C. W. Chou *et al.*, *Nature* **438**, 828 (2005).
- [58] D. A. Braje, V. Balić, S. Goda, G. Y. Yin, and S. E. Harris, “Frequency Mixing Using Electromagnetically Induced Transparency in Cold Atoms,” *Phys. Rev. Lett.* **93**, 183601 (2004).
- [59] V. Balić, D. A. Braje, P. Kolchin, G. Y. Yin, and S. E. Harris, “Generation of Paired Photons with Controllable Waveforms,” *Phys. Rev. Lett.* **94**, 183601 (2005).
- [60] P. Michler, A. Kiraz, C. Becher, W. V. Schoenfeld, P. M. Petroff, L. Zhang, E. Hu, and A. Imamoglu, “A Quantum Dot Single-Photon Turnstile Device,” *Science* **290**, 2282 (2000).
- [61] C. Santori, M. Pelton, G. Solomon, Y. Dale, and Y. Yamamoto, “Triggered Single Photons from a Quantum Dot,” *Phys. Rev. Lett.* **86**, 1502 (2001).
- [62] M. Pelton, C. Santori, J. Vučković, B. Z. G. S. Solomon, J. Plant, and Y. Yamamoto, “Efficient Source of Single Photons: A Single Quantum Dot in a Micropost Microcavity,” *Phys. Rev. Lett.* **89**, 233602 (2002).
- [63] R. Brouri, A. Beveratos, J.-P. Poizat, and P. Grangier, “Photon Antibunching in the Fluorescence of Individual Color Centers in Diamond,” *Opt. Lett.* **25**, 1294 (2000).
- [64] C. Kurtsiefer, S. Mayer, P. Zadra, and H. Weinfurter, “Stable Solid-State Source of Single Photons,” *Phys. Rev. Lett.* **85**, 290 (2000).
- [65] B. Darquie, M. P. A. Jones, J. Dingjan, J. Beugnon, S. Bergamini, Y. Sortais, G. Messin, A. Browaeys, and P. Grangier, “Controlled Single-Photon Emission from a Single Trapped Two-Level Atom,” *Science* **309**, 454 (2005).

- [66] M. Keller, B. Lange, K. Hayasaka, W. Lange, and H. Walther, “Continuous Generation of Single Photons with Controlled Waveform in an Ion-Trap Cavity System,” *Nature* **431**, 1075 (2004).
- [67] B. Lounis and W. E. Moerner, “Single Photons on Demand from a Single Molecule at Room Temperature,” *Nature* **407**, 491 (2000).
- [68] M. G. Raymer and I. A. Walmsley, in *Progress in Optics*. Vol. XXVIII, (ed. Wolf., E.) 181-270 (North-Holland, Amsterdam, 1996).
- [69] M. Fleischhauer and M. D. Lukin, “Dark-state Polaritons in Electromagnetically Induced Transparency,” *Phys. Rev. Lett.* **84**, 5094 (2000).
- [70] B. Julsgaard, J. Sherson, J. I. Cirac, J. Fiurášek, and E. S. Polzik, “Experimental Demonstration of Quantum Memory for Light,” *Nature* **432**, 482 (2004).
- [71] S. E. Harris, “Electromagnetically Induced Transparency,” *Phys. Today* **50**, 36 (1997).
- [72] M. O. Scully and M. S. Zubairy, *Quantum Optics* (Cambridge Univ. Press, Cambridge, 1997).
- [73] L. V. Hau, S. E. Harris, Z. Dutton, and C. H. Behroozi, “Light Speed Reduction to 17 Metres per Second in an Ultracold Atomic Gas,” *Nature* **397**, 594 (1999).
- [74] A. Mair, J. Hager, D. F. Phillips, R. L. Walsworth, and M. D. Lukin, “Phase Coherence and Control of Stored Photonic Information,” *Phys. Rev. A* **65**, 031802(R) (2002).
- [75] M. Fleischhauer and M. D. Lukin, “Quantum Memory for Photons: Dark-State Polaritons,” *Phys. Rev. A* **65**, 022314 (2002).
- [76] O. A. Collins and *et al*, in preparation.
- [77] M. D. Eisaman, A. André, F. Massou, M. Fleischhauer, A. S. Zibrov, and M. D. Lukin, “Electromagnetically Induced Transparency with Tunable Single-Photon Pulses,” *Nature* **438**, 837 (2005).
- [78] C. Cohen-Tannoudji, J. Dupont-Roc, and G. Grynberg, *Photons and Atoms, Introduction to Quantum Electrodynamics* (Wiley, New York, 1989).
- [79] C. Cohen-Tannoudji, J. Dupont-Roc, and G. Grynberg, *Atom-Photon Interactions, Basic Processes and Applications* (Wiley, New York, 1992).
- [80] H. J. Metcalf and P. van der Strated, *Laser Cooling and Trapping* (Springer, New York, 1999), chap. 4, and references therein.
- [81] D. A. Steck, “Rubidium 87 D Line Data,” <http://steck.us/alkalidata/>; accessed July 2006 2003.

- [82] H. J. Metcalf and P. van der Strated, *Laser Cooling and Trapping* (Springer, New York, 1999), and references therein.
- [83] M. E. Rose, *Elementary Theory of Angular Momentum* (Dover, New York, 1957).
- [84] M. E. Rose, *Elementary Theory of Angular Momentum* (Dover, New York, 1957), chap. 6.
- [85] S. D. Jenkins, D. Salerno, S. Minardi, G. Tamošauskas, T. A. B. Kennedy, and P. Di Trapani, “Quantum-Noise-Initiated Symmetry Breaking of Spatial Solitons,” *Phys. Rev. Lett.* **95**, 203902 (2005).
- [86] S. Haroche, J. M. Raimond, and M. Brune, in *Experimental Quantum Computation and information*, eds. F. de Martini and C. Monroe), 37-66 (Proc. Int. School of Physics Enrico Fermi, course CXLVIII, IOS Press, Amsterdam, 2002).
- [87] D. A. Braje and S. E. Harris, private communication.
- [88] L. Mandel, “Quantum Effects in One-Photon and Two-Photon Interference,” *Rev. Mod. Phys.* **71**, S274 (1999).
- [89] A. Zeilinger, “Experiment and the Foundations of Quantum Physics,” *Rev. Mod. Phys.* **71**, S288 (1999).
- [90] L. Mandel and E. Wolf, *Optical Coherence and Quantum Optics* (Cambridge University Press, 1995).
- [91] J. F. Clauser, M. A. Horne, A. Shimony, and R. A. Holt, “Proposed Experiment to Test Local Hidden-Variable Theories,” *Phys. Rev. Lett.* **23**, 880 (1969).
- [92] L. M. Duan, J. I. Cirac, and P. Zoller, “Three-Dimensional Theory for Interaction between Atomic Ensembles and Free-Space Light,” *Phys. Rev. A* **66**, 023818 (2002).
- [93] T. A. B. Kennedy, “Photon Polarization Correlations using an Atomic Ensemble,” 2005, unpublished notes.
- [94] M. Arndt, S. I. Kanorsky, A. Weis, and T. W. Hänsch, “Long Electronic Spin Relaxation Times of Cs Atoms in Solid ^4He ,” *Phys. Rev. Lett.* **74**, 1359 (1995).
- [95] N. E. Rehler and J. H. Eberly, “Superradiance,” *Phys. Rev. A* **3**, 1735 (1971).
- [96] R. Friedberg and S. R. Hartmann, “Superradiant lifetime: Its Definitions and Relation to Absorption Length,” *Phys. Rev. A* **13**, 495 (1976).
- [97] Q. H. F. Vreken, H. M. J. Hikspoors, and H. M. Gibbs, “Quantum Beats in Superfluorescence in Atomic Cesium,” *Phys. Rev. Lett.* **38**, 764 (1977).

- [98] J. D. Franson, “Bell inequality for position and time,” *Phys. Rev. Lett.* **62**, 2205 (1989).
- [99] D. Branning, W. P. Grice, R. Erdmann, and I. A. Walmsley, “Engineering the Indistinguishability and Entanglement of Two Photons,” *Phys. Rev. Lett.* **83**, 955 (1999).
- [100] C. K. Law, I. A. Walmsley, and J. H. Eberly, “Continuous Frequency Entanglement: Effective Finite Hilbert Space and Entropy Control,” *Phys. Rev. Lett.* **84**, 5304 (2000).
- [101] A. Aspect, P. Grangier, and G. Roger, “Experimental Tests of Realistic Local Theories via Bell’s Theorem,” *Phys. Rev. Lett.* **47**, 460 (1981).
- [102] P. Grangier, G. Roger, and A. Aspect, “Experimental Evidence for a Photon Anticorrelation Effect on a Beam Splitter: A New Light on Single-Photon Interferences,” *Europhys. Lett.* **1**, 173 (1986).
- [103] C. Cabrillo, J. I. Cirac, P. Garcia-Fernández, and P. Zoller, “Creation of Entangled States of Distant Atoms by Interference,” *Phys. Rev. A* **59**, 1025 (1999).
- [104] E. Knill, R. Laflamme, and G. J. Milburn, “A Scheme for Efficient Quantum Computation with Linear Optics,” *Nature* **409**, 46 (2001).
- [105] T. B. Pittman, B. C. Jacobs, and J. D. Franson, “Single Photons on Pseudodemand from Stored Parametric Down-Conversion,” *Phys. Rev. A* **66**, 042303 (2002).
- [106] E. Jeffrey, N. A. Peters, and P. G. Kwiat, “Towards a Periodic Deterministic Source of Arbitrary Single-Photon States,” *New J. Phys.* **6**, 100 (2004).
- [107] C. K. Hong and L. Mandel, “Experimental Realization of a Localized One-Photon State,” *Phys. Rev. Lett.* **56**, 58 (1986).
- [108] A. T. Black, J. K. Thompson, and V. Vuletić, “On-Demand Superradiant Conversion of Atomic Spin Gratings into Single Photons with High Efficiency,” *Phys. Rev. Lett.* **95**, 133601 (2005).
- [109] W. P. Smith, J. E. Reiner, L. A. Orozco, S. Kuhr, and H. M. Wiseman, “Capture and Release of a Conditional State of a Cavity QED System by Quantum Feedback,” *Phys. Rev. Lett.* **89**, 133601 (2002).
- [110] T. Fischer, P. Maunz, P. W. H. Pinkse, T. Puppe, and G. Rempe, “Feedback on the Motion of a Single Atom in an Optical Cavity,” *Phys. Rev. Lett.* **88**, 163002 (2002).
- [111] C. W. Gardiner and P. Zoller, *Quantum Noise: a Handbook of Markovian and Non-Markovian Quantum Stochastic Methods with Applications to Quantum Optics*, 2nd ed. (Springer-Verlag, Berlin, 2000).

- [112] R. Loudon, *The Quantum Theory of Light*, third ed. (Oxford University Press, New York, 2000).
- [113] A. B. U'Ren, C. Silberhorn, J. L. Ball, K. Banaszek, and I. A. Walmsley, "Characterization of the Nonclassical Nature of Conditionally Prepared Single Photons," *Phys. Rev. A* **72**, 021802(R) (2005).
- [114] J. F. Clauser, "Experimental Distinction Between the Quantum and Classical Field-Theoretic Predictions for the Photoelectric Effect," *Phys. Rev. D* **9**, 853 (1974).
- [115] H. Y. Ling, Y.-Q. Li, and M. Xiao, "Coherent Population Trapping and Electromagnetically Induced Transparency in Multi-Zeeman-Sublevel Atoms," *Phys. Rev. A* **53**, 1014 (1996).
- [116] K. J. Boller, A. Imamoglu, and S. E. Harris, "Observation of Electromagnetically Induced Transparency," *Phys. Rev. Lett.* **66**, 2593 (1991).
- [117] D. Felinto, C. W. Chou, H. de Riedmatten, S. V. Polyakov, and H. J. Kimble, "Control of Decoherence in the Generation of Photon Pairs from Atomic Ensembles," *Phys. Rev. A* **72**, 053809 (2005).
- [118] J. Schmiedmayer, C. R. Ekstrom, M. S. Chapman, T. D. Hammond, and D. E. Pritchard, "Magnetic Coherences in Atom Interferometry," *J. Physique II* **4**, 2029 (1994).
- [119] G. A. Smith, S. Chaudhury, A. Silberfarb, I. H. Deutsch, and P. S. Jessen, "Continuous Weak Measurement and Nonlinear Dynamics in a Cold Spin Ensemble," *Phys. Rev. Lett.* **93**, 163602 (2004).
- [120] Y. L. Lim, S. D. Barrett, A. Beige, P. Kok, and L. C. Kwek, "Repeat-Until-Success Quantum Computing Using Stationary and Flying Qubits," *Phys. Rev. A* **73**, 012304 (2006).
- [121] C. A. Sackett, D. Kielpinski, B. E. King, C. Langer, V. Meyer, C. J. Myatt, M. Rowe, Q. A. Turchette, W. M. Itano, D. J. Wineland, and C. Monroe, "Experimental Entanglement of Four Particles," *Nature* **404**, 256 (2000).
- [122] S. Bose, P. L. Knight, M. B. Plenio, and V. Vedral, "Proposal for Teleportation of an Atomic State via Cavity Decay," *Phys. Rev. Lett.* **83**, 5158 (1999).
- [123] A. S. Sørensen and K. Mølmer, "Probabilistic Generation of Entanglement in Optical Cavities," *Phys. Rev. Lett.* **90**, 127903 (2003).
- [124] L.-M. Duan, "Entangling Many Atomic Ensembles through Laser Manipulation," *Phys. Rev. Lett.* **88**, 170402 (2002).
- [125] M. Weber, *Quantum Optical Experiments Towards Atom-Photon Entanglement*, PhD thesis University of Munich 2005.

- [126] H. M. Wiseman and J. A. Vaccaro, “Entanglement of Indistinguishable Particles Shared Between Two Parties,” *Phys. Rev. Lett.* **91**, 097902 (2003).
- [127] B. Julsgaard, A. Kozhekin, and E. S. Polzik, “Experimental Long-Lived Entanglement of two Macroscopic Objects,” *Nature* **413**, 400 (2001).
- [128] D. Tupa and L. W. Anderson, “Effect of Radiation Trapping on the Polarization of an Optically Pumped Alkali-Metal Vapor in a Weak Magnetic Field,” *Phys. Rev. A* **36**, 2142 (1987).
- [129] S. J. van Enk and H. J. Kimble, “COMMENT ON ”Quantum State Transfer Between Matter and Light”,” *Science* **309**, 1187b (2005).
- [130] D. N. Matsukevich and A. Kuzmich, “RESPONSE TO COMMENT ON ”Quantum State Transfer Between Matter and Light” .,” *Science* **309**, 1187c (2005).
- [131] Q. A. Turchette, C. S. Wood, B. E. King, C. J. Myatt, D. Leibfried, W. M. Itano, C. Monroe, and D. J. Wineland, “Deterministic Entanglement of Two Trapped Ions,” *Phys. Rev. Lett.* **81**, 3631 (1998).
- [132] H.-H. Jen and *et al*, in preparation.
- [133] R. Bonifacio and L. A. Lugiato, “Cooperative Radiation Processes in Two-Level Systems: Superfluorescence,” *Phys. Rev. A* **11**, 1507 (1975).
- [134] R. Bonifacio and L. A. Lugiato, “Cooperative Radiation Processes in Two-Level Systems: Superfluorescence. II,” *Phys. Rev. A* **12**, 587 (12).
- [135] L. N. Trefethen, *Spectral Methods in MATLAB* (Society of Industrial and Applied Mathematics, Philadelphia, 2000).
- [136] M. J. Collett, “Exact Density-Matrix Calculations for Simple Open Systems,” *Phys. Rev. A* **38**, 2233 (1988).